UNIVERSIDADE FEDERAL DE MINAS GERAIS

Escola de Engenharia

Programa de Pós-Graduação em Engenharia Elétrica

Gabriel Vilkn Ramos

A ZERO HARMONIC DISTORTION GRID-FORMING CONVERTER FOR MEDIUM VOLTAGE SYSTEMS

Belo Horizonte

2025

Gabriel Vilkn Ramos

A ZERO HARMONIC DISTORTION GRID-FORMING CONVERTER FOR MEDIUM VOLTAGE SYSTEMS

Tese apresentada ao Programa de Pós-Graduação em Engenharia Elétrica da Universidade Federal de Minas Gerais, como requisito à obtenção do grau de Doutor em Engenharia Elétrica.

Orientador: Prof. Dr. Braz de Jesus Cardoso Filho
Coorientador: Prof. Dr. Thiago Morais Parreiras

Belo Horizonte
2025

Ramos, Gabriel Vilkn.
R175z A zero harmonic distortion grid-forming converter for medium voltage systems [recurso eletrônico] / Gabriel Vilkn Ramos. - 2025.
1 recurso online (216 f. : il., color.) : pdf.

Orientador: Braz de Jesus Cardoso Filho.
Coorientador: Thiago Morais Parreiras.

Tese (doutorado) - Universidade Federal de Minas Gerais, Escola de Engenharia.

Inclui bibliografia.
Exigências do sistema: Adobe Acrobat Reader.

1. Engenharia elétrica - Teses. 2. Geração distribuída de energia elétrica - Teses. 3. Sistemas elétricos de potência 4. Conversores eletrônicos - Teses. I. Cardoso Filho, Braz de Jesus. II. Parreiras, Thiago Morais. III.Universidade Federal de Minas Gerais. Escola de Engenharia. IV. Título.

CDU: 621.3(043)

Ficha catalográfica elaborada pelo bibliotecário Reginaldo César Vital dos Santos - CRB-6/2165
Biblioteca Prof. Mário Werneck - Escola de Engenharia da UFMG

UNIVERSIDADE FEDERAL DE MINAS GERAIS

Escola de Engenharia

COLEGIADO DO CURSO DE PÓS-GRADUAÇÃO EM ENGENHARIA ELÉTRICA

FOLHA DE APROVAÇÃO

"A Zero Harmonic Distortion Grid-forming Converter For Medium Voltage Systems"

Gabriel Vilkn Ramos

Tese de Doutorado submetida à Banca Examinadora designada pelo Colegiado do Programa de Pós-Graduação em Engenharia Elétrica da Escola de Engenharia da Universidade Federal de Minas Gerais, como requisito para obtenção do grau de Doutor em Engenharia Elétrica.

Aprovada em 05 de dezembro de 2025.

Por:

Prof. Dr. Braz de Jesus Cardoso Filho
DEE (UFMG) - Orientador

Prof. Dr. Thiago Morais Parreiras
DEE (CEFET-MG) - Coorientador

Prof. Dr. Danilo Iglesias Brandão
DEE (UFMG)

Prof. Dr. Sidelmo Magalhães Silva
DEE (UFMG)

Prof. Dr. José Antenor Pomílio
DEE (Unicamp)

Prof. Dr. Luiz Antônio de Souza Ribeiro
DEE (UFMA)

Documento assinado eletronicamente por **Braz de Jesus Cardoso Filho**, **Professor do Magistério Superior**, em 17/12/2025, às 11:56, conforme horário oficial de Brasília, com fundamento no art. 5º do Decreto nº 10.543, de 13 de novembro de 2020.

Documento assinado eletronicamente por **Sidelmo Magalhaes Silva**, **Professor do Magistério Superior**, em 23/12/2025, às 13:47, conforme horário oficial de Brasília, com fundamento no art. 5º do Decreto nº 10.543, de 13 de novembro de 2020.

Documento assinado eletronicamente por **Thiago Morais Parreiras**, **Professor(a)**, em 23/12/2025, às 15:12, conforme horário oficial de Brasília, com fundamento no art. 5º do Decreto nº 10.543, de 13 de novembro de 2020.

Documento assinado eletronicamente por **Danilo Iglesias Brandao**, **Professor do Magistério Superior**, em 23/12/2025, às 17:02, conforme horário oficial de Brasília, com fundamento no art. 5º do Decreto nº 10.543, de 13 de novembro de 2020.

Documento assinado eletronicamente por **Jose Antenor Pomilio**, **Usuário Externo**, em 30/12/2025, às 14:20, conforme horário oficial de Brasília, com fundamento no art. 5º do Decreto nº 10.543, de 13 de novembro de 2020.

Documento assinado eletronicamente por **Luiz Antonio de Souza Ribeiro**, **Usuário Externo**, em 05/01/2026, às 18:24, conforme horário oficial de Brasília, com fundamento no art. 5º do Decreto nº 10.543, de 13 de novembro de 2020.

A autenticidade deste documento pode ser conferida no site https://sei.ufmg.br/sei/controlador_externo.php?acao=documento_conferir&id_orgao_acesso_externo=0, informando o código verificador **4782561** e o código CRC **ACC35978**.

Referência: Processo nº 23072.273736/2025-13 SEI nº 4782561

A Deus, à minha família e aos meus amigos.

Acknowledgements

Ao professor Braz de Jesus Cardoso Filho, meu orientador acadêmico, pelo apoio, pela oportunidade, pelos ensinamentos de vida, pela confiança depositada e pelo acolhimento no Laboratório Tesla. As lições mais importantes que aprendi com você foram, sem dúvida, as não técnicas.

Ao professor Thiago Morais Parreiras, meu coorientador, agradeço pela parceria e pela orientação atenta aos mínimos detalhes. Obrigado pela oportunidade de dar continuidade ao seu trabalho.

Aos professores Danilo Iglesias Brandão e Sidelmo Magalhães Silva, pelas valiosas ideias e contribuições a este trabalho.

Aos professores Marcelo Martins Stopa e Alex-Sander Amável Luiz, por me guiarem até o Laboratório Tesla.

À minha esposa — que era minha namorada quando tudo começou — Jéssica Correia Vilkn, pelo amor, paciência, compreensão e companheirismo, mesmo durante os meses em que estive em Aalborg. Obrigado pela dádiva de me tornar pai. Este trabalho foi concluído por causa disso.

Aos meus pais, Ivan e Ana Elisa, pelo apoio e suporte durante todos esses anos. Obrigado por nunca me deixarem desistir dos meus sonhos.

Aos amigos do Laboratório Tesla — Arlete, Dener, Rodrigo, Mariana, João, Bianca, William, Kassiane, Bruna, Aldo, Pedro, Naiara, Leonardo e Vinícius — pela parceria, amizade e momentos de descontração. Ao meu amigo Dener Brandão, meu muito obrigado pela parceria e por estar presente nos momentos mais difíceis e também nos mais felizes. Ao meu amigo Rodrigo Rodrigues Bastos, expresso minha gratidão por ser uma pessoa ímpar. Aprendi muito com você de como devemos ser pessoas melhores.

Minha gratidão também por ter conhecido e convivido com Armando Abrantes de campina grande, meu amigo durante o período em Aalborg. Aprendi muito com você sobre a vida.

Now some words in English:

I would like to thank Professor Xiongfei Wang for the opportunity to work in his group in Aalborg, Denmark, and also Fangzhou Zhao and Heng Wu for their support during the seven months abroad. Thank you, Fangzhou, for the weekly meetings and for helping me with my PhD project — my full gratitude. I am also thankful to Yifei for the conversations and Asim Alameen, and Rajsekharreddy Ambati for the time spent together

at Tornhøjparken 61.

A todos aqueles que anonimamente contribuíram de alguma forma para a realização deste trabalho.

Ao Conselho Nacional de Desenvolvimento Científico e Tecnológico (CNPq) e a Coordenação de Aperfeiçoamento de Pessoal de Nível Superior (CAPES) pelo suporte financeiro durante o doutorado e o doutorado sanduíche.

A Deus, acima de tudo.

"I believe you have to be willing to be misunderstood if you're going to innovate."

Jeff Bezos

"For in Him we alive, and move, and have our being..."

Acts 17:28

Resumo

O mundo tem passado por uma rápida mudança na produção e uso de energia elétrica. O sistema elétrico responsável por fornecer energia, localizado longe dos centros de consumo, está passando por um processo de mudança devido à alta penetração de geração distribuída por meio de fontes de energia renovável instaladas próximas aos consumidores. A evolução da geração distribuída abre caminho para o conceito de conversores formadores de rede, melhorando a estabilidade de tensão e frequência em microrredes, aplicações em sistemas isolados e posteriormente em sistemas de energia em larga escala devido ao crescimento de fontes de energia renováveis em conversores eletrônicos conectados diretamente em níveis de tensão de distribuição. O presente trabalho propõe a aplicação do conversor de distorção harmônica zero (ZHD), que não requer o uso de filtros senoidais, como um conversor formador de rede devido à sua característica inerente de fonte de tensão sem o uso de filtros de saída que impactam negativamente custos, eficiência, tamanho e possíveis problemas de ressonância com a rede. Este trabalho contribui com a técnica de controle para o conversor ZHD operar como um conversor formador de rede. O conversor elimina todos os harmônicos considerados pelos padrões internacionais por meio de um transformador com dois secundários em conjunto com a técnica de eliminação seletiva de harmônicos (SHEPWM). Simulações e resultados em *hardware-in-the-loop* mostram o desempenho do conversor ZHD como um conversor formador de rede.

Palavras-Chaves: Geração Distribuída, Conversor Formadores de rede, Microrredes de Corrente Alternada, Sistemas Elétricos, SHEPWM, Conversores Eletrônicos de Potência.

Abstract

The world has been experiencing a fast change in production and use of electrical energy. The electric power system responsible for delivering energy and located far from consumption centers, is in changing process due to the high penetration of distributed generation using renewable energy sources installed near the consumers. The evolution of distributed generation paves the way for the concept of grid-forming converters improving voltage and frequency stability in microgrids, small islands applications, and later in bulk power systems due to the growth of inverter-based resources in distribution level. The present work proposes the application of the zero harmonic distortion converter (ZHD) that does not require the use of sinusoidal filters, as a grid-forming converter due to your inherently voltage source characteristic without the use of output filters that negatively impact in costs, efficiency, size and possible resonances problems with the grid. This work contributes with the control technique for the ZHD converter to operate as a grid-forming converter applications. The converter eliminates all harmonics considered by international standards through a transformer of two secondaries in conjunction with the selective harmonic elimination technique (SHEPWM). Simulation and hardware in the loop results shows the converter performance for the ZHD converter as a grid-forming converter.

Keywords: Distributed generation, grid forming converters, AC Microgrids, Power systems, SHEPWM, Power converters.

List of Figures

List of Tables

List of abbreviations and acronyms

ANPC	Active Neutral Point Converter
BESS	Batterry Energy Storage System
CHB	Cascaded H-bridge Converter
DER	Distributed Energy Resource
DB	Dead-Beat
DG	Distributed Generation
DDSRF-PLL	Decoupled Double-Synchronous Reference Frame PLL
dVOc	Dispatchable Virtual Oscillator
ESS	Energy Storage System
GC	Grid-Connected Mode
CCM	Current Control Mode
GFL	Grid-Following
GFM	Grid-Forming
GS	Grid-Supporting
GSGf	Grid-Supporting Grid-Feeding
GSGF	Grid-Supporting Grid-Forming
HIL	Hardware in the Loop
IEEE	Institute of Electrical and Electronic Engineers
LQR	Linear Quadratic Regulator
LV	Low Voltage
MC	Matching Control
MG	Microgrid
MMC	Modular Multilevel Converters

MV	Medium Voltage
P	Proportional
PCC	Point of Commom Couple
PLL	Phase-Locked Loop
PR	Proportional Resonant
PV	Photovoltaic
PWM	Pulse Width Modulation
qZSI	quasi-Z-source Converter
RES	renewable Energy Resources
SG	Synchronous Generator
SOC	State of Charge
SHE PWM	Selective Harmonic Elimination Pulse Width Modulation
SMC	Sliding Mode Control
THD	Total Harmonic Distortion
TUPF	True Unity Power Factor
VCM	Voltage Control Mode
VSI	Voltage Source Inverter
VOC	Virtual Oscillator Control
VSG	Virtual Synchronous Generator
ZHD	Zero Harmonic Distortion Converter
ZSI	Z-source Converter

List of symbols

k_p	Frequency droop coefficient
k_q	Voltage droop coefficient
V	Output Voltage amplitude
f	Output Frequency
V_N	Rated Voltage amplitude
f_N	Rated Output Frequency
L	Stator Windings self inductance
M	Mutual inductance
R_s	Stator Windings resistance
R_f	Rotor Windings resistance
L_f	Rotor Windings self inductance
θ	Rotor angle
M_f	Maximum mutual inductance
M_a	Phase a mutual inductance
M_b	Phase b mutual inductance
M_c	Phase c mutual inductance
i_a	Phase a stator current
i_b	Phase b stator current
i_c	Phase c stator current
i_f	rotor field current
L_s	Stator phase A inductance
ϕ	Stator flux linkage
v	Phase terminal voltages

e	Back Electromotive Force
v_f	Field terminal voltage
R_f	Rotor winding resistance
J	Rotor inertia
ω	Angular frequency
T_m	Mechanical torque
T_e	Electromagnetic torque
ω_g	Angular frequency of the grid
ω_{VSG}	Rotating speed of the VSG
D	Damping torque
E	Energy stored in the machine magnetic field
T_a	Mechanical time constant
N	Number of harmonics
k	Harmonic components
P_{REF}	Active power reference
P_{out}	Output power
k_d	Damping coefficient
$\widehat{v}$	VOC reference voltage
V_{dc}	DC bus voltage
C_{dc}	DC bus capacitor
R_{dc}	DC bus resistance
i_{dc}	DC bus current
i_{cdc}	DC bus capacitive current
i_{Rdc}	DC bus resistive current
α_M	Precalculed switching angle
a_n	Fourier coefficient series

m	Modulation index
M	Number of switching angles
$V_{1ms6step}$	Maximum fundamental voltage available
f_{sw}	Switching frequency
$Z_{AFE\Delta}$	Impedance of converter connected in Δ secondary
Z_{AFEY}	Impedance of converter connected in Y secondary
Z_P	Transformer impedance referred to primary
V_{aY}	Phase A voltage applied in secondary in wye
V_{bY}	Phase B voltage applied in secondary in wye
V_{cY}	Phase C voltage applied in secondary in wye
$V_{a\Delta}$	Phase A voltage applied in secondary Δ
$V_{b\Delta}$	Phase B voltage applied in secondary Δ
$V_{c\Delta}$	Phase C voltage applied in secondary Δ
$Z_{s\Delta}$	Impedances of the reactors in series with secondaries Y
Z_{sY}	Impedances of the reactors in series with secondaries Δ
$Z_{P\Delta}$	Series impedance referred to the primary
a	Transformer turns ratio
$V_{aY'}$	Wye referred phase A voltage
$V_{bY'}$	Wye referred phase B voltage
$V_{cY'}$	Wye referred phase C voltage
$V_{\Delta'a}$	Delta referred phase A voltage
$V_{\Delta'b}$	Delta referred phase B voltage
$V_{\Delta'c}$	Delta referred phase C voltage
$V_{TH'}$	Thevenin voltage
$Z_{TH'}$	Thevenin impedance
λ	Flux linkage

I_d	Direct-axis current component
I_q	Quadrature-axis Current component
V_d	Direct-axis voltage component
V_q	Quadrature-axis voltage component

Contents

1 Introduction

This chapter highlights the significance of the research, focusing on the ZHD converter as a grid-forming converter in medium-voltage and high-power systems. The increasing penetration of distributed generation brings significant opportunities, challenges, and flexibility. In this context, Grid-forming converters emerge as a feasible solution for regulating voltage and frequency in microgrids and power systems, effectively addressing the intermittent nature of distributed generation. The ZHD converter is a promising alternative for such applications due to its intrinsic voltage source characteristics, eliminating the need for complex filters and control loops. Its commercially established structure widely adopted in the industry further reinforces its viability.

1.1 Context and Relevance

The electric power system has been transformed due to the high penetration of the distributed generation (DG). Environmental and sustainable issues and the increasing of energy demand leads to the increase of power generation based on renewable energy inverter-interfaced plants, such as solar and wind energy, as well as energy storage devices like batteries (see Fig. 1). These newer sources vary in size from residential scale rooftop systems, to utility-scale power plants. (Kroposki et al., 2017; Medina et al., 2014; Hatziargyriou et al., 2007).

In this context, the DG emerges as a solution that contributes through an energy generation closer to the consumers, offering opportunities related to efficiency, investments, flexibility, stability and power quality (Milano et al., 2018; Vartanian et al., 2018; Braun et al., 2018).

The concept of microgrids (MGs) has emerged as a result of the evolution of distributed generation (DG) representing a shift towards a more decentralized and sustainable approach to energy generation. An MG essentially consists of a collection of loads, storage elements, and microsources. These microsources are typically based on renewable energy sources such as solar, wind, and biomass (Lasseter; Paigi, 2004).

The inverter-based resources of an MG can be classified depending on their control capability as: 1) grid-feeding converter, 2) grid-forming converter and 3) grid-supporting converter. The grid-feeding converters are designed to deliver power to the grid and are controlled as a current source in the active/reactive power (PQ) mode. Grid-forming converters operate as a voltage source in the voltage and frequency (V-F) mode setting voltage amplitude and frequency of the local grid. Finally, grid-supporting converters can

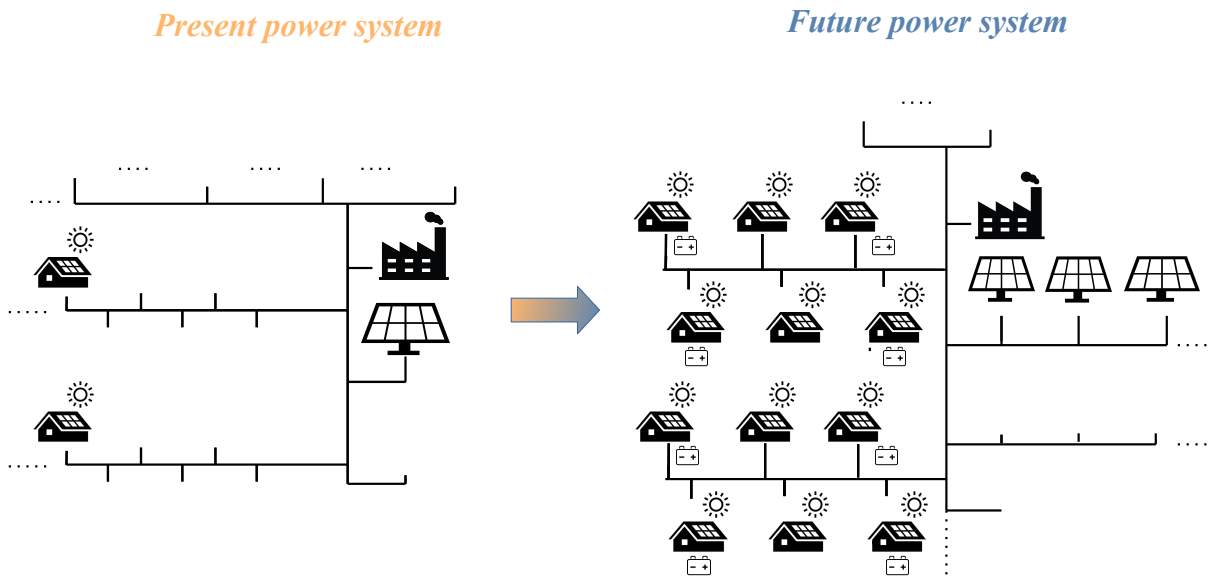

Figure 1 – a) The present eletric power system has historically been dominated by synchronous generators with a relatively modest amount of inverter-based resources, such as photovoltaics, wind, and batteries. b) Future electric power systems dominated by the renewable energy inverter-interfaced ones.

be controlled as current or voltage source, regulating active and reactive power, providing ancillary services, harmonic compensation and low-voltage ride-through capabilities (Rocabert et al., 2012).

Since the MG can operate in connected or in islanded mode, the grid-forming converters are necessary to the stable operation of the MG. When connected, the voltage and the frequency are imposed by the grid. However, in islanded mode, at least one grid-forming converter equipped with an energy storage system (ESS) will be responsible to setting the voltage and frequency references to the MG. Furthermore, the grid-forming converter must respond to load variation and manage the transition between connected and island mode (Rocabert et al., 2012).

The proliferation of distributed energy resources (DERs) connected at the distribution level has introduced dynamic stability concerns when the substation voltage source is lost due to events such as extreme weather and natural disasters. To address this issue, the concept of grid-forming has emerged as a potential solution for deployment in bulk power systems. This approach seeks to improve dynamic stability by regulating voltage and frequency at the point of common coupling (PCC) in power systems, for example integrating wind and solar farms (Lasseter; Chen; Pattabiraman, 2020a; Rosso et al., 2021; Matevosyan et al., 2023; Zhang et al., 2021; Du et al., 2021).

In this context, a wide range of open research questions related to grid-forming converters must be adressed and significant additional research, development, and field trials are needed to expand the control concept. Fig. 2 shows the phased implementation

of grid-forming converters, starting from smaller microgrids which are already being incorporated in a variety of areas for example, rural villages, university campuses, and military bases (Lin et al., 2022; Anttila et al., 2022).

As the grid-forming concept implementation matures in MGs, the next step is its application to larger isolated power systems such as Hawaii and the carribean. These systems are significantly larger and more complex than microgrids, presenting new challenges and opportunities for grid-forming technology. Finally, the successful implementation in these larger isolated power systems will pave the way for further advancements with operational experience, technical support requirements and standards, making possible the control concept extension to interconnected continental scale power systems (Lin et al., 2022; Anttila et al., 2022).

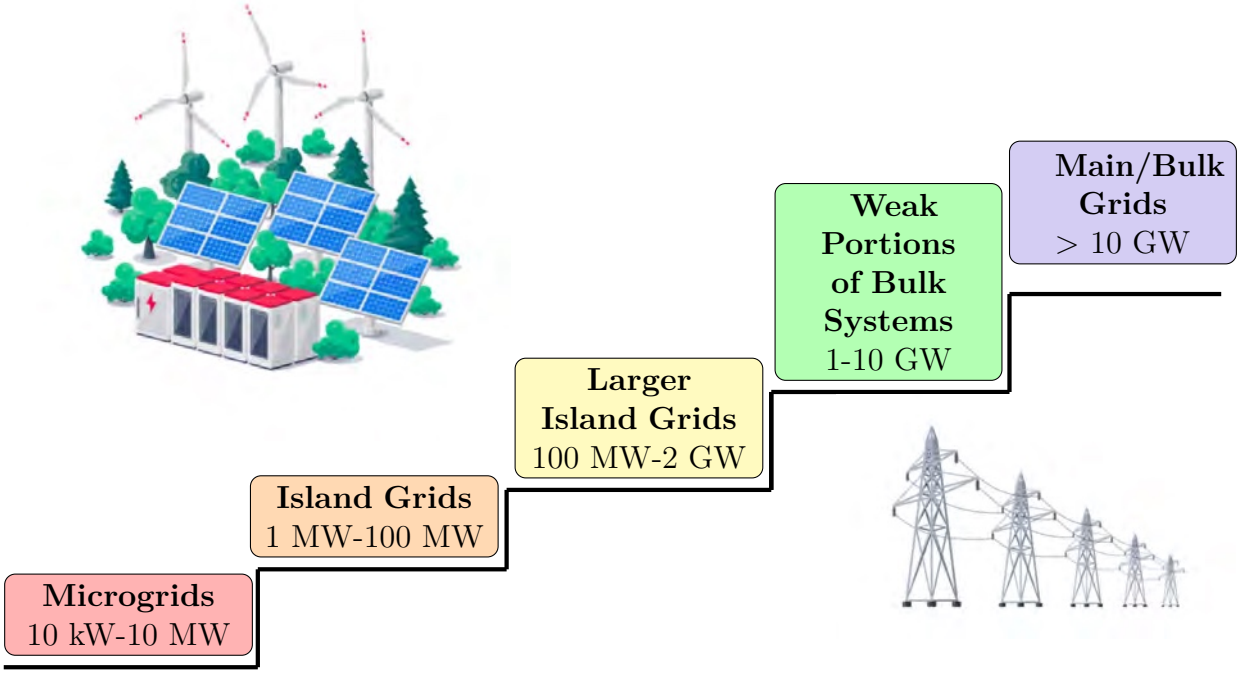

Figure 2 – Implementation phases of grid-forming converters from microgrids to interconnected bulk power systems. *Adapted from* (Lin et al., 2022; Anttila et al., 2022).

Due to the increasing interest in grid-forming technology, numerous projects and funding initiatives have been announced to explore the potential of integrating this new technology to existing systems. The ultimate goal is to create a unified power system in which all components work seamlessly together. Table 1 provides a summary of some of the noteworthy grid-forming projects currently underway (Anttila et al., 2022; Tuckey; Round, 2022).

The majority of the grid-forming projects is present in Australia, since the renewable energy generation grew from 14% in 2009 to 51% in 2018, dominated by wind power. Combined with limited interstate transmission capacity, its power system has experienced

high power injection from wind generation in excess of 140 %, the highest for any major power system in the world. (Anttila et al., 2022; Tuckey; Round, 2022).

Table 1 – Summary of recents Grid-Forming Converters projects. *Adapted from* (Anttila et al., 2022; Tuckey; Round, 2022).

Project	**Owner**	**Location**	**Year**	**Rated Power**	**Application**
(Peacok, 2021)	AGL	Australia	2021	250MW/250MWh	BESS
(Roscoe A.; Brogan, 2019)	SPR	Scotland	2019	69MW/-MWh	Wind Farm
(Nestor, 2022)	CBA	Australia	2022	150MW/300MWh	BESS
(Sales, 2022)	Hitachi ABB Power Grids	Australia	2021	30MW/8MWh	BESS
(Tuckey; Round, 2022)	Hitachi	Australia	2020	1MW/1MWh	BESS
(Limited, 2022)	-	Scotland	2020	1400MW/-MWh	HVDC

1.2 Grid-Forming Converter Realization

In the literature, a wide range of grid-forming converter applications is based on two-level and three-level (NPC) VSI converters (Du et al., 2021; Bahrani; Rufer, 2013; Gonzalez-Espin et al., 2014; Singh Luiz A.C. Lopes, 2015; Azevedo et al., 2013; Rese; Costa; Silva, 2012; Ortjohann et al., 2006; Ninad; Lopes, 2012; Silva; Ribeiro; Matos, 2014; Miao et al., 2014; Bratcu; Aulagnier, 2015; Gervasio et al., 2015; Antunes et al., 2017a; Machado et al., 2017; Antunes et al., 2017b).

Since the DERs based on these converters topologies usually interfaces the grid/load side through LC or LCL output filters to provide switching harmonics attenuation, resonances points at various frequencies can arise. The induced resonances can affect both transient and steady-state control performances and even lead to severe stability issues. Therefore, robust control techniques are required to maintain a suitable operation. (Lourenço et al., 2021; Saim et al., 2019; Wang; Blaabjerg, 2019).

In medium voltage (MV) systems, these two and three-level topologies require a step-up transformer for applications connected to MV grids and constitute the majority of commercially available applications (Wang et al., 2016a; Steimer; Manjrekar, 2001; Dias; Alves; Torri, 2016; Hiller; Sommer; Beuermann, 2008; Xavier et al., 2019).

Futhermore, transformerless converters technologies are being applied such as Modular Multilevel Converters (MMC). Recent works showed the MMC as a solution for power systems in the grid-forming operation (Lourenço et al., 2021; Freytes et al., 2021; Taoufik et al., 2022; Henninger; Schroeder; Jaeger, 2018). Usually, it is considered a physical capacitance at the PCC, although in (Freytes et al., 2021; Taoufik et al., 2022) a control implementation without output capacitors is discussed, since the series connection of N cells can generate a quasi-sinusoidal voltage waveform at the output. However, the

control problem associated with the MMC is more complex than the one associated with two or three-level VSCs. The complexity arises from the growth in the number of control variables compared to the two and three-level VSCs, resulting from the converter circulating current and the internal energy stored in the submodules of the capacitors (Bergna-Diaz; Suul; D'Arco, 2018; Sánchez-Sánchez; Prieto-Araujo; Gomis-Bellmunt, 2020; Oliveira et al., 2021).

This work proposes a grid-forming converter based on the Zero Harmonic Distortion (ZHD) technology. The ZHD converter does not generate any characteristic harmonics up to the 50^{th}, which is the maximum limit considered in the IEEE 519 and IEEE 1547 standards (IEEE. . . , 2022; IEEE. . . , 2018). This performance is achieved by employing two three-phase converters—either two- or three-level—using Selective Harmonic Elimination Pulse Width Modulation (SHE-PWM) connected to a three-winding transformer. As a result, the converter exhibits an inherently sinusoidal voltage-source characteristic without the need for capacitive filtering elements that typically increase cost, reduce efficiency, enlarge system size, and introduce complex resonance, ferroresonance (Lourenço et al., 2021; Saim et al., 2019; Wang; Blaabjerg, 2019; Almeida; Filho, 2017; Saim et al., 2019; Mozina, 2013; Monadi et al., 2013), and converter reliability issues (Yao et al., 2024). The converter operates as a voltage source that defines its own voltage and frequency references without relying on control loops, maintaining a simple and widely adopted industrial structure based on conventional two- or three-level voltage source converters (VSCs), suitable for high-power and medium-voltage applications. This inherent voltage-source nature not only eliminates the need for external control loops but also simplifies the transition between grid-following (GFL) and islanded modes. Moreover, when operating in grid-forming (GFM) grid-connected mode, it prevents control interactions and resonance phenomena typically observed in conventional control-based grid-forming converters.

1.3 Objectives

The main objective of this work is to present a Zero Harmonic Distortion (ZHD) converter–based grid-forming approach for microgrid and power system applications.

1.3.1 Specific Objectives

To achieve the main objective of this work, the following specific objectives are defined:

a) To present a control structure for the ZHD converter operating as a voltage source in islanded mode, supporting both stand-alone and parallel operation.

b) To present a control structure for synchronized operation with the main grid, enabling grid-following (GFL) operation with seamless transition between grid-connected

and islanded modes, while considering voltage sags, grid disconnections, and smooth automatic reconnection to the main grid.

c) To present a control structure for synchronized operation enabling grid-forming (GFM) grid-connected mode with inherent current-limiting capability under fault conditions.

1.4 Contributions

This work presents several original contributions toward the development, control, and validation of the Zero Harmonic Distortion (ZHD) converter as an advanced grid-forming solution for microgrid and power system applications. The main contributions are summarized as follows:

a) Presentation of the ZHD converter operating in grid-forming mode for both microgrid and power system applications.

b) Development of an open-loop voltage control structure enabling ZHD converter operation in islanded mode, establishing voltage and frequency references for both two- and three-level converter topologies.

c) Sensitivity assessment of the ZHD converter open-loop structure under impedance estimation errors.

d) Presentation of the ZHD converter's power-sharing capability during islanded operation.

e) Desmonstration of ZHD black-start capability.

f) Design of a control structure for the ZHD converter operating in grid-following (GFL) grid-connected mode, ensuring seamless transitions between islanded and grid-connected operation, and vice versa.

g) Implementation of a voltage-controlled grid-connected mode for the ZHD converter.

h) Modeling of a three-winding three-phase transformer using fundamental and harmonic per-phase equivalent circuits to analyze power flow in the converter.

i) Development of a virtual impedance–based current-limiting technique for ZHD converter operation in voltage-controlled grid-connected mode.

j) Evaluation of ZHD converter performance in both grid-connected modes under symmetrical and asymmetrical fault conditions.

1.5 Organization of this Ph.D Thesis Dissertation

This text is organized in 7 chapters according to the structure presented in Fig.3. Chapter 1 presented the motivations and objectives of the present Ph.D dissertation. Chapter 2 provides a bibliographic review of power electronic converters, focusing on control strategies and converter topologies. In particular, ZHD converters are selected for their suitability as Grid-Forming Converters (GFM). Chapter 3 discusses the concept of a ZHD converter, including its modeling and design aspects. Chapter 4 analyzes the operation of the ZHD converter in voltage-source mode under islanded conditions. Chapter 5 revisits the GFL operation of the ZHD converter and proposes its operation as a utility-interactive converter, functioning in Grid-Following (GFL) mode when synchronized with the grid, and in GFM mode under islanded conditions. Chapter 6 presents the grid synchronization of the ZHD converter as a GFM converter. Finally, Chapter 7 summarizes the main conclusions and outlines potential directions for future research and development.

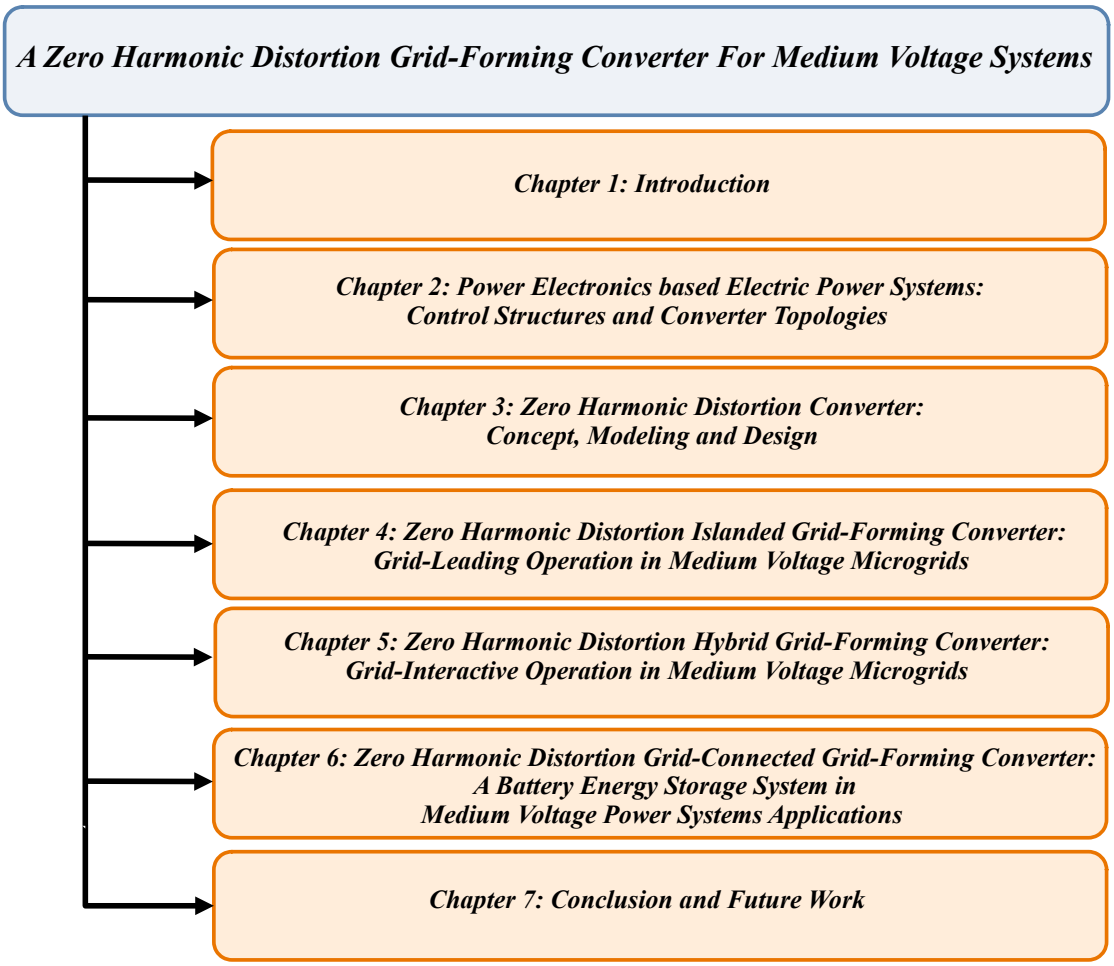

Figure 3 – Structure of PhD thesis organization.

2 Power Electronics-Based Electric Power Systems: Control Structures and Converter Topologies

This chapter aims to provide a thorough overview of Grid-Forming Converters, exploring their classifications, control structures, and topologies. The selection of ZHD converters is well-justified due to their remarkable capacity to handle high-power and medium-voltage applications, making them a highly suitable choice for commercial and industrial setups. These converters are thoughtfully designed based on two and three-level configurations, further enhanced by the integration of a low-frequency transformer.

2.1 Introduction

There have been significant changes in the traditional electric power system due to the increasing penetration of Distributed Generation (DG) based on Renewable Energy Sources (RES). DG contributes to electricity generation closer to consumers, offering advantages in terms of efficiency, investment deferral, flexibility, system stability, and power quality. This paradigm shift has motivated the development of new architectures capable of integrating multiple distributed energy resources in a coordinated manner (Lasseter; Paigi, 2004).

In this context, the concept of microgrids (MGs) has emerged as a natural evolution of distributed generation, representing a move toward a more decentralized and sustainable energy system. A microgrid consists of an interconnected group of loads, energy storage systems, and distributed energy resources—typically based on renewable sources such as solar, wind, and biomass—interfaced through power electronic converters, which can operate in both grid-connected and islanded modes(Lasseter; Paigi, 2004).

In the near future, Distributed Generation (DG) sources, such as wind and solar photovoltaic (PV) systems, are expected to play a pivotal role in the power systems at both distribution and transmission levels. This integration is primarily driven by environmental considerations, with a strong emphasis on reducing carbon emissions. Moreover, the substantial cost reductions observed in recent years have accelerated large-scale deployments of these renewable energy technologies worldwide (Kroposki et al., 2017).

Historically, the power system stability and services were mainly ensured by syn-

chronous machines, while power converters are only injecting active and reactive power relaying on the grid information. Some research projects shown that to achieve a power system with 100% power electronics penetration, the power converters should be able to ensure the same specifications as synchronous generators with better dynamic performances (Kroposki et al., 2017). Energy systems without dedicated synchronous generators has been widely discussed in MGs (Katiraei et al., 2008), Uninterruptible Power Supply (Guerrero et al., 2009) and it starts to be extended to large interconnected system (Cossart; Colas; Kestelyn, 2018). Australia, Germany, Ireland and Denmark have already achieved a high penetration of RES. Considering the power system stability, the penetration rate of RESs must be monitored in order to keep the same level of reliability of the conventional power systems (Kroposki et al., 2017; Tuckey; Round, 2022).

The efficient management of electrical power from RES heavily relies on the control strategies implemented in power electronic converters interfaces. Substantial developments have been made in control strategies over time, with numerous studies addressing this area (Qoria et al., 2019a; Jouini; Arghir; Dörfler, 2017; Hesse; Turschner; Beck, 2009; Beck; Hesse, 2007; Zhong et al., 2014; Driesen; Visscher, 2008; Ashabani et al., 2016; Johnson et al., 2014). The proliferation of diverse control methods documented in the literature has brought increased attention to classifying and characterizing power converters, making it a highly relevant and trending research topic.

2.2 Power Converters Classification

2.2.1 Microgrid Context

Conventional classification of the power electronic converters used in AC MG context depends on the implemented control strategies or operation mode, and can be categorized as Grid-Following (GFL), Grid-Forming (GFM), or Grid-Supporting (GS) (Rocabert et al., 2012).

The GFL converter is responsible for exchanging power produced by an energy source, such as an RES, with the grid. It typically features a fast current control mechanism that ensures the AC grid perceives it as a controlled current source with high output impedance, connected in parallel to the grid. The current source should be precisely synchronized with the AC voltage at the Point of Common Coupling (PCC) to enable accurate regulation of active and reactive power exchange with the grid (Rocabert et al., 2012; Anttila et al., 2022). This synchronization is achieved using a Phase-Locked Loop (PLL) synchronization technique that estimates the frequency and phase in the PCC. The system then utilizes the value of the angle of synchronism and the angular frequency of the grid to control the system. (Ali et al., 2018) provides an overview of the advanced PLL algorithms for grid-connected systems.

The GFM converter is specifically designed for island operation, and it is controlled to establish a consistent local grid by setting the voltage amplitude and frequency. In this way, it can be represented as an ideal AC voltage source with low-output impedance (Rocabert et al., 2012). Synchronization is also a critical aspect since GFM converters require a more precise synchronization system to work in parallel with others converters (Han et al., 2016).

Finally, GS converters are designed to provide ancillary services, and control the AC grid voltage amplitude (reactive power) and frequency (active power) of either a stand-alone or inter-connected grid allowing power sharing for power balancing. They support the grid, either alone or with other GS converter (Rocabert et al., 2012).

The Fig. 4 summarize the operation modes of converters in a MG according to (Rocabert et al., 2012).

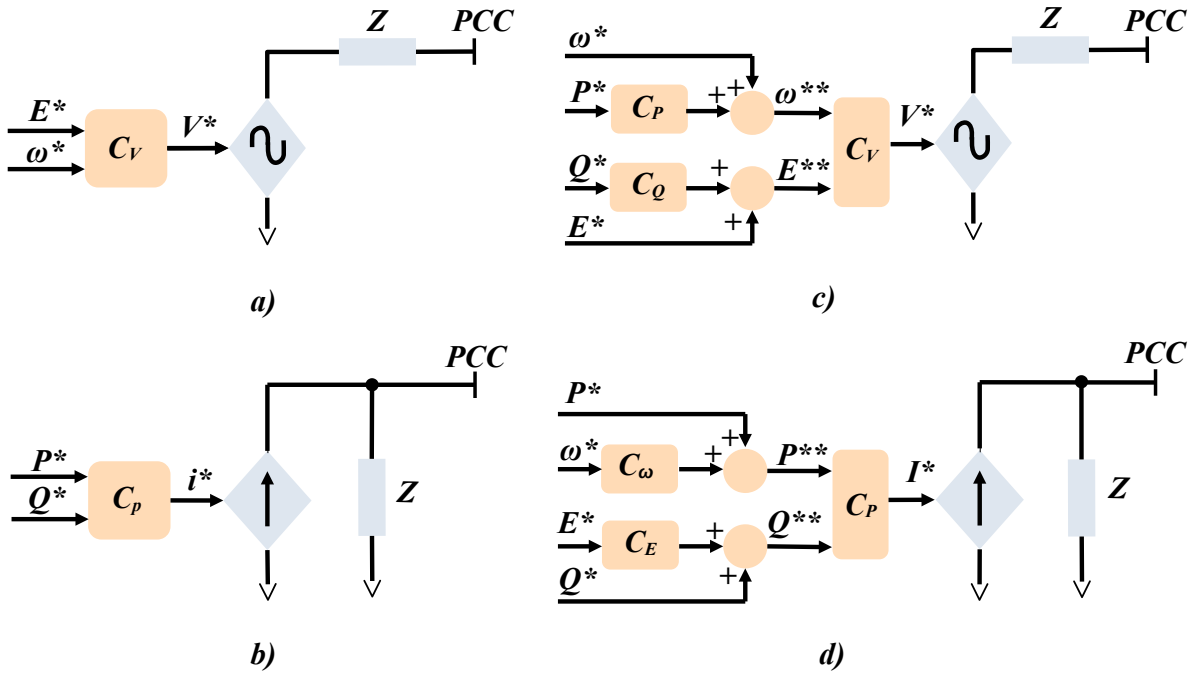

Figure 4 – a) grid-forming converter b) grid-following converter c) voltage-source grid-supporting converter d) current-source grid-supporting converter. *Adapted from* (Rocabert et al., 2012).

However, GS classification from (Rocabert et al., 2012) remains generic and does not allow to classify precisely the contributions of power converters from their system level, since, it is an extension of both GFM or GFL controls with the same system inputs and outputs.

In this way, (Katiraei et al., 2008) suggest that each control technique could be classified into non-interactive and grid interactive strategies, where the grid-feeding and grid-forming are defined as a non-interactive controls. Grid-supporting control is defined as an interactive control since it uses the grid information with or without communication

to provide services.

In order to avoid confusions about GS controls, (Rocabert et al., 2012) and (Paquette et al., 2014) divide the GS converter into GSGf (grid-supporting grid-feeding) and GSGF (grid-supporting grid-forming). In this hand, (Markovic et al., 2018) propose a subdivision of the grid-supporting grid-forming in AC voltage forming, frequency forming or grid-forming.

These classifications are relative and consider only the contribution of power converters to the AC grid, however with the increase of control strategies, some of them do not belong to any category, can contribute to misunderstands in the the vocabulary (Qoria et al., 2019c).

2.2.2 Power Systems Context

Another classification approach characterizing power systems applications, distinguishes the converters by two principle levels: Low and High level controls. Low level control characterizes the nature of the power source (i.e.; current controlled VSC or AC voltage controlled VSC) characterizing the converter dynamic behavior. High level control is related to the synchronization of power converters and different types of services to the AC grid. From the perspective of the power system, a converter can feed the grid with power, form the grid, provide ancillary services, support the grid, or even offer a combination of these services simultaneously (Qoria et al., 2019c).

In this sense, (Qoria et al., 2019c) outlines various control strategies based on four distinct criteria, as it can be seen in Fig.5: source nature defined by the low level control (whether the source is a current or voltage source), grid contribution (such as feeding, voltage or frequency support, virtual inertia emulation, etc.), synchronization (whether the source is droop or grid-synchronized), and operation mode (whether it is in grid-connected or island mode) the last three defined by the High level control.

In this context, (Qoria et al., 2019c) presents a comprehensive overview of diverse control strategies based on four distinct criteria, illustrated in Fig. 5:

Determined by the low-level control:

1. **Source nature**: this criterion identifies whether the converter operates in a current control (CCM) or voltage source mode (VCM).

Defined by the High-level control:

2. **Grid contribution**: various aspects of the power source's interaction with the grid are considered, including feeding, voltage or frequency support, virtual inertia emulation, and more.

3. **Synchronization**: this criterion categorizes the power source as either droop-

Table 2 – Comparison of Grid-Following and Grid-Forming control strategies. *Adapted from* (Tuckey; Round, 2022)

Control	Advantages	Disadvantages
Grid-Following (Current Source)	• Simple control • Fast response time • Inherently current limit during faults • Suitable for DC bus voltage control • Suitable for grid interface	• Does not contribute to grid strength • Requires a stiff grid • Loses grid-synchronism during faults • Can not form the grid • Limited percentage on a grid
Grid-Forming (Voltage Source)	• Can run in stand-alone mode • Can run in weak grids • Natural power regulation • Inertia emulation capacity	• Complex Controls • Needs a current limit strategy

synchronized or grid-synchronized.

4. **Operation mode**: establish whether the power source is in a grid-connected mode or an island mode.

By considering these four key criteria, the control can be classified into GFL and GFM controls helping researchers gain valuable insights into the multitude of control strategies employed in power electronic converter interfaces for RES.

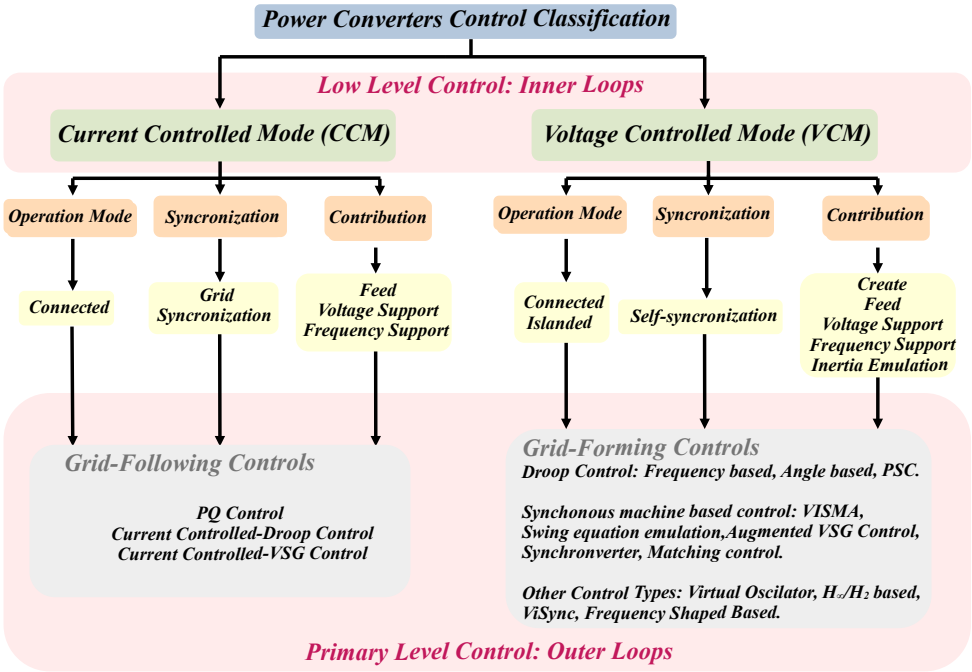

Figure 5 – Classification of converter control according to the source nature, operation mode, synchronization and contribution. *Adapted from* (Qoria et al., 2019c)

In these context, Table 2 shows the comparison between GFL and GFM controls characteristics. It is possible to observe that GFM controls have some advantages over GFL controls in the context of increase of RES in electric systems, mainly due to the inertia emulation capacity and operation in connected and islanded modes.

2.2.3 Timeline: Characterization according to operation modes and grid-synchronization

In order to clarify the classifications, a historical overview is shown in Fig. 6 make it possible to see the timeline of converters control structures until today. It is possible to highlight vector current control (VVC) similar to the one used in ac motor drives since the 1970s (Blaschke, 1972), the Droop control for load sharing in standalone AC supply systems (Chandorkar; Divan; Adapa, 1993), inertial power control for inertial emulation (Larsen; Delmerico, 1998), the virtual synchronous machine for dynamics (Beck; Hesse, 2007) and Virtual synchronous generator (Driesen; Visscher, 2008), power synchronization control for stability robustness in ultraweak grids (Zhang; Harnefors; Nee, 2010), the Synchronverter in (Zhong; Weiss, 2011), in 2013 (D'Arco; Suul, 2013) shows the equivalence between the droop control and the VISMA, in 2016 (Johnson et al., 2016) the virtual oscillator control until the universal hybrid control for grid-connected voltage source converters (Harnefors et al., 2021).

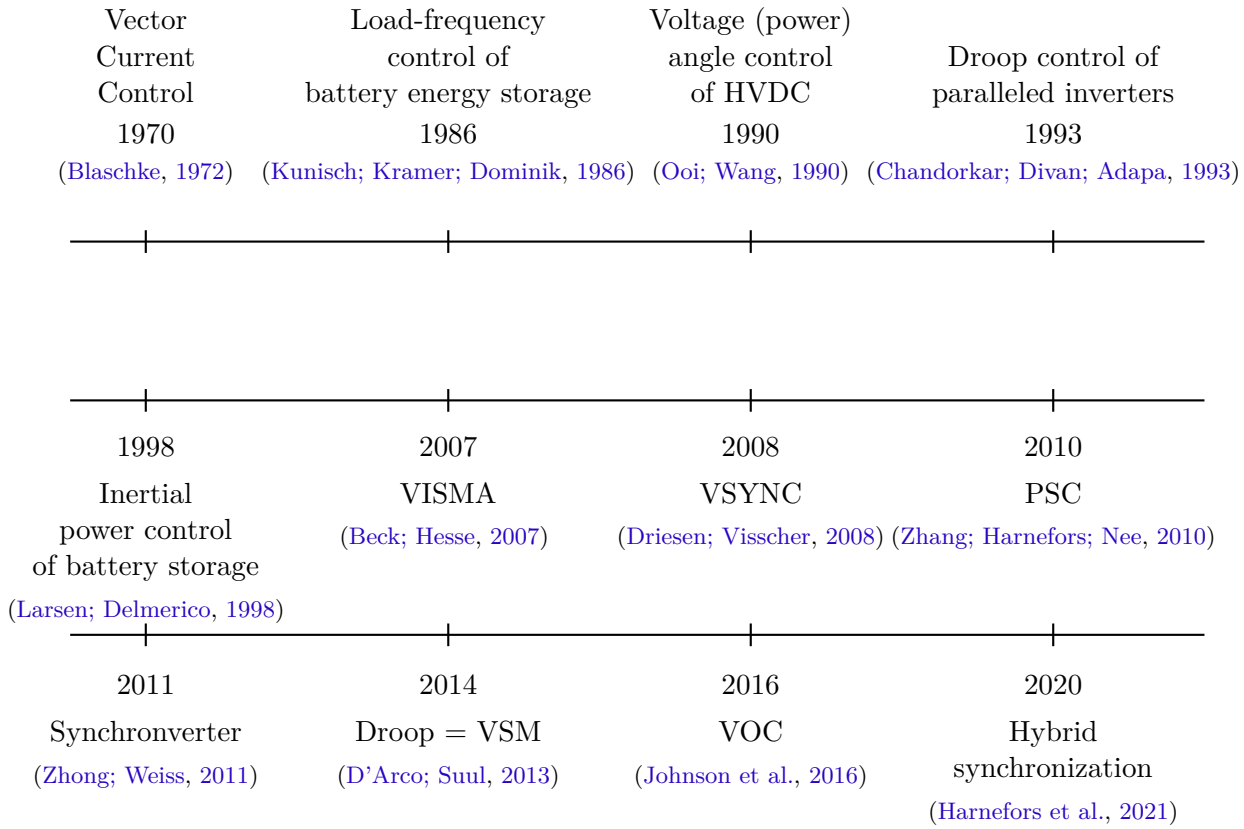

Figure 6 – Historical overview of control techniques for power electronic converters.

Based on that, Fig. 7 shows the classification proposed in this work considering the timeline overview of Fig. 6 where the control structures are categorized in operation modes according to: island or grid-connected modes. In islanded mode, at least one converter assume the grid-forming mode regulating the voltage and the frequency in isochronous mode in the case of one centralized converter, or power sharing mode in the case of

multiple converters (Rocabert et al., 2012; Han et al., 2016), in this work we refer to this converter as grid-leading converters (GLC). In grid-connected case, the synchronism with the grid can be classified as : voltage-based, which is the case of GFL converters, or power/current-based synchronizations, which is the case of GFM converters (Wang et al., 2020).

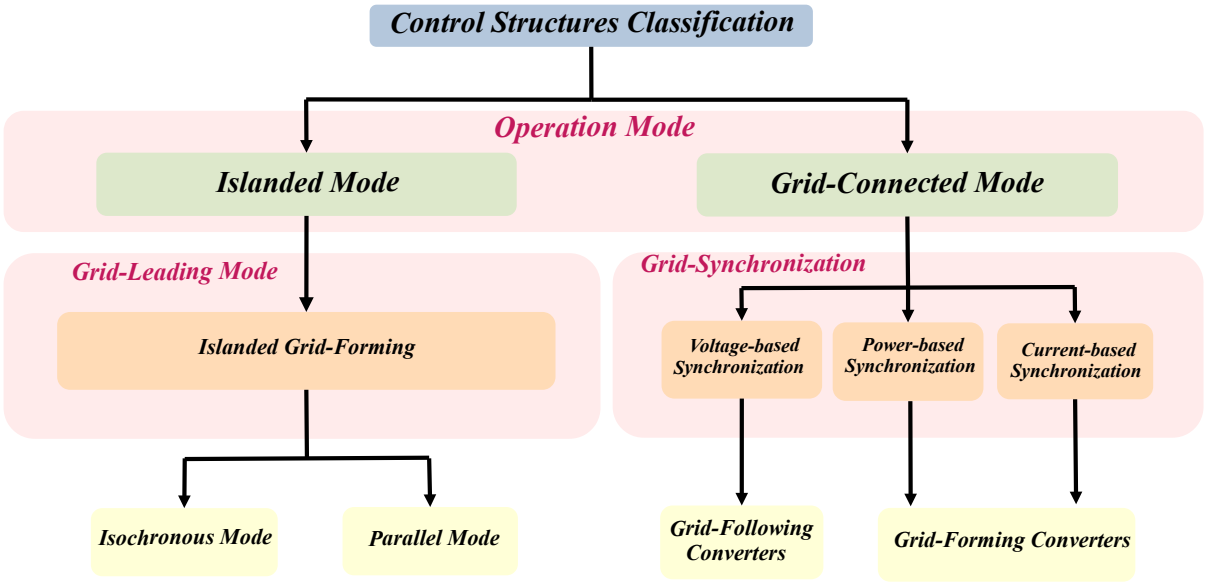

Figure 7 – Classification according operating mode and grid-synchronization.

The general representation of the control structures are shown in the following Fig. 8. In (a) the islanded GFM converter, in (b) the grid-connected GFL converter, and in (c) and (d) the grid-connected GFM structures based in power and current synchronization. In all cases, the converter works as a power interface between a primary energy resource based on renewable energy resources (RES) or an energy storage systems (ESS) with the AC side through sinusoidal filters with capacitive elements, in order to mitigate switching harmonics generated by the converters operated by Pulse Width Modulation (PWM) techiques, and improve the power quality delivered to the PCC. (Anttila et al., 2022; Hossain et al., 2017).

In island mode there is no synchronization with the main grid and at least one converter must be the reference of voltage and frequency to islanded/isolated systems. There exists the possibility of one converter or various converters working as an islanded grid-forming converter in parallel mode with autonomous power sharing among the other converters (Rocabert et al., 2012; Han et al., 2016).

In grid-connected operation with a grid-following (GFL) mode, synchronization relies on the grid voltage, which is used — either directly measured or sensorless estimation — to determine the frequency and phase at the point of common coupling (PCC). The extracted phase information is then applied within vector current control strategies (Luna et al., 2015) or direct power control strategies to regulate active and reactive power exchanged

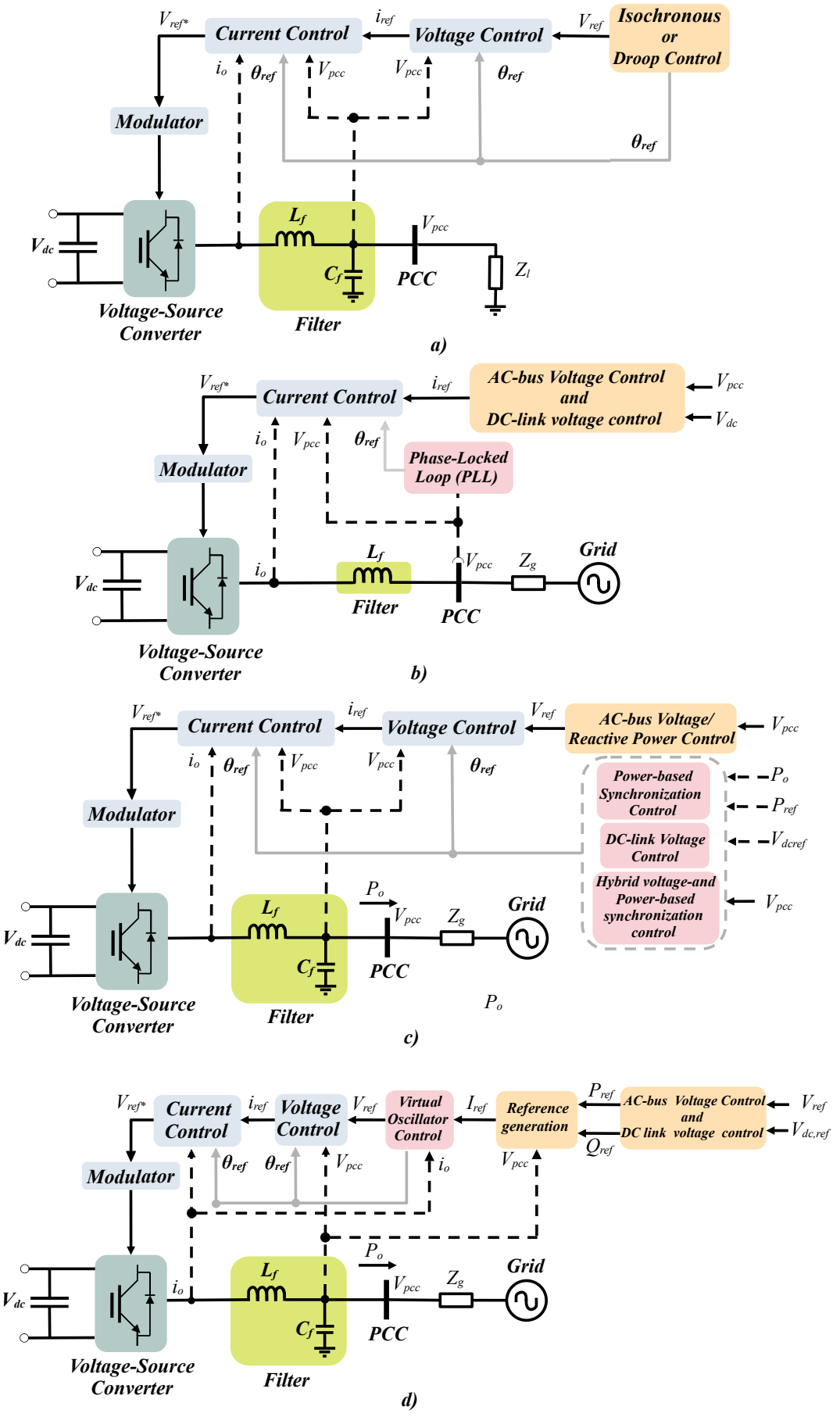

Figure 8 – (a) Islanded GFM converter: Grid-Leading Converter (GLC), (b) Grid-connected GFL converter, (c) Grid-connected GFM converter power-based synchronization and (d) Grid-connected GFM converter current-based synchronization.

with the grid (Teodorescu; Liserre; Rodriguez, 2007). This voltage-based synchronization approach is referred to as grid-following control, as it continuously tracks the phase of the grid voltage (Lasseter; Chen; Pattabiraman, 2020a).

In grid-connected GFM (grid-forming) mode, grid synchronization can be achieved through power-based or current-based methods, both of which directly dictate the phase of the PCC voltage by regulating the converter active power. The general concept is to employ active power–frequency (P–ω) droop control — a technique widely used with synchronous generators — to synchronize the converters with the grid (J.Machowski J.W.Bialek, 2007). To track and regulate the generated PCC voltage phase, voltage control is required, which distinguishes these converters from their grid-following counterpart. Such voltage-controlled converters have recently been referred to as grid-forming converters (Lasseter; Chen; Pattabiraman, 2020a).

Currently, GFL converters are the state-of-the-art technology for integrating renewable energy generation, which is commonly found in modern power systems based on power-electronics (Kroposki et al., 2017). The high-level increase in these renewable energy resources based on inverters poses some challenges to the traditional synchronous generator powered power system, such as reduced inertia and stiffness of the power grid (Lasseter; Chen; Pattabiraman, 2020a).

In this scenario, interest in GFM control has been growing since, differently from GFL control that handles VSC as a current source depending on the grid voltage, the GFM-VSC is controlled as a voltage source behind an impedance, and its stable operation does not depend on the strength of the ac grid, exhibiting improved performance compared to GFL in weak grids (Li; Gu; Green, 2022a).

Among the numerous advantages of GFM converters, such as black start capability, inertia, and damping, numerous studies demonstrate that they can enhance voltage stiffness, thereby improving the stability of renewable energy resources interfaced by GFL converters under weak-grid conditions, such as those found in offshore wind power plants (WPPs) and solar farms (Pattabiraman; Lasseter.; Jahns, 2018; Lasseter; Chen; Pattabiraman, 2020a).

The difference between the grid-synchronization between GFL and GFM converters impacts directly in their transient behavior. GFM converters provide natural power regulation following a disturbance, resulting in a fast response time. On the other hand, GFL converters react to these disturbances using control dynamics, leading to a longer response time (Qoria et al., 2019c; Lasseter; Chen; Pattabiraman, 2020a).

The natural power regulation of GFM converters plays a crucial role ensuring the stable operation of microgrids and bulk interconnected power systems. As a result, the importance of GFM converters integrating electric systems is expected to increase, making

them an essential technology for the future of power systems. (Rocabert et al., 2012; Qoria et al., 2019c; Lasseter; Chen; Pattabiraman, 2020a).

Operating the converter in GFL mode on GC mode is a less complex control structure as it does not require voltage control for the PCC. In GC mode the inverter would still need to inject or absorb power, either from an RES or to charge/discharge an ESS, which is more convenient in CCM mode (Azevedo et al., 2013). On the other hand, the GFL operating mode adds the complexity of having to change the operating mode when islanding occurs, requiring extremely fast island detection to prevent high inrush currents and triggering electrical protection (Zhong et al., 2014; Kulkarni; Doolla; Fernandes, 2017a; Lo; Chen, 2020a; Ganjian-Aboukheili et al., 2020). However, the converter operating in the GFM mode has proven to be more effective in voltage support, as, for example, in week grids (Pattabiraman; Lasseter.; Jahns, 2018; Lasseter; Chen; Pattabiraman, 2020a), inherently transitioning to island mode without changing the operating mode.

Table 3 shows a comparison between the GFM and GFL converters according to the main important aspects such as: voltage response, fault current, frequency support, islanded operation and black-start capability.

2.2.4 Power Converter Control Architeture

The hierarchical structure involving the control of converters is divided into the following levels: current and voltage control, primary, secondary and tertiary control, as seen in Fig. 9 (Hossain et al., 2017; Tuckey; Round, 2022).

2.2.4.1 Inner Control

In the case of GLC converters in island mode, and grid-connected GFM converters as could be seen in Fig. 8 (a)(c) and (d), the inner loops are composed of the inner voltage and current loops responsible for regulating the voltage at the PCC (Rocabert et al., 2012; Han et al., 2016). The GFL converters on the other hand uses only a inner current loop control in order to regulate the current exchange with the grid (Wang et al., 2020).

The first level or unit level, consists of inner loops, which typically includes a outer voltage control loop and an inner current control loop. This control strategy is known in the literature as cascade control. At this level, the control is responsible for instantaneous tracking of the system voltage and power quality issues. The inner control loop is the device level control related to current and voltage control which aims to stabilize the inverter, for example, protecting from over currents (Ullah et al., 2021).

However, in (Ojo; Watson; Lestas, 2019) the inner current loop is replaced by a single voltage control loop to reduce lags/delays and oscillatory response. Although the advantage of the cascaded control structure is the possibility of integrating a current

Table 3 – Comparison between GFM and GFL controls

Technical Capabilities	**GFL Converter**	**GFM Converter**
Voltage sensitivity	• Unstable with low short-circuit ratio (SCR >1)	• Unstable with high SCR or stiff voltage sources
Impedance passivity	• Non-dissipative around synchronous frequency	• Non-dissipative around synchronous frequency
Loss of synchronism	• Voltage-angle swing dynamics of PLL	• Power-angle dynamics • Sensitive to phase jump
Voltage support	• Delayed by voltage magnitude/Q control, PLL	• Near-instantaneous (few ms) Q response
Fast fault current	• Voltage-magnitude-dependent reactive current • Delayed reactive current response by PLL	• Current limit makes difference • Near-instantaneous (few ms) current response
Voltage balancing	• Negative-sequence reactive current injection • Prioritized positive-sequence reactive current	• Balanced internal voltage (within current limit) • No sequence priority (within current limit)
Frequency support	• Fast Frequency Response (FFR) • Delayed power response by frequency detection	• Inertial response without measuring frequency • Near instantaneous (few ms) P response
Islanding operation	• Usually not possible • Well-developed islanding detection	• Capable with smooth transition • Open issue with islanding detection
Black start	• Usually not possible	• With energy storage and short-term overcurrent

limiter between the voltage and the current loop, as discussed by (Gkountaras; Dieckerhoff; Sezi, 2015).

GFM converters require a control strategy that limits and regulates the output current during faults or load imbalance to be able to remain connected and protect the components of the converter. The converter components heat rapidly, and therefore the current needs to be limited in a short time frame (Bottrell; Green, 2014).

A transformation of the controlled parameters is a common strategy to improve the controller performance. Therefore, the inner control applied to GFM converters can be implemented in different reference frames such as: natural reference frame (abc), synchronous reference frame (dq) and stationary reference frame ($\alpha\beta$).

The abc reference frame is also called a natural reference frame. Linear and non-linear control strategies can be implemented in this frame of reference. Balanced three-phase variables in the natural reference frame can be transformed into two-phase variables in the system rotating reference defined by the d and q axes perpendicular to each other (Baimel

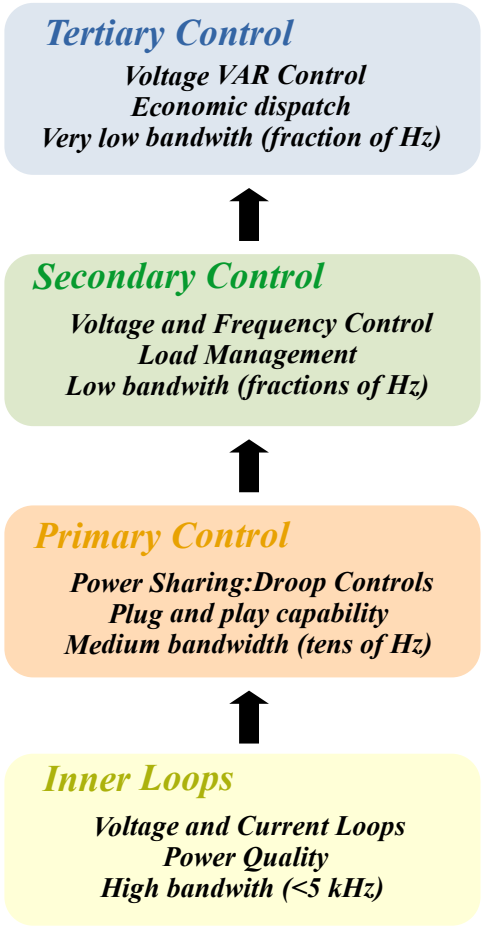

Figure 9 – Hierarchical control levels. *Adapted from* (Anttila et al., 2022; Ishaq et al., 2022; Tuckey; Round, 2022)

et al., 2017).

The synchronous reference frame has a rotating position with respect to the stationary system of *abc* axes. They are related by the angle between the axes a and d. The dq axes rotate in space at an angular speed derived from the angle variation over time. If the space vector rotates in space with the same speed as the dq system, the angle between the axes a and d will be constant (the phase angle of the grid voltage should be extracted in this implementation). As a result, the dq components will be DC variables (Baimel et al., 2017).

The stationary reference frame is a type of control scheme where the three-phase electrical quantities are transformed into $\alpha\beta$. The result of this transformation is bi-phase CA quantities where the phase angle information is not necessary (O'Rourke et al., 2019).

Table **??** presents a classification of voltage and current controllers applied to the inners loops, according *abc*, dq and $\alpha\beta$ reference frames. In the literature one finds works utilizing Hysteresis, Proportional (P), Dead-Beat (DB), Proportional Integral (PI), Proportional Resonant (PR), Repetitive, Predictive, Sliding Mode and Linear Quadratic

Regulator (LQR) Controllers.

Table 4 – Summary of inner control strategies for power converters. *Adapted from* (Bouzid et al., 2015; Miveh et al., 2016)

Reference Frame	**Current Control**	**Voltage Control**
abc	• Hysteresis (Jain et al., 2016) • Proportional (P) (Hosseinpour; Mohamadian; Varjani, 2014) • Deadbeat (DB) (Mattavelli, 2005)	• Repetitive (Cardenas et al., 2013) • Proportional-Resonant (PR) (Hosseinpour; Mohamadian; Varjani, 2014) • Deadbeat (DB) (Kojima et al., 2004) • Predictive (Cortes et al., 2009) • Sliding-mode (Yang et al., 2014) • Hysteresis (Zhang; Wang; Li, 2010)
dq	• Proportional-Integral (PI) (Vechiu et al., 2007)	• Proportional-Integral (PI) (Yao; Xiao; Yan, 2010) • Linear Quadratic Regulator (LQR) (Qoria et al., 2019b)
$\alpha\beta$	• Proportional-Resonant (PR) (Nazifi; Radan, 2013)	• Proportional-Resonant (PR) (Rokrok; Golshan, 2009)

For the case of GLC and GFM converters, since they regulate the voltage at the PCC, current limiting methods are necessary in order to limit the current at the converter and several methods are proposed in the literature. *Instantaneous saturation* limit the real and imaginary parts of the current separately. It is more appropriate for GFL inverters since when used in a VSI the voltage loop is broken, reducing the two-loop control to a single current control loop (Plet et al., 2011). Consequently, the inverter behaves as a constant current source. A disadvantage of the method is that the rated current of the inverter is not used at full capacity since the P/Q ratio remains fixed.

Vector amplitude limitation,limits the absolute value of the current or voltage, as discussed in (Gkountaras; Dieckerhoff; Sezi, 2015). This overcomes the drawback of DQ component limiting. Voltage amplitude limitation is used for current limitation in (Bloemink; Iravani, 2012). Static or dynamic limits to the commanded output voltage magnitude and phase within a range around the PCC voltage are compared. Dynamic

limits tighten the limits when the current is above the rated value of the inverter and relax them below the rated value. Dynamic limits are shown to significantly reduce fault currents compared to static limits. A current limiting function based on a combination of instantaneous saturation limits and vector amplitude limits for droop-controlled microgrids is proposed in (Baghaee et al., 2017).

Another option for current limitation is the *virtual impedance* (Paquette; Divan, 2015; Lu et al., 2018; Gouveia; Moreira; Lopes, 2019). This method emulates the effect of an impedance when the current exceeds the converter nominal value, limits the current by limiting the voltage reference, and prevents the voltage regulator from commanding an excessive current. Vector amplitude limitation and non-linear virtual impedance control methods in a GFM inverter are compared in (Gkountaras; Dieckerhoff; Sezi, 2015). Vector amplitude limitation is found to work better when the converters operate in parallel with an SG while the non-linear virtual impedance method provides a smoother transition in stand-alone operation.

2.2.4.2 Primary Control

The second level comprises the primary control, which encompasses strategies related to ensuring system stability, voltage and frequency stability, and efficient power sharing. The primary control plays a vital role in providing references for the inner loops, aligning them with system-level requirements. For instance, it facilitates ancillary services like scheduling and dispatch, reactive power and voltage control, and the provision of virtual inertia. These crucial functions collectively contribute to the overall efficiency and reliability of the system (Ullah et al., 2022; Tuckey; Round, 2022).

In the case of GFL converters, the primary controls can consist of active and reactive power control or AC-bus voltage control and DC-link voltage control, depending on the operation and the objective of application of the converters (Wang et al., 2020; Luna et al., 2015; Wu et al., 2025).

In case of GLC and GFM, various primary control strategies employed for GFM converters have been extensively discussed in (Han et al., 2016) with the task of generating the voltage and angle references for the inner control loops. Among these strategies, drift control stands out as the most prevalent, offering the ability to achieve island operation and enabling power sharing among inverters connected in parallel (Barklund et al., 2008; Aboushal; Moustafa, 2019).

A more recent advancement is the Virtual Synchronous Generator (VSG), which has garnered considerable interest and been the subject of numerous studies (Serban; Ion, 2017; D'Arco; Suul, 2013; Wu et al., 2017). Its primary objective is to emulate synchronous generators, effectively increasing grid inertia and enhancing overall grid stability.

In addition to droop control and VSG, there are other promising emerging control strategies, such as virtual oscillator control (Johnson et al., 2014), dispatchable virtual oscillator control (Groß et al., 2019; Colombino et al., 2019), and machine matching control (Arghir; Jouini; Dörfler, 2018).

2.2.4.2.1 Droop Control

Droop control is a widely used control strategy to enable load sharing in distributed networks with parallel connected inverters. The fact that it does not rely on communication links between converters makes it the most common control method and is used in nearly all experimentally implemented microgrids (Arachchige; Rajapakse, 2011).

The droop control works by regulating the active and reactive power (Pogaku; Prodanovic; Green, 2007). The conventional droop characteristics are illustrated in Figure 10, where the droop coefficients k_p and k_q depends of the properties of the electric system (Khadem; Basu; Conlon, 2011). For example, for a high voltage grid (inductive grid), the equations for conventional droop control are shown in (2.1) for stand-alone and grid-connected modes (Bouzid et al., 2015; Vasquez et al., 2010).

$$\begin{array}{l|l} f = f_N - k_p P & f = f_N - k_p(P - P_o) \\ V = V_N - k_q Q & V = V_N - k_q(Q - Q_o) \end{array} \tag{2.1}$$

V and f are the output voltage amplitude and frequency of the converter, respectively. V_N and f_N are the rated output voltage and frequency during no-load conditions and P and Q are the measured active and reactive power, respectively. The stand-alone and grid-connected droop control diagrams are shown in Fig. 11. A low-pass filter in the active and reactive power droop filter the measurement noises and emulate the inertia effect of the synchronous machine (Taoufik et al., 2019).

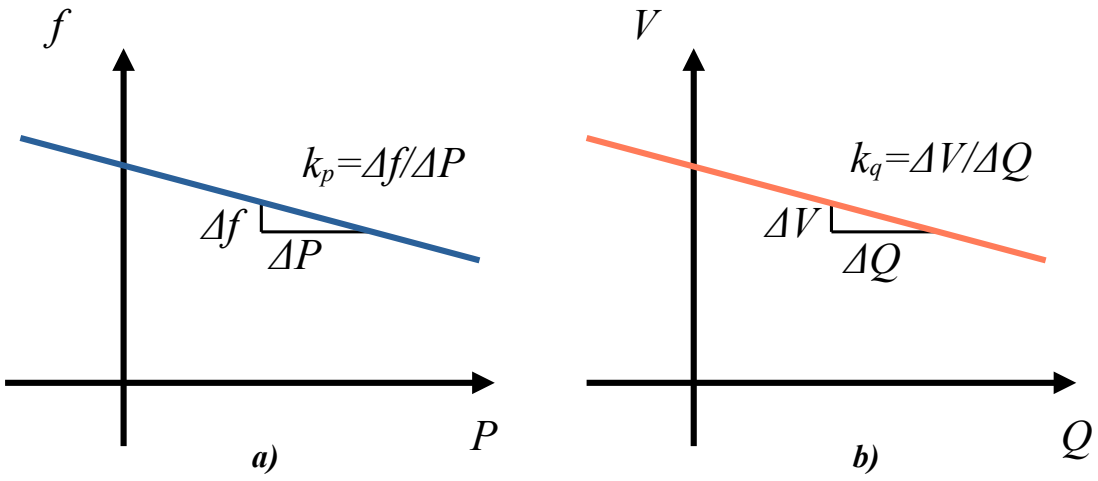

Figure 10 – Droop control strategy: a) P-f droop b) Q-V droop.

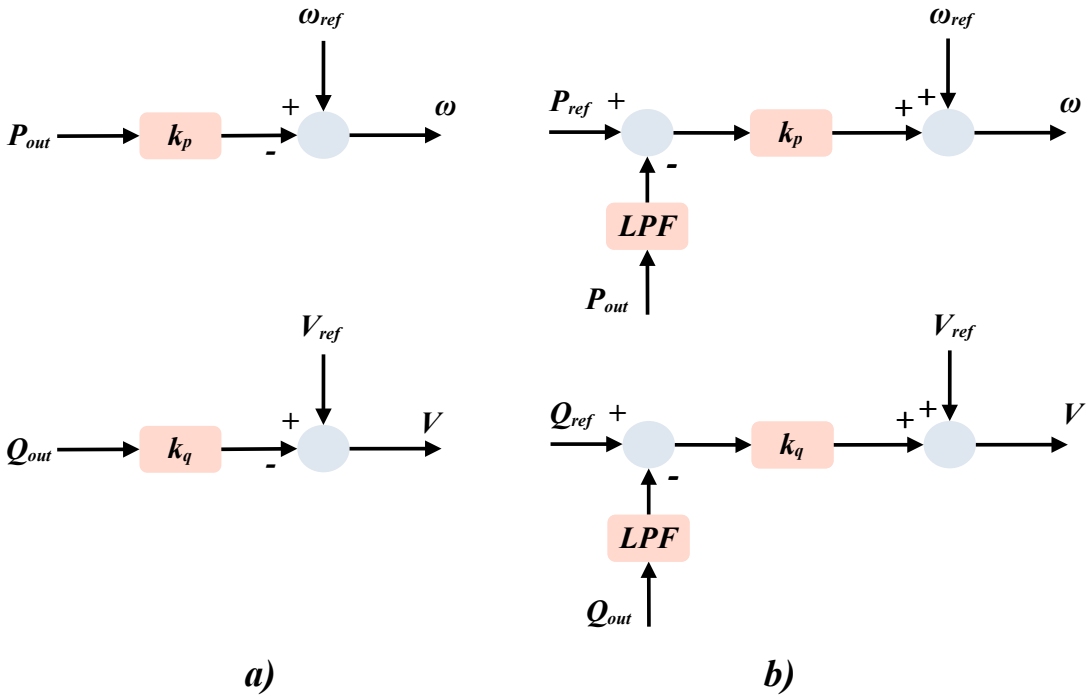

Figure 11 – Droop control strategy: a) Stand-alone droop b) Grid-connected droop control.

Some drawbacks comes from the assumption of purely inductive lines. Since the resistive effect of the power lines cannot be neglected, a cross-coupling between the P/f and Q/V droop loops may occurs. Other challenges for which various solutions have been proposed in the literature (Andishgar; Gholipour; Hooshmand, 2017; Tayab et al., 2017; Planas et al., 2013); the necessity to compromise between load sharing and voltage and frequency regulation (Guerrero et al., 2011; Majumder et al., 2010; Kim; Choi; Cho, 2002; Hu et al., 2014); line impedance impact on performance (Vasquez et al., 2009; Rokrok; Golshan, 2010; Li; Kao, 2009); difficulty to supply an unbalanced system (Savaghebi et al., 2013); harmonic load sharing (Wang; Blaabjerg; Chen, 2012; Liu et al., 2014); coupling inductances (Guerrero et al., 2005); dynamic response time (Sao; Lehn, 2005; Mohamed; El-Saadany, 2008).

In recent studies on droop control techniques, these limitations are addressed and suggestions on how to enhance the droop control design for implementation in a microgrid are presented (Tayab et al., 2017).

2.2.4.2.2 Virtual Synchronous Generator

The Virtual Synchronous Generator (VSG) is a relatively new concept that has gained attention and has been the subject of several studies (Serban; Ion, 2017; D'Arco; Suul, 2013; D'Arco; Suul; Fosso, 2015; Bevrani; Ise; Miura, 2014). The primary objective of VSG is to emulate Synchronous Generators (SGs) in order to enhance grid inertia, as they currently play a crucial role as frequency regulators in the grid.

The complete 7th order model of SG, as described in, (Machowski; Bialek; Bumby, 2012) is often considered overly complex (D'Arco; Suul, 2013). The crucial characteristics that are typically sought to be emulated are the inertial properties and the damping of electromechanical oscillations in the SG. To achieve this without unnecessary complexity, a control strategy is employed to make the inverter equivalent to an SG, enabling it to exhibit the same frequency droop characteristics as those observed in traditional SG.

(Zhong; Weiss, 2011) divides VSG in two parts: electrical part and mechanical part, as can be seen in Fig. 12. The electrical description of VSG is shown in Fig. 12a). The stator windings of the VSG can be represented as concentrated coils with self-inductance L, mutual inductance M and resistance R_s. The rotor winding can be considered as a centralized coil with an inductance of L_f and a resistance R_f.

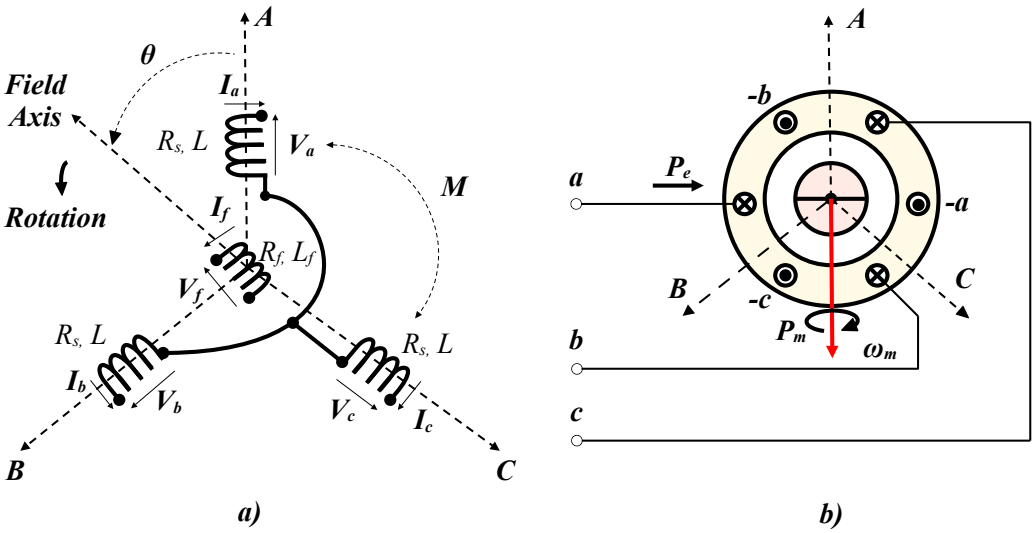

Figure 12 – Virtual synchronous generator: (a) Electrical representation. (b) Mechanical representation. *Adapted from* (Zhong et al., 2014; Belila et al., 2020)

The mutual inductance between the field coil and each of the three stator coils varies with the rotor angle θ as shown in (2.2). M_f is the maximum mutual inductance between the field winding and the three-phase stator windings.

$$\begin{aligned} M_{af} &= M_f cos\theta \\ M_{bf} &= M_f cos(\theta - \tfrac{2\pi}{3}) \\ M_{cf} &= M_f cos(\theta + \tfrac{2\pi}{3}) \end{aligned} \tag{2.2}$$

The flux linkage of each winding is shown in (2.3), where i_a, i_b, and i_c are the stator phase currents and i_f is the rotor field current.

$$\begin{aligned}\Phi_a &= Li_a - Mi_b - Mi_c + M_{af}i_f \\ \Phi_b &= -Mi_a + Li_b - Mi_c + M_{bf}i_f \\ \Phi_c &= -Mi_a - Mi_b + Li_c + M_{cf}i_f \\ \Phi_f &= M_{af}i_a + M_{bf}i_b + M_{cf}i_c + L_f i_f\end{aligned} \tag{2.3}$$

Defining:

$$\Phi = \begin{bmatrix}\Phi_a \\ \Phi_b \\ \Phi_c\end{bmatrix}, \quad i = \begin{bmatrix}i_a \\ i_b \\ i_c\end{bmatrix}, \quad [\widetilde{\cos}\theta] = \begin{bmatrix}\cos\theta \\ \cos\left(\theta - \frac{2\pi}{3}\right) \\ \cos\left(\theta + \frac{2\pi}{3}\right)\end{bmatrix}, \quad [\widetilde{\sin}\theta] = \begin{bmatrix}\sin\theta \\ \sin\left(\theta - \frac{2\pi}{3}\right) \\ \sin\left(\theta + \frac{2\pi}{3}\right)\end{bmatrix} \tag{2.4}$$

Assuming that the neutral line is not connected, the sum of stator currents is zero.

$$i_a + i_b + i_c = 0 \tag{2.5}$$

The stator flux linkages can be rewritten in (2.6), Where $L_s = L + M$.

$$\Phi = L_s i + M_f i_f \widetilde{cos}\theta \tag{2.6}$$

The field flux linkage can be expressed as (2.7), where $\langle ., . \rangle$ denotes the conventional inner product and the term $M_f\langle i, \widetilde{cos}\theta\rangle$, called armature reaction, that is constant in case of the three phase sinusoidal, as functions of θ, and balanced currents. It is possible to mention that $\sqrt{\frac{2}{3}}\langle i, \widetilde{cos}\theta\rangle$ is called the d-axis component of the current.

$$\Phi_f = L_s i + M_f\langle i, \widetilde{cos}\theta\rangle \tag{2.7}$$

Assuming R_s as the windings stator resistance, the phase terminal voltages $v = [v_a v_b v_c]^T$ can be obtained in (2.8)

$$v = -R_s i - \frac{d\phi}{dt} = -R_s i - L_s\frac{di}{dt} + e \tag{2.8}$$

The back electromotive force due to the rotor movement $e = [e_a e_b e_c]^T$ is show in (2.9). The voltage vector e is also called no-load voltage or synchronous internal voltage.

$$e = -M_f i_g \theta\widetilde{sin}\theta - M_f\frac{di_f}{dt}\widetilde{cos}\theta \tag{2.9}$$

According to (2.7) the field terminal voltage is show in (2.10), where R_f is the resistance of the rotor winding.

$$v_f = -R_f i_f - \frac{d\phi_f}{dt} \tag{2.10}$$

The mechanical description of VSG is shown in Fig.12b) and is given by (2.11), which is used to provide the phase voltage angle reference to the converter.

$$J\frac{d\omega}{dt} = T_m - T_e - D(\omega - \omega_g) \tag{2.11}$$

J is the inertia of the rotor, ω is the angular frequency of VSG, T_m the mechanical torque, T_e the electrical torque ω_g the angular frequency of the grid, and D a coefficient accounting for the damping torque of the damper windings that occur during transient conditions.

The electromagnetic torque (T_e) can be found from the energy E stored in the machine magnetic field:

$$\begin{gathered} E = \tfrac{1}{2}\langle i, \Phi\rangle + \tfrac{1}{2}\langle i_f, \Phi_f\rangle \\ = \tfrac{1}{2}\langle i, L_s + M_s i_f \widetilde{cos}\rangle + \tfrac{1}{2}\langle L_f i_f + M_f\langle i, \widetilde{cos}\theta\rangle\rangle \\ = \tfrac{1}{2}\langle i, L_s i\rangle + M_s i_f\langle i, \widetilde{cos}\theta\rangle + \tfrac{1}{2}L_f i_f^2 \end{gathered} \tag{2.12}$$

From simple energy considerations ((Zhong et al., 2014)):

$$T_e = \frac{\partial E}{\partial \theta}|_{\Phi, \Phi_{Constant}} \tag{2.13}$$

Since constant flux linkages mean no back EMF, all the power flow is mechanical. It is not difficult to verify (using the formula for the derivative of the inverse of a matrix function) that this is equivalent to:

$$T_e = -\frac{\partial E}{\partial \theta}|_{i, i_f Constant} \tag{2.14}$$

Then,

$$T_e = -M_f i_f i_0 \langle i, \frac{\partial}{\partial \theta}\widetilde{cos}\theta\rangle = M_F i_f \langle i, \widetilde{sin}\theta\rangle \tag{2.15}$$

We mention that $-\sqrt{\frac{2}{3}}\langle i, \widetilde{sin}\theta\rangle$ is called the q-axis component of the current. Note that if $i = i_0\widetilde{sin}\Phi$ for some arbitrary angle Φ, then:

$$T_e = M_f i_f i_0 \langle \widetilde{sin}\Phi, \widetilde{sin}\theta\rangle = \frac{3}{2} M_f i_f i_0 cos(\theta - \Phi) \tag{2.16}$$

For a constant i_f, (2.9) and (2.15) yields:

$$T_e\dot{\theta} = \langle i, e \rangle \tag{2.17}$$

The inertial dynamics of the VSG can be approximated in the Laplace domain by using the p.u. power balance for the SG (Machowski; Bialek; Bumby, 2012):

$$T_a * s * \omega_{VSG} \approx P_{REF} - P_{out} - k_d(\omega_{VSG} - \omega_g) \tag{2.18}$$

$T_a(2H)$ is the mechanical time constant which represent the rotor inertia, P_{REF} is the active power reference, P_{out} is the power output from the VSG, k_d is the damping coefficient. ω_{VSG} is supposed to represent the rotating speed and ω_g is the grid angular frequency when the VSG is connected to a strong grid, if it is operating in island mode it will be the frequency reference signal provided by a secondary controller.

A Droop control and VSG control comparison is performed in (D'Arco; Suul, 2014), showing that the both strategies present strong similarities and are even equal assuming a constant reference of grid angular frequency and a constant reference of active power. A comparison related with dynamic response of VSG and active power droop control shows better damping and lower overshoot in case of VSG control (Ofir et al., 2018).

(Liu; Miura; Ise, 2016) reveals that VSG has better frequency stability due to larger inertia compared to droop control which is of interest in low inertia systems such as microgrids. However, the output active power of VSG presents a more oscillatory behavior.

VSG challenges are discussed in (Bevrani; Ise; Miura, 2014) finding that measurement and computing techniques with modelling and analysis tools still need to be improved in order to possibility VSG control to work in large scale systems. The coordination between VSGs and SGs as well as the revision of existing standards is also highlighted as a key issue.

2.2.4.2.3 Dispatchable Virtual Oscillator Control

Other strategies proposed in the literature include the Virtual Oscillator Control (VOC) and Dispatchable Virtual Oscillator Control (dVOC) (Johnson et al., 2014; Groß et al., 2019). VOC control cannot be dispatched and does not require the explicit calculation of real and reactive power at the inverter terminal (Colombino et al., 2019; Awal et al., 2020b). However, dVOC is dispatchable and requires only local measurements to induce GFM behaviour with programmable droop characteristics (Awal et al., 2020a).

VOC control does not require frequency as a signal. (Johnson et al., 2017) and (Shi et al., 2019) makes a comparison of droop and VOC control. VOC is a non-linear time-domain controller and differs from droop control and VSG as not rely on phasor

approximation (Johnson et al., 2014; Johnson et al., 2016; Dhople; Johnson; Hamadeh, 2013).

According to (Tayyebi et al., 2019; Colombino et al., 2019; Aghdam; Agamy, 2022), generating an AC voltage signal based on the pre-defined magnitude and frequency the law of dVOC is given in 2.19.

$$\hat{v} = \omega_{\text{REF}}\, J_2 \hat{v} + \eta\left[K(p_{\text{REF}}, q_{\text{REF}})\hat{v} - R_2(k)\, i + \alpha\left(1 - \frac{\|\hat{v}\|^2}{V_{\text{REF}}^2}\right)\hat{v}\right] \tag{2.19}$$

$\widehat{v} = [v_\alpha e_\beta]^T$ is the reference voltage, $i = [i_\alpha i_\beta]^T$ is the current injection of the inverter, the angle is $k = tan^{-1}\frac{l\omega^*}{r}$ (v^* and $||\widehat{v}||$ are the reference and measured voltage magnitude), power injection from its nominal value p^* and frequency deviations from its nominal value w^*. Furthermore we have:

$$R_2(k) = \begin{bmatrix} \cos k & -\sin k \\ \sin k & \cos k \end{bmatrix}, \qquad \frac{1}{v^{*2}} R_2(k) = \begin{bmatrix} p^* & -q^* \\ q^* & p^* \end{bmatrix} \tag{2.20}$$

The dVOC does not contain the term of typical oscillator (L,C), in this method a mathematical equation duplicating a conventional oscillator is implemented (Aghdam; Agamy, 2022), as can be seen in Fig. 13.

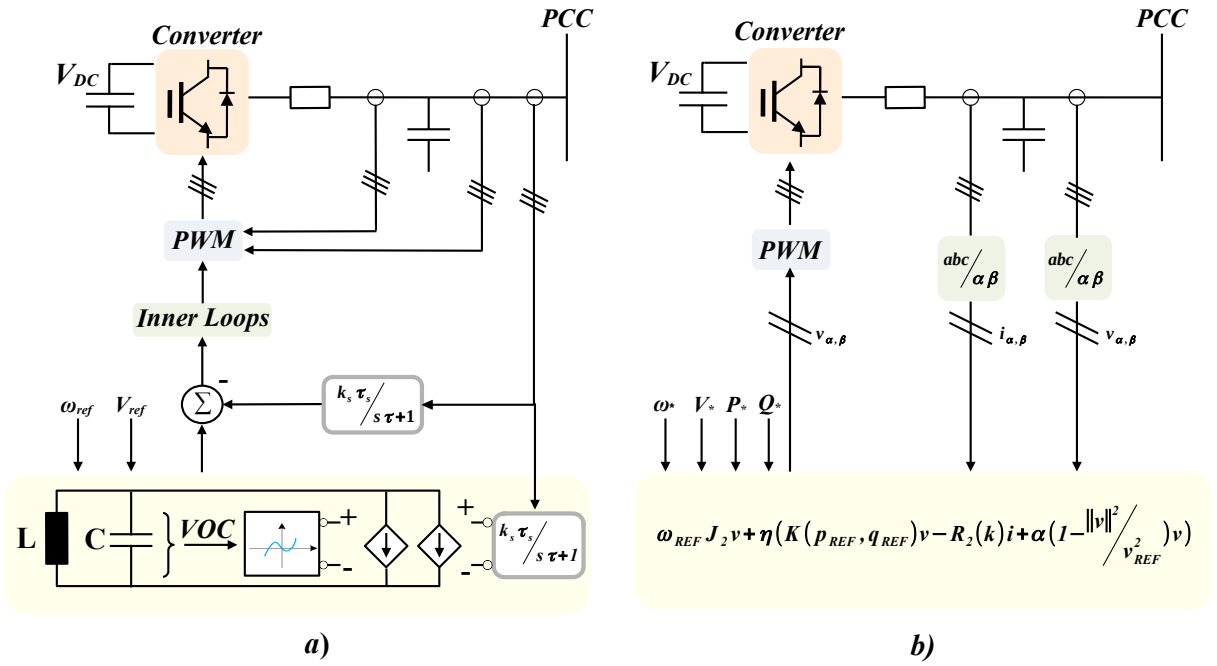

Figure 13 – Control diagram strategy: a) Virtual Oscillator Control (VOC) b) Dispatchable Virtual Oscillator Control (dVOC).

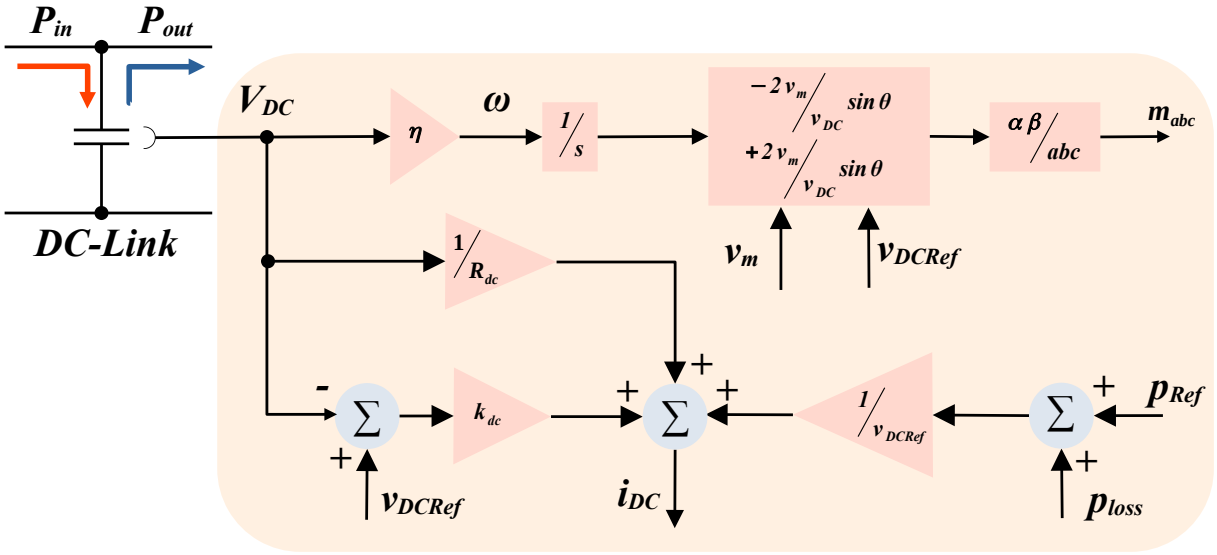

Figure 14 – Matching control structure diagram.

2.2.4.2.4 Machine Matching Control

Machine Matching Control (MC) is another emerging control technique which aims at creating a coupling between the frequency and active power balance by achieving a crucial coupling between the DC-side voltage and the AC-side frequency (Arghir; Jouini; Dörfler, 2018). (Aragon et al., 2022) show these equivalences that can be observed in (2.21).

$$\omega_{\mathrm{VSG}} = \frac{1}{2H}\left[\frac{T_m - T_e}{\omega_{\mathrm{VSG}}} - k_d(\omega_{\mathrm{VSG}} - \omega_g)\right] \quad \rightleftharpoons \quad v_{\mathrm{dc}} = \frac{1}{C_{\mathrm{dc}}}\left(i_{\mathrm{dc}} - i_{\mathrm{cdc}} - i_{R\mathrm{dc}}\right) \tag{2.21}$$

In this way, in case of a power imbalance on the AC side of the network, the MC control uses the energy stored in the DC-link bus capacitor to regulate the frequency. However, the power losses caused by R_{dc} behave as the damping term of the SG, as can be seen in Fig. 14.

2.2.4.2.5 Sliding Mode Control

Sliding Mode Control (SMC) is a non-linear control method. In (Li et al., 2017) the SMC control was applied between the inner current loop mixed with H_2/H_∞ optimal control in the outer voltage loop. Robustness of the control system with parameters variation, fast dynamic response and ability to reject disturbances are obtained.

The advantages and disadvantages of Droop control, VSG, dVOC, VOC, MC and SMC are summarized below in Table 5.

Finally, the third and fourth levels are the secondary and tertiary controls whose main function is to restore voltage and frequency values. Furthermore, at these levels,

Table 5 – Summary of different GFM control methods. *Adapted from* (Anttila et al., 2022).

Control Methods	Advantages	Disadvantages
Droop (Chandorkar; Divan; Adapa, 1993; Lidula; Rajapakse, 2011)	• Simplest implementation of the first-order swing equation • Enables parallel converter operation • No communication links needed for parallel operation	• High droop coefficients improve power sharing but degrade voltage regulation • Slow transient response in conventional droop control • Inability to handle harmonic load sharing between parallel converters • Limited frequency stability at low loads
VSG (D'Arco; Suul, 2013; Zhong; Weiss, 2011)	• Implements second-order swing equation • Variable inertia moment capacity	• Complexity and tuning challenges • Traditional VSG cannot compensate negative sequence components, causing unbalanced current and power oscillation
Synchronverter (Zhong; Weiss, 2011)	• Direct emulation of synchronous generator dynamics • Natural inertia and damping characteristics • Intuitive power-frequency droop behavior • Compatible with conventional power system operation	• Requires careful parameter tuning (inertia, damping) • May exhibit slow response during large disturbances • Complex implementation compared to basic droop control • Sensitivity to grid impedance variations
dVOC (Colombino et al., 2019; Seo et al., 2019)	• Enhanced frequency stability • Improved transient response • Dispatchable: permits power set point specification • Without set point, subsumes VOC control	• Complex implementation • Requires accurate grid parameters
VOC (Colombino et al., 2019; Awal et al., 2020b)	• Accurate frequency regulation • Robustness to parameter variations • No reference frame transformations needed • Fast disturbance response	• Complexity and precise parameter tuning • Non-dispatchable, reducing flexibility
MC (Arghir; Jouini; Dörfler, 2018)	• Simple design • Improved grid-forming capability • Enhanced system stability	• Recent strategy with limited validation • Intrinsic switching in control
SMC (Li et al., 2017)	• Robust to parameter variations • Suitable for nonlinear systems • Fast dynamic response and disturbance rejection	• Complexity • Requires precise current control • Chattering phenomenon (needs modifications for practical use)

the controller determines the ideal operating points of the DG units connected to the system by calculating the values of generation and demand. Furthermore, the design in secondary/tertiary control is based on optimization algorithms, maintaining megawatt exchanges between zones, remote bus set points, and optimal operation based on forecasts (Ishaq et al., 2022; Tuckey; Round, 2022).

2.3 Power Converter Topologies

A wide range of converters topologies for GFM operation it is found in literature in single and three-phase topologies (Antunes et al., 2017a). Three-phase converters has a wide application in industries systems and eletricity supply, however the use of single-phase inverters due to the low final cost production also can be notted (Antunes et al., 2017a; Gonzatti et al., 2014; Peña et al., 2014).

2.3.1 Single-Phase Topologies

One of the most important single-phase topologies is the single-phase full-bridge converter. The topology in GFM operation needs a LC or LCL filter to produce a sinusoidal output voltage (Gonzatti et al., 2014; Peña et al., 2014). Fig. 15 shows a few possible configurations for a full-bridge converter founded in literature. These single-phase topologies associated to obtain three-phase converters in delta and zig-zag connections can also be found in the literature (Antunes et al., 2017a).

2.3.2 Three-Phase Two-level Topologies

Fig. 16 shows a very common three-phase two-level VSI converter topology with an LC output filter. A disadvantage of this topology is the impossibility of load with neutral connection (Antunes et al., 2017a; Bahrani; Rufer, 2013; Yazdani; Iravani, 2010b; Gonzalez-Espin et al., 2014; Singh Luiz A.C. Lopes, 2015).

Another configuration of the three-phase topology of Fig. 16, is shown in Fig. 17 with the neutral conductor connection derived from the DC central point, increasing the complexity of converter control (Azevedo et al., 2013; Rese; Costa; Silva, 2012; Ortjohann et al., 2006; Antunes et al., 2017a).

In Fig. 18 a fourth arm three-phase two level converter is presented in order to obtain a neutral conductor, but with two additional switches (Ninad; Lopes, 2012; Antunes et al., 2017a; Blas et al., 2017; Vyawahare, 2019).

An output low frequency transformer can be implemented in output of the converter in Fig. 19 to provide galvanic isolation of DC level and zero sequence harmonics and creates a four-wire system to supply single-phase loads. The filter can appear on the primary

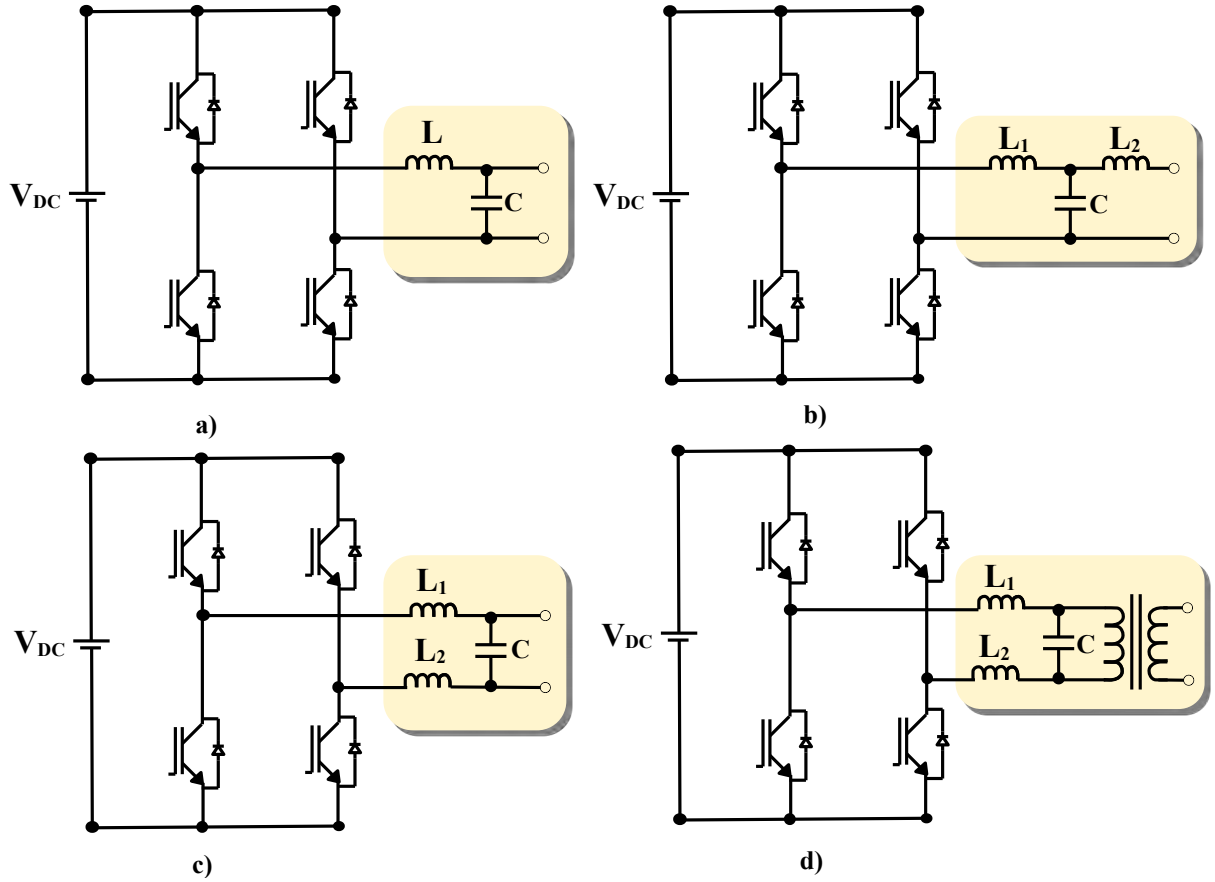

Figure 15 – Single-phase full-bridge converter configuration with: a) LC filter b) LCL filter c) LC filter d) LC filter with galvanic isolation.

or secondary side (Antunes et al., 2017a; Silva; Ribeiro; Matos, 2014; Miao et al., 2014; Bratcu; Aulagnier, 2015).

2.3.3 Three-Phase Three-level Topologies

A three-level three-phase converter is shown in Fig. 20, with the advantage of higher power quality performance due to the smoother waveform, lower switching frequency, and reduced sizes of LC/LCL filters due to the synthesized three-level output voltage where the switches must support one half of the DC link voltage (Antunes et al., 2017a; Gervasio et al., 2015; Sharma et al., 2023).

These traditional 2 and 3 levels topologies deal with problems related to limited switching frequency, high losses and the necessity of output capacitive filters to be connected in the AC side (Antunes et al., 2017a; Anttila et al., 2022).

Since the distributed energy resources (DERs) usually interfaces the point of common coupling (PCC) through LC or LCL output filters to provide switching harmonics attenuation, several resonances points at various frequencies can arise. The induced resonances can affect both transient and steady-state control performances and even lead to severe stability issues (Saim et al., 2019; Lourenço et al., 2021; Han et al., 2016;

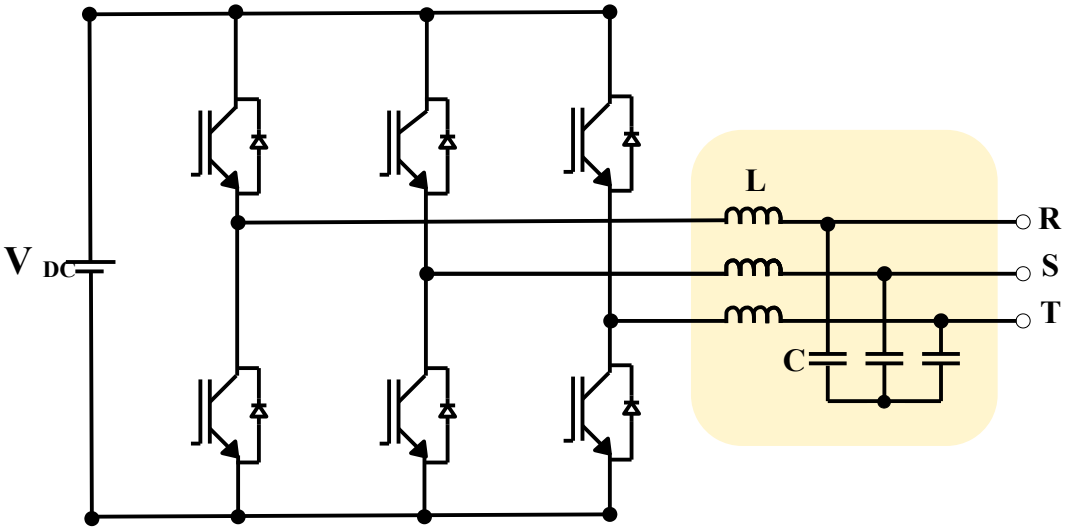

Figure 16 – Three-Phase 2 level converter with LC output filter.

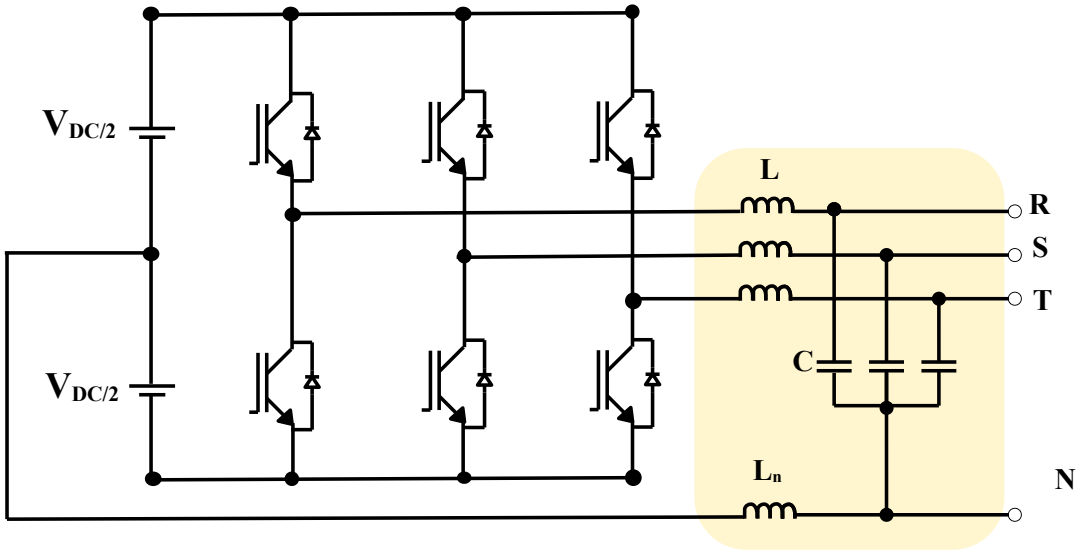

Figure 17 – Three-Phase 2-level converter with LC output filter with neutral connection.

Vandoorn et al., 2013).

2.3.4 Medium Voltage Converters Configurations

The fast growing of DERs connected at medium voltage (MV) level results in a increasing demand for MV Three-phase converters topologies on MV applications. These converters can been classified into two groups: with transformer and transformerless (Wang et al., 2016a; Xavier et al., 2019).

2.3.4.1 Converter topologies with transformer

In medium voltage (MV) systems, two and three-level converter topologies require a step-up transformer for applications connected to MV grids (Wang et al., 2016a; Steimer;

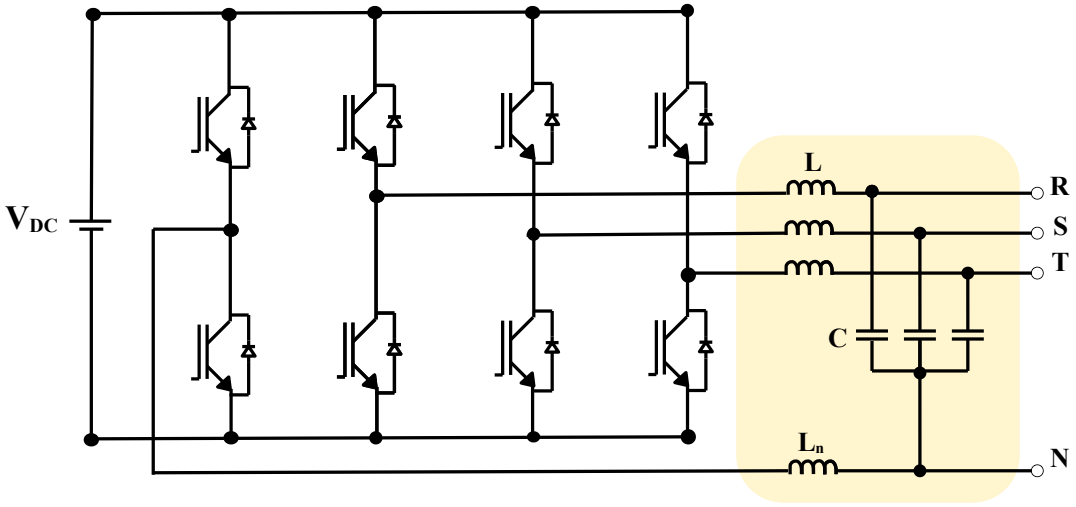

Figure 18 – Three-Phase fourth arm 2-level converter with LC output filter.

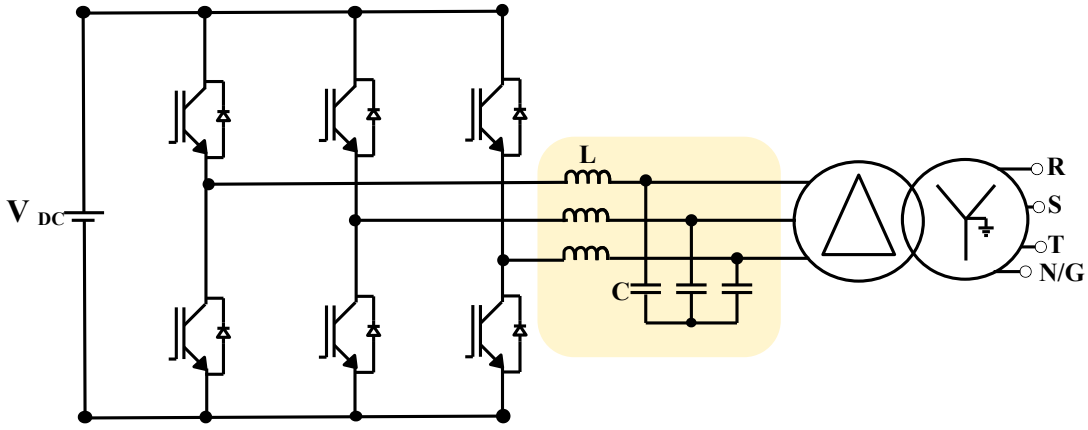

Figure 19 – Three-Phase 2-level converter with LC output filter and output transformer.

Manjrekar, 2001; Dias; Alves; Torri, 2016; Hiller; Sommer; Beuermann, 2008; Xavier et al., 2019).

Fig. 21 shows the conventional converter structure based on two- and three-level topologies connected to the MV power grid. Two-level converters generally are based on the voltage source converter (VSC), ZSI (Z-source converter) and qZSI (quasi-Z-source converter). The three-level converters, in other hand, based on NPC, Flying capacitor and ANPC topologies (Wang et al., 2016a; Xavier et al., 2019).

It is possible to observe that the output LC/LCL filters usually employed, are connected to a transformer (Tx) that is used to step-up the low voltage (LV) from the inverter side to the MV system (Wang et al., 2016a; Xavier et al., 2019). Two-level converters are the most commonly used topologies (Gervasio et al., 2015; Gkountaras; Dieckerhoff; Sezi, 2015; Antunes et al., 2017a; Gervasio et al., 2015).

For high power applications, a parallel association in power blocks could be used to avoid power concentration in a single system. However, multilevel converters could be necessary when low output voltage distortion are required and high output voltage levels

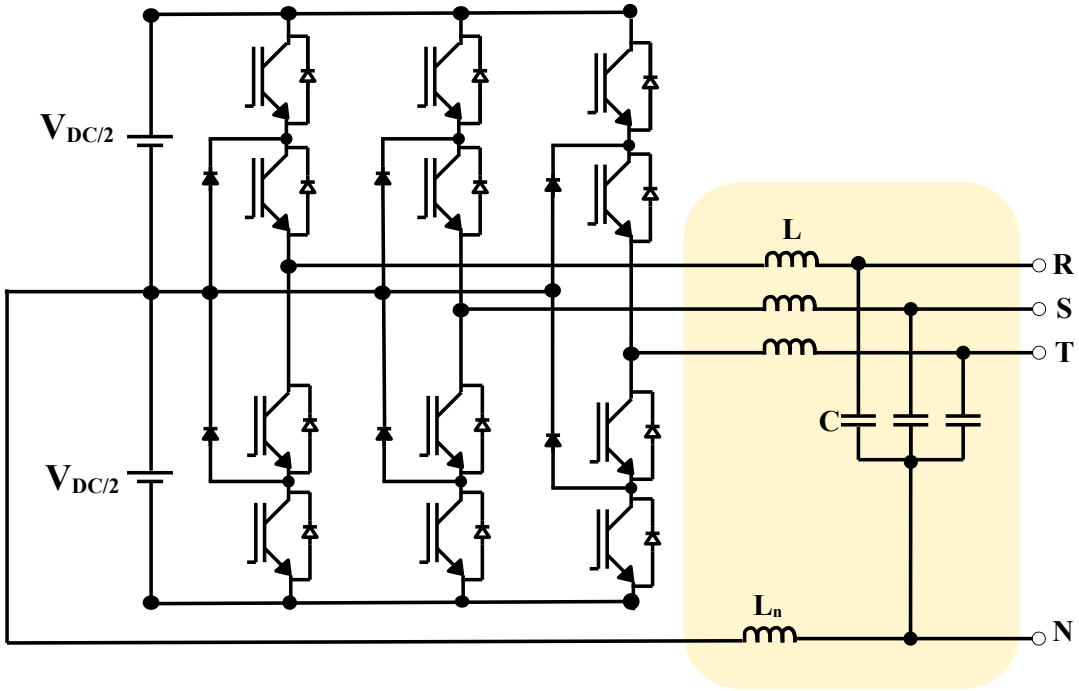

Figure 20 – Three-phase 3-level converter with LC ouput filter.

(Wang et al., 2016a; Xavier et al., 2019).

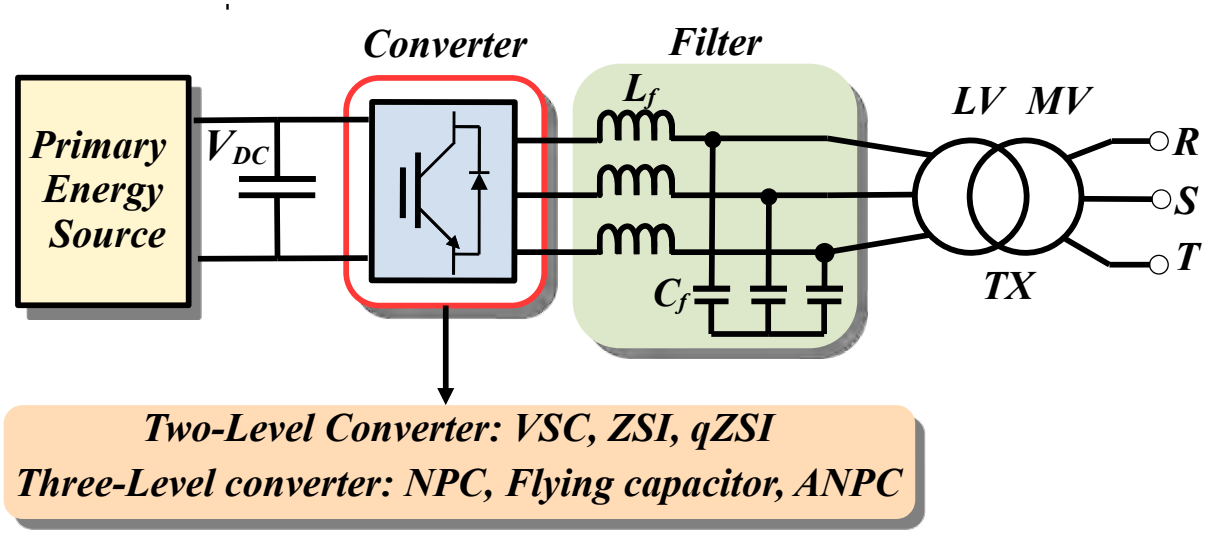

Figure 21 – Conventional Structure connected to the MV power grid.

2.3.4.2 Transformerless Topologies

Transformeless topologies dismiss the employment of transformer, thus the converter can be directly connected to the MV level (Wang et al., 2016a; Xavier et al., 2019).

Two-level topologies can still be used for direct connection to MV grid. In this configuration, several insulated gate bipolar transistors (IGBTs) are usually connected in series. This connection can be understood as a single IGBT capable to block voltages in the range of kV. The main disadvantage of this topology is the increased complexity in the

gate drive circuits, in order to ensure the synchronization between the on and off states of the switches. It is easy to observe that the greater the numbers of switches in series, the more complex the converter design is. This topology is also designed to operate with low switching frequency, in order to limit the switching losses. However, a low switching frequency increases the filtering requirements (Wang et al., 2016a; Xavier et al., 2019).

Multilevel topologies have demonstrated prominent technologies in recent researches on BESSs related with the direct connection to the MV grid. These topologies make it easier to deal with the state of charge (SOC) unbalance of the batteries. They also present low losses, modularity and scalability, among other characteristics. The cascaded H-bridge converter (CHB) and the modular multilevel converters (MMC) are the most discussed multilevel topologies (Wang et al., 2016a; Xavier et al., 2019). Fig. 22 shows the CHB converter consisting of three-phase legs, each having multiple H-bridge cells connected in series making it possible to boost LV cells to MV levels without the use of transformers with the advantages of modularity, good harmonic performance, and the ability to accommodate heterogeneous energy storage. However, each bridge requires an independent dc source, limiting the applications of the converter topology (Wang et al., 2016a; Tang; Yang; Blaabjerg, 2022; Farivar et al., 2023; Leon; Vazquez; Franquelo, 2017).

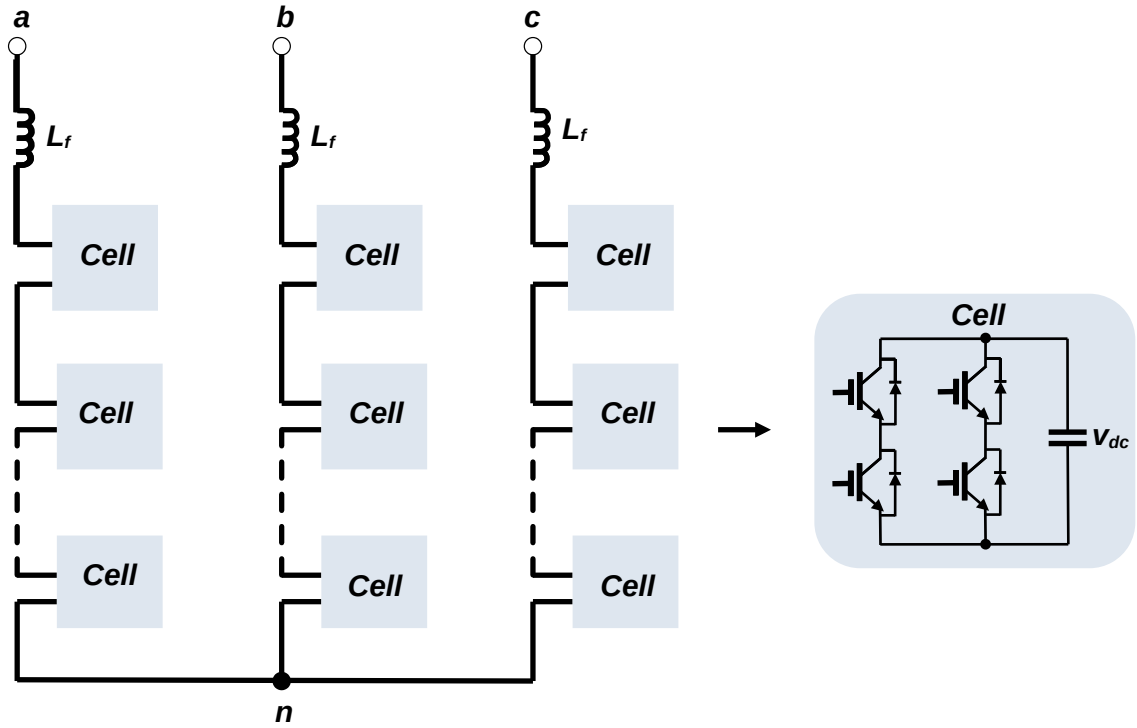

Figure 22 – Cascaded H Bridge converter.

The MMC topology is widely employed in high-power systems due to its effectiveness and reliability. This topology enables the combination of inverters in series and parallel, with the main concept being the division of the total voltage or current among multiple smaller inverters. This approach allows for the generation of intermediate voltage or current

levels, which in turn facilitates the synthesis of an alternating waveform with minimal harmonic distortion (Rokrok et al., 2020). Fig.23 shows the MMC topology.

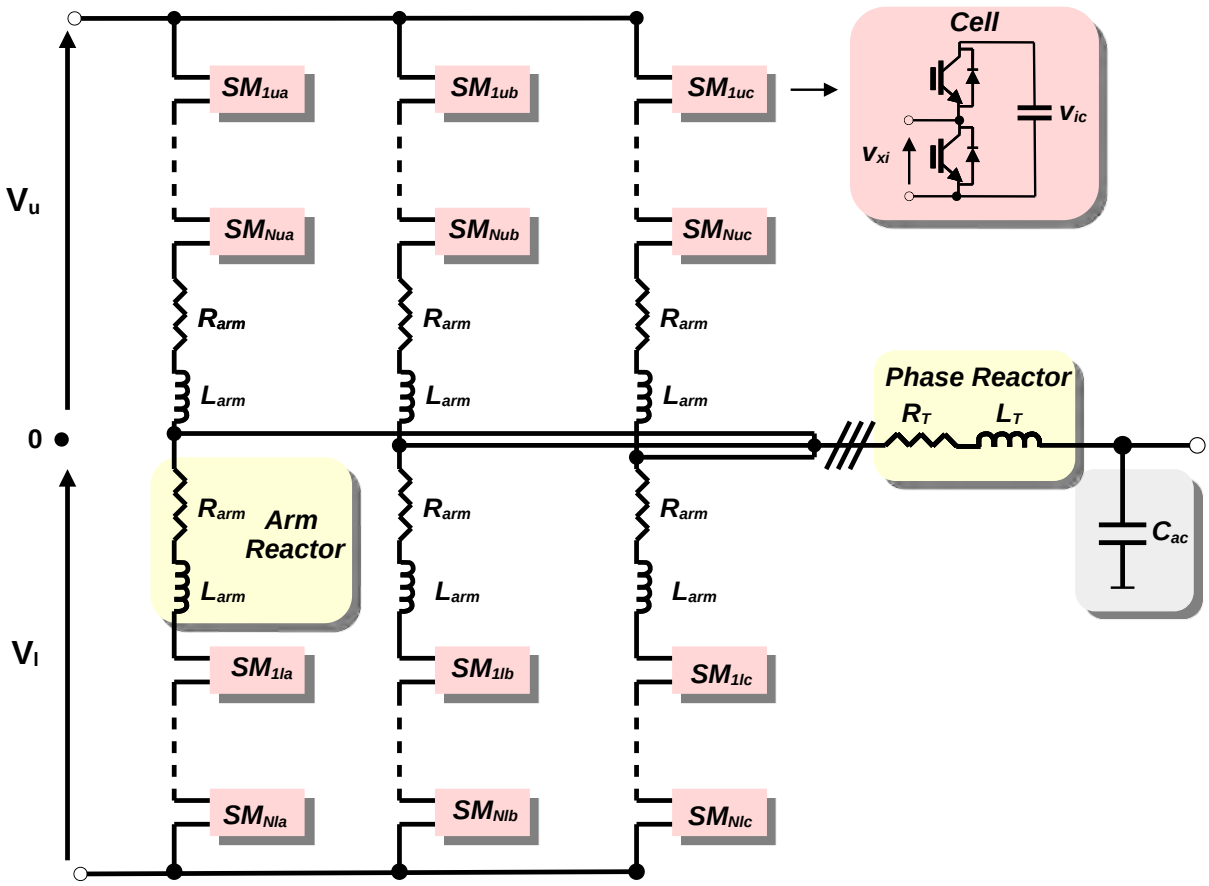

Figure 23 – Modular Multilevel Converter.

Recent works showed the MMC converters as a solution for power systems in the grid-forming operation (Rokrok et al., 2020; Lourenço et al., 2021; Freytes et al., 2021; Taoufik et al., 2022; Henninger; Schroeder; Jaeger, 2018; Sánchez-Sánchez; Prieto-Araujo; Gomis-Bellmunt, 2020). Usually, it is considered a physical capacitance at the PCC, although in (Freytes et al., 2021) and in (Taoufik et al., 2022) control implementations without output capacitors are discussed, since the series connection of N cells can generate a quasi-sinusoidal voltage waveform at the output.

However, the control problem associated with the MMC is more complex than the one associated with converters based on two or three-level VSCs. The complexity arises from the growth in the number of variables to be controlled, the converter circulating currents, the internal energy stored in the submodule capacitors, and the high number of power cells necessary to reach a low distortion of output voltage (Sánchez-Sánchez; Prieto-Araujo; Gomis-Bellmunt, 2020; Bergna-Diaz; Suul; D'Arco, 2018; Oliveira et al., 2021).

Although there are transformerless topologies as the CHB and MMC converters, the majority of commercial systems still makes use of 2 or 3-level VSCs with low frequency

transformers in high power converters to interface with the Medium Voltage (MV) grid (Wang et al., 2016a; Gkountaras; Dieckerhoff; Sezi, 2015; Tang; Yang; Blaabjerg, 2022). The association of VSCs with multiple winding transformers is very common, for example in BESS applications, to reach more power in MV and HV levels, as illustrated in Fig. 24.

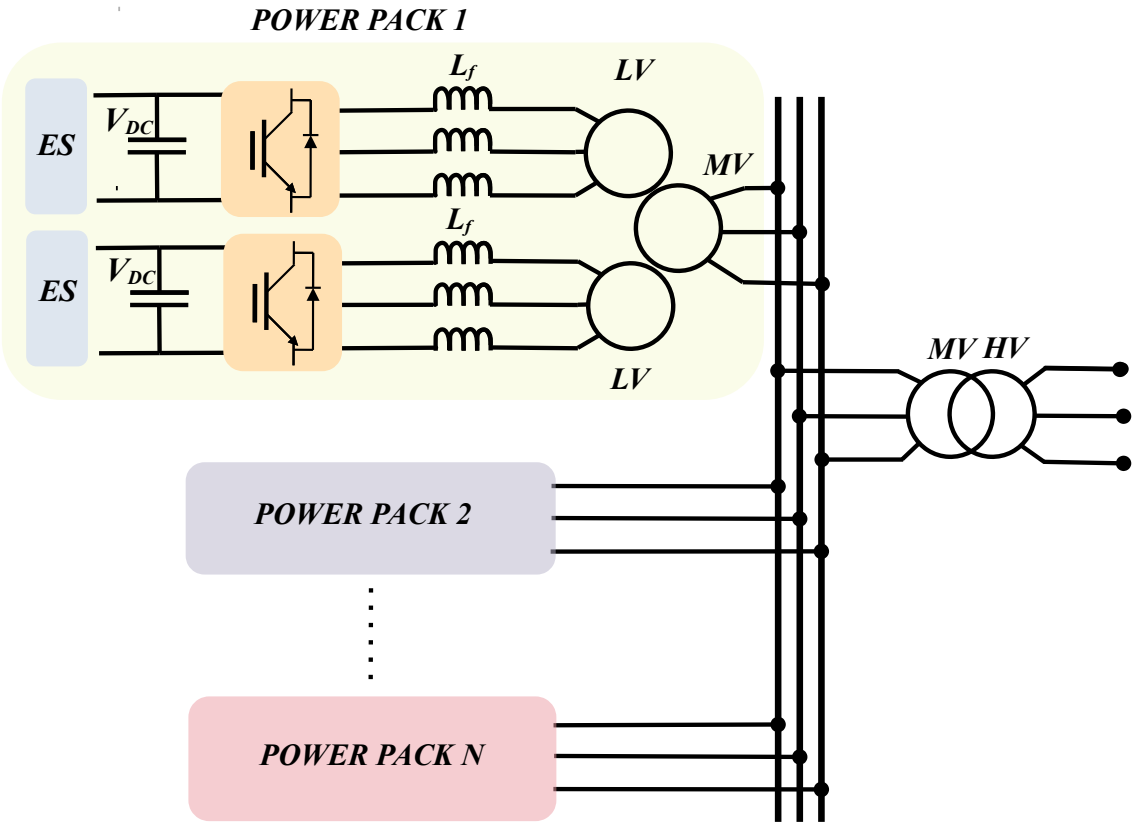

Figure 24 – Association of three-phase low voltage converters in structures based on multiple winding transformers.

The competitive cost of these configurations, and the necessity to provide the galvanic isolation desired in renewable energy integration and required by standards of grid-connected battery energy systems, make these conventional topologies the main choice for industrial solutions since the filterless topologies has the additional cost of the higher amount of capacitors and seminconductors and necessity of the dc-dc converters, necessary to isolation purposes. (Wang et al., 2016a; Tang; Yang; Blaabjerg, 2022; Utility. . . , 1997).

2.3.5 Zero Harmonic Distortion Converter

This work proposes a GFM converter based in the Zero Harmonic Distortion (ZHD) technology. The ZHD converter proposed in (Parreiras; Justino; Filho, 2015) was already explored as a grid-feeding converter in solar (Alves; Parreiras; Filho, 2019), wind (Almeida; Filho, 2017), four quadrant motor drives (Parreiras et al., 2015; Parreiras et al., 2021),

battery charge systems (Parreiras et al., 2020), reactive compensator (Brandão et al., 2022b) and fast charging stations (Justino; Parreiras; Filho, 2014; Brandão et al., 2022).

In this scenario, this work proposes the application of ZHD converter shown in Fig. 25 as a GFM converter without the use of capacitive filters that negatively impact costs, efficiency, size, resonances, feroresonance, and reliability problems (Almeida; Filho, 2017; Saim et al., 2019; Mozina, 2013; Monadi et al., 2013; Yao et al., 2024) for GFM operation in microgrids and power systems applications, that can be implemented utilizing conventional/commercial two- or three-level converters.

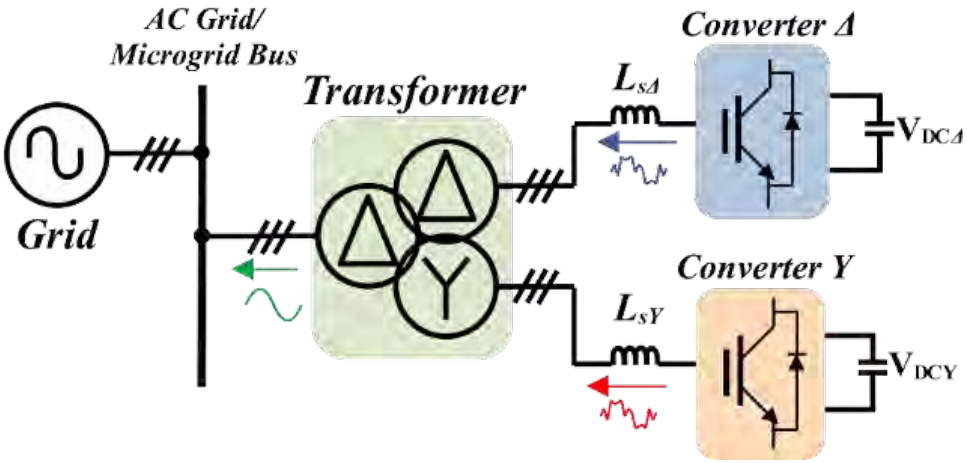

Figure 25 – ZHD converter.

The ZHD converter exhibits an inherently sinusoidal voltage source characteristic without the need of capacitive filtering elements, achieved by the proper combination of harmonic cancellation in a three-winding transformer and harmonic elimination using the Selective Harmonic Elimination Pulse Width Modulation (SHE PWM). In this way, in VCM mode the ZHD converter dismiss inner voltage and current loops for GFM operation in power systems and MG applications, usually found in other converters topologies.

2.4 Summary of Grid-Forming Converter Topologies

Table 6 shows a summary of the main grid-forming topologies found in literature in terms of control complexity, use of capacitive filters and number of components. It is possible to verify that the ZHD converter as based in conventional 2 or 3-level VSCs presents low number of components, low control complexity and due to the inherently sinusoidal voltage source characteristic, the absence of LC/LCL filters and low output voltage distortion. These characteristics make of ZHD converter a excellent choice in MV GFM applications.

Table 6 – Summary of Grid-Forming Converters topologies.

Topology	Control Complexity	Capacitive Filters	Number of components
2/3-Level VSCs	**Low**: (Tuckey; Round, 2022) (Bahrani; Rufer, 2013) (Gonzalez-Espin et al., 2014) (Antunes et al., 2017b) (Azevedo et al., 2013)	**Required**: (Singh Luiz A.C. Lopes, 2015) (Ortjohann et al., 2006) (Ninad; Lopes, 2012) (Silva; Ribeiro; Matos, 2014) (Gervasio et al., 2015) (Antunes et al., 2017a) (Machado et al., 2017) (Bratcu; Aulagnier, 2015) (Azevedo et al., 2013)	**Low**: (Wang et al., 2016a) (Xavier et al., 2019) (Tang; Yang; Blaabjerg, 2022)
CHB	**Medium**: (Farivar et al., 2023) (Leon; Vazquez; Franquelo, 2017)	**Not Required**: (Farivar et al., 2023) (Leon; Vazquez; Franquelo, 2017)	**High**: (Farivar et al., 2023) (Leon; Vazquez; Franquelo, 2017)
MMC	**High**: (Sánchez-Sánchez; Prieto-Araujo; Gomis-Bellmunt, 2020) (Bergna-Diaz; Suul; D'Arco, 2018) (Oliveira et al., 2021)	**Not Required**: (Freytes et al., 2021) (Taoufik et al., 2019)	**High**: (Sánchez-Sánchez; Prieto-Araujo; Gomis-Bellmunt, 2020) (Bergna-Diaz; Suul; D'Arco, 2018) (Oliveira et al., 2021) (Wang et al., 2016a)
ZHD	**Low**: (Justino; Parreiras; Filho, 2014) (Parreiras; Filho, 2014) (Parreiras; Justino; Filho, 2015) (Parreiras et al., 2015) (Parreiras, 2015) (Justino; Parreiras; Filho, 2016) (Parreiras et al., 2015) (Almeida; Filho, 2017) (Almeida; Filho, 2018) (Alves; Parreiras; Filho, 2019) (Almeida, 2019) (Parreiras et al., 2020) (Parreiras et al., 2020) (Alves, 2020) (Parreiras, 2020) (Parreiras et al., 2021) (Brandão, 2021) (Brandão et al., 2021) (Brandão et al., 2022b) (Brandão et al., 2022a) (Brandão et al., 2022)	**Not Required**: (Justino; Parreiras; Filho, 2014) (Parreiras; Filho, 2014) (Parreiras; Justino; Filho, 2015) (Parreiras et al., 2015) (Parreiras, 2015) (Justino; Parreiras; Filho, 2016) (Parreiras et al., 2015) (Almeida; Filho, 2017) (Almeida; Filho, 2018) (Alves; Parreiras; Filho, 2019) (Almeida, 2019) (Parreiras et al., 2020) (Parreiras et al., 2020) (Alves, 2020) (Parreiras, 2020) (Parreiras et al., 2021) (Brandão, 2021) (Brandão et al., 2021) (Brandão et al., 2022b) (Brandão et al., 2022a) (Brandão et al., 2022)	**Low**: (Justino; Parreiras; Filho, 2014) (Parreiras; Filho, 2014) (Parreiras; Justino; Filho, 2015) (Parreiras et al., 2015) (Parreiras, 2015) (Justino; Parreiras; Filho, 2016) (Parreiras et al., 2015) (Almeida; Filho, 2017) (Almeida; Filho, 2018) (Alves; Parreiras; Filho, 2019) (Almeida, 2019) (Parreiras et al., 2020) (Parreiras et al., 2020) (Alves, 2020) (Parreiras, 2020) (Parreiras et al., 2021) (Brandão, 2021) (Brandão et al., 2021) (Brandão et al., 2022b) (Brandão et al., 2022a) (Brandão et al., 2022)

2.5 Conclusions

In this chapter, we have provided a comprehensive contextualization and classification of Grid-Forming Multi-Inverter (GFM) converters, highlighting their significance in shaping the future energy systems. We have thoroughly examined the power converter control structure for grid-forming converters, discussing their objectives in detail.

A comprehensive review of various control approaches available in the literature has been presented, organized within the hierarchical structure outlined earlier. Additionally, we have briefly discussed the most significant single and three-phase converter topologies in low voltage applications, as well as three-phase converter structures in medium voltage applications.

Among the converter topologies studied, the ZHD converter has emerged as a promising option due to its reliance on 2 or 3-level Voltage Source Converters (VSCs), which are commonly used in various commercial applications. The advantages offered by the ZHD converter make it an attractive choice for future energy systems.

3 Zero Harmonic Distortion Converter: Concept, Modeling and Design

In this chapter, we present a comprehensive analysis of the ZHD converter, focusing on its operating principles, equivalent per-phase circuit modeling, flux harmonic cancellation at the transformer, potential converter topologies, and overall technical feasibility.

3.1 Total Harmonic Distortion and Applicable Normalization

A sinusoidal waveform X can be characterized in terms of the Total Harmonic Distortion (THD) shown in (3.1), as a waveform where all harmonic components of order k=2, 3,..., N are zero.

$$THD_X = 100\frac{\sqrt{\sum_{k=2}^{N} X_{krms}}}{X_{1rms}} \tag{3.1}$$

In practice, the calculation of THD must be done with limited number of harmonics and according to some important international standards show in Table 7. It is clear that harmonics until the 50^{th} are enough to characterize harmonic voltage and current distortion and fulfill the requirements across the world.

Table 7 – Maximum Values of Harmonic Order For THD calculation.

Standard	Section	Reference	N
IEEE Standard 519-2022	4	(IEEE..., 2022)	50
IEC 61000-4-7	3.3.1	(Electromagnetic..., 2009)	40
IEEE Standard 1566	15.2	(IEEE..., 2015)	49
IEEE Standard 2800-2022	8.2	(IEEE..., 2022)	50
IEEE Standard 1547-2018	7.3	(IEEE..., 2018)	50
IEC 61800-3	5	(Adjustable..., 2022)	40
IEC 61892-1	4.5	(Mobile..., 2019)	50
IEC 61000-2-4	5	(Electromagnetic..., 2002)	50

Although there are currently no specific standards for GFM converters, there are some significant technical reports available (Grid..., 2021; Grid-Forming..., 2021; High..., 2019; Lin Yashen; Ellis., 2020). One of them has already identified a relevant harmonic range of 2 kHz ($N \cong 40$)(High..., 2019).

All the standards of Table 7 were developed to attend harmonic control to applications connected to the grid. In islanded systems there is no harmonic standards,

however some works follow the standards of Table 7 as a guide for harmonic power quality, especially IEEE 519 and IEEE 1547 (IEEE. . . , 2022; IEEE. . . , 2018). In this sense, a grid-forming converter that can deliver a voltage waveform free from harmonics below the 50^{th} order can be assumed as a sinusoidal voltage power source with zero harmonic distortion.

3.2 Zero Harmonic Distortion Converter

Following the standards in Table 7, Fig. 26 and Fig. 27 show the proposed ZHD converter. It consists of two 2-level or 3-level VSCs connected to a three-winding transformer. The VSCs are connected in the star and delta secondaries of transformer. Due to the phase shift of 30 degrees between secondaries, it is expected a harmonic cancellation according to (3.2).

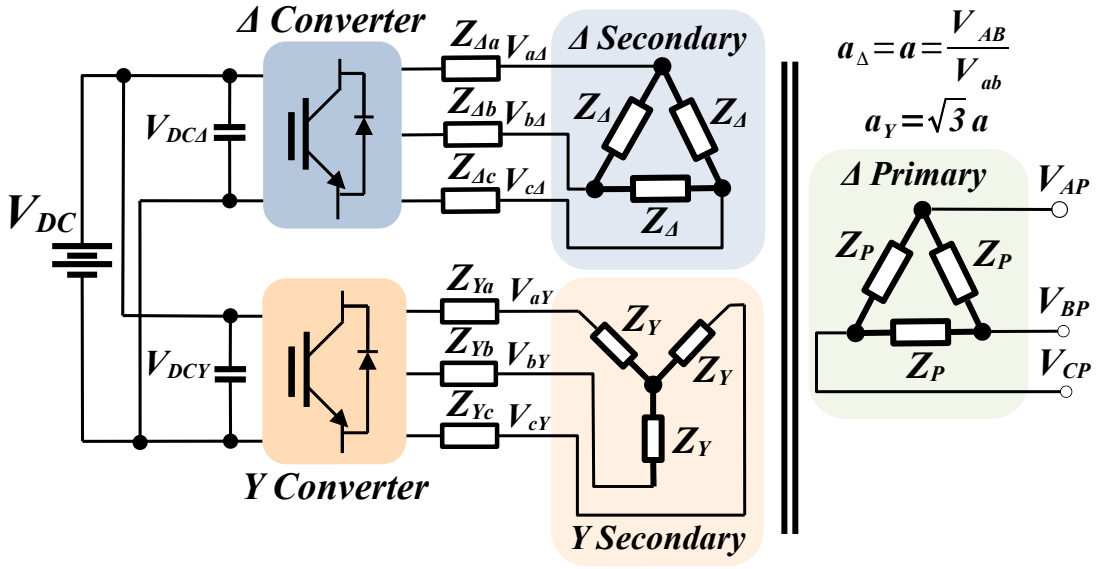

Figure 26 – 2-Level ZHD Grid-Forming converter.

$$h = 6k \pm 1 \;\; \forall \;\; k \; odd \; and \; integer \tag{3.2}$$

In this context, it is possible to obtain a voltage waveform free from all the considered harmonics until the 50^{th} order, by utilizing the SHE PWM technique to eliminate the harmonics not cancelled by the transformer. Table 8 shows the cancelled harmonics by the transformer and the eliminated ones by the SHE PWM technique.

3.3 Selective Harmonic Elimination

The SHEPWM modulation proposed in (Patel; Hoft, 1973) is very well established for two- and three level converters applications and in (Patel; Hoft, 1974) is extended to

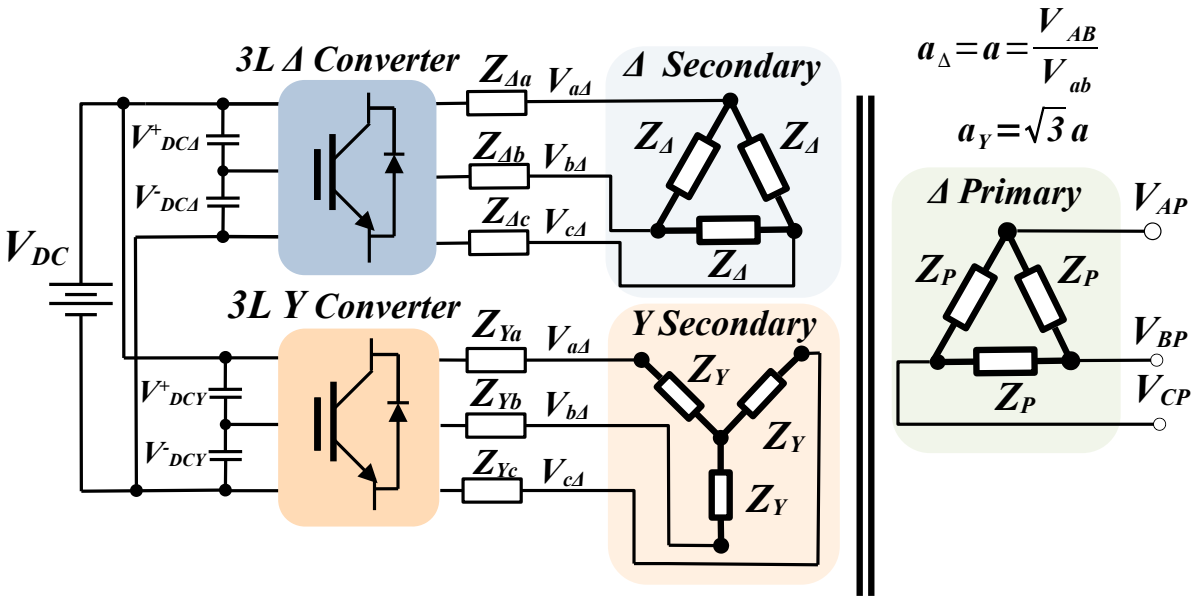

Figure 27 – 3-Level ZHD Grid-Forming converter.

Table 8 – ZHD Converter Harmonic Elimination and Cancellation.

Equipment	**Harmonic Order**
Transformer:	$5^{th}, 7^{th}, 17^{th}, 19^{th}, 29^{th}, 31^{th}, 41^{th}, 43^{th}, \ldots$
VSCs:	$11^{th}, 13^{th}, 23^{th}, 25^{th}, 35^{th}, 37^{th}, 47^{th}, 49^{th}$

cases where the fundamental amplitude control is required.

Fig. 28 shows the voltage waveform generated in one phase of a two-level and three-level converter for a voltage modulation index m. The waveform is generated using the precalculus of switching angles $\alpha_1, \alpha_2, \alpha_3, \alpha_4, ..., \alpha_M$ related to the harmonics selected to be eliminated or mitigated, according to the coefficients of the Fourier series: (3.3) and (3.4) for two and three-level converters respectively, determining the number of switches in one period of the waveform (Patel; Hoft, 1973; Patel; Hoft, 1974).

$$\begin{cases} a_n = \dfrac{4}{n_i\pi}\left[1 + 2\sum\limits_{k=1}^{M}(-1)^k \cos(n_i\alpha_k)\right], & \text{odd } n_i, \\ a_n = 0, & \text{even } n_i, \\ b_n = 0, & \text{all } n_i. \end{cases} \tag{3.3}$$

$$\begin{cases} a_n = \dfrac{4}{n_i\pi}\sum\limits_{k=1}^{M}(-1)^k \cos(n_i\alpha_k), & \text{odd } n_i, \\ a_n = 0, & \text{even } n_i, \\ b_n = 0, & \text{all } n_i. \end{cases} \tag{3.4}$$

The calculation process of the switching angles takes place through the solution of

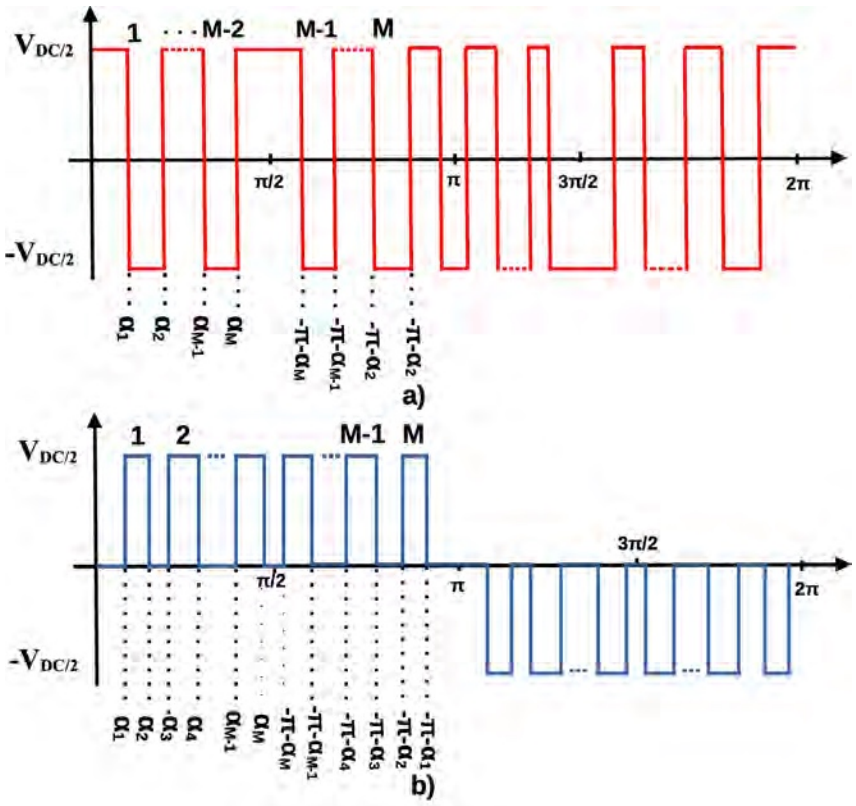

Figure 28 – Voltage waveform generated by SHE PWM in: a) Two-level converter and in b)Three-level converter.

transcendental equations, using interactive methods such as the Newton-Raphson method. Equations (3.5) and (3.6) show the angles obtained for each value of modulation index m for two and three-level converters, respectively. The angle matrix order is equal to the desired number of switching angles to be calculated (Patel; Hoft, 1973; Patel; Hoft, 1974).

$$\vec{f} = \begin{bmatrix} 1 - 2\cos(\alpha_1) + 2\cos(\alpha_2) + \cdots + 2(-1)^M \cos(\alpha_M) \\ 1 - 2\cos(n_2\alpha_1) + 2\cos(n_2\alpha_2) + \cdots + 2(-1)^M \cos(n_2\alpha_M) \\ \vdots \\ 1 - 2\cos(n_i\alpha_1) + 2\cos(n_i\alpha_2) + \cdots + 2(-1)^M \cos(n_i\alpha_M) \end{bmatrix} = \begin{bmatrix} m \\ 0 \\ \vdots \\ 0 \end{bmatrix} \tag{3.5}$$

$$\vec{f} = \begin{bmatrix} cos(\alpha_1) - cos(\alpha_2) + ... + (-1)^{M+1} cos(\alpha_M) \\ cos(n_2\alpha_1) - cos(n_2\alpha_2) + ... + (-1)^{M+1} cos(n_2\alpha_M) \\ \vdots \\ cos(n_i\alpha_1) - cos(n_i\alpha_2) + ... + (-1)^{M+1} cos(n_i\alpha_M) \end{bmatrix} = \begin{bmatrix} m \\ 0 \\ \vdots \\ 0 \end{bmatrix} \tag{3.6}$$

The modulation index m is described by (3.7), where V_{1m} is the fundamental amplitude desired and $V_{1m6step}$ the maximum fundamental voltage available at the terminals defined by (3.8), where V_{dc} is the voltage on the DC bus (Parreiras; Filho, 2014).

$$m = \frac{v_{1m}}{V_{1ms6step}} \tag{3.7}$$

$$V_{1ms6step} = \frac{2V_{dc}}{\pi} \tag{3.8}$$

The transcendental and nonlinear eq. (3.5) and (3.6) require a numerical method in order to achieve a solution. The method is illustrated in Fig. 29 where the Jacobian matrices are expressed in (3.9) and (3.10).

$$\frac{\partial \vec{f}}{\partial \vec{\alpha}} = \begin{bmatrix} 2n_1 \sin(n_1\alpha_1) - 2n_1 \sin(n_1\alpha_2) + \cdots \pm 2n_1 \sin(n_1\alpha_M) \\ 2n_2 \sin(n_2\alpha_1) - 2n_2 \sin(n_2\alpha_2) + \cdots \pm 2n_2 \sin(n_2\alpha_M) \\ \vdots \\ 2n_M \sin(n_M\alpha_1) - 2n_M \sin(n_M\alpha_2) + \cdots \pm 2n_M \sin(n_M\alpha_M) \end{bmatrix} \tag{3.9}$$

$$\frac{\partial \vec{f}}{\partial \vec{\alpha}} = \begin{bmatrix} -n_1 \sin(n_1\alpha_1) + n_1 \sin(n_1\alpha_2) + \cdots \pm n_1 \sin(n_1\alpha_M) \\ -n_2 \sin(n_2\alpha_1) + n_2 \sin(n_2\alpha_2) + \cdots \pm n_2 \sin(n_2\alpha_M) \\ \vdots \\ -n_M \sin(n_M\alpha_1) + n_M \sin(n_M\alpha_2) + \cdots \pm n_M \sin(n_M\alpha_M) \end{bmatrix} \tag{3.10}$$

To obtain the solution of this matrix an approximation of an initial solution is necessary and is updated with each new interaction of the method, until a minimum error is reached, as shown in (3.11) and (3.12) (Patel; Hoft, 1973; Patel; Hoft, 1974).

$$\vec{f}^{\,0} + \frac{\partial \vec{f}^{\,0}}{\partial \vec{\alpha}}\, d\vec{\alpha} = 0 \tag{3.11}$$

$$\vec{\alpha}^{\,1} = \vec{\alpha}^{\,0} + d\vec{\alpha} \tag{3.12}$$

The numerical solution algorithm of Fig. 29 for all modulation indexes start from zero up to the maximum value of modulation index. An initial guess for the angles is necessary and the solution is updated for the next interaction (Patel; Hoft, 1973; Patel; Hoft, 1974). The offline calculation, according to the numerical solution algorithm of the Fig. 29, results in the commutation angles shown in Fig. 30 and 31 for two and three-level converter, respectively in function of the modulation index responsible for the elimination of harmonics listed in Table 8. The amplitude of the non-eliminated harmonics as a function of the modulation indexes is given in Fig. 32 and 33 for 2L and 3L, respectively.

The SHE-PWM modulator implementation for the ZHD converter in GFM mode is show in Fig. 34, where the commutation angles are stored in look up tables as a function of the modulation index. Output frequency and voltage references are submitted

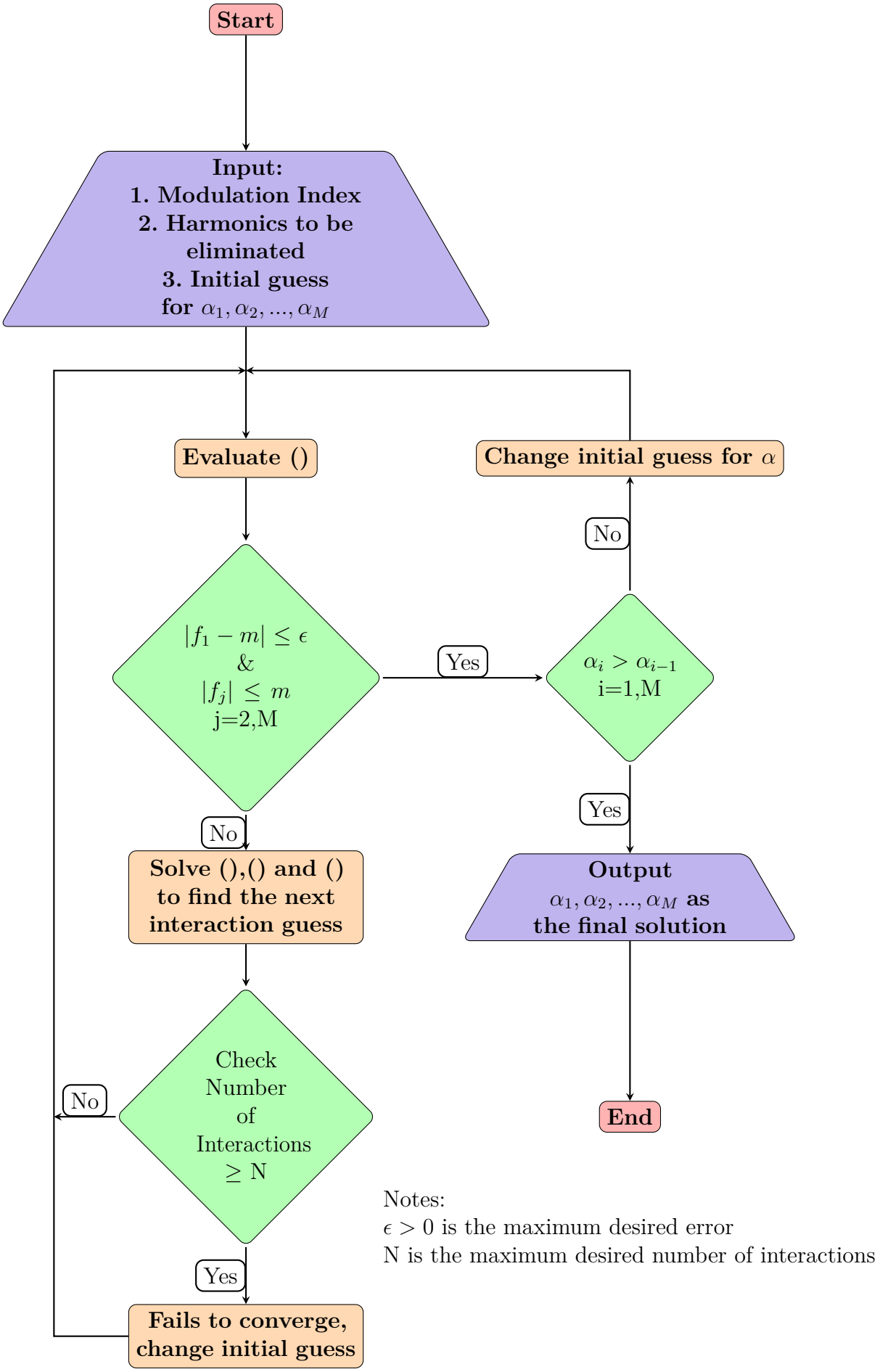

Figure 29 – Algorithm for numerical solution of $\alpha_1, \alpha_2, ..., \alpha_M$.

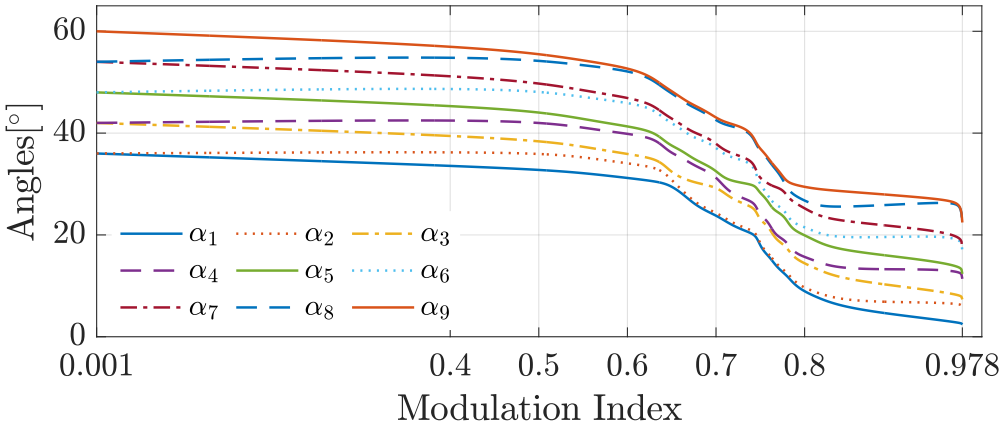

Figure 30 – 2L VSC switching angles.

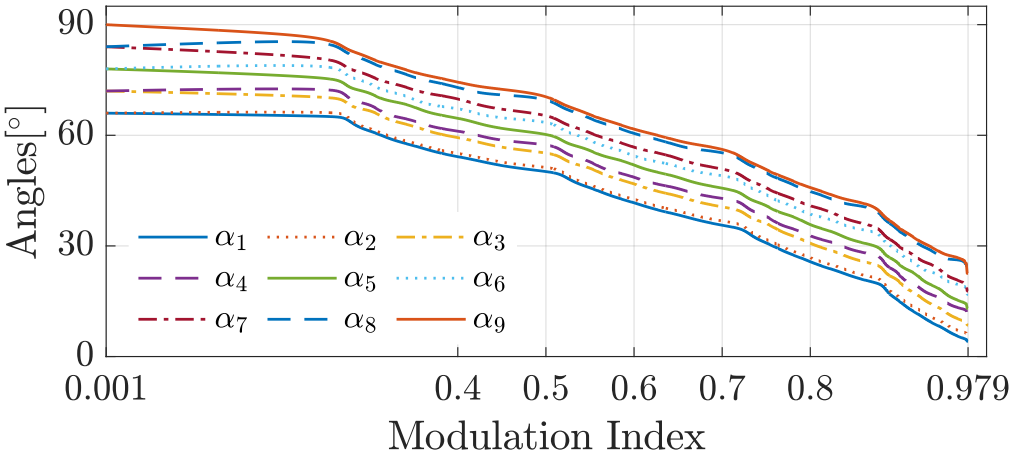

Figure 31 – 3L VSC switching angles.

to the modulators in order to synthesize output voltages shifted by 30 degrees, that make harmonic elimination possible in the three-winding transformer.

Fig. 35 and 36 shows the signal generation for two and three-level converters. The pulse generation to the converters occurs by the comparison between the angle of reference frequency with the stored angles, according to the calculated modulation index (3.7) related with the voltage reference.

As a result of this implementation, in the case of the two-level ZHD, the equivalent switching frequency of the two-level SHE PWM can be expressed by (3.13), resulting in a frequency of 1.14 kHz for a 9 precalculed switching angles and a fundamental frequency of 60 Hz.

$$f_{sw} = (2M + 1)f_1 \tag{3.13}$$

In the case of the three-level ZHD, the equivalent switching frequency of the three-level SHE PWM can be expressed by (3.14), resulting in a frequency of 1.08 kHz for a 9 precalculed switching angles and a fundamental frequency of 60 Hz.

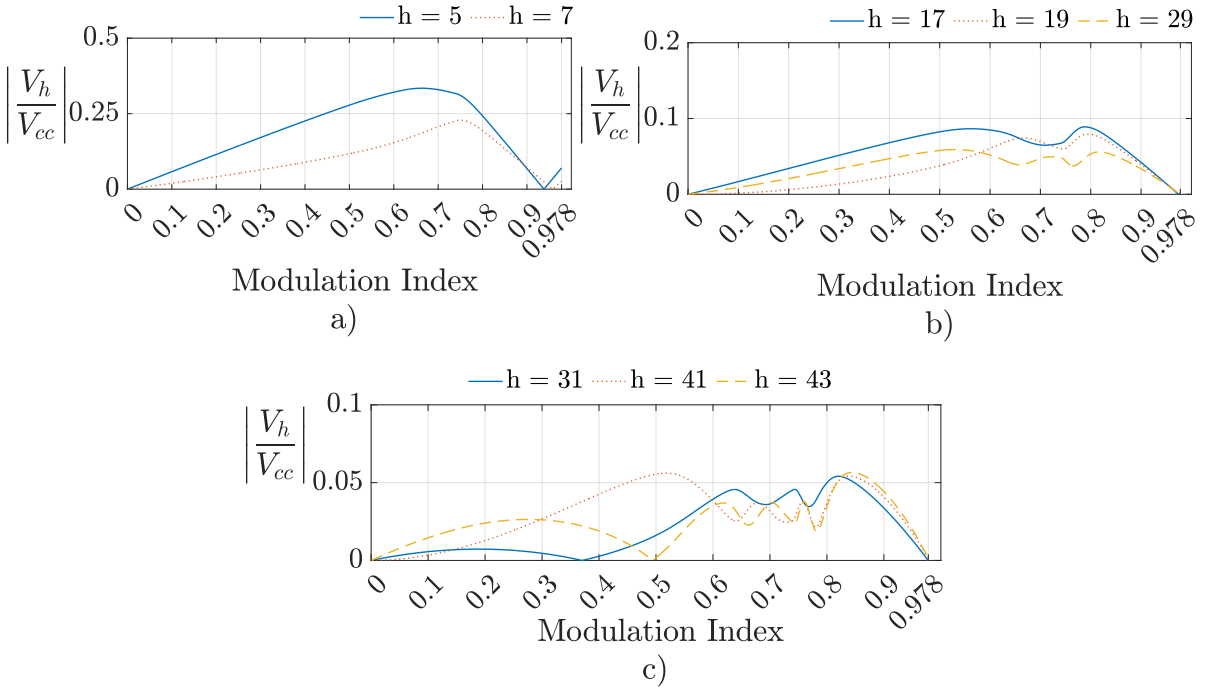

Figure 32 – Amplitude of non-eliminated harmonics versus modulation index for the 2L VSC: (a) 5th and 7th; (b) 17th, 19th, and 29th; and (c) 31st, 41st, and 43rd.

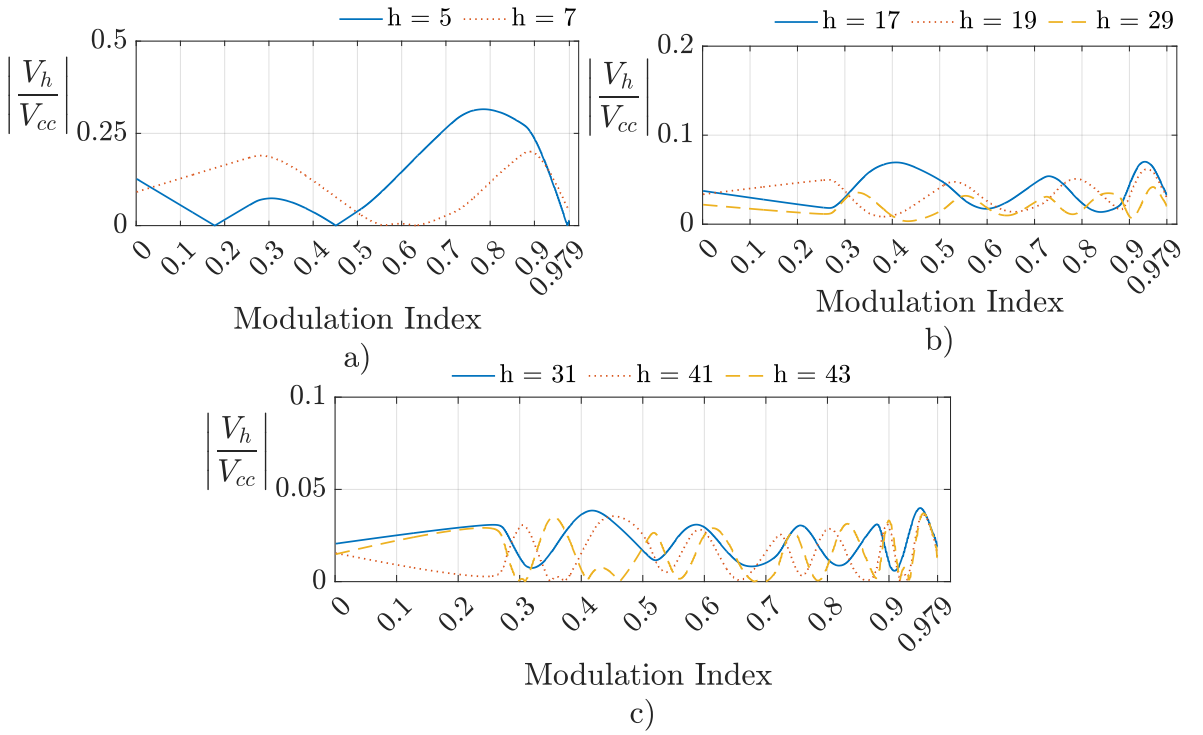

Figure 33 – Amplitude of non-eliminated harmonics versus modulation index for the 3L VSC: (a) 5th and 7th; (b) 17th, 19th, and 29th; and (c) 31st, 41st, and 43rd.

$$f_{sw} = 2Mf_1 \tag{3.14}$$

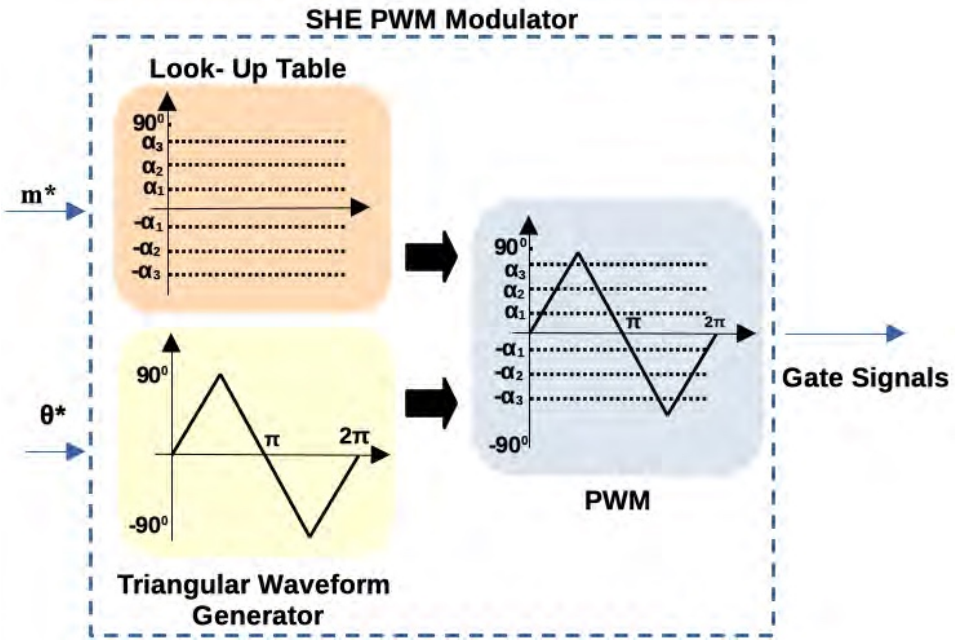

Figure 34 – SHEPWM Modulator.

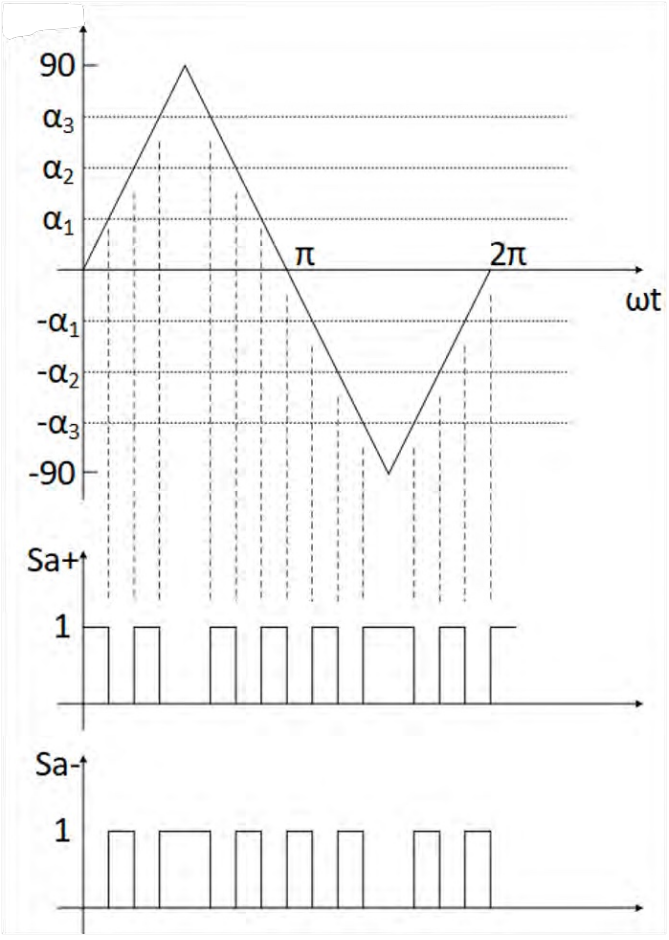

Figure 35 – Signals generation for two-level converters.

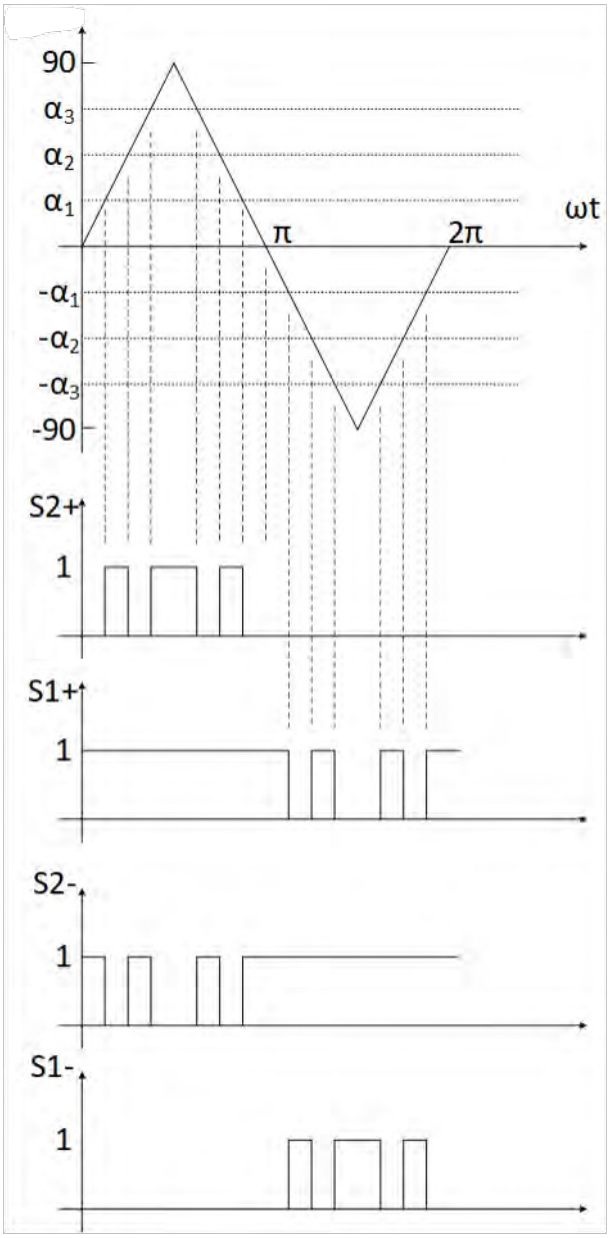

Figure 36 – Signals generation for three-level converters.

3.4 Three Phase Three-Winding Analytical Approach

3.4.1 Equivalent per-phase Circuit

The ZHD converter can be represented as two three-phase voltage sources applied to the secondaries of the three-winding three-phase transformer, as shown in Fig. 37.

The voltage sources represent the converters synthesizing voltage waveforms with a phase shift of 30 degrees according the constructive lags between transformer secondaries. Considering only the harmonics non-eliminated by the SHE PWM modulation, the harmonic voltages generated by the converters can be seen in (3.15) and (3.16) for Y and Δ secondaries, respectively.

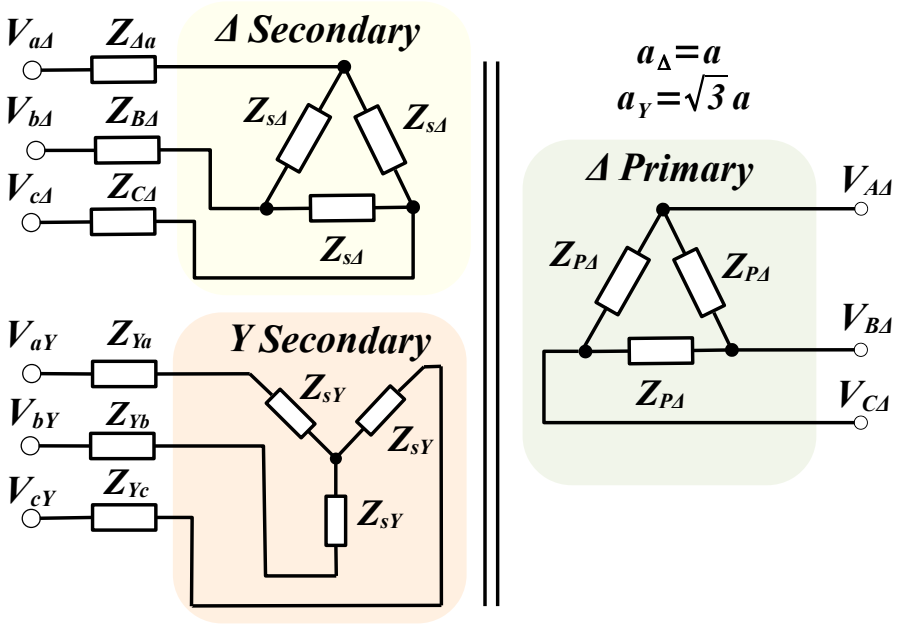

Figure 37 – Three-Phase Three-winding transformer.

$$\begin{aligned} V_{aY} &= V_{hy} \cdot cos[(6k \pm 1)\omega t] \\ V_{bY} &= V_{hy} \cdot cos[(6k \pm 1)\omega t \mp \tfrac{2\pi}{3}] \\ V_{cY} &= V_{hy} \cdot cos[(6k \pm 1)\omega t \pm \tfrac{2\pi}{3}] \end{aligned} \tag{3.15}$$

$$\begin{aligned} V_{a\Delta} &= V_{h\Delta} \cdot cos[(6k \pm 1)\omega t - (6k \pm 1)\tfrac{\pi}{6}] \\ V_{b\Delta} &= V_{h\Delta} \cdot cos[(6k \pm 1)\omega t - (6k \pm 1)\tfrac{5\pi}{6}] \\ V_{c\Delta} &= V_{h\Delta} \cdot cos[(6k \pm 1)\omega t + (6k \pm 1)\tfrac{\pi}{2}] \end{aligned} \tag{3.16}$$

An wye equivalent circuit of the ZHD converter can be obtained referring the impedance of the reactors and the series impedance of the secondaries Y and Δ, showed in (3.17), to the primary winding.

$$\begin{aligned} Z_{s\Delta} &= Z_{\Delta a} + \tfrac{Z_{s\Delta}}{3} \\ Z_{sY} &= Z_{Ya} + Z_{sY} \end{aligned} \tag{3.17}$$

An equivalent series impedance of the converter is shown in (3.18) as a function of the turns ratio of the three winding transformer.

$$Z_{P\Delta} = \left(a^2\left(Z_{\Delta a} + \frac{Z_{s\Delta}}{3}\right) \parallel a^2(Z_{Ya} + Z_{sY})\right) + \frac{Z_P}{3} \tag{3.18}$$

Fig. 38 shows the per-phase equivalent circuit of the ZHD converter referred to the primary. The three-phase voltages $V_{Y'}$ and $V_{\Delta'}$ referred to the primary are given by (3.19) and (3.20), respectively.

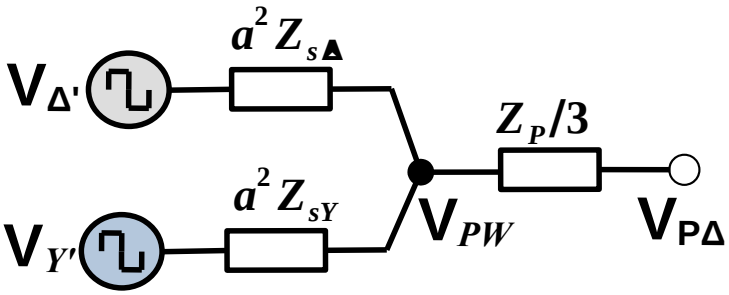

Figure 38 – ZHD Per Phase primary referred equivalent circuit.

$$\begin{aligned} V_{aY'} &= a_y V_{hy} \cdot cos[(6k \pm 1)\omega t]) \\ V_{bY'} &= a_y V_{hy} \cdot cos[(6k \pm 1)\omega t \mp \tfrac{2\pi}{3}] \\ V_{cY'} &= a_y V_{hy} \cdot cos[(6k \pm 1)\omega t \pm \tfrac{2\pi}{3}] \end{aligned} \tag{3.19}$$

$$\begin{aligned} V_{\Delta' a} &= a_\Delta (V_{a\Delta} - V_{b\Delta}) = a_\Delta \sqrt{3} V_{h\Delta} \cdot cos[(6k \pm 1)\omega t - (6k \pm 1)\pi] \\ V_{\Delta' b} &= a_\Delta (V_{b\Delta} - V_{c\Delta}) = a_\Delta \sqrt{3} V_{h\Delta} \cdot cos[(6k \pm 1)\omega t \pm (6k \pm 1)\tfrac{\pi}{3}] \\ V_{\Delta' c} &= a_\Delta (V_{c\Delta} - V_{a\Delta}) = a_\Delta \sqrt{3} V_{h\Delta} \cdot cos[(6k \pm 1)\omega t \mp (6k \pm 1)\tfrac{\pi}{3}] \end{aligned} \tag{3.20}$$

Equivalent Thévenin voltage and impedance are given by (3.21). Analyzing the Thévenin voltage, it is possible to observe that the converter can deliver voltage waveforms free of harmonics of order $6k \pm 1$, due to the cancelation between (3.19) and (3.20) since the transformer ratio between the secondaries assumes $a_y = \sqrt{3} a_\Delta$. Fig. 39 shows harmonic cancellation in the phasor diagrams for negative and positive sequence.

$$\begin{aligned} V_{TH'} &= \tfrac{V_{\Delta'} Z_y + V_{Y'} Z_\Delta}{Z_\Delta + Z_Y} \\ Z_{TH'} &= a^2(Z_{s\Delta}) // a^2(Z_{sY}) \end{aligned} \tag{3.21}$$

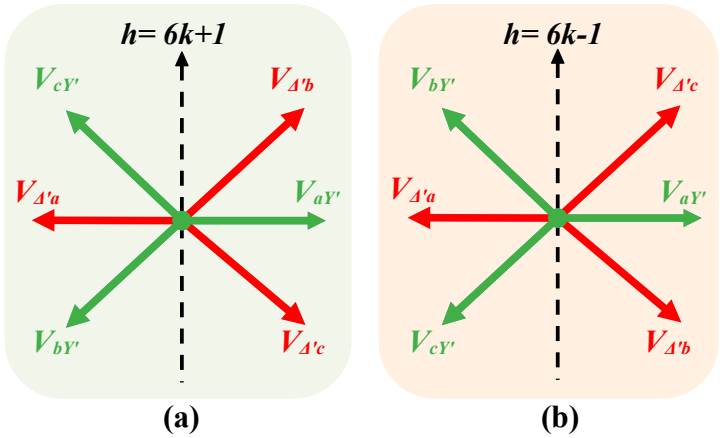

Figure 39 – Harmonic cancellation in Thevenin's voltage for: a) Negative sequence b) Positive sequence.

Finally, Fig. 40 shows the equivalent fundamental and harmonic circuits, connected to the point of common coupling (PCC) of the MG through a line impedance. In this

way, the equivalent circuit of the converter reinforce the idea that no harmonic until the 50th order is generated by the converter, delivering in practical terms, a sinusoidal voltage waveform. However, just like any other converter, if the MG demands harmonic currents, the generated voltage waveforms are disturbed due to the voltage drops in the series impedance of the circuit Fig. 40b).

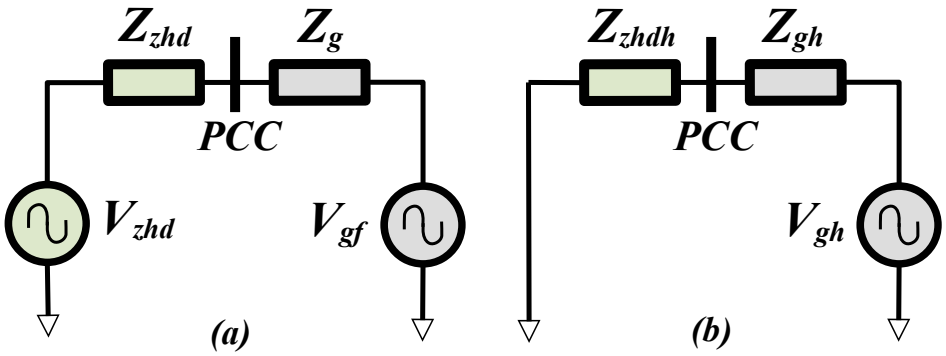

Figure 40 – ZHD per phase: a) Fundamental Equivalent Circuit b) Harmonic Equivalent Circuit.

In the presence of nonlinear loads, besides the disturbance on the output voltage, the flux of harmonic currents in the ZHD converter also impacts the Δ and Y secondary currents. Fig. 41 shows the per-phase equivalent circuit of the ZHD converter of Fig. 38, considering a drained harmonic current I_{hL} from the ZHD converter.

The ZHD harmonic equivalent circuit can analyzed by the circuit laws, and the secondary currents $I'_{s\Delta}$ and I'_{sY} can be expressed in (3.22).

$$\begin{aligned} I'_{s\Delta} &= \sum_{h=2}^{N} \left\{ \frac{V'_{\Delta}(h) - V'_{Y}(h)}{a^2[Z_{\Delta}(h) + Z_{Y}(h)]} + \frac{I_{hL}(h) Z_{Y}(h)}{Z_{\Delta}(h) + Z_{Y}(h)} \right\} \\ I'_{sY} &= \sum_{h=2}^{N} \left\{ \frac{V'_{Y}(h) - V'_{\Delta}(h)}{a^2[Z_{\Delta}(h) + Z_{Y}(h)]} + \frac{I_{hL}(h) Z_{\Delta}(h)}{Z_{\Delta}(h) + Z_{Y}(h)} \right\} \end{aligned} \tag{3.22}$$

The first terms of each secondary referred current in (3.22), correspond to the current flowing naturally due to the harmonic content in the VSCs synthesized waveform. These terms will cancel out and not appear in the primary current ($I_P = I'_{s\Delta} + I'_{sY}$) since there is a 180º phase among them.

In the case of $Z_{\Delta} = Z_Y$, as the converter is designed to be, the harmonic currents will distribute equally (i.e. $\frac{I_{hL}}{2}$) among secondaries. It is important to note, however, that each I_{hL} harmonic component will interact in a different way with each VSC self-harmonic component due to the aforementioned 180º phase. This may lead to distinct harmonic distortion on each secondary without affecting the primary.

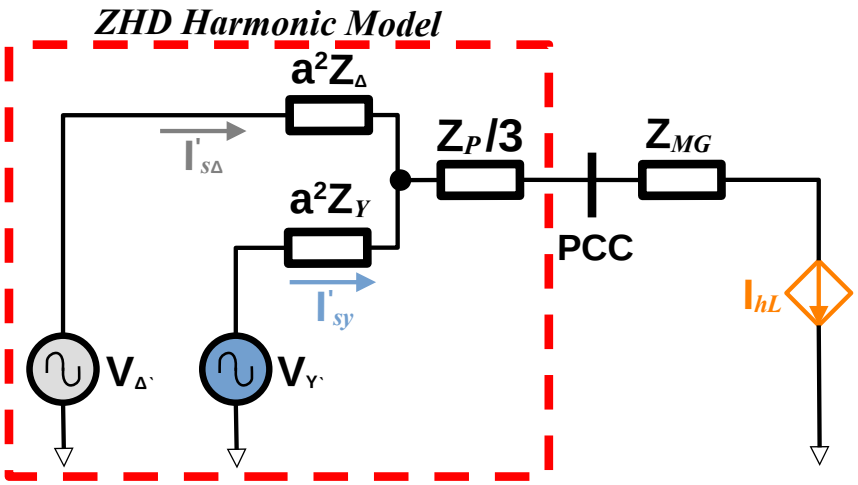

Figure 41 – Harmonic equivalent circuit considering the Δ and Y secondaries currents.

3.4.2 Flux Linkage Approuch Analysis

3.4.2.1 Flux Harmonic cancellation at transformer

Although the cancellation can be observed through the equivalent circuit, it is important to highlight that the harmonic cancellation happens in the linked flux of the three-widing transformer (Parreiras, 2020).

The past model analysis to show the behavior of what really happens in the flux of the transformer and what happens in the current of the secondaries of the transformer.

Considering the harmonic voltages generated by SHE PWM in (3.15) and (3.16), a superposition analysis considering the three winding transformer shown in Fig. 37 can be done in order to find what is the flux produced by each secondary harmonic voltage. The currents in the each phases of each secondary can be calculated individually considering the superposition theorem, as shown in (3.23) and (3.24).

$$\begin{aligned} I_{aY} &= \frac{V_{aY}}{Z_{sY}} \\ I_{bY} &= \frac{V_{bY}}{Z_{sY}} \\ I_{cY} &= \frac{V_{cY}}{Z_{sY}} \end{aligned} \tag{3.23}$$

$$\begin{aligned} I_{a\Delta} &= \frac{V_{a\Delta}}{Z_{s\Delta}} \\ I_{b\Delta} &= \frac{V_{b\Delta}}{Z_{s\Delta}} \\ I_{c\Delta} &= \frac{V_{c\Delta}}{Z_{s\Delta}} \end{aligned} \tag{3.24}$$

Consequently each per phase secondary currents generate the per-phase flux in the core of the transformer according to (3.25) shown in (3.26) and (3.27).

$$\lambda = \frac{N^2 i}{\Re} \tag{3.25}$$

$$\begin{aligned}
\lambda_{aY'} &= \frac{N_Y^2 V_{hy}}{\Re(Z_\Delta + Z_Y)} cos[(6k \pm 1)\omega t]) \\
\lambda_{bY'} &= \frac{N_Y^2 V_{hy}}{\Re(Z_\Delta + Z_Y)} cos[(6k \pm 1)\omega t \mp \tfrac{2\pi}{3}]) \\
\lambda_{cY'} &= \frac{N_Y^2 V_{hy}}{\Re(Z_\Delta + Z_Y)} cos[(6k \pm 1)\omega t \pm \tfrac{2\pi}{3}])
\end{aligned} \tag{3.26}$$

$$\begin{aligned}
\lambda_{a'\Delta} &= \frac{N_\Delta^2 \sqrt{3} V_{h\Delta}}{\Re(Z_\Delta + Z_Y)} cos[(6k \pm 1)\omega t - (6k \pm 1)\pi] \\
\lambda_{b'\Delta} &= \frac{N_\Delta^2 \sqrt{3} V_{h\Delta}}{\Re(Z_\Delta + Z_Y)} cos[(6k \pm 1)\omega t \pm (6k \pm 1)\tfrac{\pi}{3}]) \\
\lambda_{c'\Delta} &= \frac{N_\Delta^2 \sqrt{3} V_{h\Delta}}{\Re(Z_\Delta + Z_Y)} cos[(6k \pm 1)\omega t \mp (6k \pm 1)\tfrac{\pi}{3}])
\end{aligned} \tag{3.27}$$

The per-phase resultant flux linkage in the core of the transformer summing the contribution of each flux per phase as shown in (3.28), is possible to observe the natural cancellation between the harmonic flux in each phase since the number of turns of each secondary obey the following relationship: $N_Y = \sqrt{3}N_\Delta$ and the amplitude of the harmonic voltages $V_{h\Delta}$ and V_{hY} are the same considering that both converter receive the same modulation index.

$$\begin{aligned}
\lambda_{aRes} &= \lambda_{aY} + \lambda_{a\Delta} \\
\lambda_{bRes} &= \lambda_{bY} + \lambda_{b\Delta} \\
\lambda_{cRes} &= \lambda_{cY} + \lambda_{c\Delta}
\end{aligned} \tag{3.28}$$

In this way, it is possible to verify that there is only harmonic current circulation at the secondaries in (3.23) and (3.24) generated by the converters, and due to the harmonic cancellation at the flux, and there is no induced voltage in the three windings by the resultant flux. In thus way, there is no harmonic in the primary side of the transformer.

3.4.2.2 Effect of harmonic at transformer primary side

In the case of presence of harmonic voltages at the primary of the transformer, the considered voltages are given by (3.29).

$$\begin{aligned}
V_{aP\Delta} &= V_{hP\Delta} \cdot cos[n\omega t + \phi_h] \\
V_{bP\Delta} &= V_{hP\Delta} \cdot cos[n\omega t + \phi_h - \tfrac{2\pi}{3}] \\
V_{cP\Delta} &= V_{hP\Delta} \cdot cos[n\omega t + \phi_h + \tfrac{2\pi}{3}]
\end{aligned} \tag{3.29}$$

Again considering the superposition theorem, the primary winding side is transformed to wye where the per-phase voltage given by (3.30) and the per phase currents at the primary winding calculated as shown in (3.31).

$$\begin{aligned}
V_{aP\Delta} &= \sqrt{3} V_{hP\Delta} \cdot cos[n\omega t + \phi_h + \tfrac{\pi}{6}] \\
V_{bP\Delta} &= \sqrt{3} V_{hP\Delta} \cdot cos[n\omega t + \phi_h - \tfrac{2\pi}{3} + \tfrac{\pi}{6}] \\
V_{cP\Delta} &= \sqrt{3} V_{hP\Delta} \cdot cos[n\omega t + \phi_h + \tfrac{2\pi}{3} + \tfrac{\pi}{6}]
\end{aligned} \tag{3.30}$$

$$\begin{aligned} I_{aP} &= \frac{V_{aP}}{Z_P/3+Z_g} \\ I_{bP} &= \frac{V_{bP}}{Z_P/3+Z_g} \\ I_{cP} &= \frac{V_{cP}}{Z_P/3+Z_g} \end{aligned} \tag{3.31}$$

The flux linkage produced by the primary harmonics currents in the core of the transformer can be calculated as shown in (3.32).

$$\begin{aligned} \lambda_{a'P} &= \frac{N_P^2\sqrt{3}V_{hP}}{\Re(Z_{P\Delta}/3+Z_g)}cos[n\omega t+\phi_h+\tfrac{\pi}{6}] \\ \lambda_{b'P} &= \frac{N_P^2\sqrt{3}V_{hP}}{\Re(Z_{P\Delta}/3+Z_g)}cos[n\omega t+\phi_h-\tfrac{2\pi}{3}+\tfrac{\pi}{6}] \\ \lambda_{c'P} &= \frac{N_P^2\sqrt{3}V_{hP}}{\Re(Z_{P\Delta}/3+Z_g)}cos[n\omega t+\phi_h+\tfrac{2\pi}{3}+\tfrac{\pi}{6}] \end{aligned} \tag{3.32}$$

The induced voltages at secondaries Y and Δ windings, according (3.33), can be given in (3.34) and (3.35).

$$V = N\frac{d\phi}{dt} \tag{3.33}$$

$$\begin{aligned} V_{a'Y} &= -\frac{N_Y N_P\sqrt{3}V_{hP}n\omega}{\Re(Z_{P\Delta}/3+Z_g)}sin[n\omega t+\phi_h+\tfrac{\pi}{6}] \\ V_{b'Y} &= -\frac{N_Y N_P\sqrt{3}V_{hP}}{\Re(Z_{P\Delta}/3+Z_g)}sin[n\omega t+\phi_h-\tfrac{2\pi}{3}+\tfrac{\pi}{6}] \\ V_{c'Y} &= -\frac{N_Y N_P\sqrt{3}V_{hP}}{\Re(Z_{P\Delta}/3+Z_g)}sin[n\omega t+\phi_h+\tfrac{2\pi}{3}+\tfrac{\pi}{6}] \end{aligned} \tag{3.34}$$

$$\begin{aligned} V_{a'\Delta} &= -\frac{N_\Delta N_P V_{hP}n\omega}{\Re(Z_\Delta+Z_g)}sin[n\omega t+\phi_h] \\ V_{a'\Delta} &= -\frac{N_\Delta N_P V_{hP}n\omega}{\Re(Z_\Delta+Z_g)}sin[n\omega t+\phi_h-\tfrac{2\pi}{3}] \\ V_{a'\Delta} &= -\frac{N_\Delta N_P V_{hP}n\omega}{\Re(Z_\Delta+Z_g)}sin[n\omega t+\phi_h+\tfrac{2\pi}{3}] \end{aligned} \tag{3.35}$$

By the way, the induced voltages can be used to calculate the induced currents at the secondaries by harmonic voltages at the primary, as shown in (3.36) and (3.37).

$$\begin{aligned} I_{aPY} &= \frac{V_{aPY}}{Z_{sY}+Z_Y} \\ I_{bPY} &= \frac{V_{bPY}}{Z_{sY}+Z_Y} \\ I_{cPY} &= \frac{V_{cPY}}{Z_{sY}+Z_Y} \end{aligned} \tag{3.36}$$

$$\begin{aligned} I_{aP\Delta} &= \frac{V_{aP\Delta}}{Z_{s\Delta}+Z_\Delta} \\ I_{bP\Delta} &= \frac{V_{bP\Delta}}{Z_{s\Delta}+Z_\Delta} \\ I_{cP\Delta} &= \frac{V_{cP\Delta}}{Z_{s\Delta}+Z_\Delta} \end{aligned} \tag{3.37}$$

By superposition, (3.23) and (3.24) can be modified to account for the presence of harmonics at the primary, where (3.38) and (3.39) shows the currents at Y and Delta secondaries and it is possible to observe the disturbance caused by the harmonics in the primary on the flux of the transformer and consequently at the secondary currents.

$$\begin{aligned} I_{aY} &= \frac{V_{aY}}{Z_{sY}} + I_{aPY} \\ I_{bY} &= \frac{V_{bY}}{Z_{sY}} + I_{bPY} \\ I_{cY} &= \frac{V_{cY}}{Z_{sY}} + I_{cPY} \end{aligned} \tag{3.38}$$

$$\begin{aligned} I_{a\Delta} &= \frac{V_{a\Delta}}{Z_{s\Delta}} + I_{aP\Delta} \\ I_{b\Delta} &= \frac{V_{b\Delta}}{Z_{s\Delta}} + I_{bP\Delta} \\ I_{c\Delta} &= \frac{V_{c\Delta}}{Z_{s\Delta}} + I_{cP\Delta} \end{aligned} \tag{3.39}$$

3.4.2.3 Effect of symmetrical and asymmetrical voltage faults on the primary side

In the presence of symmetrical and asymmetrical faults, is also necessary to asses the behavior of the transformer flux linkage. Considering fundamental voltages, (3.40), (3.42) and (3.43) show the per-phase voltages at secondaries Y, Δ and primary Δ, respectively.

$$\begin{aligned} V_{aY'} &= V_{fy} \cdot cos[\omega t] \\ V_{bY'} &= V_{fy} \cdot cos[\omega t - \tfrac{2\pi}{3}] \\ V_{cY'} &= V_{fy} \cdot cos[\omega t + \tfrac{2\pi}{3}] \end{aligned} \tag{3.40}$$

$$\begin{aligned} V_{a\Delta} &= V_{f\Delta} \cdot cos[\omega t - \tfrac{\pi}{6}] \\ V_{b\Delta} &= V_{f\Delta} \cdot cos[\omega t - \tfrac{2\pi}{3} - \tfrac{\pi}{6}] \\ V_{f\Delta} &= V_{f\Delta} \cdot cos[\omega t + \tfrac{2\pi}{3} - \tfrac{\pi}{6}] \end{aligned} \tag{3.41}$$

$$\begin{aligned} V_{\Delta' a} &= V_{a\Delta} - V_{b\Delta} = \sqrt{3} V_{h\Delta} \cdot cos[\omega t] \\ V_{\Delta' b} &= V_{b\Delta} - V_{c\Delta} = \sqrt{3} V_{h\Delta} \cdot cos[\omega t - \tfrac{2\pi}{3}] \\ V_{\Delta' c} &= V_{c\Delta} - V_{a\Delta} = \sqrt{3} V_{h\Delta} \cdot cos[(\omega t + \tfrac{2\pi}{3}] \end{aligned} \tag{3.42}$$

$$\begin{aligned} V_{aP\Delta} &= V_{Pf\Delta} \cdot cos[\omega t + \phi_h - \tfrac{\pi}{6}] \\ V_{bP\Delta} &= V_{Pf\Delta} \cdot cos[\omega t + \phi_h - \tfrac{2\pi}{3} - \tfrac{\pi}{6}] \\ V_{cP\Delta} &= V_{Pf\Delta} \cdot cos[\omega t + \phi_h + \tfrac{2\pi}{3} - \tfrac{\pi}{6}] \end{aligned} \tag{3.43}$$

By superposition, the generated per phase flux of each three-phase voltages windings is shown in (3.44), (3.46) and (3.46). It is possible to see that the generated flux of each converter works adding one to the other, what makes sense since from the point of view of fundamental equivalent circuit, the converters works as two parallel converter summing power. In the other side, the flux generated by the voltage at the primary act disturbing the flux on the transformer in a symmetrical or asymmetrical way.

$$\begin{aligned} \lambda_{aY} &= \frac{N_Y^2 V_f}{\Re(Z_{sY} + Z_y)} cos[n\omega t] \\ \lambda_{bY} &= \frac{N_Y^2 V_f}{\Re(Z_{sY} + Z_y)} cos[n\omega t - \tfrac{2\pi}{3}] \\ \lambda_{cY} &= \frac{N_Y^2 V_f}{\Re(Z_{sY} + Z_y)} cos[n\omega t + \tfrac{2\pi}{3}] \end{aligned} \tag{3.44}$$

$$\begin{aligned}\lambda_{a\Delta} &= \frac{N_\Delta^2\sqrt{3}V_f}{\Re(Z_{s\Delta}/3+Z_\Delta)}cos[n\omega t]\\ \lambda_{b\Delta} &= \frac{N_\Delta^2\sqrt{3}V_f}{\Re(Z_{s\Delta}/3+Z_\Delta)}cos[n\omega t-\frac{2\pi}{3}]\\ \lambda_{c\Delta} &= \frac{N_\Delta^2\sqrt{3}V_f}{\Re(Z_{s\Delta}/3+Z_\Delta)}cos[n\omega t+\frac{2\pi}{3}]\end{aligned} \tag{3.45}$$

$$\begin{aligned}\lambda_{aP} &= \frac{N_P^2\sqrt{3}V_{fP}}{\Re(Z_{P\Delta}/3)}cos[n\omega t+\phi_h]\\ \lambda_{bP} &= \frac{N_P^2\sqrt{3}V_{fP}}{\Re(Z_{P\Delta}/3)}cos[n\omega t+\phi_h-\frac{2\pi}{3}]\\ \lambda_{cP} &= \frac{N_P^2\sqrt{3}V_{fP}}{\Re(Z_{P\Delta}/3)}cos[n\omega t+\phi_h+\frac{2\pi}{3}]\end{aligned} \tag{3.46}$$

The resultant flux at the core of the transformer can be calculated by the sum of each per phase flux contribution, as given by (3.47).

$$\begin{aligned}\phi_{afRes} &= \phi_{aY}+\phi_{a\Delta}+\phi_{aP}\\ \phi_{bfRes} &= \phi_{bY}+\phi_{b\Delta}+\phi_{bP}\\ \phi_{cfRes} &= \phi_{cY}+\phi_{c\Delta}+\phi_{cP}\end{aligned} \tag{3.47}$$

In (3.48) shows the resultant flux at the core of the transformer for all the three phases. The first term is the produced flux by the converters connected at the secondary side and the second term the portion produced by the primary voltage. The resultant flux can be disturbed by possible changes in the primary side voltage.

$$\begin{aligned}\phi_{afRes} &= \frac{(N_Y+\sqrt{3}N_\Delta)V_f}{\Re Z_s}cos[n\omega t]+\frac{N_P\sqrt{3}V_{fP}}{\Re(Z_{P\Delta}/3)}cos[n\omega t+\phi_h]\\ \phi_{bfRes} &= \frac{(N_Y+\sqrt{3}N_\Delta)V_f}{\Re Z_s}cos[n\omega t-\frac{2\pi}{3}]+\frac{N_P\sqrt{3}V_{fP}}{\Re(Z_{P\Delta}/3)}cos[n\omega t+\phi_h-\frac{2\pi}{3}]\\ \phi_{cfRes} &= \frac{(N_Y+\sqrt{3}N_\Delta)V_f}{\Re Z_s}cos[n\omega t+\frac{2\pi}{3}]+\frac{N_P\sqrt{3}V_{fP}}{\Re(Z_{P\Delta}/3)}cos[n\omega t+\phi_h+\frac{2\pi}{3}]\end{aligned} \tag{3.48}$$

The secondaries currents can be calculated in (3.49) and (3.50) by the difference between the voltage of the converters and the induced voltage divided by the secondaries impedance. It is possible to see that the currents change according to the voltages induced by the resultant flux given in (3.48).

$$\begin{aligned}I_{aY} &= \frac{V_{afy}-N_Y d\phi_{aRes}/dt}{Z_Y}\\ I_{bY} &= \frac{V_{bfy}-N_Y d\phi_{bRes}/dt}{Z_Y}\\ I_{cY} &= \frac{V_{cfy}-N_Y d\phi_{cRes}/dt}{Z_Y}\end{aligned} \tag{3.49}$$

$$\begin{aligned}I_{a\Delta} &= \frac{V_{af\Delta}-N_\Delta(d\phi_{aP}/dt-d\phi_{bP}/dt)}{Z_\Delta}\\ I_{b\Delta} &= \frac{V_{bf\Delta}-N_\Delta(d\phi_{bP}/dt-d\phi_{cP}/dt)}{Z_\Delta}\\ I_{c\Delta} &= \frac{V_{cf\Delta}-N_\Delta(d\phi_{cP}/dt-d\phi_{aP}/dt))}{Z_\Delta}\end{aligned} \tag{3.50}$$

It is important to highlight that theoretically even with asymmetrical faults, the harmonic flux cancellation remains zero, since the disturbance is only in the fundamental

component and as the converters receive the same modulation indexes, the harmonic content does not change, only the current fundamental amplitude. On the hand, in some practical cases where the cancellation will not be perfect, the voltage will suffer a harmonic deterioration related to the amplitude of the non-eliminated harmonic according to the modulation index as shown in Fig. 32 and 33.

3.5 ZHD Technical Feasibility

3.5.1 Converter Topologies

Since the ZHD converter can be constructed with 2L and 3L converters, all the avaliable commercial topologies can be used. For 2L converters the three traditional 2L converters VSC, ZSI and qZSI topologies can be used as shown in Fig. 42 (Vazquez et al., 2010; Krishnamoorthy et al., 2014).

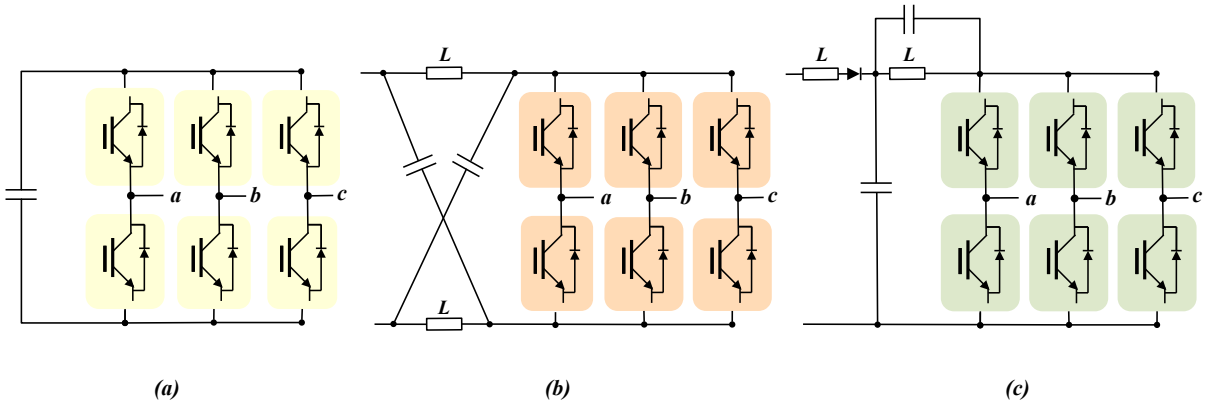

Figure 42 – Conventional 2-Level Converters: (a) VSC, (b) ZSI and, (c) qZSI.

In the VSC configuration, the battery bank can be connected either directly to the DC/AC stage capacitor or through a DC/DC stage. A drawback of this topology is its limitation to buck-mode operation, meaning the output voltage must remain lower than the DC bus voltage. Additionally, the upper and lower switches of each phase leg cannot be turned on simultaneously, requiring the implementation of a dead time between switching transitions. This dead time introduces distortion in the output waveform.

The Z-source inverter (ZSI) and its quasi-Z version (qZSI) were developed to address the limitations inherent to conventional VSC topologies (Peng, 2003; Anderson; Peng, 2008). These converters are capable of operating in boost mode thanks to an additional impedance network composed of capacitors and inductors in the DC link. This configuration allows the use of a short-circuit state to transfer energy within the network and increase the DC-link voltage. As a result, the qZSI has been widely adopted in the integration of renewable energy sources with battery storage systems, enabling direct grid connection without the need for an additional DC/DC converter and reducing the overall

number of semiconductors in the system (Cintron-Rivera et al., 2011; Liu et al., 2013). Nevertheless, despite these benefits, the conventional VSC remains the most commonly used solution due to its structural simplicity.

The 3-level ZHD converter can be implemented using commercial 3L topologies such as Neutral Point Clamped (NPC) (Nabae; Takahashi; Akagi, 1981), Active Neutral Point Clamped (ANPC) (Bruckner; Bernet; Guldner, 2005), and Neutral Point Piloted (NPP) (Guennegues et al., 2009) configurations, shown in Fig. 43.

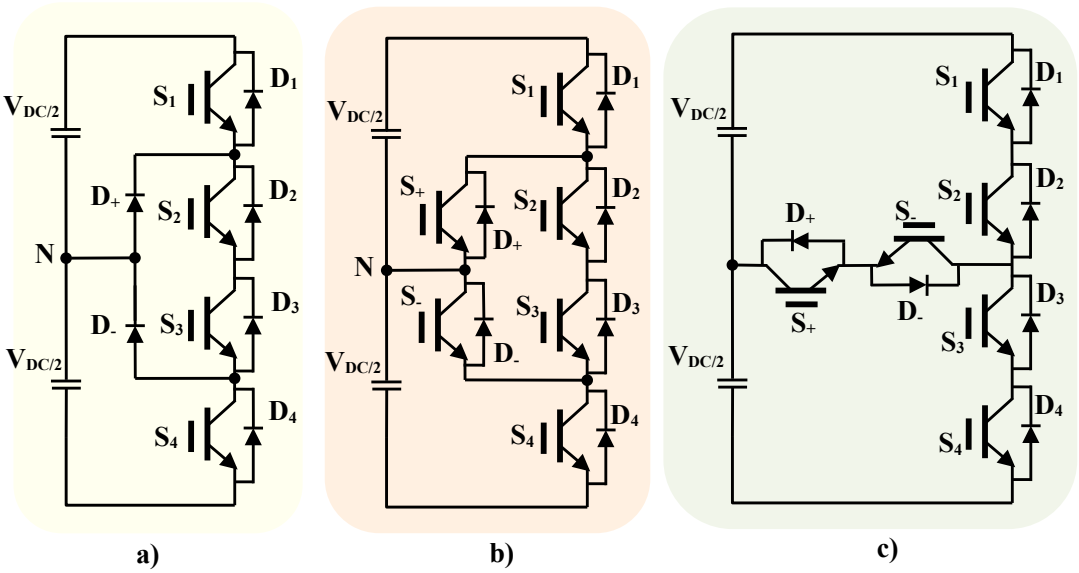

Figure 43 – Per phase diagram: (a) 3L NPC VSC, (b) 3L ANPC VSC and (c) 3L NPP VSC.

3.5.2 Output Impedance and Power Range

Compared to 2-level, 3-level converters has the capacity to deals with higher voltage levels, utilization of power switches of lower cost and the utilization of lower reactors impedances $Z_{\Delta\phi}$ and $Z_{Y\phi}$ on the secondaries due to the multilevel output voltage.

Fig. 44 (a) shows the comparison between the reactor impedances for 2 and 3-level converters. The reduced reactors in the 3-level case give an improved output voltage response in the presence of nonlinear loads in MV systems, where the harmonic voltage constraints are more restrictive than in LV systems.

Given the current availability of 1.2 kV and 1.7 kV IGBTs used in industrial solutions based in battery energy storage systems (BESS), it is possible to construct the ZHD converter based on 2L converters up to 2.5 MVA considering 1.2 kV IGBTs and 4 MVA considering 1.7 kV IGBTs as shown in Fig. 44 (b) and (c), respectively. In case of 3L converters, it is possible to construct the ZHD up to 6.08 MVA using modules from manufacturers such as Infineon and Hitachi, as illustrated in Fig. 44 (d) (Hitachi. . . , 2024; Infineon. . . , 2024).

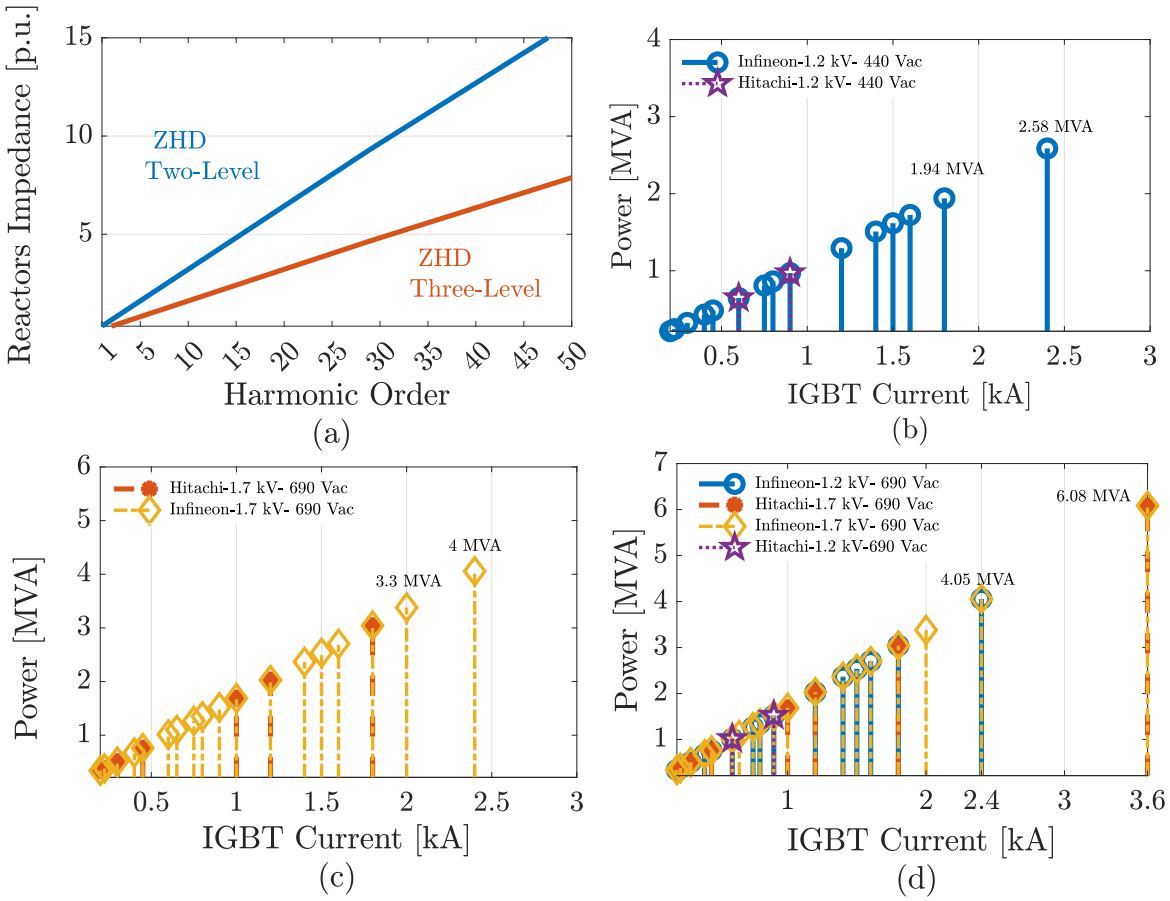

Figure 44 – (a) Two-level and Three-level comparison between secondaries reactors impedance, b) 2 -level ZHD power according to the 1.2 kV IGBT blocking voltage and current capacity, c) 2-level ZHD power according to the 1.7 kV IGBT blocking voltage and current capacity, d) 3-level ZHD power according to the 1.2 kV and 1.7kV IGBT blocking voltage and current capacity.

3.6 Conclusions

In this chapter, a comprehensive explanation and contextualization of the ZHD converter's operation, with a focus on its architecture, was presented. A detailed model incorporating the SHE-PWM modulation and the three-phase three-winding transformers was developed, enabling the derivation of a per-phase equivalent circuit for the ZHD converter. The technical feasibility of the ZHD converter was also explored by presenting the possible converter topologies and corresponding power ratings.

4 Zero Harmonic Distortion Islanded Grid-Forming Converter: Grid-Leading Operation in Medium Voltage Microgrids

Grid-forming converters in islanded microgrids face power quality problems due to disturbing loads and possible resonance issues caused by multiple electronically interfaced systems. In addition, grid-forming converters require complex control, filters or topology structures. This chapter proposes the application of the Zero Harmonic Distortion Converter (ZHD) as a grid-leading converter due to its inherently sinusoidal voltage source characteristic without the need for capacitive filtering elements that negatively impact costs, efficiency, size, and can originate resonance conditions. Simulation, hardware-in-the-loop, and experimental results show the ZHD converter setting voltage and frequency to an islanded microgrid, delivering sinusoidal voltage waveforms respecting the IEEE 519 harmonic limits, even in the presence of nonlinear loads considering two and three-level converters.

4.1 Introduction

A microgrid as defined in Chapter 2 can be characterized as shown in Fig. 45 as a set of distributed generation (DG) units, energy storage systems, and electrical loads, capable of operating in grid-connected mode or autonomously. One of its key features is the ability to island, that is, disconnect from the main utility grid and continue to supply power to local loads during faults or planned isolation events (Lasseter; Paigi, 2004).

During islanded operation, the microgrid loses the frequency and voltage reference typically provided by the utility grid. Consequently, power electronic converters, particularly grid-forming converters (GFMs), must assume this role, establishing and regulating the voltage and frequency of the system (Rocabert et al., 2012; Han et al., 2016).

Although GFM converters enable stable autonomous operation by emulating the behavior of synchronous machines, island microgrids still face significant challenges, including degradation of power quality caused by non-linear or dynamic loads, and potential resonance phenomena resulting from the interaction of multiple electronic interfaced by LC and LCL filters such as distributed and storage energy resources (DER) (Saim et al., 2019).

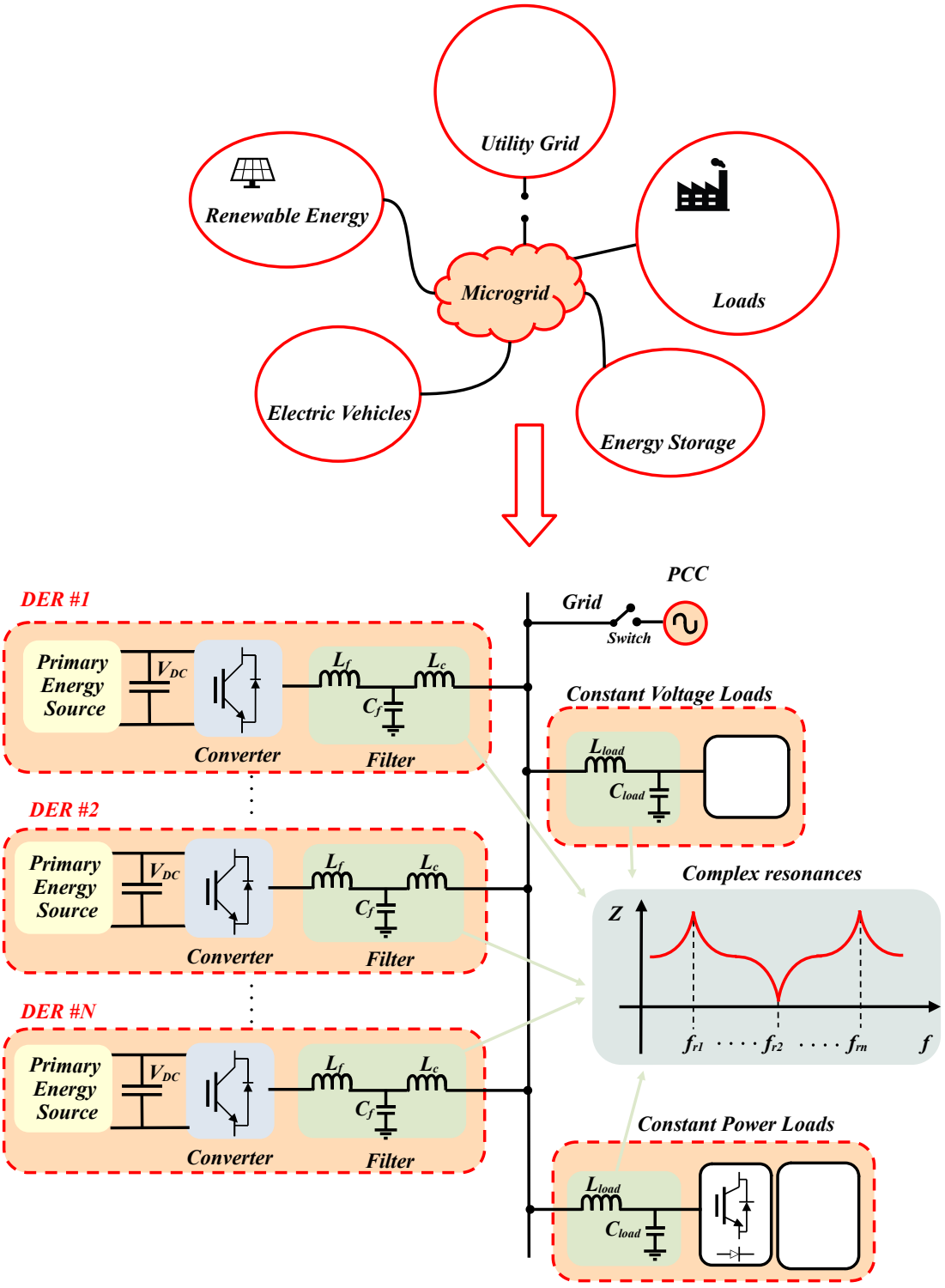

Figure 45 – Microgrid in islanded mode: interaction between interconnected passive filters generating complex resonance phenomena in microgrid islanded mode.

4.2 ZHD Grid-Forming Control Structure

The ZHD converter presents advantages over typical converters due to the inherent voltage source characteristic, the converter needs neither the voltage and current controls

nor the AC voltage capacitors for voltage source operation.

The voltage response in the dq frame is shown in (4.1). E_d and E_q are the voltages synthesized by the converter, and V_d, V_q, I_d and I_q are the output voltages and currents, respectively. R_{zhd} and L_{zhd} are the output resistance and inductance of the converter impedance given by (3.18), and ω_0 is the fundamental frequency.

$$\begin{aligned} V_d &= E_d + \omega_0 L_{zhd} i_q - R_{zhd} i_d - L_{zhd} \frac{di_d}{dt} \\ V_q &= E_q - \omega_0 L_{zhd} i_d - R_{zhd} i_q - L_{zhd} \frac{di_q}{dt} \end{aligned} \tag{4.1}$$

The block diagram of the voltage command control is indicated in Fig. 46 and reveals that only a disturbance feedforward control is responsible for rejecting the load variations (voltage drop on the ZHD series impedance), therefore compensating the voltage reference command, as can be shown in (4.2).

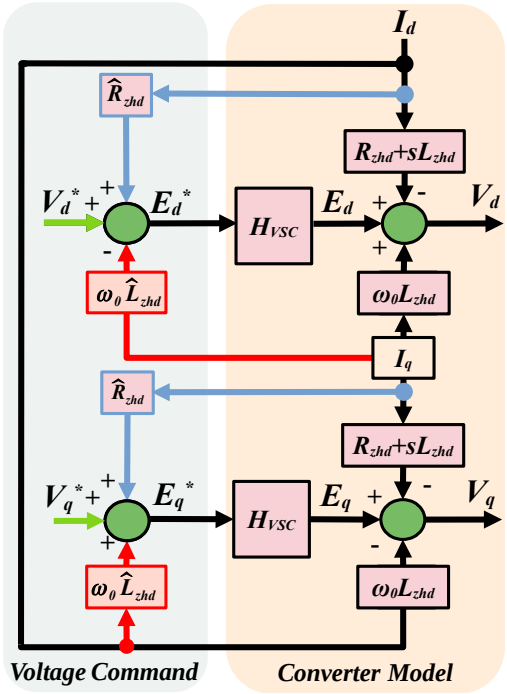

Figure 46 – Control of ZHD Grid-Forming converter in islanded operation.

$$\begin{aligned} E_d^* &= V_d^* - \omega_0 \hat{L}_{zhd} i_q + \hat{R}_{zhd} i_d \\ E_q^* &= V_q^* + \omega_0 \hat{L}_{zhd} i_d + \hat{R}_{zhd} i_q \end{aligned} \tag{4.2}$$

Fig. 47 shows the full ZHD grid-forming control. The total measured output current in the synchronous rotating frame, I_d and I_q, generates a compensating signal that is added to the command voltages V_d^* and V_q^*. Based on a virtual impedance concept, this structure allows the output voltage amplitude and phase compensation in the primary of the ZHD converter. $\hat{R}_{zhd}$ and $\hat{L}_{zhd}$ are the estimated ZHD converter series resistance

and inductance. There is also the possibility of current limitation in case of fault and of impedance emulation that will be aborded in Chapter 6.

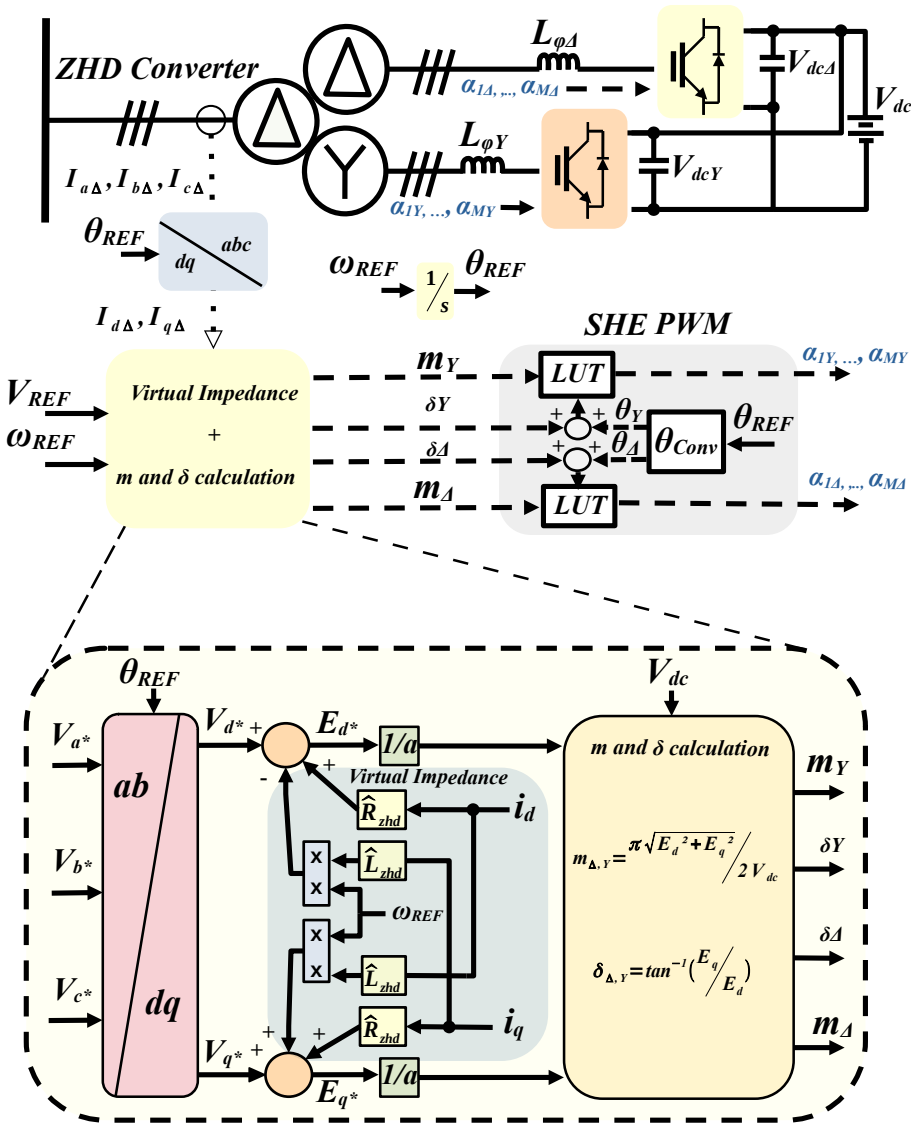

Figure 47 – Control of ZHD Grid-Forming converter in islanded operation.

E_d^* and E_q^* represent the compensated voltage commands. Taking into account the transformer winding ratio a, these commands are used to calculate the modulation indexes $m_{\Delta,Y}$ and phase compensation $\delta_{\Delta,Y}$. The modulation signals and the sum of phase compensation and the angle references θ_Y and θ_Δ are compared in the LUTs generating the power switches command signals $\alpha_{1Y}, .., \alpha_{MY}$ and $\alpha_{1\Delta}, .., \alpha_{M\Delta}$ to the VSCs.

4.3 Simulation Results

4.3.1 Voltage and frequency regulation

The control performance of the ZHD grid-forming converter was analyzed based on typical load variation scenarios. The simulated microgrid using the MATLAB/Simulink platform is shown in Fig. 48. The system parameters are described in Table 9. The nonlinear load was parameterized according to ((UPS)-Part. . . , 1999).

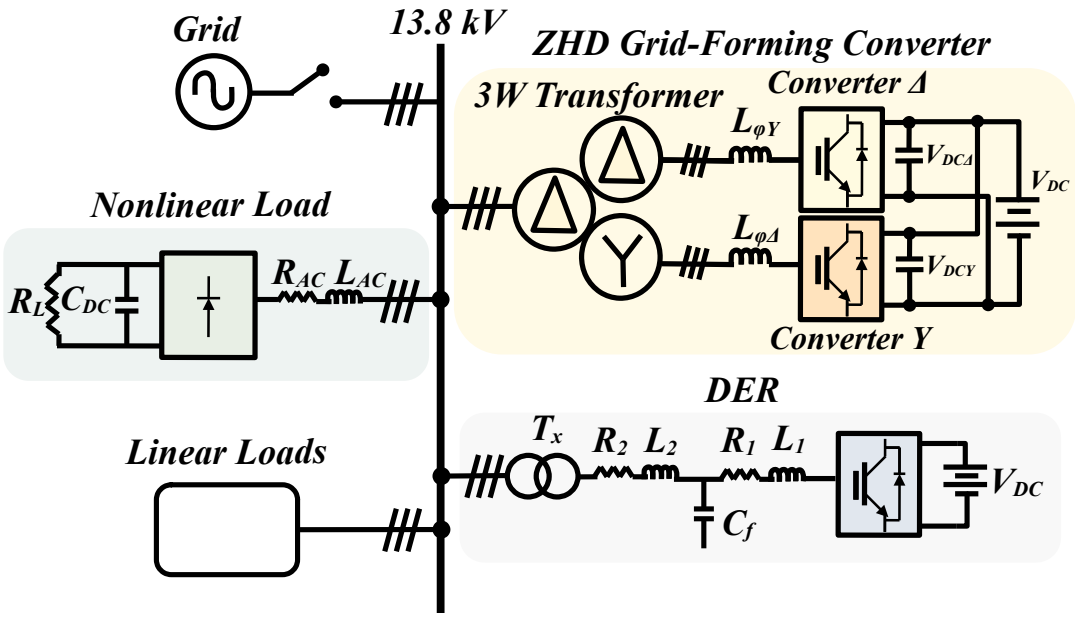

Figure 48 – Islanded MG with a ZHD Grid-Forming converter.

In the first scenario of the MG, a simulation time equal to 1.2 s is adopted. In order to evaluate the ZHD voltage and frequency regulation capability, the connection of loads and of the DER below are listed:

- t = 0.03 s → (I) → R load is connected;
- t = 0.43 s → (II) → RL load is connected;
- t = 0.55 s → (III) → The DER is adjusted to 100 A;
- t = 0.7 s → (IV) → The RL load is disconnected;
- t = 0.75 s → (V) → RC load is connected;
- t = 0.85 s → (VI) → The RC load is disconnected;
- t = 0.9 s → (VII) → The nonlinear load is connected;
- t = 1 s → $(VIII)$ → The DER is adjusted to 0 A.

Table 9 – Converter Data for Simulation Results.

ZHD CONVERTER			
Parameters	**Values**	**Parameters**	**Values**
Rated Power	280 kVA	Frequency	60 Hz
Primary Voltage	13.8 kV	Δ Secondary Voltage	440 V
Winding Connections	Dd0y1	Y Secondary Voltage	440 V
$L_{\phi\Delta}$ and $L_{\phi Y}$ reactors	0.16 p.u $\rightarrow$ 0.59/0.506 mH	DC link voltage	600 V
THREE-WINDING THREE-PHASE TRANSFORMER - Dd0y1			
Parameters	**Values**	**Parameters**	**Values**
R_m	526.7 $k\Omega$	$R_{s\Delta}$	19.4 $m\Omega$
L_m	534.5 H	$L_{s\Delta}$	3.33 μH
$R_{P\Delta}$	10.5 Ω	R_{sY}	16 $m\Omega$
$L_{P\Delta}$	108.7 mH	L_{sY}	84.26 μH
DER			
Parameters	**Values**	**Parameters**	**Values**
R_1	0.1 Ω	L_1 and L_2	500 μH
R_2	0.1 Ω	T_x	440 V/ 13.8 kV
C_f	110 μF	V_{DC}	800 V
LINEAR LOAD - R LOAD			
Parameters	**Values**	**Parameters**	**Values**
Active Power (P)	100kW	Reactive Power (Q)	0 var
LINEAR LOAD - RL LOAD			
Parameters	**Values**	**Parameters**	**Values**
Active Power (P)	48 kW	Reactive Power (Q)	36 kvar
LINEAR LOAD - RC LOAD			
Parameters	**Values**	**Parameters**	**Values**
Active Power (P)	48 kW	Reactive Power (Q)	-36 kvar
NONLINEAR LOAD			
Parameters	**Values**	**Parameters**	**Values**
R_{AC}	152.35 Ω	L_{AC}	2.2 μH
C_{dc}	2.59 μH	R_L	34.56 $k\Omega$

Fig. 49 shows the active and reactive power flow at the PCC during the simulation events. Even in the presence of load variation and DER active power injection as shown in Fig. 49 (a), the ZHD converter was capable of regulating voltage and frequency at the PCC, always rejecting the disturbances and following the references, as can be seen in Fig. 50 (a) and (g), respectively.

The zoomed view of I, II, V, and VIII simulation events can be observed in Fig. 50 (c), (d), (e), and (f), respectively, instants where the converter supply resistive, inductive, capacitive and nonlinear loads. It is possible to observe the sinusoidal shape of the delivered voltage waveforms in the case of linear loads (Fig. 50 (c), (d), and (e)), and that the waveform deteriorates in the presence of the nonlinear load (Fig. 50 (f)).

4.3.2 Harmonic Perfomance

Fig. 51 shows the FFT of the phase A load voltage for each type of load. As expected, the delivered voltage waveform for linear loads is free from any harmonic up to

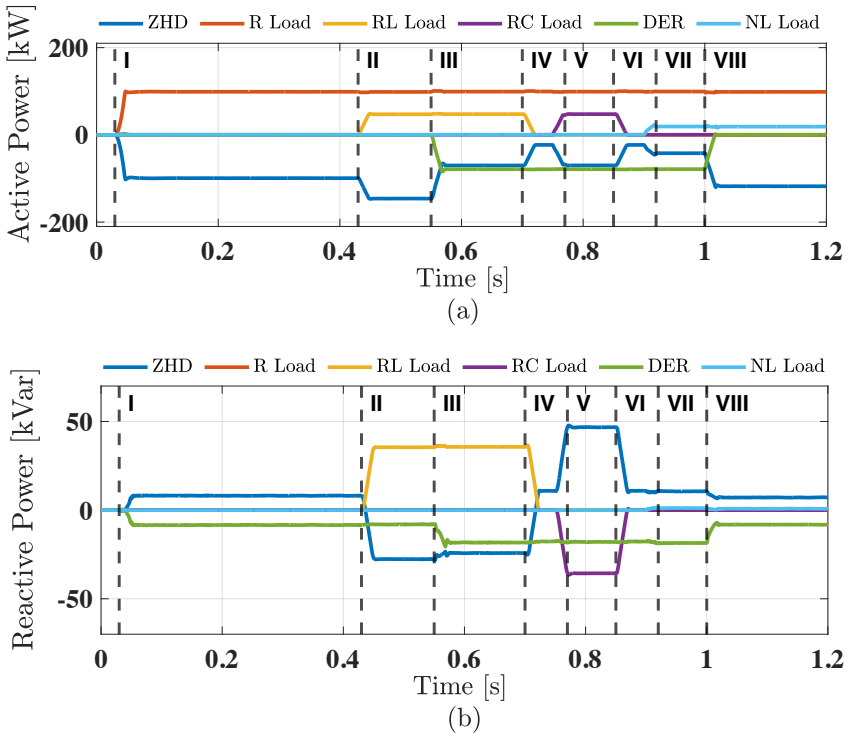

Figure 49 – (a) Active power flow and (b) reactive power flow at the PCC.

order 50^{th}, confirming that the converter does not produce any harmonic component in this range. However, when the nonlinear load is connected, Fig. 51 (d) reveals the voltage is disturbed by the demanded harmonic current.

Fig. 52 (a) and (b) shows the voltage and current waveforms in the secondaries, at the terminals of the three-winding transformer, for the instant of time considering resistive load (I). Fig. 52 (c) shows that the voltages in the secondaries are practically free from harmonics up to the 50^{th} order. The slight difference observed in the voltages THD, while the fundamental remains the same, is due to different design of the secondary reactors $L_{\phi\Delta}$ and $L_{\phi Y}$. This is necessary to compensate the differences in the transformer series secondary inductances. Notably, the lower voltage drop across the reactors connected to the Y secondary leads to slightly higher harmonic voltages. However, it is important to highlight that in the primary winding, the voltage remains free from harmonics up to the 50th order (Fig. 51 (a)). Finally, the currents FFT shown in Fig. 52 (d) presents only the harmonics that will be canceled by the transformer.

On the other hand, in the case of nonlinear load (VIII) Fig. 52 (e) and (f) shows the voltage and current waveforms in the secondaries. The secondaries voltage FFT shown in Fig. 52 (g) shows that in the same way of primary voltage (Fig. 51 (d)) the secondaries voltages is disturbed by the harmonic current. The currents FFTs shown in Fig. 52 (h) shows that in the presence of nonlinear loads the load current harmonics distribute equally among secondaries but interact in distinct ways with the ones due to the switching pattern

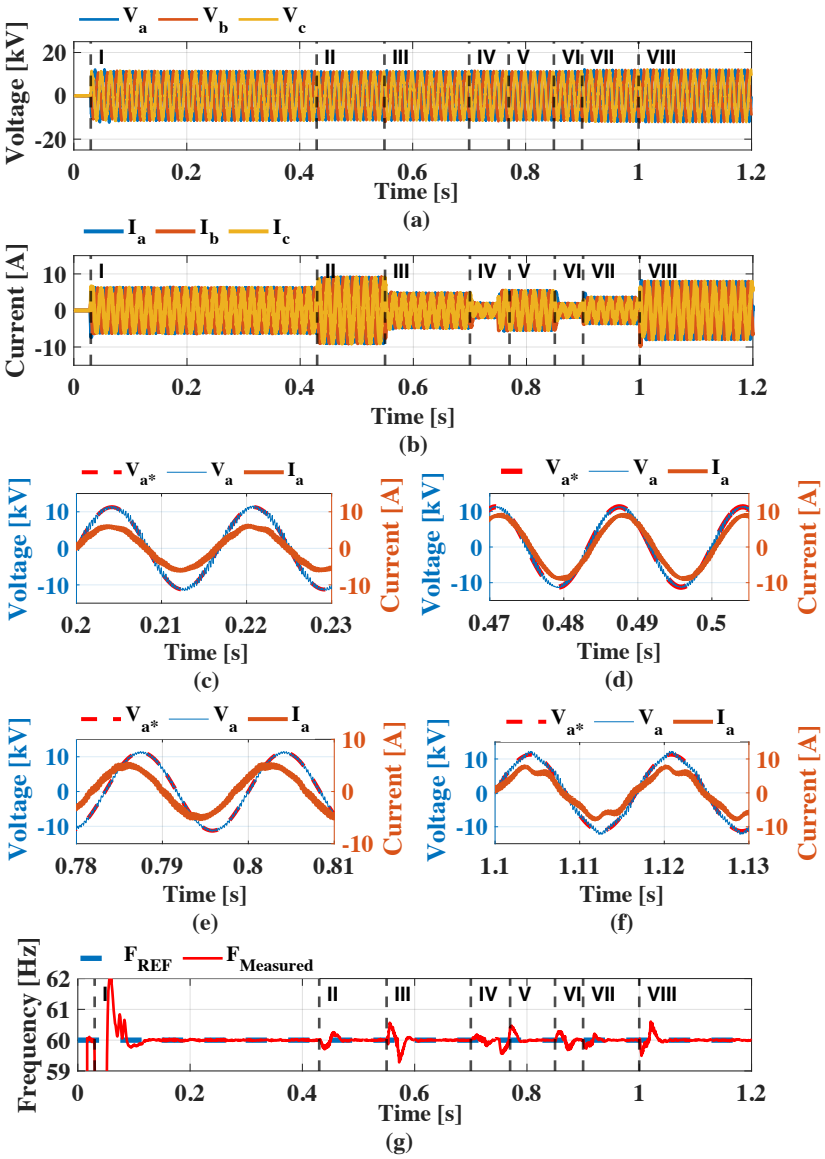

Figure 50 – (a) Voltage at PCC between: 0 and 1.2s, (b) output current at ZHD converter between: 0 and 1.2s, Voltage at PCC and ZHD converter output current between (c) 0.2s and 0.23s, (d) 0.47s and 0.505s (e) 0.78s and 0.81s (f) 1.1 and 1.13s and (g) frequency regulation at PCC.

(see the ZHD harmonic model of Fig. 41), making in this case, the harmonic distortion of the Y secondary greater than the Δ one.

In this context, the results show that the power quality is directly affected by nonlinear loads, especially with 5^{th} and 7^{th} harmonics, connected in the PCC, since the ZHD converter does not contribute with harmonic generation in the range defined by the standards.

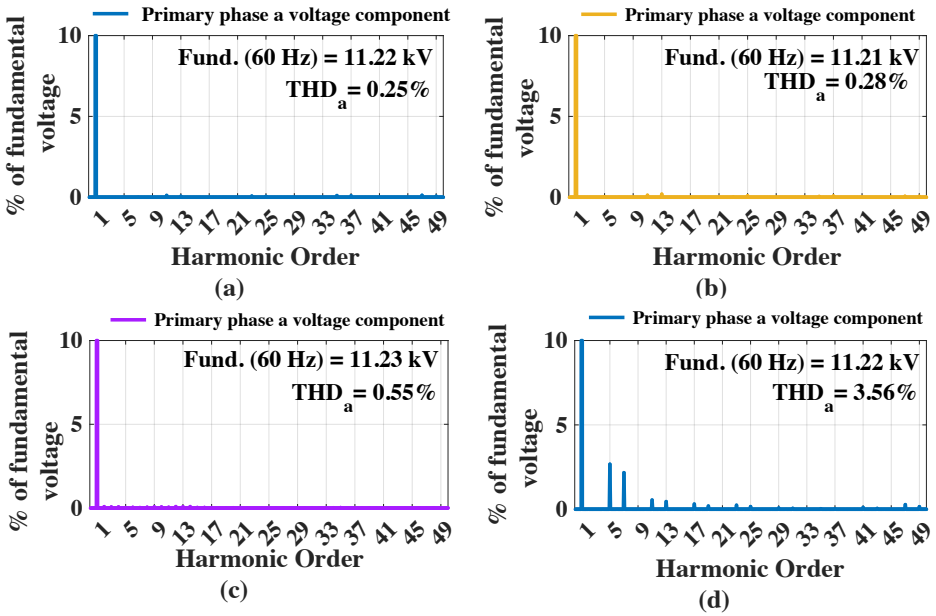

Figure 51 – Output FFT voltages for: (a) linear Load, (b) inductive Load, (c) capacitive load and (d) nonlinear Load.

4.3.3 Secondaries Reactors Design vs. Harmonic Distortion Performance Under Nonlinear Loads Conditions

It is necessary to characterize the converter harmonic limits since the distortion in the output of the ZHD converter is directly affected by the harmonic voltage drop in its output impedance (Fig. 40 (b)).

In the case of medium voltage levels, the individual harmonic voltage must be limited to 3%. An analysis considering the output impedance of the converter, expressed by (3.18), with four different values of series reactors inductances (0.16, 0.15, 0.14, and 0.13 p.u.) was done in Fig. 53 (a). As seen in Fig. 51 (d), the 5^{th} harmonic is the most critical therefore a zoomed view of the 5^{th} harmonic reactance can be seen in Fig. 53 (b).

Table 10 presents calculated ZHD series reactances considering 5th-order harmonic distortion of 3% (according to IEEE 519) for voltage and 2%, 3%, and 4% for current.

Table 10 – Harmonic Characterization Scenarios

Scenario	**% of 5^{th} Harmonic in Voltage[1]**	**% of 5^{th} Harmonic in Current**	**Maximum 5^{th} harmonic reactance**
1	3%	2%	x_{sc1} = 1.5 p.u.
2	3%	3%	x_{sc2} = 1 p.u.
3	3%	4%[2]	x_{sc3}= 0.75 p.u.

[1] Maximum voltage harmonic percentage in MV level in IEEE 519.

[2] Maximum current harmonic percentage in MV level by IEEE 519.

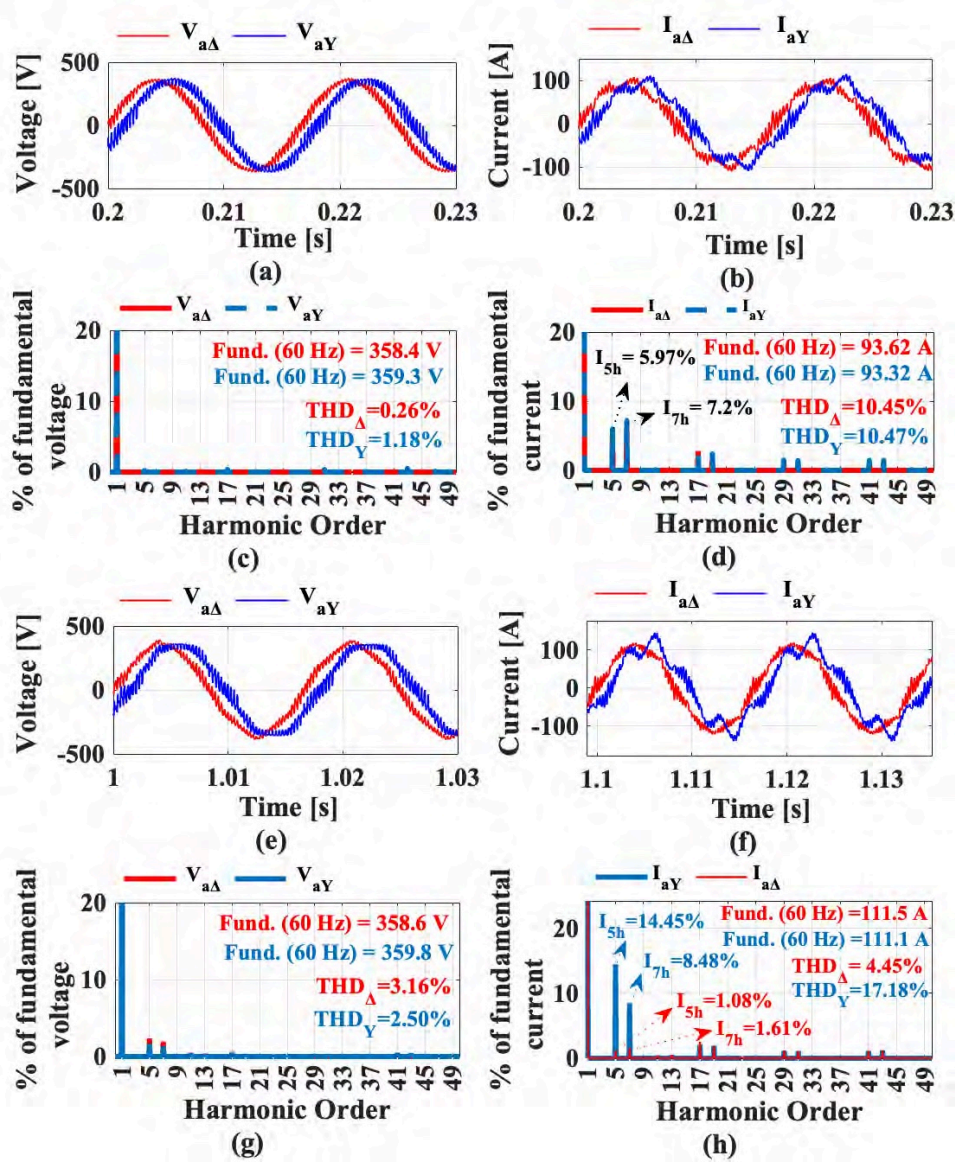

Figure 52 – Secondaries: (a) voltages for linear load, (b) currents for linear Loads, (c) voltages FFT for linear load (d) currents FFT for linear load (e) voltages for nonlinear load , (f) currents for nonlinear load , (g) voltages FFT for nonlinear load and (h) currents FFT for nonlinear load.

x_{sc1}, x_{sc2} and x_{sc3} are the maximum 5^{th} harmonic reactances. These reactances work as design references, since the more distorted the current, the lower the output impedance must be.

It can be noted that only the third scenario imposes a restriction since the other two can be fullfilled with any reactors inductance presented in Fig. 53. Important is to note that a reduction of the inductors values reduces the PCC voltage distortion for a given nonlinear load, but increase the current distortion at the VSCs side due to the switching harmonics.

Figs. 54 and 55 shows simulation results for the scenarios of 2% and 4% of 5^{th} order harmonic in the current, considering series inductances of 0.16 and 0.13 p.u., respectively,

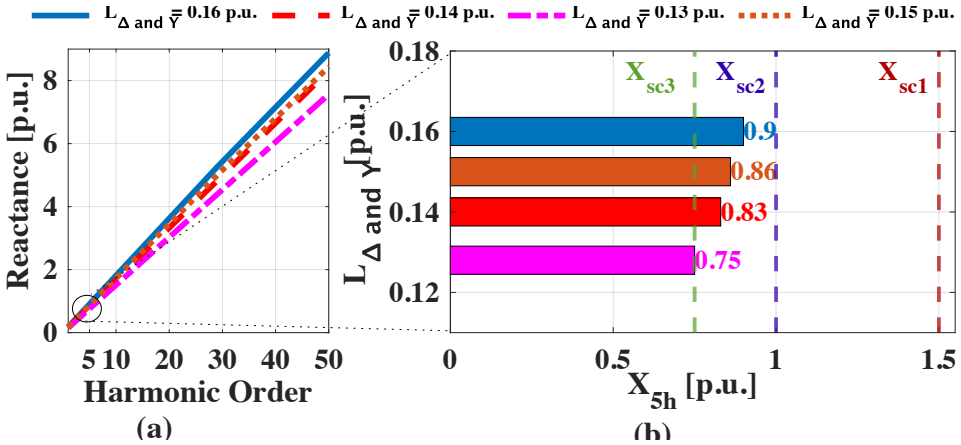

Figure 53 – (a) ZHD output reactance, (b) 5^{th} harmonic impedance characterization considering the three scenarios.

with the load parameters described in Table 11.

For the load current harmonic profile presented in Fig. 54 (a) with the inductance of 0.16 p.u., Fig. 54 (b) shows that the individual primary voltage harmonic content is above the IEEE 519 limit for 4% of 5^{th} harmonic and below the IEEE 519 limit for 2% of 5^{th} harmonic, as predicted in Fig. 53 (b). Fig. 54 (c) and (d) show the secondary currents FFT for 4% and 2% cases, respectively. These results show an unequal harmonic distortion among secondaries currents, as predicted in Chapter 3.

For the same load currents (Fig. 55 (a)), but with the inductance of 0.13 p.u., Fig. 55 (b) shows the PCC voltage satisfying the individual and total distortion limits for both scenarios, as expected in Fig. 53 (b). However, Fig. 55 (c) and (d) show the distortion of secondaries currents waveforms increased when compared to Fig. 54 (c) and (d). In this way, the appropriate design of secondaries reactors must be done in order to obtain a trade off between output voltage distortion and harmonic current flow in the converters.

Table 11 – Loads simulated for Harmonic Characterization Scenarios

LINEAR LOAD - R LOAD			
Parameters	**Values**	**Parameters**	**Values**
Active Power (P)	100kW	Reactive Power (Q)	0 Var
NONLINEAR LOAD			
Parameters	**Values**	**Parameters**	**Values**
R_{AC}	152.35 Ω	L_{AC}	2.2 μH
C_{dc}	25.98 μF	$R_{L4\%}$/ $R_{L2\%}$	17.28 kΩ / 69.12 kΩ

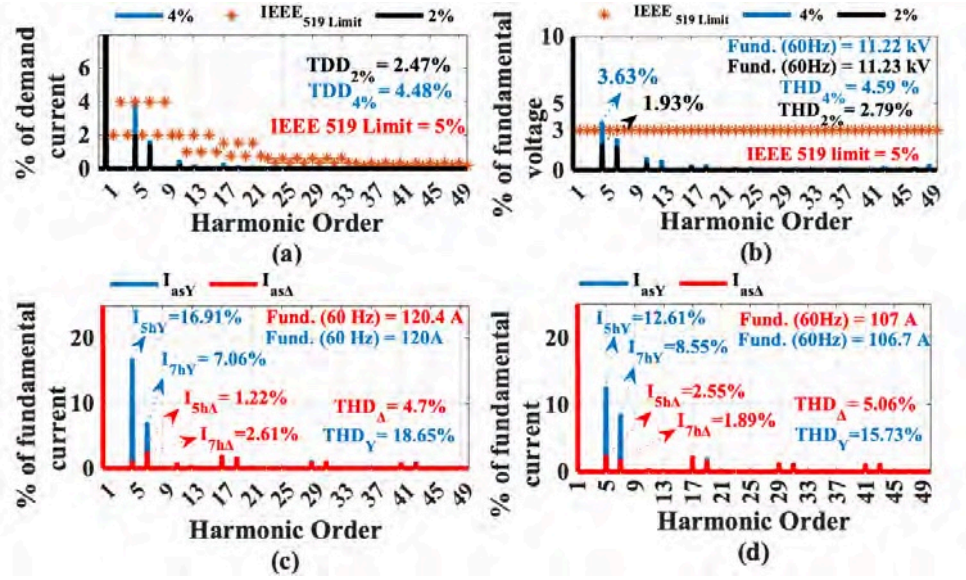

Figure 54 – $L_{\Delta,Y}$= 0.16 p.u: (a) FFTs for load current with 4% and 2% of 5^{th} harmonic , (b) PCC FFT voltage, (c) secondaries currents for 4% of 5^{th} harmonic, and (d) secondaries currents for 2% of 5^{th} harmonic.

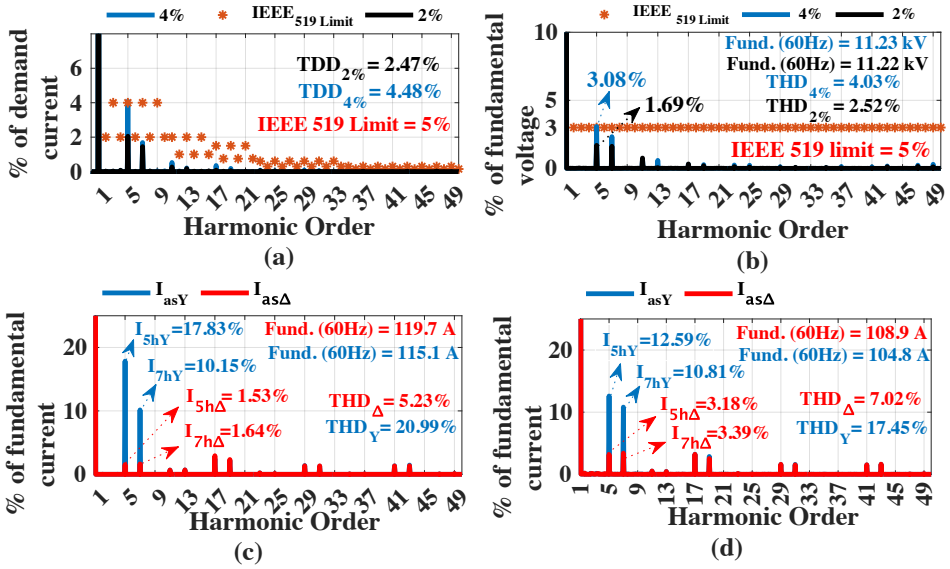

Figure 55 – $L_{\Delta,Y}$= 0.13 p.u.: (a) FFTs for load current with 4% and 2% of 5^{th} harmonic , (b) PCC FFT voltage, (c) secondaries currents for 4% of 5^{th} harmonic, and (d) secondaries currents for 2% of 5^{th} harmonic.

4.4 Hardware-in-the-loop Results

The ZHD converter was implemented in a real-time simulation platform. Fig. 56 shows the real controller connected to the HIL, where the steady-state and transient performance were evaluated with the parameters described in Table 12, considering linear and nonlinear loads.

The ZHD controller rack contains a power supply board, a controller board (equipped with a Texas Instruments TMS320F28335 microcontroller) responsible for the voltage

Table 12 – Loads simulated in HIL

LINEAR LOAD - R LOAD			
Parameters	**Values**	**Parameters**	**Values**
Active Power (P)	150kW	Reactive Power (Q)	0 Var
NONLINEAR LOAD- Three-phase six pulse rectifier -150 kW			
Parameters	**Values**	**Parameters**	**Values**
R_{AC}	135.35 $m\Omega$	L_{AC}	2.2 μH
C_{dc}	25.98 μF	R_L	3.80 kΩ

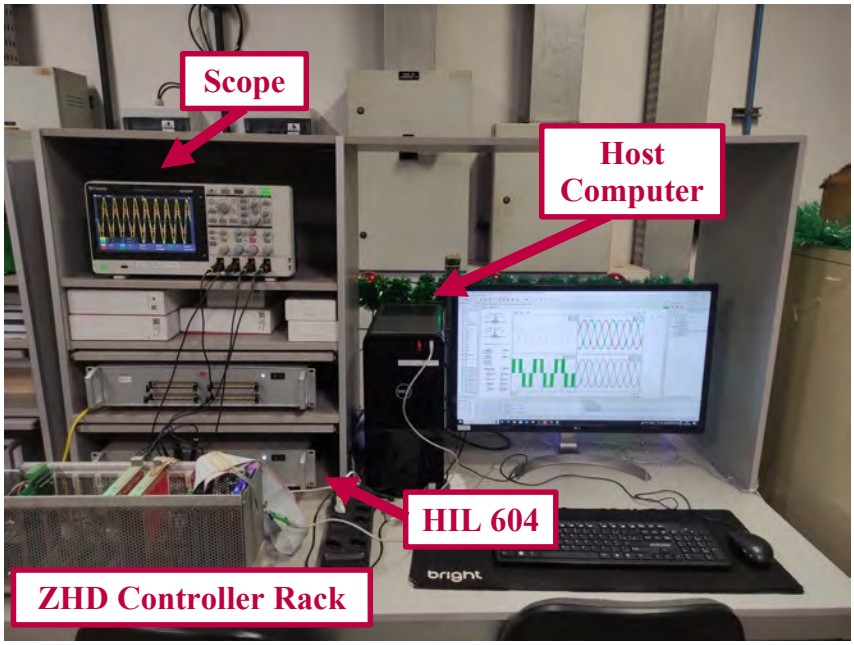

Figure 56 – Structure of tests and validation in Hardware-in-the-Loop.

control, and an FPGA board (equipped with an FPGA model MAX 10 from Intel) that handles the SHE PWM operating at a sufficiently high sampling frequency (250 kHz).

Fig. 57 shows the results for a linear load. The synthesized voltage was capable of following the reference and both, voltage and current, are practically free from harmonics up to the 50^{th} order.

Fig. 58 shows the results for the nonlinear load. In this case, the converter keeps tracking the fundamental voltage reference, but the voltage drop in the series impedance due to the load current harmonic content causes distortion in the voltage.

The voltage and frequency regulation were also evaluated in case of load variation. Fig. 59 shows the case where the load changes from linear load to nonlinear load, and Fig. 60 shows the case when the converter is supplying a linear load and a DER injects 120 kW active power at PCC. In both cases, the converter was able to regulate voltage and frequency with negligible transient.

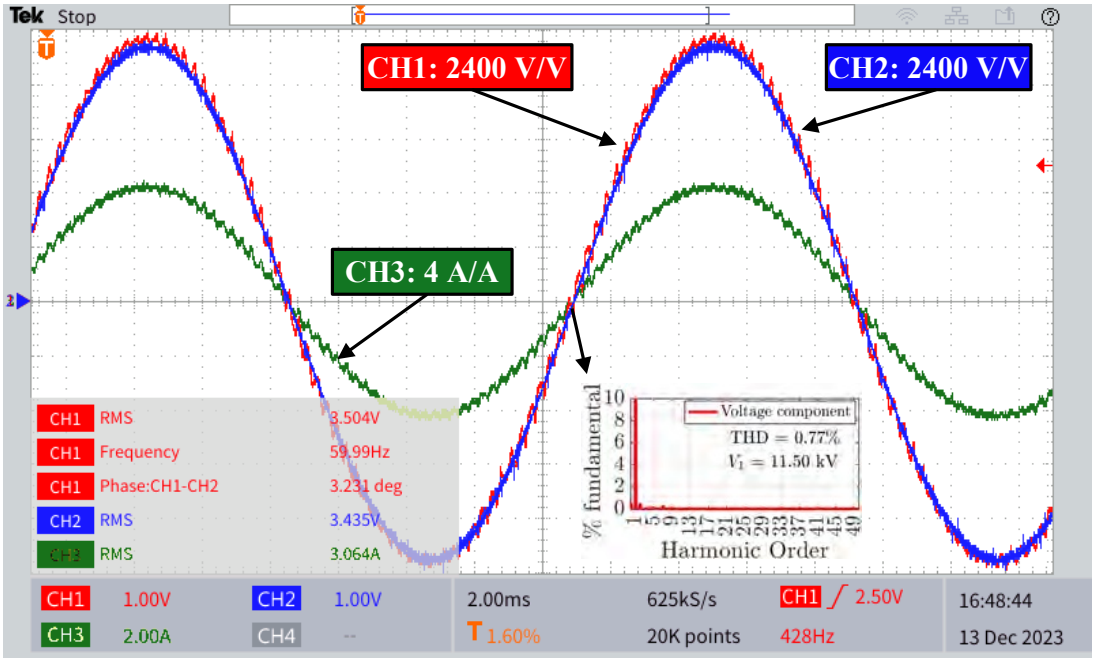

Figure 57 – HIL results for linear load (phase A): PCC voltage (CH1), voltage reference (CH2) and current (CH3).

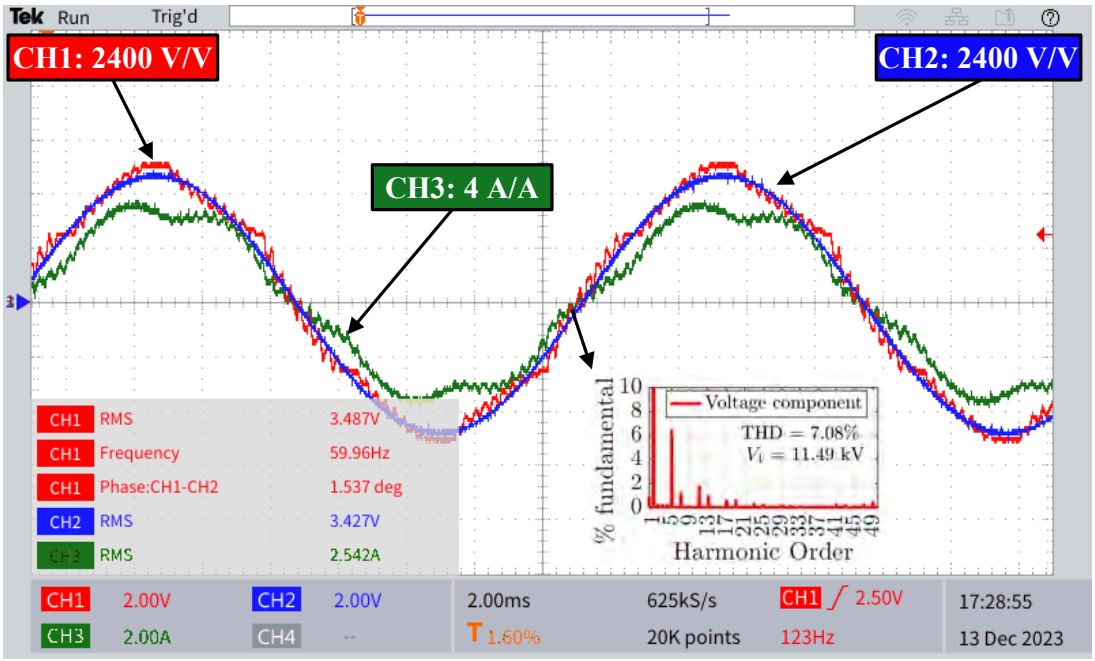

Figure 58 – HIL results for nonlinear load (phase A): PCC voltage (CH1), voltage reference (CH2) and current (CH3).

4.5 Experimental Results

Fig. 61 shows the low voltage 280 kVA prototype used to collect experimental results. Fig. 62 shows the schematic of the ZHD converter operating in grid-forming mode for a 4 kW load with 220 V line voltage. DC-link voltage is obtained through diode rectifier bridges connected to a 220 V grid. Table 13 shows the parameters of the used converter.

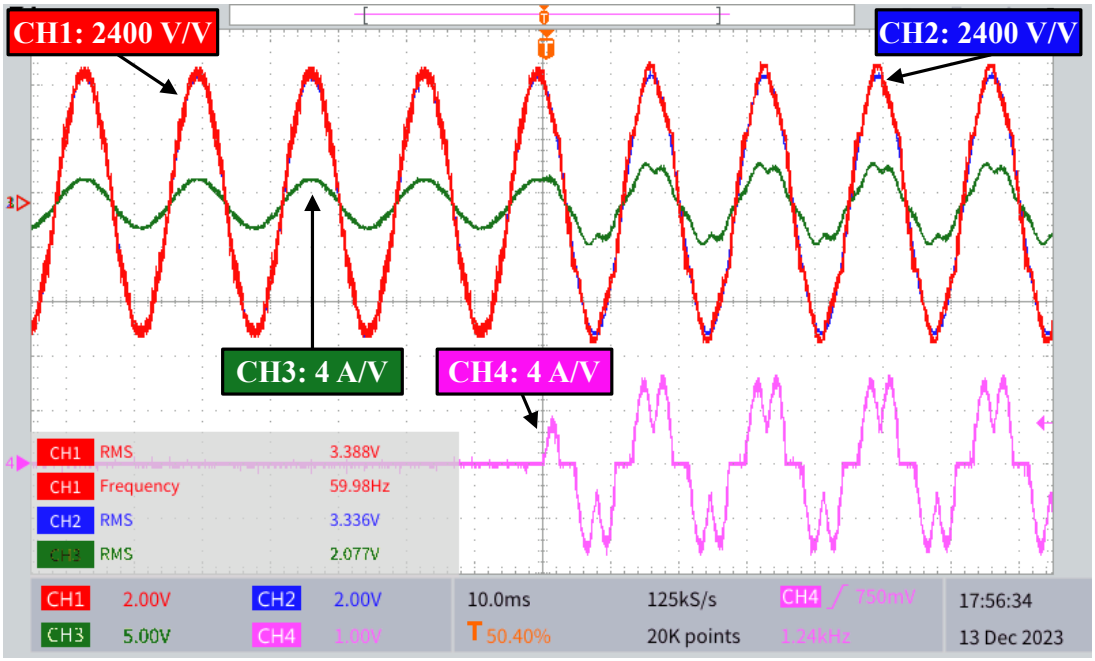

Figure 59 – Transition between linear load and nonlinear load (phase A): PCC voltage (CH1), voltage reference (CH2), converter current (CH3) and nonlinear load current (CH4).

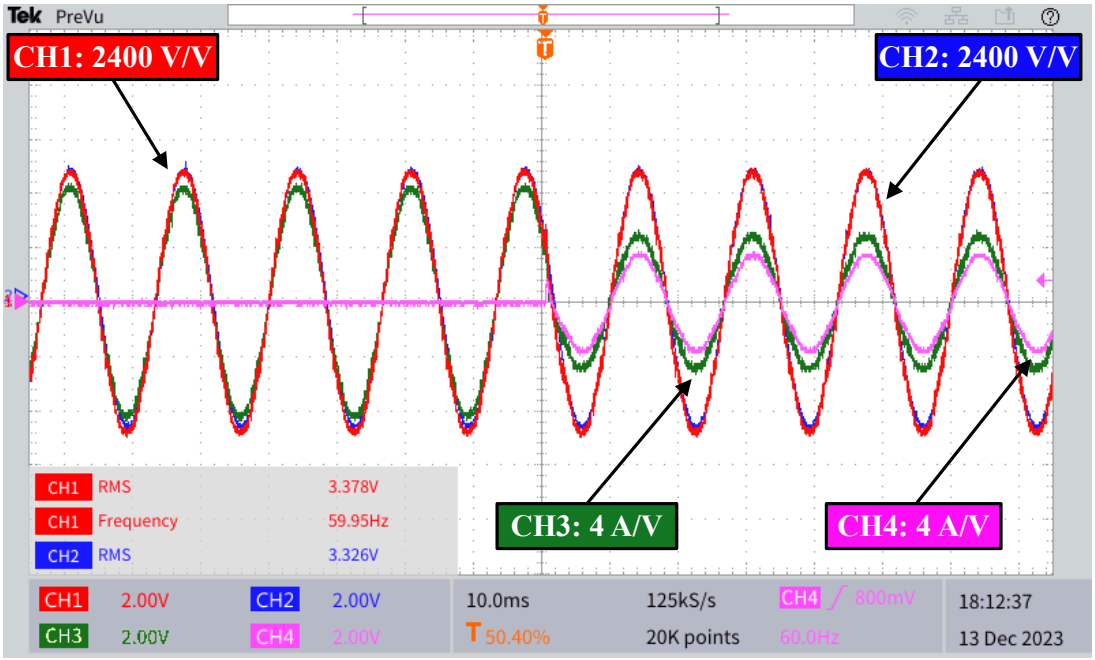

Figure 60 – Voltage regulation when the converter is supplying a linear load and a DER injects active power at the PCC (phase A): PCC voltage (CH1), voltage reference (CH2), converter current (CH3), and DER current (CH4).

The control rack is the same one used for the HIL experiments, with the addition of current and voltage measurement boards and an I/O interface board.

Fig. 63 shows the line voltage and load current, as well as the Δ and wye secondary currents. Although the secondary currents have high distortion, the load current has a

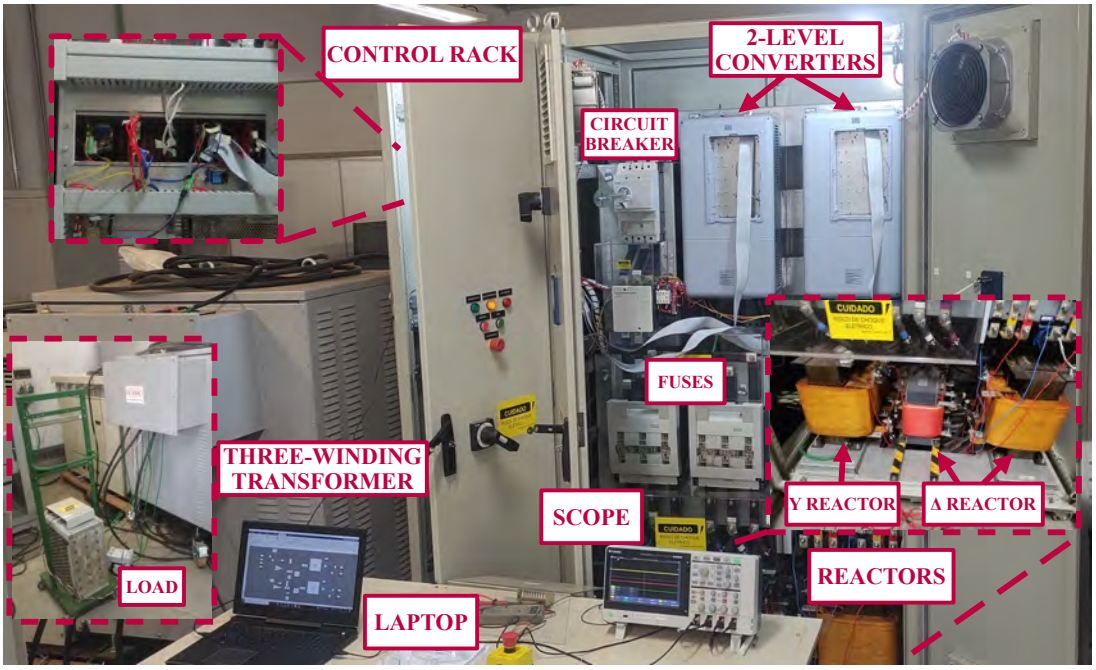

Figure 61 – ZHD prototype.

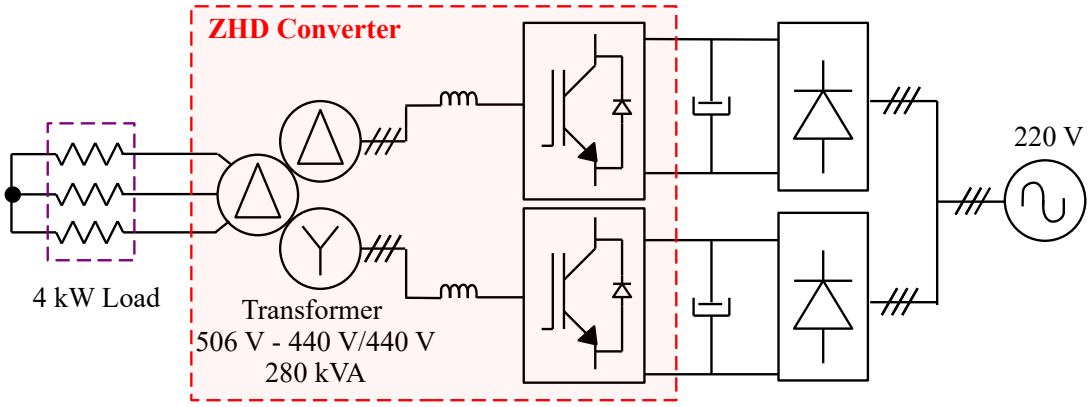

Figure 62 – Schematic of the experiment using the ZHD converter.

Table 13 – ZHD Prototype Parameters

Element	Parameter	Value
Secondary reactors	Δ reactor (mH)	0.6
	Y reactor (mH)	0.51
Transformer	Nominal Power (kVA)	300
	Primary Voltage (V)	506
	Secondaries Voltage (V)	440
	Connection	Dd0y1
VSC	Topology	2-Level
DC link	Voltage (V)	311
	Capacitance (mF)	10.5

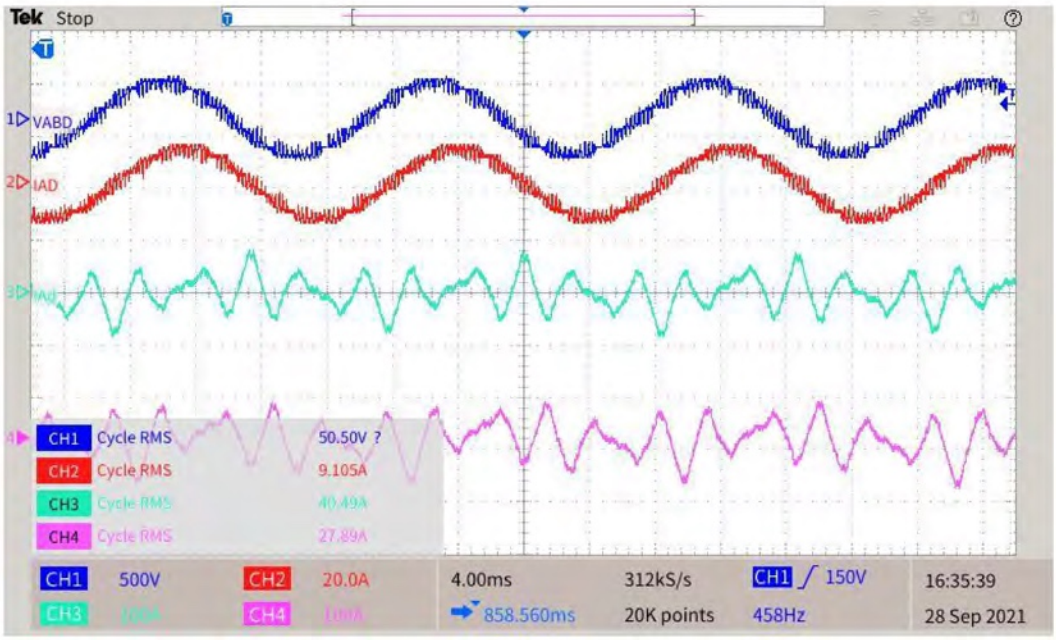

Figure 63 – CH1: primary voltage. CH2: primary current. CH3: Δ secondary current. CH4: wye secondary current.

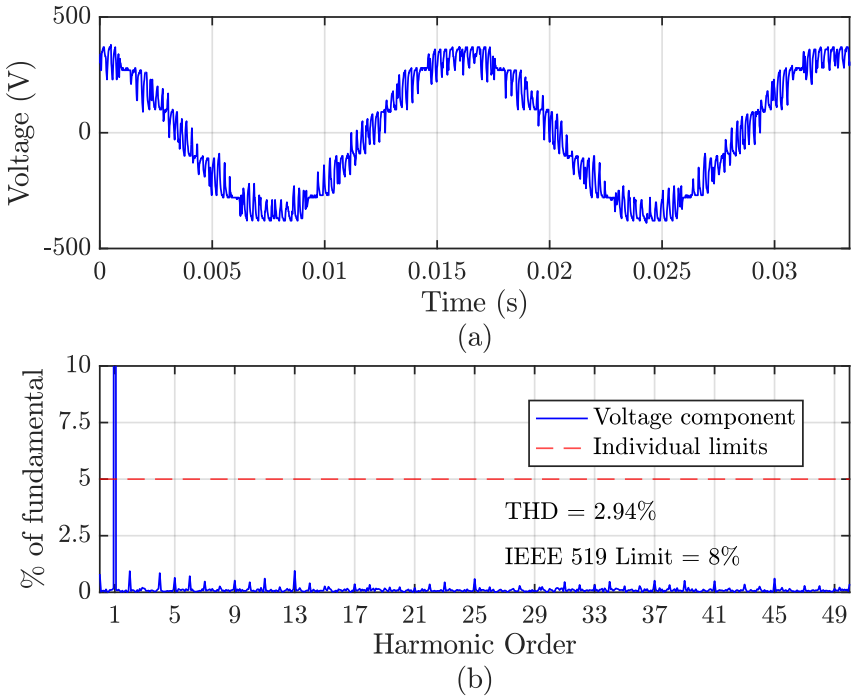

Figure 64 – Load voltage: (a) waveform. (b) harmonic spectrum.

sinusoidal waveshape. The output voltage also has a sinusoidal appearance.

As the test was performed with a low load, the output voltage is more influenced by high-order harmonics (above 3 kHz). Fig. 64 shows the harmonic content of the line voltage at the load. The load voltage has individual and total distortion levels well below the limits established by IEEE 519 for 1 kV systems.

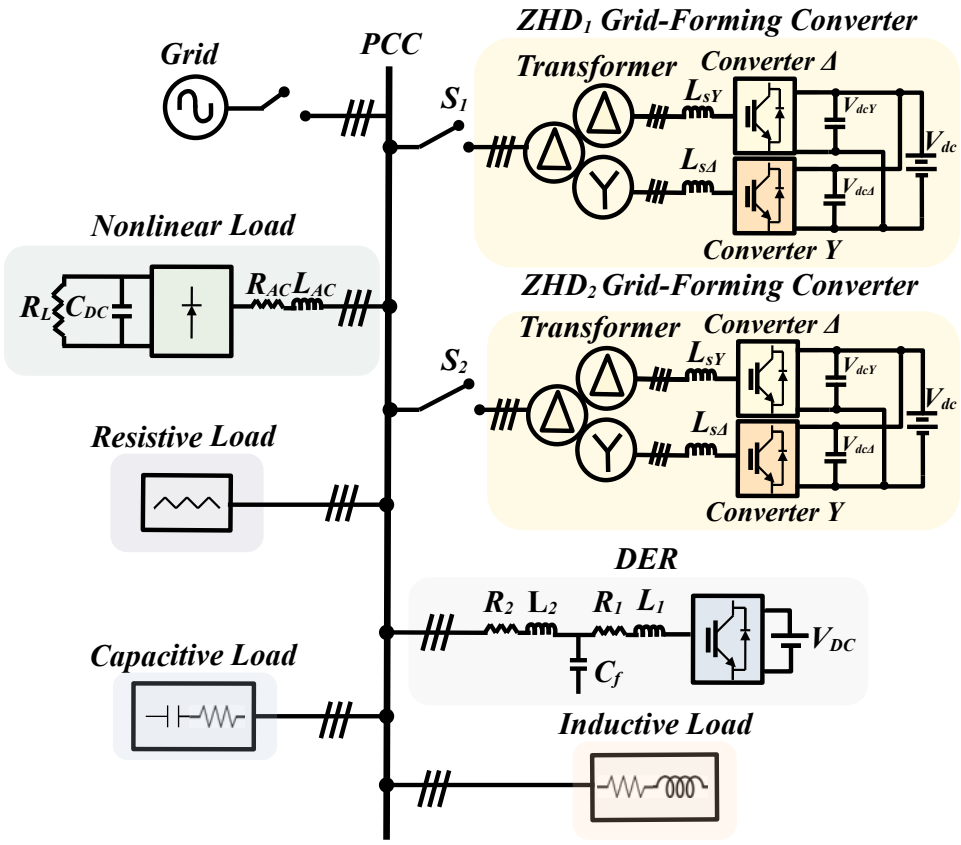

Figure 65 – Islanded MG with ZHD Grid-Forming converter.

4.6 ZHD Control Performance Assessment: Stand-alone and Parallel Modes

The control performance of the ZHD grid-forming converter considering the stand-alone and parallel modes was analyzed based on typical load connection and disconnection scenarios. These scenarios consist in the connection or disconnection of loads with different characteristics: resistive, capacitive, inductive, nonlinear and DERs. Considering both operation modes, the ZHD converter was simulated in a microgrid using MATLAB/Simulink platform, as shown in Fig. 65. The system parameters are described in Table 14.

In a first moment, a period of simulation of 1.6s is adopted. In order to evaluate the ZHD voltage and its frequency regulation capacity, the connection of loads and of the DER are in this sequence:

- t = 0 s $\rightarrow$ (I) $\rightarrow$ S_1 is closed and ZHD_1 starts in isochronous mode and R load is connected ;
- t = 0.43 s $\rightarrow$ (II) $\rightarrow$ RL load is connected;
- t = 0.55 s $\rightarrow$ (III) $\rightarrow$ The DER is adjusted to 100 A;

Table 14 – Converter Data for Simulation Results

ZHD CONVERTER			
Parameters	**Values**	**Parameters**	**Values**
Rated Power	280 kVA	Frequency	60 Hz
Primary Voltage	13.8 kV	Δ and Y Secondary Voltages	440 V
$L_{\phi\Delta}$ and $L_{\phi Y}$ reactors	0.59/0.506 mH	DC link voltage	600 V
THREE-WINDING THREE-PHASE TRANSFORMER - Dd0y1			
Parameters	**Values**	**Parameters**	**Values**
R_m	526.7 $k\Omega$	$R_{s\Delta}$	19.4 $m\Omega$
L_m	534.5 H	$L_{s\Delta}$	3.33 μH
$R_{P\Delta}$	10.5 Ω	R_{sY}	16 $m\Omega$
$L_{P\Delta}$	108.7 mH	L_{sY}	84.26 μH
DER			
Parameters	**Values**	**Parameters**	**Values**
R_1	0.1 Ω	L_1 and L_2	500 μH
R_2	0.1 Ω	T_x	440 V/ 13.8 kV
C_f	110 μF	V_{DC}	800 V
LINEAR LOADS - R, RL and RC LOADS			
Parameters	**Values**	**Parameters**	**Values**
Active Power (P)	100kW	Reactive Power (Q)	0 var
Active Power (P)	40 kW	Reactive Power (Q)	30 kvar
Active Power (P)	40 kW	Reactive Power (Q)	-30 kvar
NONLINEAR LOAD			
Parameters	**Values**	**Parameters**	**Values**
R_{AC}	152.35 Ω	L_{AC}	2.2 μH
C_{dc}	2.59 μH	R_L	34.56 $k\Omega$

- t = 0.7 s $\rightarrow$ (IV) $\rightarrow$ The RL load is disconnected;
- t = 0.75 s $\rightarrow$ (V) $\rightarrow$ RC load is connected;
- t = 0.85 s $\rightarrow$ (VI) $\rightarrow$ The RC load is disconnected;
- t = 0.9 s $\rightarrow$ (VII) $\rightarrow$ The nonlinear load is connected;
- t = 1 s $\rightarrow$ $(VIII)$ $\rightarrow$ The DER is adjusted to 0 A.
- t = 1.2 s $\rightarrow$ (IX) $\rightarrow$ S_2 is closed and both ZHD_1 and ZHD_2 starts in droop control mode ($k_p = 1.78x10^{-7}Hz/W$, $k_q = 6.415x10^{-5}V/Var$);
- t = 1.5 s $\rightarrow$ (X) $\rightarrow$ The nonlinear load is disconnected;

Fig. 66 (a), (b), (c) and (d) shows active, reactive power flow, voltage at PCC and output currents at ZHD converters and frequency at PCC, respectively. It shows that the ZHD converter has the capacity of regulate the voltage and frequency at the PCC, always rejecting the disturbances and following the references. The zoomed view of I, II, V, VIII, IX and X simulation events can be observed in (e)-(p) and show that the converter can follow the voltage and angle references in case of resistive, inductive, capacitive and

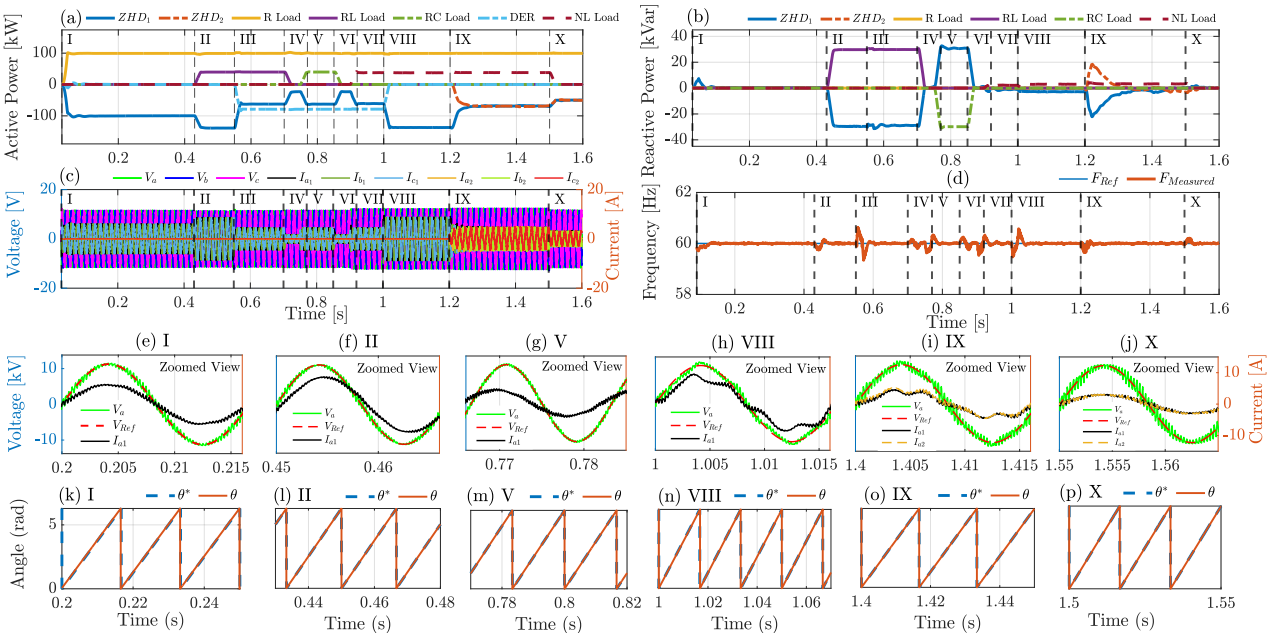

Figure 66 – (a) Active power flow, (b) reactive power flow, (c) voltage at PCC and output currents at ZHD converters, (d) frequency at PCC, Zoomed view of phase A reference, measured voltage at PCC and current in ZHD converters in time instants: (e) I, (f) II, (g) V, (h) VIII, (i) IX, (j) X, reference and measured angle in time instants: (k) I, (l) II, (m) V, (n) VIII, (o) IX, (p) X.

nonlinear loads and also can operates in parallel with other voltage controlled converters in power sharing mode.

Fig. 66 also shows the sinusoidal shape of the delivered voltage waveform in case of linear loads ((e), (f), (g) and (j)), and that the waveform is deteriorated in the presence of the nonlinear load ((h) and (i)).

Fig. 67 shows the phase A voltage FFT for each case. As can be expected, the delivered voltage waveform for linear loads is practically free from harmonics until the 50^{th} order ((a),(b), (c), (f)). However, when the nonlinear load is connected, the phase A voltage is disturbed by the demanded harmonic current. Fig. 67 (d) and (e) reveals the presence of harmonics not produced by the converter, but generated by the nonlinear load. Finally, Fig. 67 (g) and (h) shows the output current FFT showing both ZHD converters sharing the same fundamental and harmonic currents in case of nonlinear and linear load, respectivily.

4.6.1 Sensitivity Analysis

Fig. 68 shows a important analysis regarding the dynamic stiffness of the command control shown in (4.3).

$$\left|\frac{I(s)}{V(s)}\right| = \frac{1}{\hat{Z}_{zhd}H_{VSC}(s) - Z_{zhd}} \tag{4.3}$$

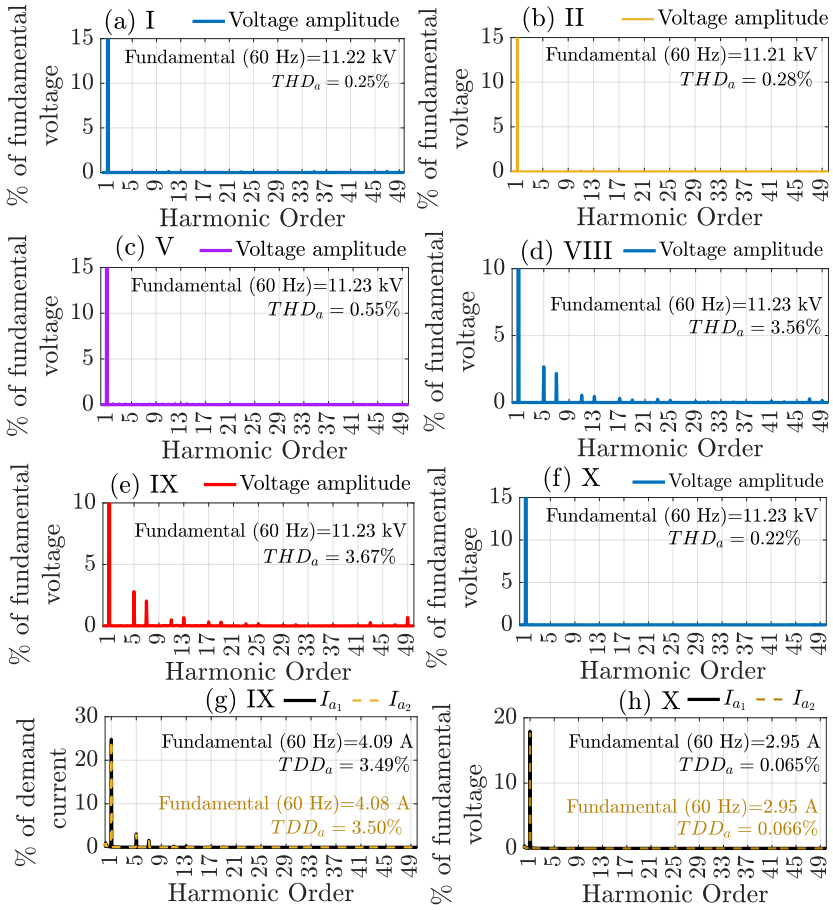

Figure 67 – Output Voltage FFT for time events: (a) I, (b) II, (c) V, (d) VIII, (e) IX, (f) X, Output Current FFT for time events: (g) IX and (h) X.

The sensitivity analysis in the control system due to error in the converter estimated output impedance, for the same scenario of the last section, but considering cases with ±20% of estimating error in the ZHD_1 converter. Fig. 68 (a)-(d) show that the converter can regulate voltage ((a),(b)) and frequency (d) with acceptable voltage regulation, as shown in (c), inside the ±5% limit recommend by standards.

Considering the isochronous operation, Fig. 68 (e)-(l) clearly show that voltage and angle references could be tracked even considering the cases of ±20% of estimating error. However, the included estimating error causes a unequal current sharing between the both ZHD converters due to the differences in the virtual impedance between them. For the scenario shown in Fig. 68 (a), Fig. 68 (m) and (n) shows the phase A reference, measured voltage at PCC and the higher output current of ZHD_1 compared with ZHD_2 converter for time events IX and X. The FFT of the currents waveforms of (m) and (n) are shown in (q) and (r), respectively, reinforcing the differences between the currents.

The scenario shown in Fig. 68 (b) analogously shows the same effect, but with the ZHD_2 converter providing more current. For this case Fig. 68 (o) and (p) shows the phase A reference, the measured voltage at PCC and the output currents for both converters in

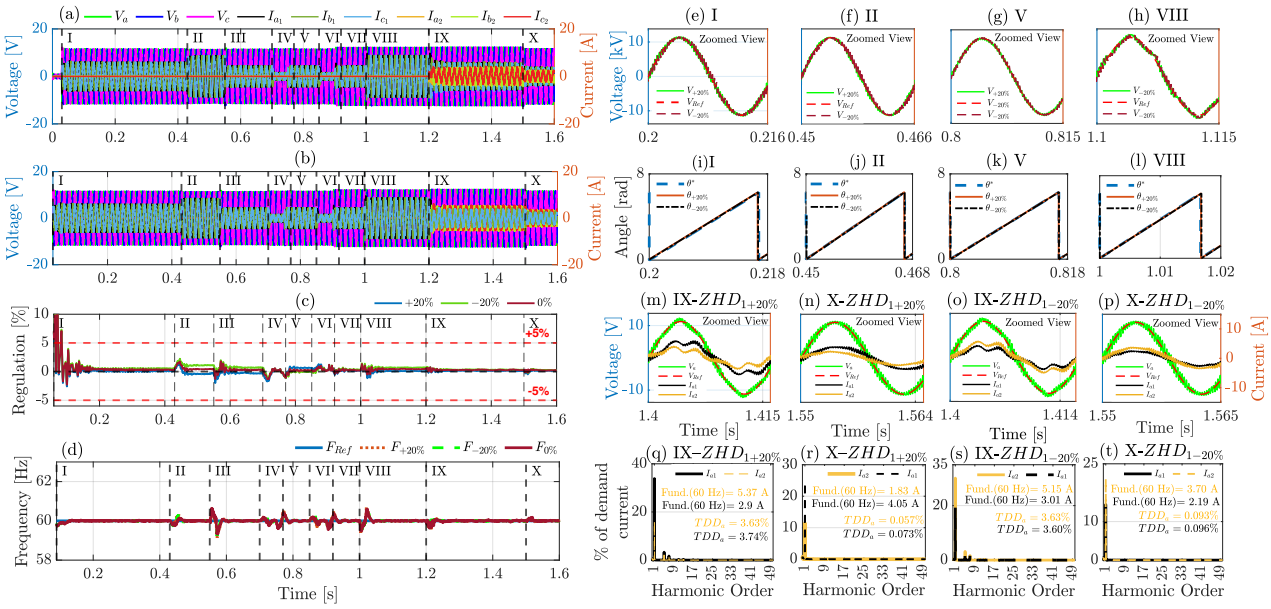

Figure 68 – Considering estimating errors of +20% and −20% in ZHD_1 converter: a) Voltages at PCC and output currents at ZHD converters considering a error of (a) +20%, (b) −20%, (c) PCC voltage regulation, (d) measured PCC frequency, zoomed view of phase A reference voltage and voltage at PCC in time instants: (e) I, (f) II, (g) V, (h) VIII, reference and measured angle in time instants: (i) I, (j) II, (k) V, (l) VIII, zoomed view of voltage at PCC and output currents at ZHD converters in time instants (m) IX, (n) X, (o) IX, (p) X, respectively, and output FFT voltage in time instants (q) IX, (r) X, (s) IX and (t) X.

time events IX and X. Fig. 68 (s) and (t) shows the FFT of the currents.

4.6.2 Hardware-in-the-loop Results

Considering the same HIL setup (Fig. 56), one ZHD converter in the isochronous mode, was evaluated in three dynamics scenarios considering output impedance estimating errors of 0% , 20% and -20%, for a 50 kVA capacitive load (PF= 0.9), followed by a step load of 130 kW. Figs. 69 to 71 show the results of each case followed by the zoomed views of phase A voltage and output current.

In all cases, it is possible to verify the control structure voltage and frequency regulation capacity, rejecting the step load disturbance and, as expected, delivering a practically sinusoidal voltage waveform. The voltage regulation also was evaluated, and even in the cases considering estimating error in the output impedance, the voltage regulation remains well below 5%.

These results show that the ZHD converter is capable to operate as a grid-forming converter regulating voltage and frequency without capacitive filters, delivering sinusoidal voltage waveforms to an islanded MG only using a feedforward disturbance command control.

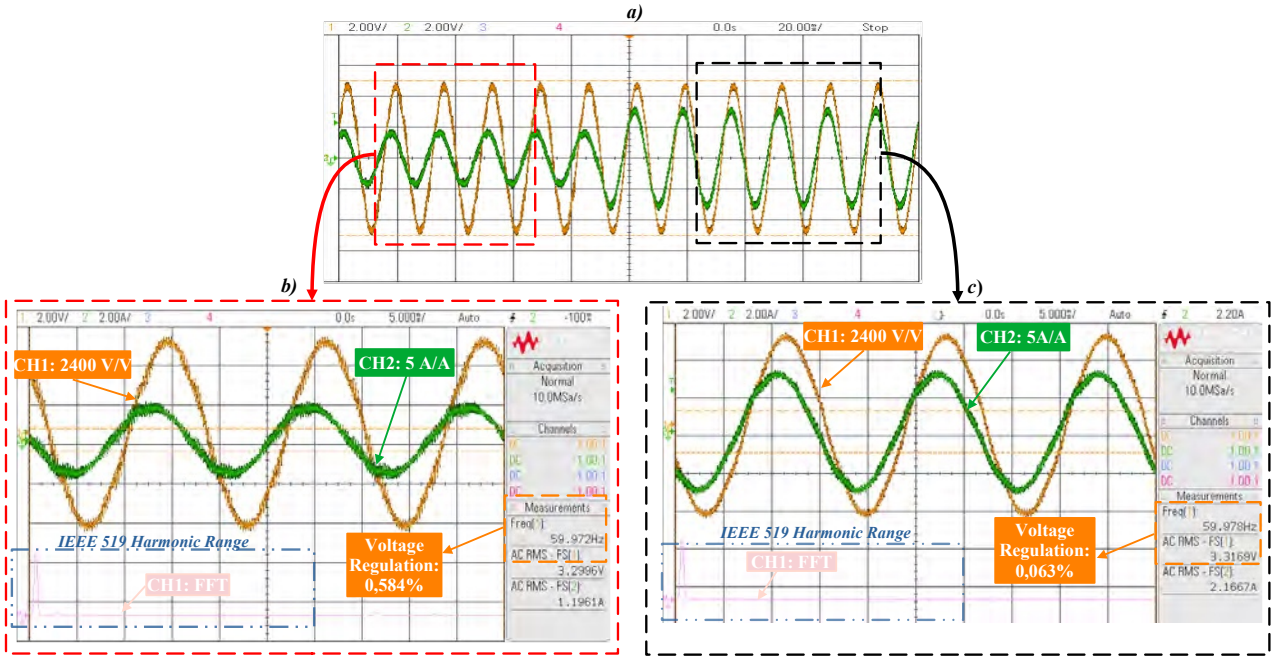

Figure 69 – a) HIL results for a step load (phase A): PCC voltage (CH1), current (CH2) and FFT voltage (CH1) considering 0% of output impedance estimating error, b) Zoomed view before step load, c) Zoomed view after step load.

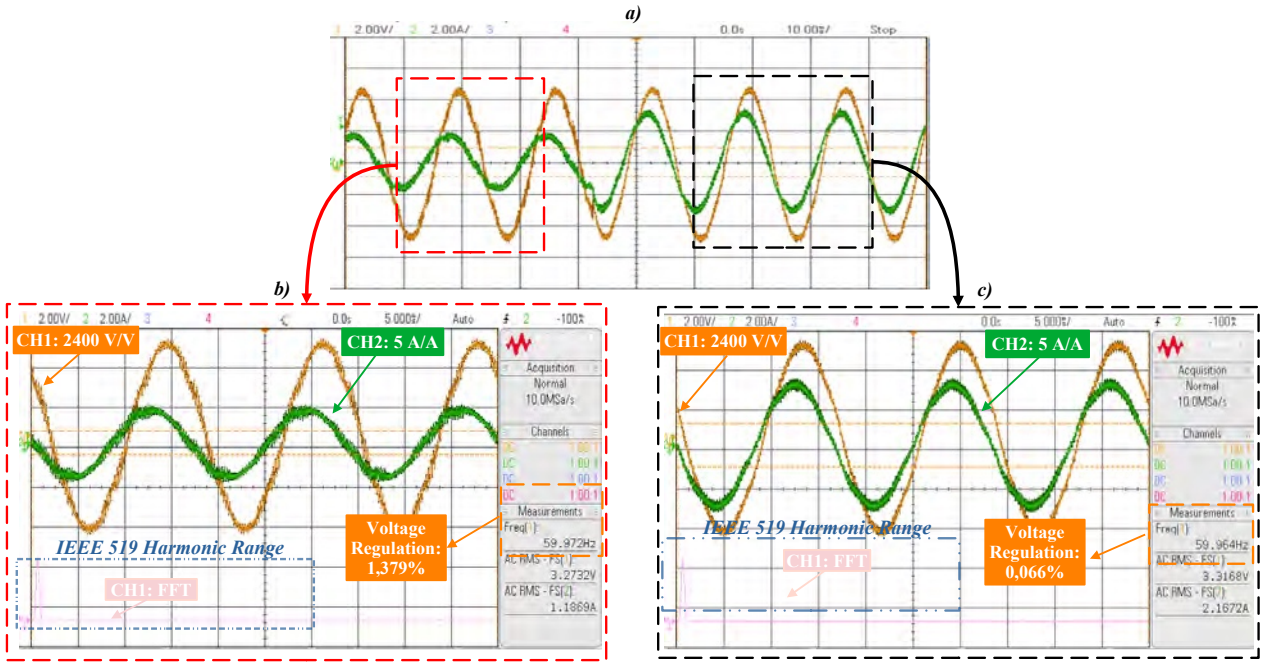

Figure 70 – a) HIL results for a step load (phase A): PCC voltage (CH1), current (CH2) and FFT voltage (CH1) considering +20% of output impedance estimating error, b) Zoomed view before step load, c) Zoomed view after step load.

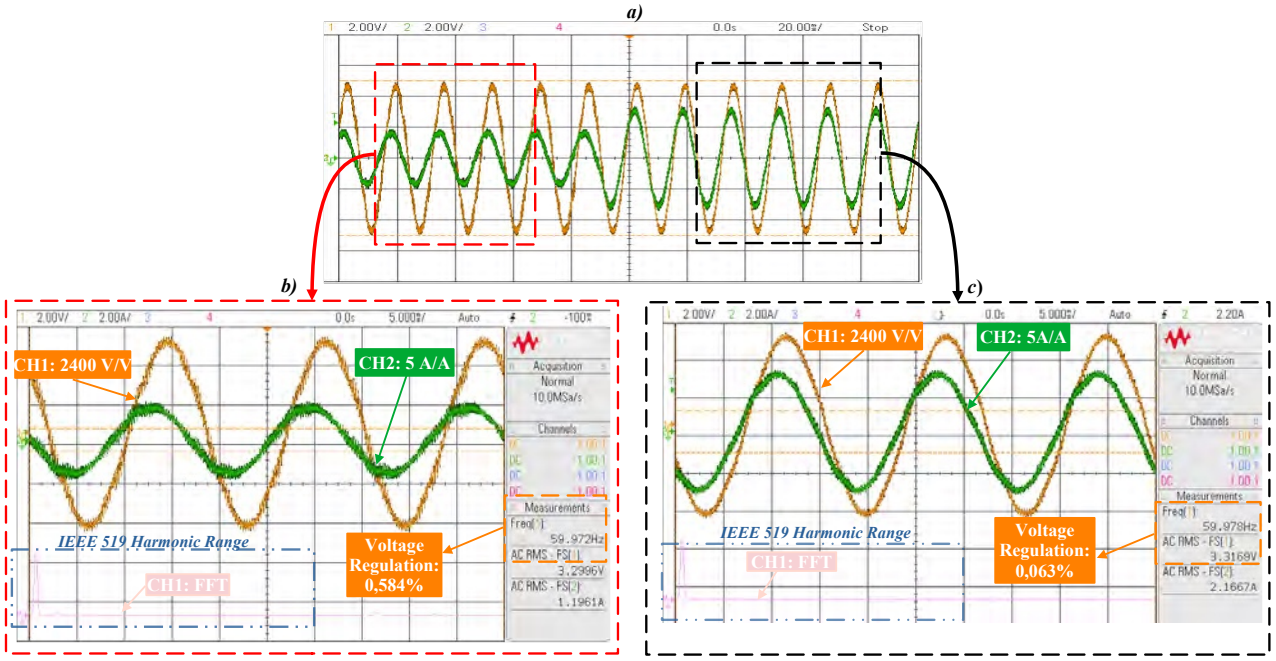

Figure 71 – a) HIL results for a step load (phase A): PCC voltage (CH1), current (CH2) and FFT voltage (CH1) considering -20% of output impedance estimating error, b) Zoomed view before step load, c) Zoomed view after step load.

4.7 The Three-level ZHD Grid-Forming converter

The ZHD Grid-Forming converter implemented with three-level converters was also assessed in island operation due to the advantages highlighted in Chapter III of: withstand higher voltage levels and lower reactors impedances on the secondaries due to the multilevel output voltages.

The control performance of the 3L-ZHD grid-forming converter also was analyzed based on typical load variation scenarios. The simulated microgrid using the MATLAB/Simulink platform is shown in Fig. 72. The system parameters are described in Table 15. The nonlinear load was parameterized according to ((UPS)-Part..., 1999).

4.7.1 Voltage and Frequency Regulation

In the first scenario of the MG, an operation of simulation time equal to 1.2 s is adopted. In order to evaluate the ZHD voltage and frequency regulation capability, the connection of loads and of the DER occurs in the following sequence:

- t = 0.03 s $\rightarrow$ (I) $\rightarrow$ R load is connected;
- t = 0.43 s $\rightarrow$ (II) $\rightarrow$ RL load is connected;
- t = 0.55 s $\rightarrow$ (III) $\rightarrow$ The DER is adjusted to 100 A;
- t = 0.7 s $\rightarrow$ (IV) $\rightarrow$ The RL load is disconnected;

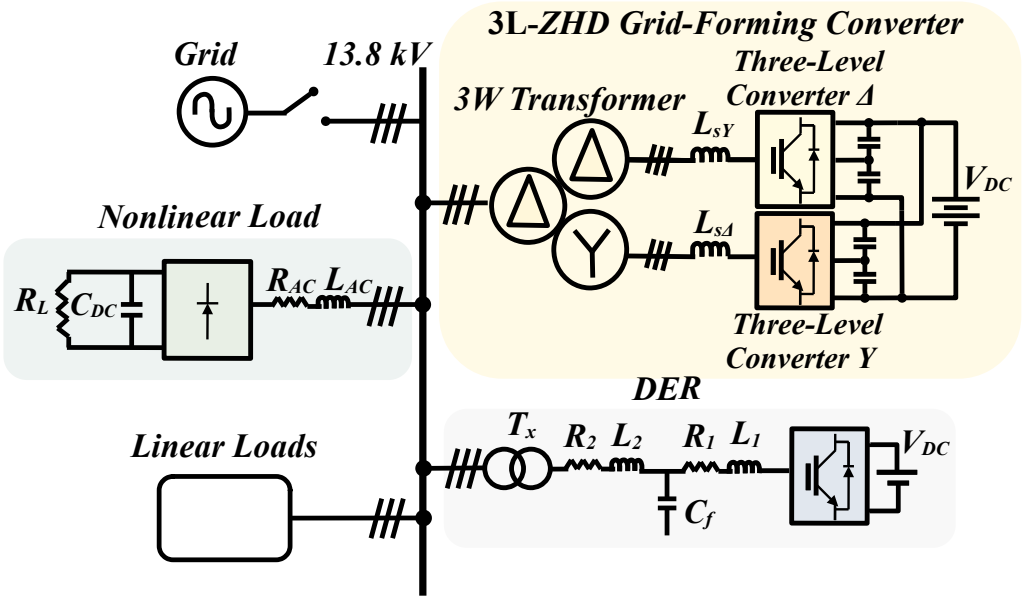

Figure 72 – Islanded MG with 3-Level ZHD Grid-Forming converter.

- t = 0.75 s → (V) → RC load is connected;
- t = 0.85 s → (VI) → The RC load is disconnected;
- t = 0.9 s → (VII) → The nonlinear load is connected;
- t = 1 s → $(VIII)$ → The DER is adjusted to 0 A.

Fig. 73 (a) and (b) shows the active and reactive power flow at PCC during the simulation events. Even in the presence of load variation and DER active power injection, the ZHD converter shows the capacity to regulate the frequency and the phase voltages in the PCC, always rejecting the disturbances and following the references, as can been seen in Fig. 73 (c) and (d), respectively.

The output voltage and angle zoomed view of I, II, V and VIII simulation events can be observed in Fig. 74 (a)-(d) respectively, and shows that the output phase A voltage follows the voltage reference and angle in each case. Assessing the voltage waveforms samples of I, II, V and VIII events, instants where the converter supply resistive, inductive, capacitive and nonlinear loads it is possible to observe the sinusoidal shape of the delivered voltage waveforms in case of linear loads (Fig. 74 (a), (c) and (e)), and that the waverform is deteriorated in the presence of the nonlinear load (Fig. 74 (g)).

Fig. 75 (a), (b), (c) and (d) shows the phase A voltage FFTs for each case. As can be expected, the delivered voltage waveform for linear loads is free of any harmonic until the 50^{th} order, confirming that the converter does not produce any harmonic component in this range. However, when the nonlinear load is connected, the phase A voltage is disturbed by the demanded harmonic current. Fig. 75 (d) reveals reveals the voltage is disturbed by the demanded harmonic current.

Table 15 – Converter Data for Simulation Results

3L-ZHD CONVERTER			
Parameters	**Values**	**Parameters**	**Values**
Rated Power	280 kVA	Frequency	60 Hz
Primary Voltage	13.8 kV	Δ and Y Secondary Voltages	690 V
Δ and Y reactors	0.72/0.52 mH	DC link voltage	1200 V
3L-ZHD:THREE-WINDING THREE-PHASE TRANSFORMER - Dd0y1			
Parameters	**Values**	**Parameters**	**Values**
R_m	526.7 $k\Omega$	$R_{s\Delta}$	47.7 $m\Omega$
L_m	534.5 H	$L_{s\Delta}$	8.18 μH
$R_{P\Delta}$	10.5 Ω	R_{sY}	39.3 $m\Omega$
$L_{P\Delta}$	108.7 mH	L_{sY}	207.21 μH
DER			
Parameters	**Values**	**Parameters**	**Values**
R_1	0.1 Ω	L_1 and L_2	500 μH
R_2	0.1 Ω	T_x	440 V/ 13.8 kV
C_f	110 μF	V_{DC}	800V
LINEAR LOADS - R, RL and RC			
Parameters	**Values**	**Parameters**	**Values**
Active Power (P)	100kW	Reactive Power (Q)	0 var
Active Power (P)	48 kW	Reactive Power (Q)	36 kvar
Active Power (P)	48 kW	Reactive Power (Q)	-36 kvar
NONLINEAR LOAD			
Parameters	**Values**	**Parameters**	**Values**
R_{AC}	152.35 Ω	L_{AC}	2.16 mH
C_{dc}	2.59 μH	R_L	34.56 $k\Omega$
LOADS SIMULATED FOR IEEE 519 LIMITS - R LOAD + NONLINEAR LOAD			
Parameters	**Values**	**Parameters**	**Values**
Active Power (P)	100kW	Reactive Power (Q)	0 var
R_{AC}	152.35 Ω	L_{AC}	2.16 mH
C_{dc}	2.59 μH	R_L	26.49 $k\Omega$
2L-ZHD CONVERTER			
Parameters	**Values**	**Parameters**	**Values**
Rated Power	280 kVA	Frequency	60 Hz
Primary Voltage	13.8 kV	Δ and Y Secondary Voltages	440 V
Δ and Y reactors	0.59/0.506 mH	DC link voltage	600 V
2L-ZHD:THREE-WINDING THREE-PHASE TRANSFORMER - Dd0y1			
Parameters	**Values**	**Parameters**	**Values**
R_m	526.7 $k\Omega$	$R_{s\Delta}$	19.4 $m\Omega$
L_m	534.5 H	$L_{s\Delta}$	3.33 μH
$R_{P\Delta}$	10.5 Ω	R_{sY}	16 $m\Omega$
$L_{P\Delta}$	108.7 mH	L_{sY}	84.26 μH

4.7.2 Sensitivity Analysis

Another important analysis realized is the sensitivity analysis of the control system due to error in the converter estimated impedance $\hat{Z}_{zhd}$. Considering the same load profile of section 4.7.1, cases with $\pm 20\%$ of estimating error was considered and Fig. 76 clearly

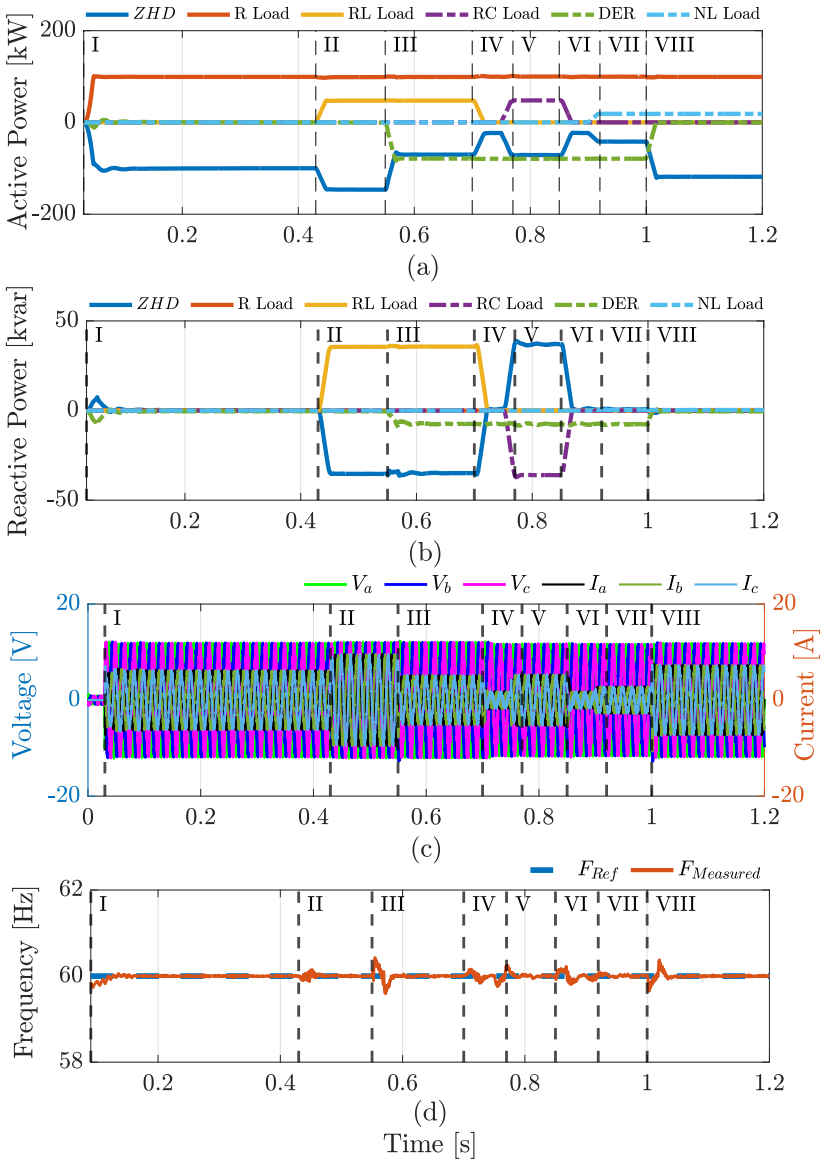

Figure 73 – (a) PCC active power, (b) PCC reactive power, (c) Output voltage and current in the ZHD converter and (d) Frequency at PCC.

show that the output voltage could be tracked with acceptable voltage regulation, inside the ±5% limit recommend by IEEE std 1547. The frequency also remains tracking the reference as shown in Fig. 76 (b) and the output voltage phase deviation stay inside in a range of ±1°.

4.7.3 2L x 3L Harmonic Performance

A harmonic performance comparison between the 2L-ZHD proposed and the 3L-ZHD converter, was realized including only linear and nonlinear loads to simulate a realistic harmonic injection in the PCC with currents within the limits outlined by IEEE 519 (Table 15). The FFT output current and voltage of the ZHD converter at this condition is shown

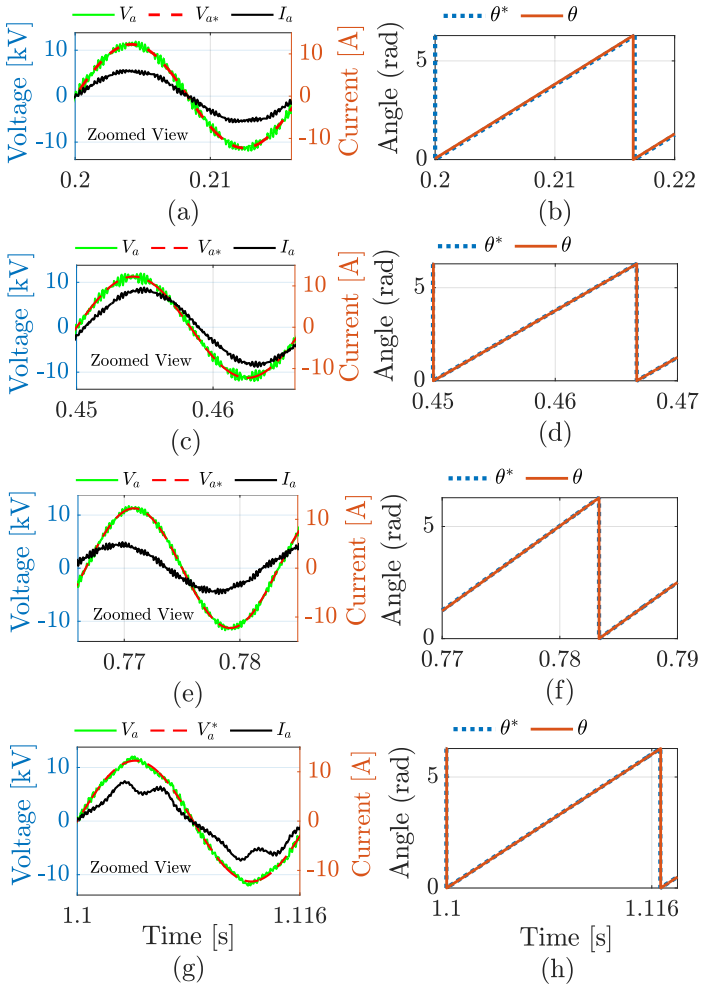

Figure 74 – (a) Reference voltage, output voltage and current in time event I, (b) reference angle and output angle in time events I , (c) Reference voltage, output voltage and current in time event II, (d) reference angle and output angle in time events II, (e) Reference voltage, output voltage and current in time event V, (f) reference angle and output angle in time event V, (g) Reference voltage, output voltage and current in time event VIII, (h) reference angle and output angle in time events VIII.

in Fig. 77 (a) and (b), considering that the connected loads reach the current harmonic limits defined by IEEE 519 at the PCC, according to maximum short-circuit and demand load currents (I_{SC}/I_L) ratio. The results clearly show that with a drained current with the 5^{th} harmonic order in the limit of the permitted level, the voltage harmonic distortion of the 3L-ZHD converter is below the IEEE 519 harmonic constraints while the 2L-ZHD converter presents a performance slightly above the limit. That happens since the 2L-ZHD converter presents higher secondary reactors necessary to limit the secondaries current harmonic flow, impacting in a worse harmonic performance in MV applications.

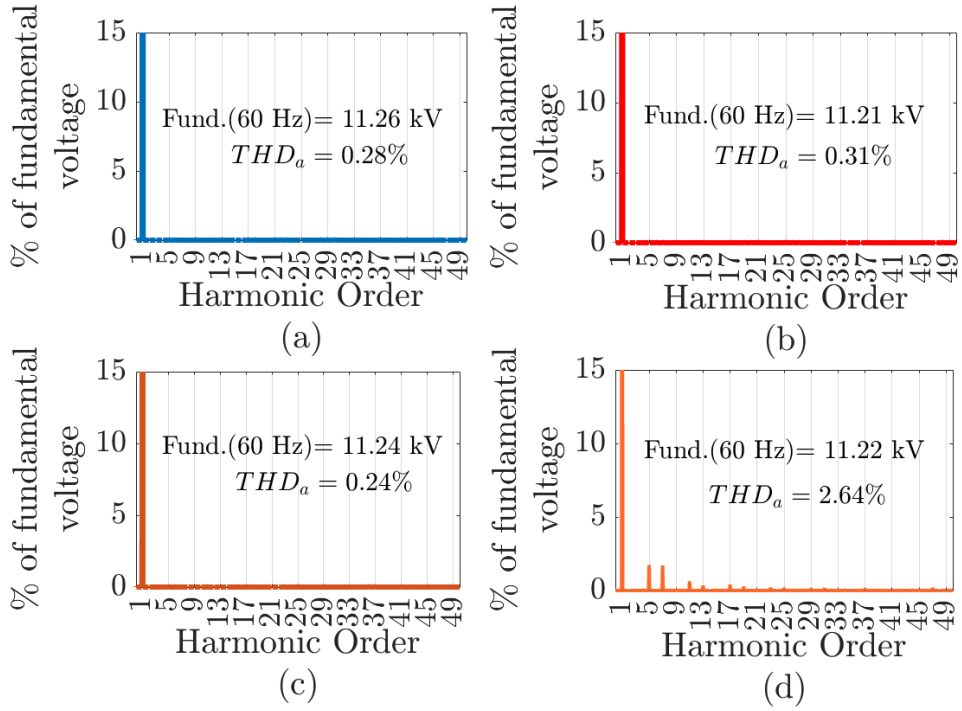

Figure 75 – Output Voltage FFT for time events: (a) I, (b) II, (c) V, (d) VIII.

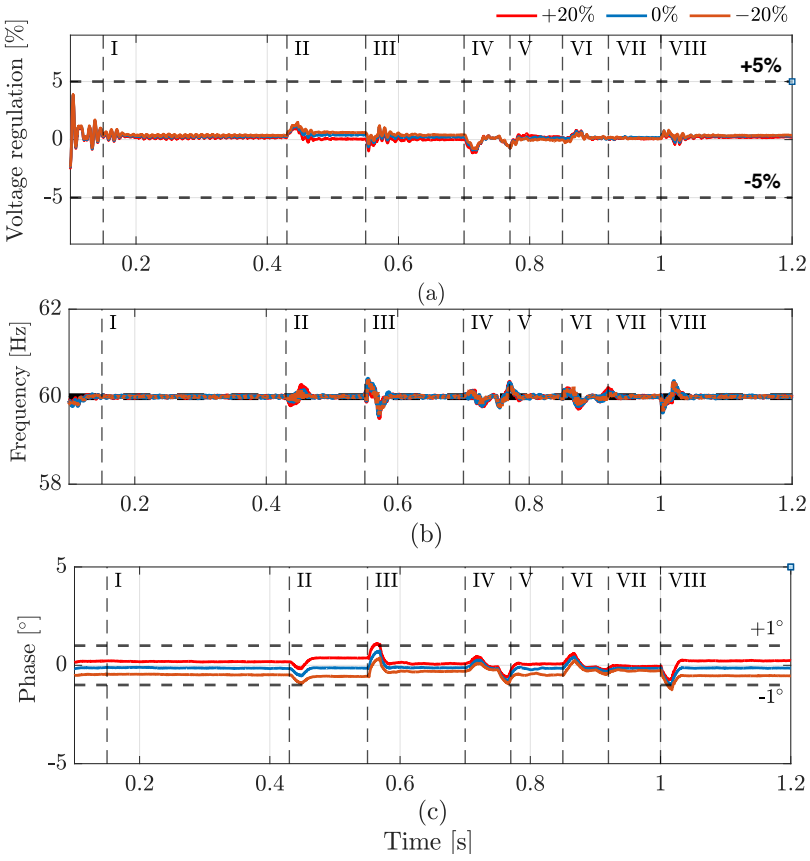

Figure 76 – 3L-ZHD output voltage: (a) regulation, (b) frequency and (c) phase considering ±20% of impedance estimating error.

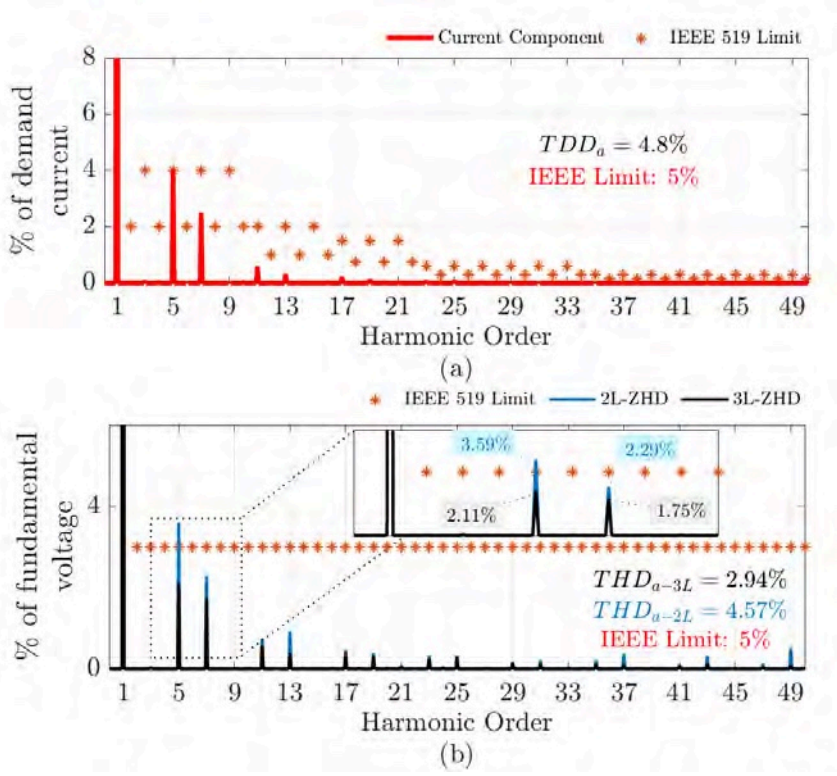

Figure 77 – (a) FFT for load current with 4% of 5^{th} harmonic, (b) Voltage FFT for 2L and 3L ZHD converter considering the load current with 4% of 5^{th} harmonic.

4.8 Conclusions

This chapter presented the application of the Zero Harmonic Distortion (ZHD) converter as an effective solution to the challenges faced by grid-forming converters in islanded microgrids. Unlike conventional approaches that require complex control schemes and capacitive filtering elements, the ZHD converter inherently operates as a sinusoidal voltage source without the need for such components, thereby improving efficiency, reducing cost and size, and minimizing the risk of resonance. Simulation, hardware-in-the-loop, and experimental results demonstrated the ZHD converter's ability to set voltage and frequency in an islanded microgrid while delivering sinusoidal voltage waveforms compliant with IEEE 519 harmonic limits, even under nonlinear loading conditions. These results confirm the ZHD converter as a promising alternative for grid-forming applications in isolated microgrids, offering significant benefits in power quality, control simplicity, and system robustness.

5 Zero Harmonic Distortion Hybrid Grid-Forming Converter: Grid-Interactive Operation in Medium Voltage Microgrids

This chapter proposes the Zero Harmonic Distortion Converter (ZHD) as a grid-interactive converter for medium voltage microgrids, delivering sinusoidal waveforms in both grid-connected and islanded mode without sinusoidal capacitive filtering elements. The ZHD ensures seamless transitions between modes using a simple control approach that eliminates the need off a voltage closed-loop control for grid-connected, islanded, and transition modes, using only a current closed-loop control for grid-connected operation. Simulation and hardware-in-the-loop results show the performance of the ZHD converter.

5.1 Introduction

In Chapter 4, the operation of the Zero Harmonic Distortion (ZHD) converter in islanded mode was analyzed in detail, demonstrating its ability to regulate voltage and frequency through an open-loop structure based solely on virtual impedance compensation. The results confirmed its inherent voltage-source behavior and the capability to generate high-quality sinusoidal waveforms without the need for voltage control loops. Building upon these findings, this chapter focuses on the operation of the ZHD converter when connected to the main grid and during transitions between operating modes.

The transition of an MG from grid-connected to islanded mode and back involves either a smooth transition or black-start procedures (Vukojevic; Lukic, 2020). In the literature, considering conventional voltage source converters (VSCs), numerous methods can be found for seamless transition that modify inverter control loops and control the islanding switch based on droop control (Li; Vilathgamuwa; Loh, 2004; Gao; Iravani, 2008; Hu et al., 2011; Arnedo et al., 2012; Mohamed et al., 2012; Araujo; Brandao, 2022; Lissandron; Mattavelli, 2014) and hybrid voltage and current mode (HVCM) control structures (Liu; Liu; Zhao, 2014; Kulkarni; Doolla; Fernandes, 2017b; Kwon; Yoon; Choi, 2012; Lo; Chen, 2020b). In droop-based control techniques the converter is always working as a voltage source showing good performance between the transition of operation modes. However, the limitation of this approach is the low dynamic of the power loops due to bandwidth restrictions between the control loops, and since the grid current is not directly controlled, the inrush grid current during the transition modes and fault occurrence always exists (Hu et al., 2011). In HVCM control techniques the converter operates in a current

control mode in the grid-connected mode, and in voltage control mode in the islanded mode. In this way, there is a need to switch between two types of controllers depending on the operation mode, where the quality of the voltage waveforms relies on this transition (Liu; Liu; Zhao, 2014; Kulkarni; Doolla; Fernandes, 2017b; Kwon; Yoon; Choi, 2012; Lo; Chen, 2020b).

In this context, the ZHD converter inherently sinusoidal output voltage seen in Chapter 4, enables the use of closed-loop current control during grid-connected operation and open-loop control in islanded mode. The transition between these modes can be achieved simply by abling or disabling the current control loop. This chapter evaluates the performance of the ZHD converter under both operating conditions, emphasizing its black-start capability and its ability to perform seamless transitions between grid-connected and islanded modes.

5.2 Revisiting the ZHD Current Source Operation

In current source operation, or GFL mode, the ZHD converter must operate as a current source, following the grid voltage parameters, i.e. voltage amplitude, frequency, and phase, as these values are needed for conducting an accurate control of the active and reactive power delivered to the grid. This mode is necessary in the grid-connected operation of the converter in MGs responding to load and grid variation. It is also a current limit mode strategy in case of faults. The ZHD converter in this operation mode was extensively explored several applications in the literature (Parreiras, 2020; Parreiras; Justino; Filho, 2015; Alves; Parreiras; Filho, 2019; Almeida; Filho, 2017; Parreiras et al., 2015; Parreiras et al., 2021; Parreiras et al., 2020; Brandão et al., 2022b; Justino; Parreiras; Filho, 2014; Brandão et al., 2022).

The control scheme for the ZHD converter is shown in Fig. 78, where synchronization with the power grid is achieved through the Decoupled Double-Synchronous Reference Frame PLL (DDSRF-PLL) proposed by (Cortés, 2005; Rodriguez et al., 2007) and illustrated in Fig. 79. This PLL is capable of aligning with the fundamental positive sequence angle even in situations of unbalanced and distorted grid conditions by using two decoupled dq coordinate axes, one for positive sequence and another for negative sequence, along with appropriate filtering and gain sizing (Parreiras, 2020).

The angle tracked by the DDSRF-PLL is used in the Park transform and its inverse, in order to achieve a alignment between the spatial voltage phasor with the d-axis, as illustrated in Fig. 80. This ensures that the quadrature-axis component of the grid voltage (V_q) is zero.

In this sense, the active power (P) and reactive power (Q) can be calculated and controlled independently by the direct-axis (I_d) and quadrature-axis (I_q) currents,

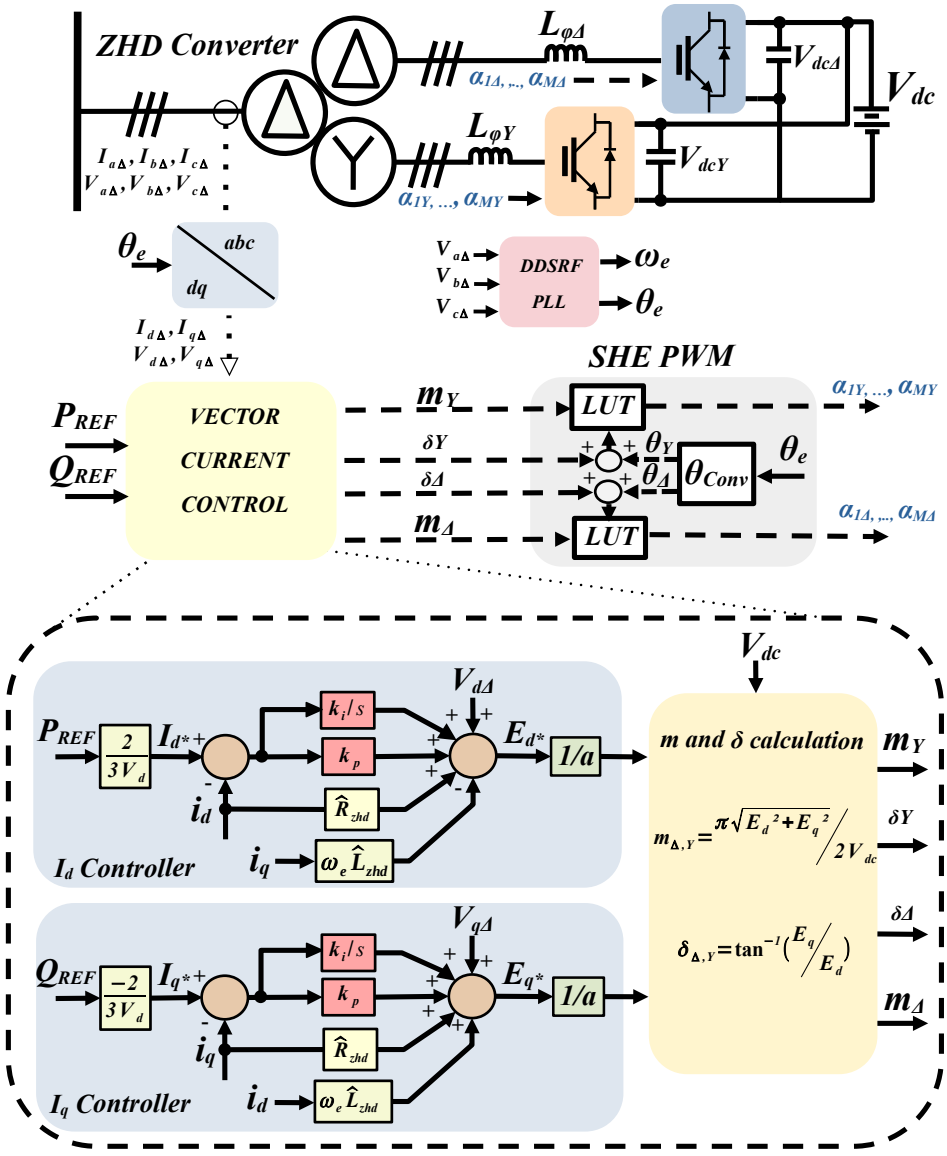

Figure 78 – ZHD current control diagram. *Adapted from.* (Parreiras, 2020)

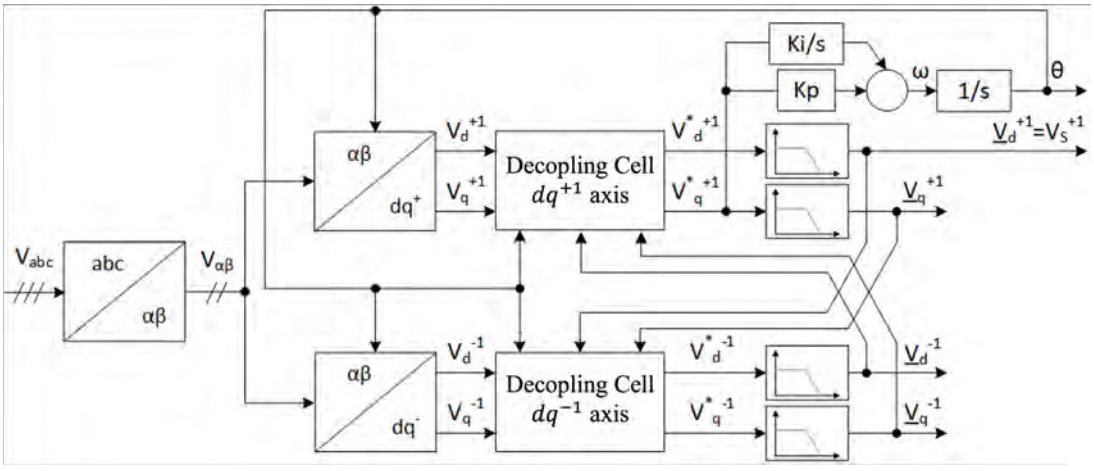

Figure 79 – Decoupled Double-Synchronous Reference Frame PLL. *Adapted from.*(Parreiras, 2020)

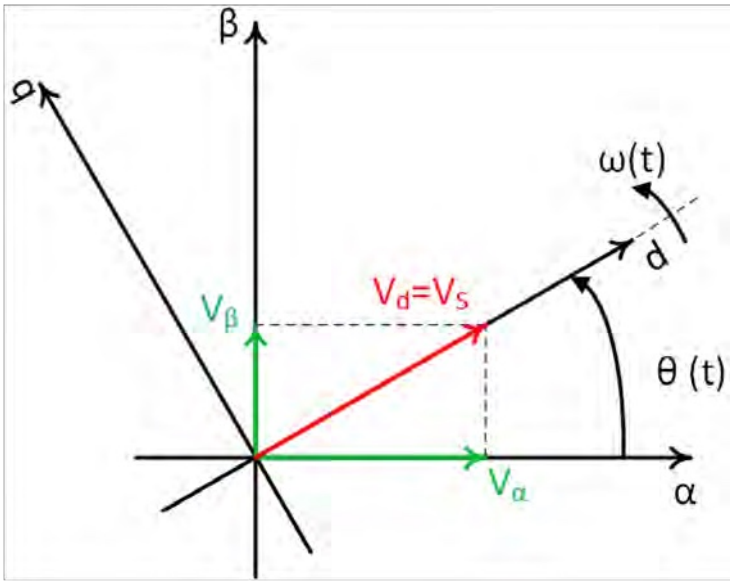

Figure 80 – Synchronous dq axes synchronized with the spatial voltage phasor of the grid. *Adapted from* (Parreiras, 2020).

respectively, as indicated in (5.1) and (5.2) (Yazdani; Iravani, 2010a).

$$P = \frac{3}{2} V_d I_d \tag{5.1}$$

$$Q = -\frac{3}{2} V_d I_q \tag{5.2}$$

Based on the differential equations describing the current response in dq coordinates of the system (5.3)-(5.4), the block diagram of the closed-loop current control for each converter is indicated in Fig. 81. A proportional-integral (PI) controller is sufficient for zero steady-state error due to the continuous nature of the I_d and I_q components. Feedforward disturbance controls are applied to eliminate or at least reduce the effects of external disturbances (grid voltage) and internal disturbances (inductor resistance and axis coupling through inductances), along with a feedforward command control to improve system performance by eliminating/reducing errors between the reference and the output.

$$L\frac{di_d}{dt} = U_d + L\omega_0 i_q - Ri_d - V_d \tag{5.3}$$

$$L\frac{di_q}{dt} = U_q - L\omega_0 i_d - Ri_q - V_q \tag{5.4}$$

5.2.1 Simulation Results

To verify the operation of the proposed closed-loop control, simulations are performed using the Simulink platform of MATLAB, using two-level converters. The parameters

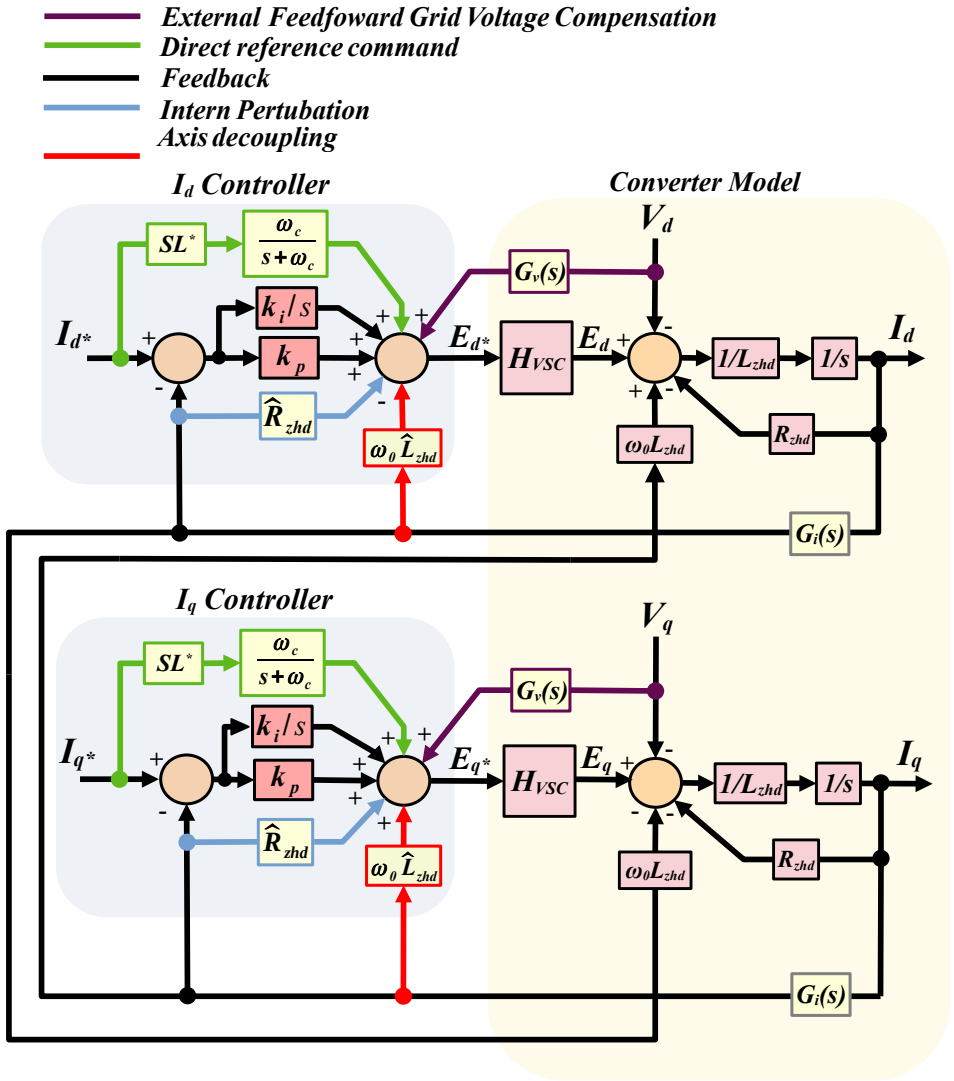

Figure 81 – DQ Current control Diagram. *Adapted from* (Parreiras, 2020)

described in Table II.

Table 16 – Converter parameters for current control simulation results

Parameter	**Value**	**Parameter**	**Value**
Rated Power	280 kVA	Frequency	60 Hz
Primary Nominal Voltage	13.8 kV	Δ Secondary Nominal Voltage	440 V
Winding Connections	Dd0y1	Y Secondary Nominal Voltage	440 V
Δ and Y Reactors	0.59 mH	DC Link Voltage	650 V
k_{pi}	0.23	k_{ii}	14.9

The adjustment of the DDSRF-PLL controllers was performed according to the calculations recommended by (Cortés, 2005), which depend on the voltage and frequency of the system. The adjustment of the current controllers, on the other hand, was carried out using the criterion of external disturbances rejection through the disturbance rejection

curve also called of dynamic stiffness (Lorenz; Lipo; Novotny, 1994), illustrated by Fig. 82 and expressed by (5.5). It can be observed that the integral gain has a greater influence on the rejection of low-frequency disturbances, the value of the design inductor rejects high frequencies, while the intermediate range is dominated by the proportional gain (Parreiras, 2020).

$$\frac{V^{dq}(s)}{I^{dq}(s)} = sL + k_p^{dq} + \frac{k_i^{dq}}{s} \tag{5.5}$$

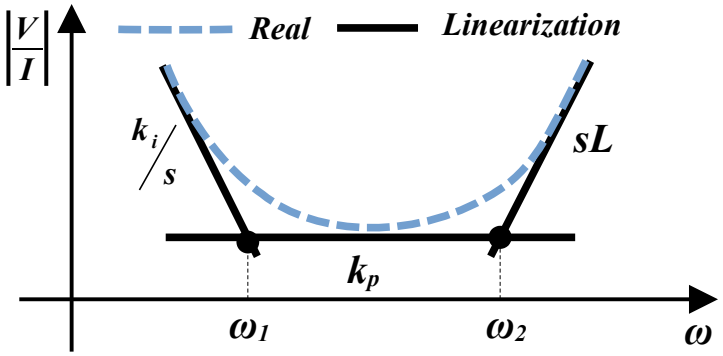

Figure 82 – Dynamic stiffness.

The main goal of adjusting the controllers is to locate the zeros of the curve dynamic stiffness curve, (5.6)-(5.7), at the highest possible frequencies in order to enable dynamic control of the current, while also not modifying the pulse pattern of the SHE PWM modulator. Additionally, it is important to maintain a sufficient distance between the two poles to avoid interference between the control actions (Parreiras, 2020).

$$\omega_1 \approx \frac{K_i}{K_p} \tag{5.6}$$

$$\omega_2 \approx \frac{K_i}{L} \tag{5.7}$$

In the first moment, the ZHD converter was simulated, delivering full power to the electrical grid. The active power reference was changed stepwise from zero to full load at time instant 0.1 s, as shown by the dq components of the total current controller in Fig. 83 a) and b). 83 c) and d) shows that in each converter connected to the secondaries Δ and Y, the current I_d has the same value in both secondaries, thus ensuring equal division of the total active power, while the current I_q was kept at zero for unity power factor.

Fig. 84 a) and b) shows the currents in phases A on both secondary and primary sides of the transformer, while c), d), e) and f) indicates these same currents in secondary and primary respectively, with their respective harmonic spectrum.

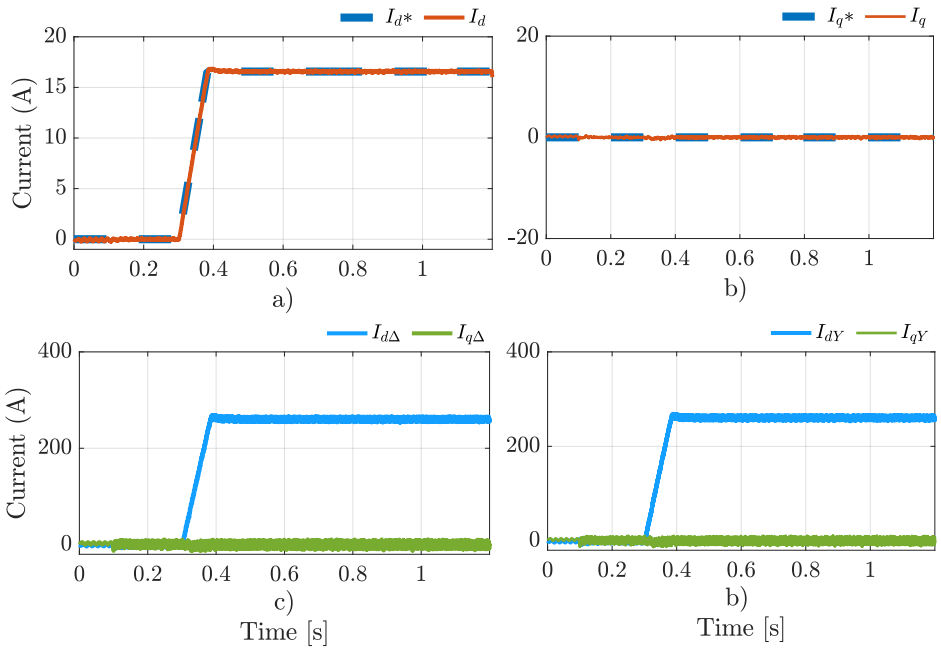

Figure 83 – Current control of: a) I_d component b) I_q component and q current components of: c) Δ secondary d) Y secondary.

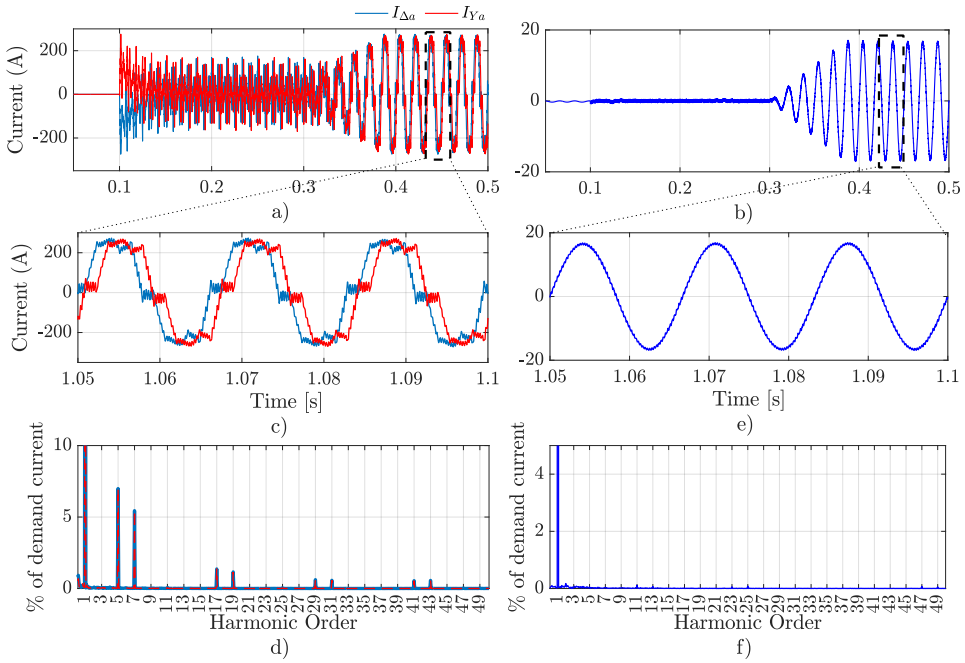

Figure 84 – a) Phase A current in each VSC, b) phase A current harmonic spectrum, c) Zoomed view of phase A current in each VSC, d) and their respective harmonic spectrum, e) Zoomed view of phase A current in primary and f) primary phase A current harmonic spectrum.

From the results, it can be observed that although the current waveforms in both converters are highly distorted, the waveform of the current in the grid is nearly sinusoidal ((e)). This was achieved by eliminating the 12k ± 1 harmonics (up to the 50th order) in the converter, resulting in currents in the three-winding transformer's secondary side with the same characteristic harmonics (d)), which are eliminated by the transformer connection. In practical terms, the absence of harmonics up to the 50th order is clearly identified in f).

Finally, to demonstrate the dynamic capability of the ZHD converter and its proper capacity to regulate the active (I_d) and reactive power (I_q) on the grid, a new simulation was performed. In this simulation, the converter changes from inverter mode to floating mode at time instant 0.6 s, and then to rectifier mode at time instant 0.8 s, as shown in Fig. 85 a) and in Fig. 85 b) the reactive power regulation injecting and absorbing reactive power in 0.3 s and 0.9 s. Fig. 85 c) shows the current in each converter connected in the secondaries, and in f) the phase A voltage and current in primary of the transformer. From these figures, it can be observed the proper functioning of the ZHD converter for bidirectional power flow, as well as its ability to track a sudden variation in active and reactive power references.

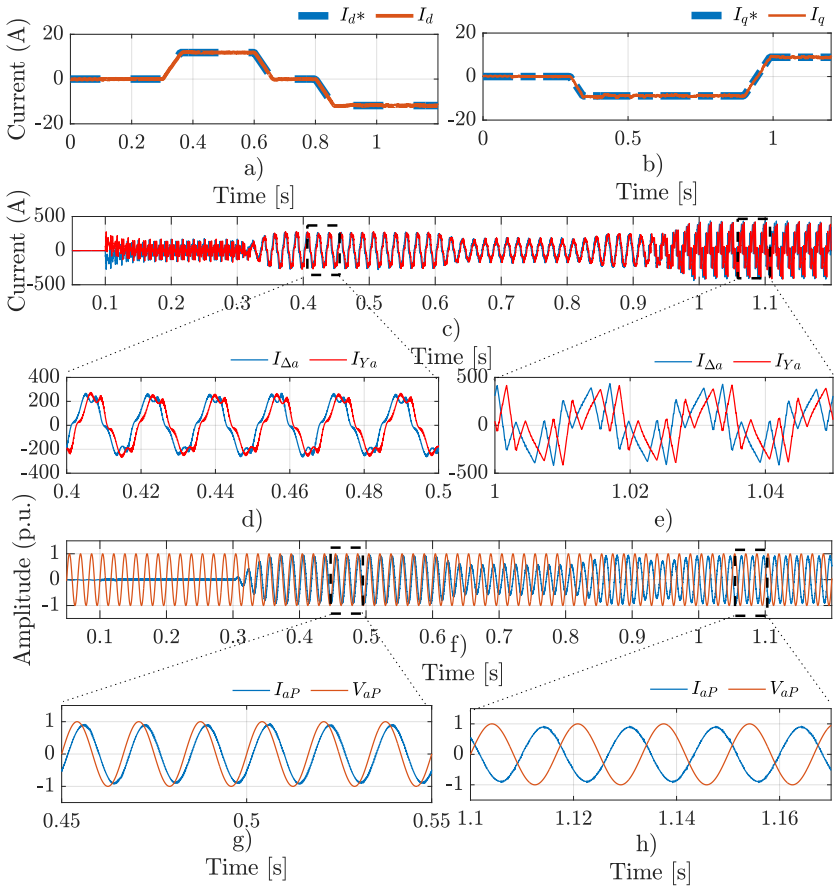

Figure 85 – Current control of: a) I_d component b) I_q component for reference variation, c) Phase Currents at: a) Δ secondary and Y secondary and zoomed views in d) and e), f) Primary voltage and current for reference variation and zoomed views in g) and h).

5.3 Current Source Operation under Symmetrical and Asymmetrical faults

5.3.1 Converter Behavior

Although the ZHD current control was well developed in previous works, operation under fault conditions was never explored before. Considering the same control structure and simulations parameters of Table **??**, the converter was submitted to symmetrical and asymmetrical faults at PCC in order to asses the behavior of the converter under faults.

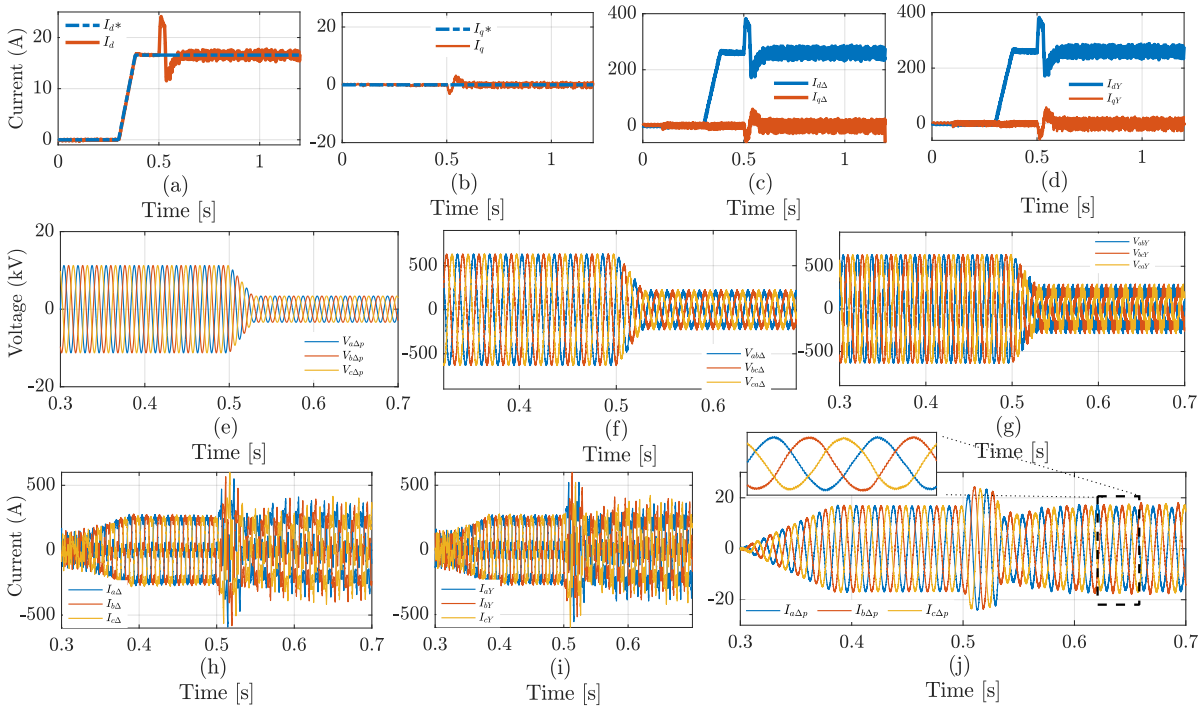

Figure 86 – Current control of (a) I_d and (b) I_q; dq components of (c) Δ and (d) Y secondaries; three-phase voltages at (e) primary, (f) Δ, and (g) Y secondaries; and three-phase currents at (h) Δ, (i) Y, and (j) primary under a three-phase fault.

Considering a three-phase symmetrical fault, Fig. 86 illustrates the current control performance. It can be observed that the controller effectively rejects the voltage sag, maintaining accurate tracking of the I_d and I_q current references, as shown in (a) and (b). Sub figures (c) and (d) present the dq-axis current components at both secondaries, which remain well regulated during the voltage sag.

The corresponding voltage waveforms at the transformer primary and both secondaries are shown in (e), (f), and (g), respectively. As expected, the primary voltage sag directly affects the transformer flux linkage and, consequently, the secondary voltage waveforms. Finally, sub figures (h), (i), and (j) show the three-phase current waveforms at both secondaries and the primary winding, where the converter capability to deliver

sinusoidal currents is clearly demonstrated.

In case of asymmetrical voltage sags, such as single- and double-phase voltage sags, the primary current waveforms still remain with a sinusoidal shape, since the voltage disturbance occurs in the fundamental voltage frequency. Since the same modulation index is sent to the both converters, the equal harmonic cancellation still remains valid. This is expected according to the analytical approach developed in Chapter III. Fig. 87 and 88 show the same results for single- and double-phase voltage sags.

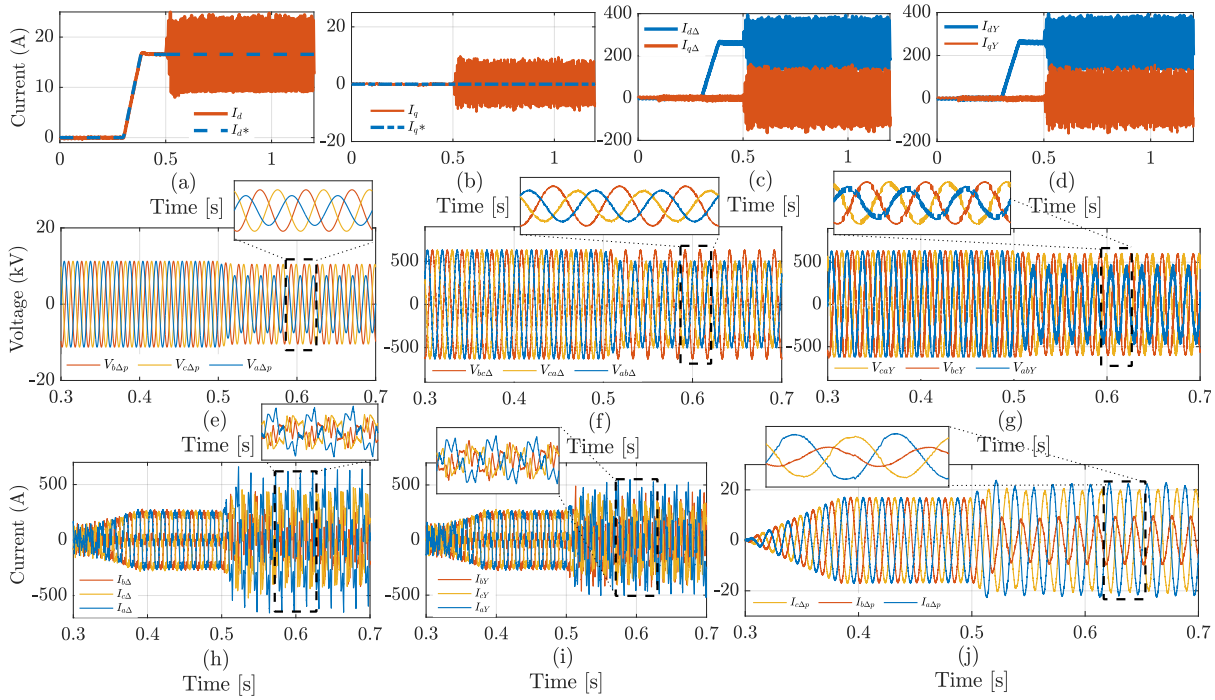

Figure 87 – Current control of (a) I_d component and (b) I_q component; dq current components of (c) Δ secondary and (d) Y secondary under a phase-A single-phase symmetrical fault; three-phase voltages at (e) primary, (f) Δ secondary, and (g) Y secondary; and three-phase currents at (h) Δ secondary, (i) Y secondary, and (j) primary under the same fault condition.

It is important to highlight the appearance of a second-order oscillatory component in the dq-frame during asymmetrical voltage sags, as observed in Fig. 87 and 88 (a)–(d).

This oscillation originates from the interaction between the positive- and negative-sequence voltage components, which, when projected onto the synchronous reference frame aligned with the positive-sequence voltage, produces a double-frequency ripple in both the dq current components and associated control variables.

The resulting oscillation is an inherent characteristic of grid-connected converters operating under unbalanced conditions, and its amplitude depends on the severity and type of voltage unbalance. Despite the presence of this oscillatory behavior, the ZHD converter maintains stable and effective control of the positive-sequence current components.

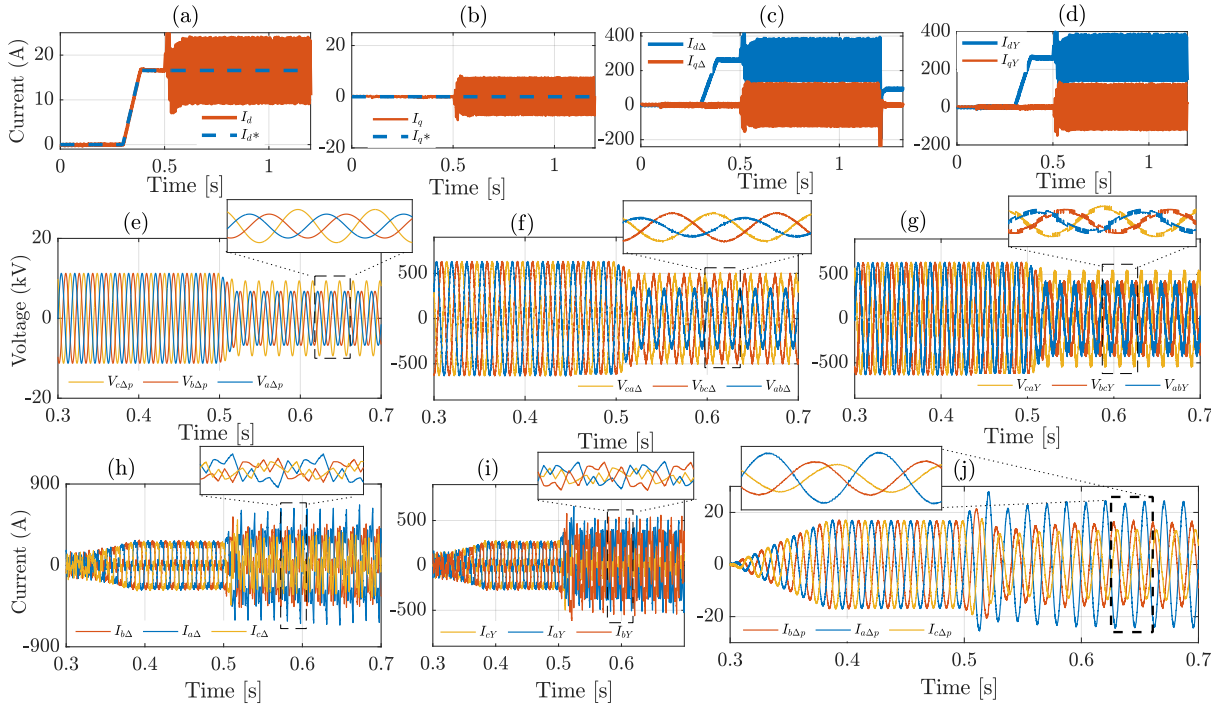

Figure 88 – Current control of (a) I_d component and (b) I_q component; dq current components of (c) Δ secondary and (d) Y secondary under a phase-A–B double-phase symmetrical fault; three-phase voltages at (e) primary, (f) Δ secondary, and (g) Y secondary; and three-phase currents at (h) Δ secondary, (i) Y secondary, and (j) primary under the same fault condition.

The current regulator continues to track the I_d and I_q as seen in (a) and (b) of each Fig. 87 and 88.

5.3.2 Voltage Support

The ZHD converter voltage support capability under these scenarios was also evaluated. Following the IEEE 1547 standard, its performance under asymmetrical fault conditions was assessed to verify LVRT functionality. For a 50% voltage sag lasting 0.5 s, single-phase, and double-phase fault cases were considered. Fig. 89 shows the results for the single-phase sag, and Fig. 90 for the double-phase sag.

In all cases, the ZHD converter maintained effective current control, regulating the positive-sequence component even during voltage sag events, while injecting reactive power by adjusting the I_q reference of the quadrature current regulator, as can be seen in Fig. 89 and 90 (b) in accordance with IEEE 1547 requirements.

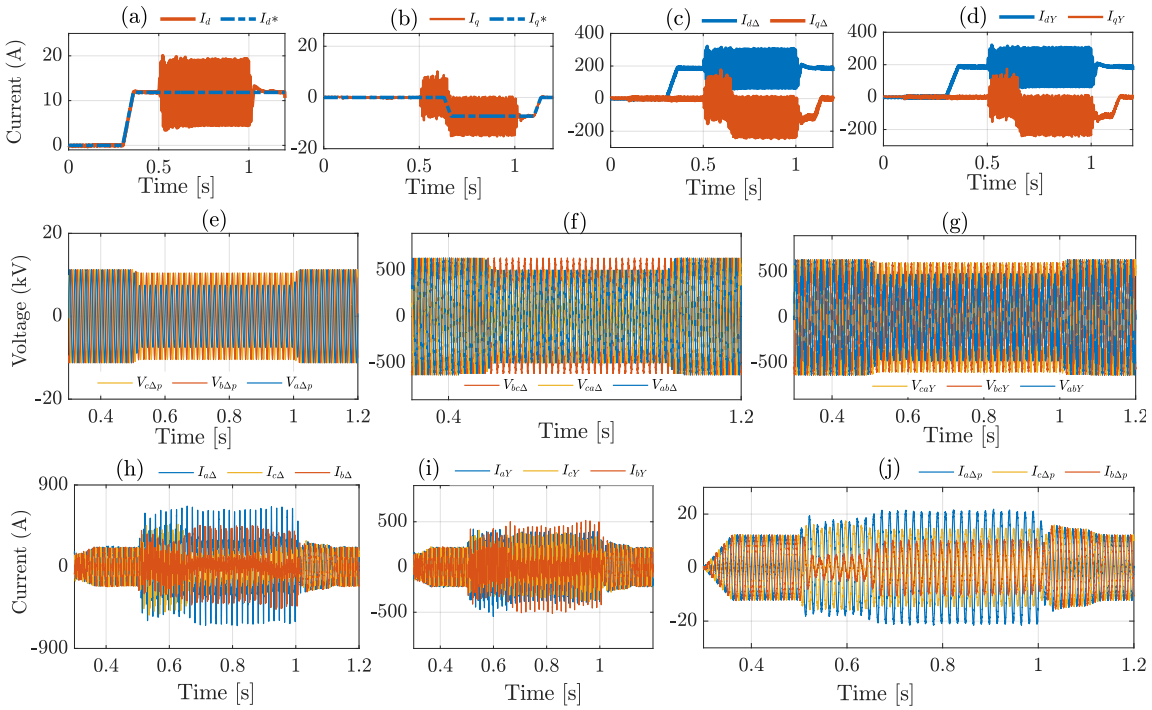

Figure 89 – ZHD converter response under a phase-A single-phase fault: (a)–(b) dq current components; (c) Δ-secondary and (d) Y-secondary dq currents; three-phase voltages at (e) primary, (f) Δ-secondary, and (g) Y-secondary; and three-phase currents at (h) Δ-secondary, (i) Y-secondary, and (j) primary.

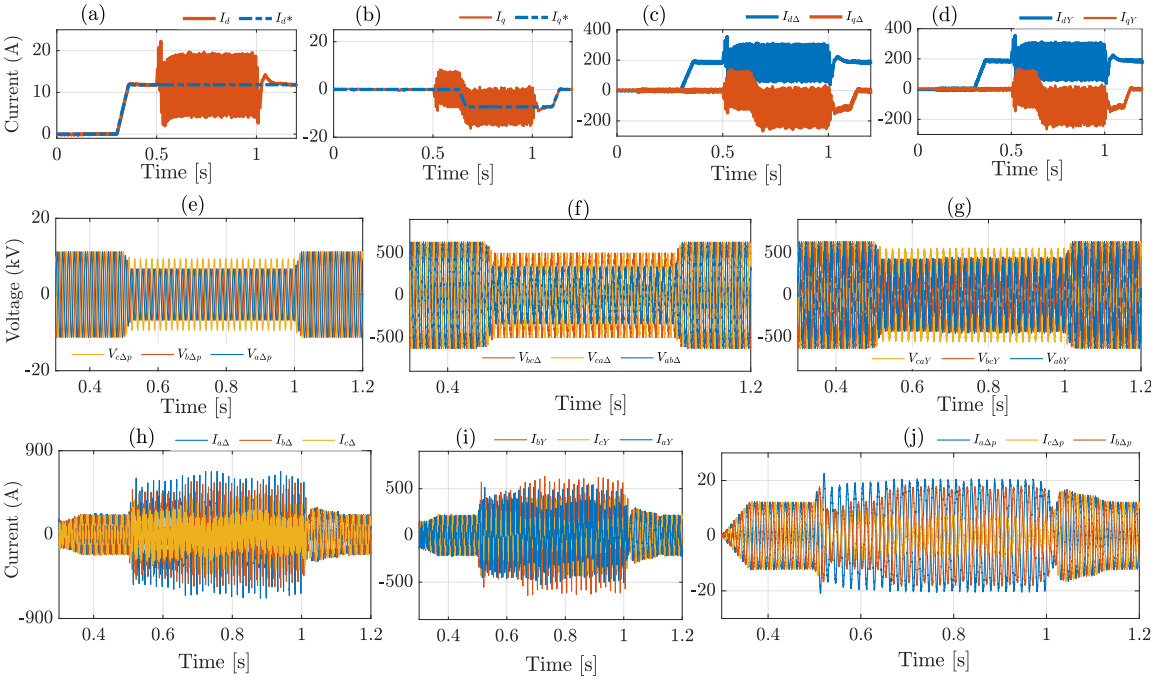

Figure 90 – ZHD converter response under a phase-A–B double-phase asymmetrical fault: (a)–(b) dq current components; (c) Δ-secondary and (d) Y-secondary dq currents; three-phase voltages at (e) primary, (f) Δ-secondary, and (g) Y-secondary; and three-phase currents at (h) Δ-secondary, (i) Y-secondary, and (j) primary.

5.4 ZHD Grid Interactive Control Structure

The present work integrates the grid-connected (grid-following) control structure, as proposed in several studies from the literature (Parreiras, 2020; Parreiras; Justino; Filho, 2015; Alves; Parreiras; Filho, 2019; Almeida; Filho, 2017; Parreiras et al., 2015; Parreiras et al., 2021; Parreiras et al., 2020; Brandão et al., 2022b; Justino; Parreiras; Filho, 2014; Brandão et al., 2022), with the islanded (grid-forming) control approach presented in Chapter 4. This integration enables the ZHD converter to operate as a multifunctional grid-interactive converter for microgrid applications, seamlessly transitioning between grid-connected and islanded modes.

Comparing the command control signals of both current and voltage controls, Fig. 81 and Fig. 46 respectively, it is possible to observe that in the ZHD converter case, the transition between modes can be made only by enabling/disabling the current regulator gains, no need for a change or a additional control structures as required in conventional converters.

In this way, the overall control of the ZHD converter is shown in Fig. 91. The ZHD converter during the grid-connected operation uses the closed-loop current control in the dq rotating reference frame with the synchronizing angle generated by the DDSRF-PLL. During the islanded mode, the microgrid master controller (MGMC), that stays inside of the ZHD, gives a command so that the DDSRF-PLL begins to generate a reference frequency, the current regulator gains k_p and k_i are disabled through k_{pEN} and k_{iEN}, and the voltage reference is directly sent to the SHE PWM modulator by the V_d^* and V_q^* feedforward commands with the disturbance feedforward voltage drop compensation of the estimated ZHD impedance parameters $\hat{R}_{zhd}$ and $\hat{L}_{zhd}$.

The reference voltage commands generated by the control are given by E_d^* and E_q^* considering the turn ratio of the transformer a. The references are utilized to calculate the modulation indexes $m_{\Delta,Y}$ and phase compensation $\delta_{\Delta,Y}$. The modulation signals and the sum of phase compensation and the angle references θ_Y and θ_Δ are compared in the LUTs generating the power switches command signals $\alpha_{1Y}, .., \alpha_{MY}$ and $\alpha_{1\Delta}, .., \alpha_{M\Delta}$ to the VSCs.

5.4.1 Simulation Results

The ZHD Converter based on a battery energy storage system structure (BESS) was assessed based on typical daily load variation and solar power injection scenarios. The microgrid system simulated using the MATLAB/Simulink platform is shown in Fig. 92. The simulation parameters are described in Table 17.

The simulation scenarios considering, black-start, grid-connection and intentional island operations are listed:

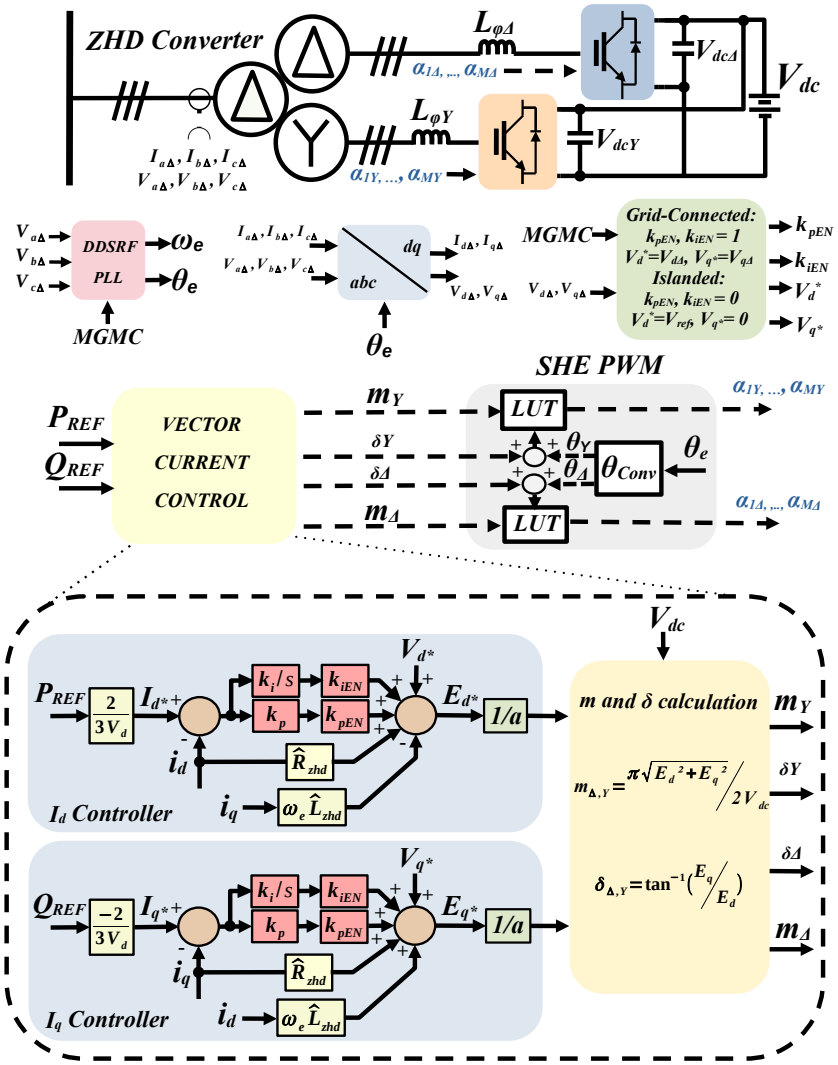

Figure 91 – Control structure of ZHD Grid-Interactive.

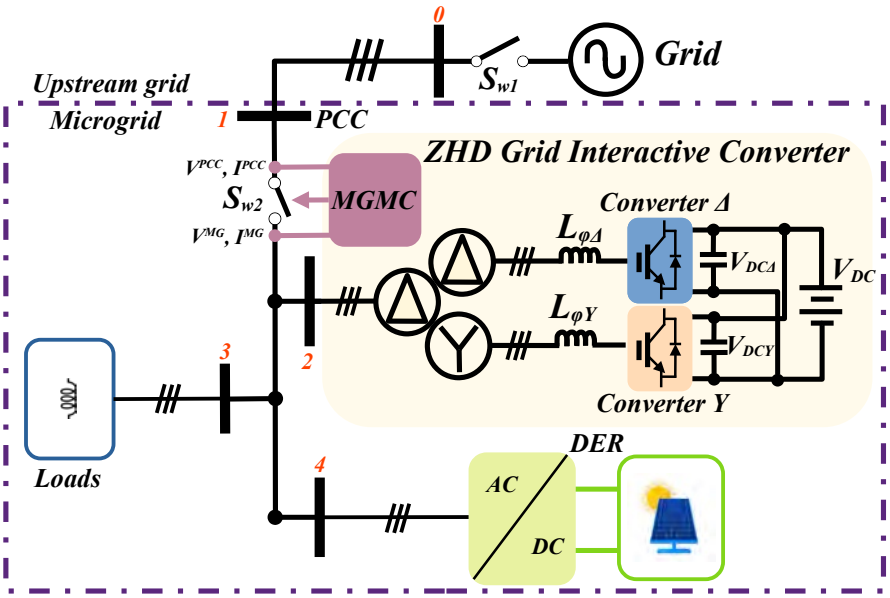

Figure 92 – Generic microgrid with the ZHD as Grid-Interactive converter.

Table 17 – Simulation Parameters

ZHD CONVERTER			
Parameters	**Values**	**Parameters**	**Values**
Rated Power	280 kVA	Frequency	60 Hz
Primary Voltage	13.8 kV	Δ Secondary Voltage	440 V
Winding Connections	Dd0y1	Y Secondary Voltage	440 V
$L_{\phi\Delta}$ and $L_{\phi Y}$ reactors	0.59/0.506 mH	DC link voltage	650 V
THREE-WINDING THREE-PHASE TRANSFORMER - Dd0y1			
Parameters	**Values**	**Parameters**	**Values**
R_m	526.7 $k\Omega$	$R_{s\Delta}$	19.4 $m\Omega$
L_m	534.5 H	$L_{s\Delta}$	3.33 μH
$R_{P\Delta}$	10.5 Ω	R_{sY}	16 $m\Omega$
$L_{P\Delta}$	108.7 mH	L_{sY}	84.26 μH
CONTROLLER PARAMETERS			
Parameters	**Values**	**Parameters**	**Values**
k_p	139.71	k_i	6320
LOAD SCENARIO 1, 2, 3 and 4			
Parameters	**Values**	**Parameters**	**Values**
Active Power (P)	100 kW	Reactive Power (Q)	0 var
Active Power (P)	148 kW	Reactive Power (Q)	36 kvar
Active Power (P)	100 kW	Reactive Power (Q)	0 var
Active Power (P)	196 kW	Reactive Power (Q)	72 kvar
DER SCENARIO 3			
Parameters	**Values**	**Parameters**	**Values**
Active Power (P)	200 kW	Reactive Power (Q)	0 kvar

- t = 0 s $\rightarrow$ (I) $\rightarrow$ Black-start and islanded operation;
- t = 1.55 s $\rightarrow$ (II) $\rightarrow$ Grid-connection and energy time shift service;
- t = 3.1 s $\rightarrow$ (III) $\rightarrow$ Islanded Transition;

Fig. 93 shows the overview results of all the scenarios considering: black start, islanded operation, grid connection, and intentional islanded. Figs. 93 (a) and (b) show the active and reactive power flow, respectively, at PCC during the events. Figs. 93 (c) and (d) show the voltage and current at the ZHD MC converter and at the grid, respectively.

5.4.2 Black-Start and Islanded operation

Considering the islanded operation time event I, Fig. 94 (a) shows the voltage and current of the ZHD MC working as a grid-forming converter. The zoomed view between 0 and 0.15 s shown in (b) shows the ZHD black-start capability, and in (c) and (d) the sinusoidal voltage waveform shape without the necessity of capacitive filters, absorbing

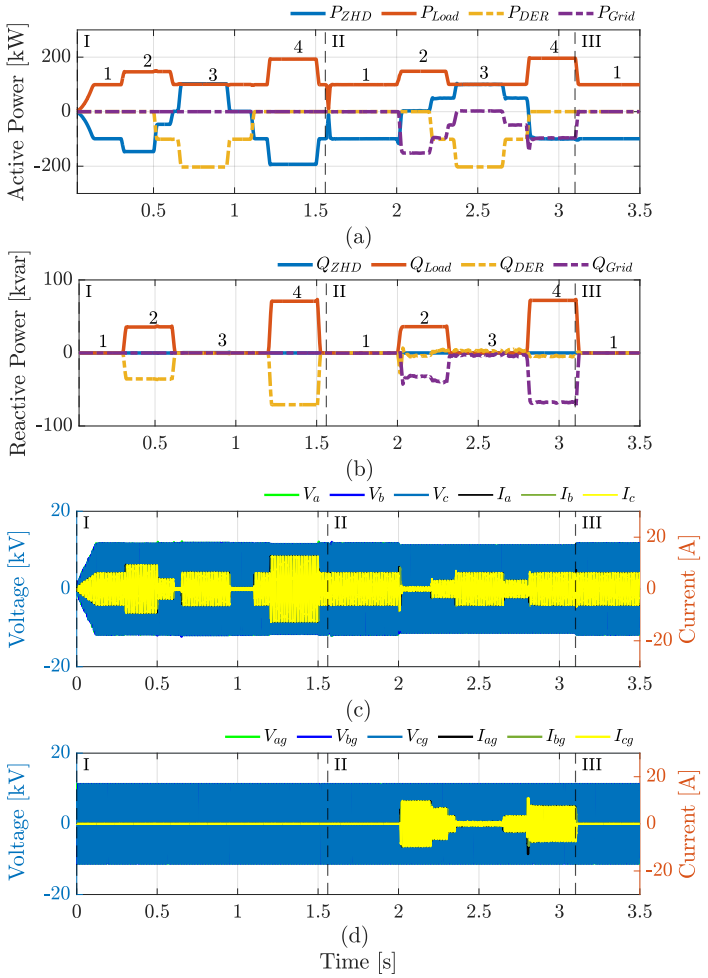

Figure 93 – (a) Active power, (b) Reactive power, (c) Voltage and current at the ZHD converter, (d) Voltage and current at the grid side.

and delivering power in Scenarios 3 and 4, respectively. Fig. 94 (e) shows the ZHD voltage magnitude and frequency regulation capability at PCC, where it is possible to verify that the voltage regulation is within an acceptable range of 5%. The output voltage FFT for all phases is shown in Fig. 94 (f) with a free harmonic range until 50^{th} order, as expected.

5.4.3 Grid-Connection and Islanding Transition

The zoomed view of voltage and current at ZHD converter and grid side even as the magnitude voltage and frequency at PCC of the time events II and III are shown in Fig. 95 (a), (g) and (l), respectively. Still in the islanded mode the converter frequency is changed to 59 Hz in time event II, as can be seen in (b) and (l), in order to start the grid-connection process. The ZHD voltage magnitude and phase are compared with the grid voltage and phase in the MGMC and the connection to the grid occurs as shown in (c) and (h) the zoomed view of the voltage and current waveforms in the ZHD converter and the grid, respectively, by only enabling the current regulator gains k_{pEN} and k_{iEN}, where the ZHD MC converter changes to the grid-following mode, synchronized with the

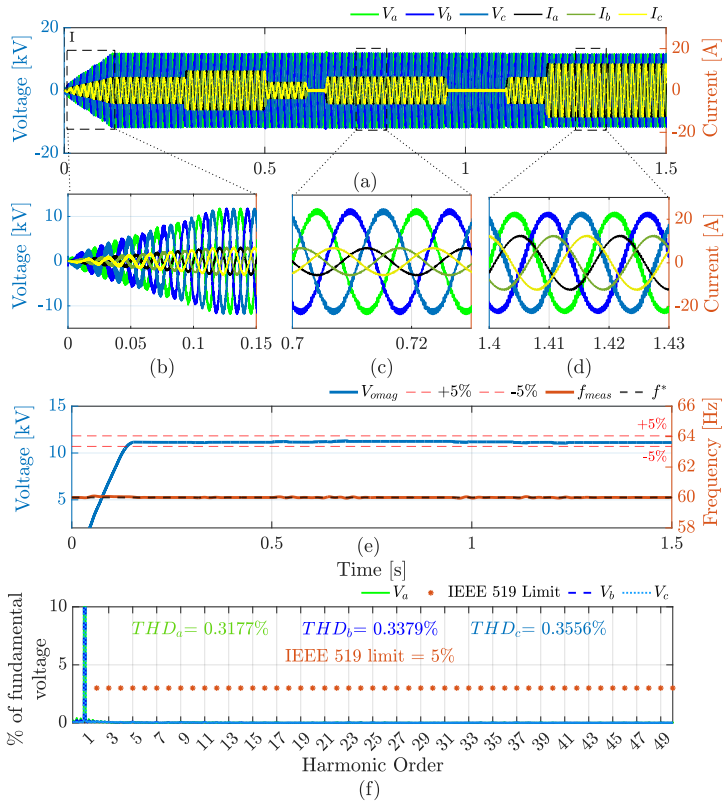

Figure 94 – Islanded operation: (a) Voltage and current at ZHD converter between: (a) 0 and 1.5 s, (b) 0 and 0.15 s, (c) 0.7 and 0.73 s, (d) 1.4 and 1.43 s, (e) voltage and frequency at the PCC and (f) output voltage FFT for all the phases.

grid by DDSRF-PLL, after the signal sent by the MGMC.

The steady-state waveforms of Fig. 95 (d) and (i) show the energy time shift service realized by the ZHD MC converter absorving power in load scenario 3 of high DER generation (Fig. 95 (d)), where the current at the grid is near zero (Fig. 95 (i)), and injecting power in scenario 4 of high load consumption (Fig. 95 (f) and (j)). These waveforms in an analogue way of the islanded case show that the ZHD converter ensures sinusoidal current injection to the MG. The output current FFT shown in (e) shows the sinusoidal current waveform shape without harmonics until the 50^{th} order.Finally, the same Fig. 95 shows in time event III the transition from the grid-connected to the islanded mode. Figs. 95 (f) and (k) show the zoomed views of voltage and current at the ZHD converter and in the grid, respectively, only by disabling the gains of the current regulators k_{pEN} and k_{iEN} after the signal sent by the MGMC with the DDSRF-PLL now generating the reference frequency.

5.4.4 Unintentional Islanded Characterization

It is important to note that the transition dynamics from grid-connected to islanded mode are directly influenced by the islanding detection time, as the converter must maintain stable operation until the grid disconnection is effectively identified. The characterization

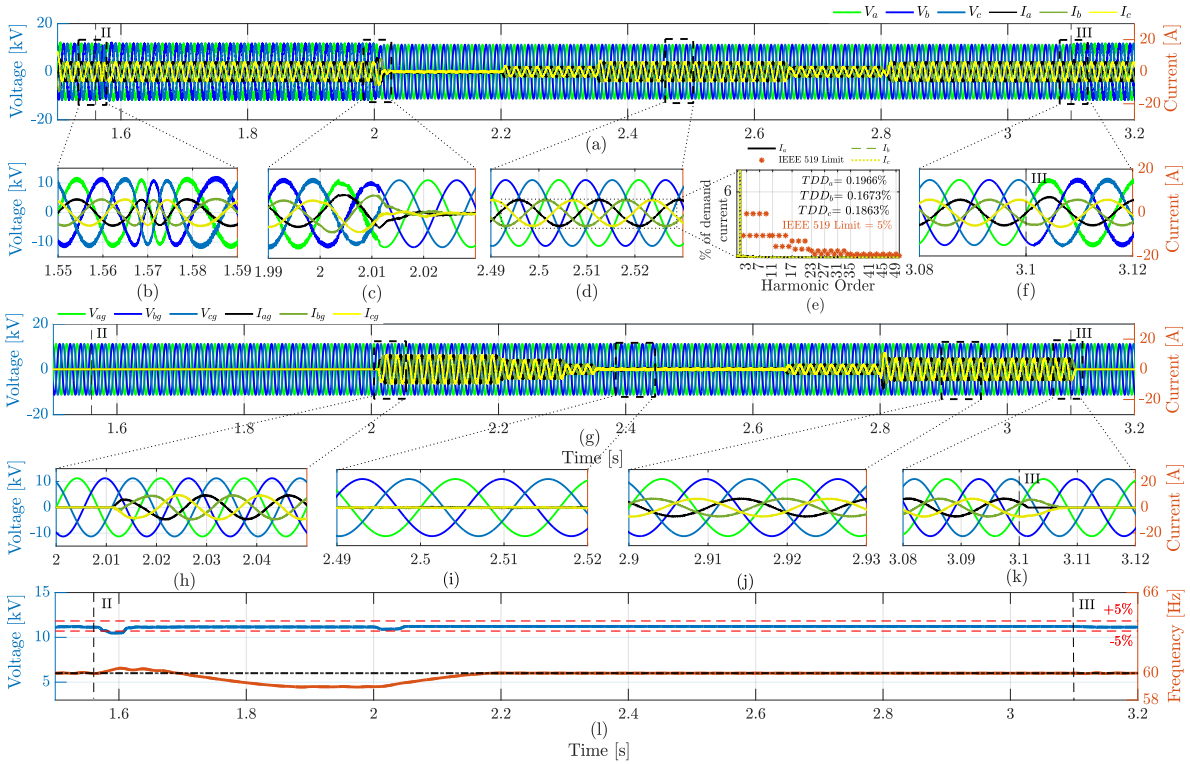

Figure 95 – Voltage and current at ZHD converter between: (a) 1.5 and 3.2 s, (b) 1.55 and 1.59 s, (c) 1.99 and 2.03 s, (d) 2.4 and 2.43 s, (e) output current FFT, (f) 3.08 and 3.12 s, voltage and current at grid side between: (h) 2 and 2.05 s, (i) 2.11 and 2.22 s, (j) 3.05 and 3.12 s, (k) voltage and frequency at PCC.

of unintentional islanding was also performed considering both nominal and faulted grid voltage conditions for the charging and discharging scenarios within the energy time-shift service operation. In all cases, the islanding detection time was defined as five fundamental cycles, representing a realistic and conservative approximation of the average operating time of protection relays during fault conditions (Vukojevic; Lukic, 2020).

5.4.4.1 Converter Response under Rated Grid Voltage Conditions

For the charging scenario under rated grid voltage conditions, Fig. 96 illustrates the transition process from grid-connected to islanded operation. During this transition, a transient response naturally occurs due to the reversal of power flow direction and the dynamic interaction between the converter and the microgrid. Nevertheless, the ZHD converter maintains stable and well-damped voltage and current waveforms, demonstrating effective control performance and smooth decoupling from the grid.

In the discharging scenario under rated grid voltage conditions, Fig. 97 presents the results of the same transition. In this case, the converter exhibits a seamless change from grid-connected to islanded mode, with minimal transient disturbances and fast stabilization of both voltage and current magnitudes. These results confirm the ZHD converter capability to ensure operation and power quality during mode transitions.

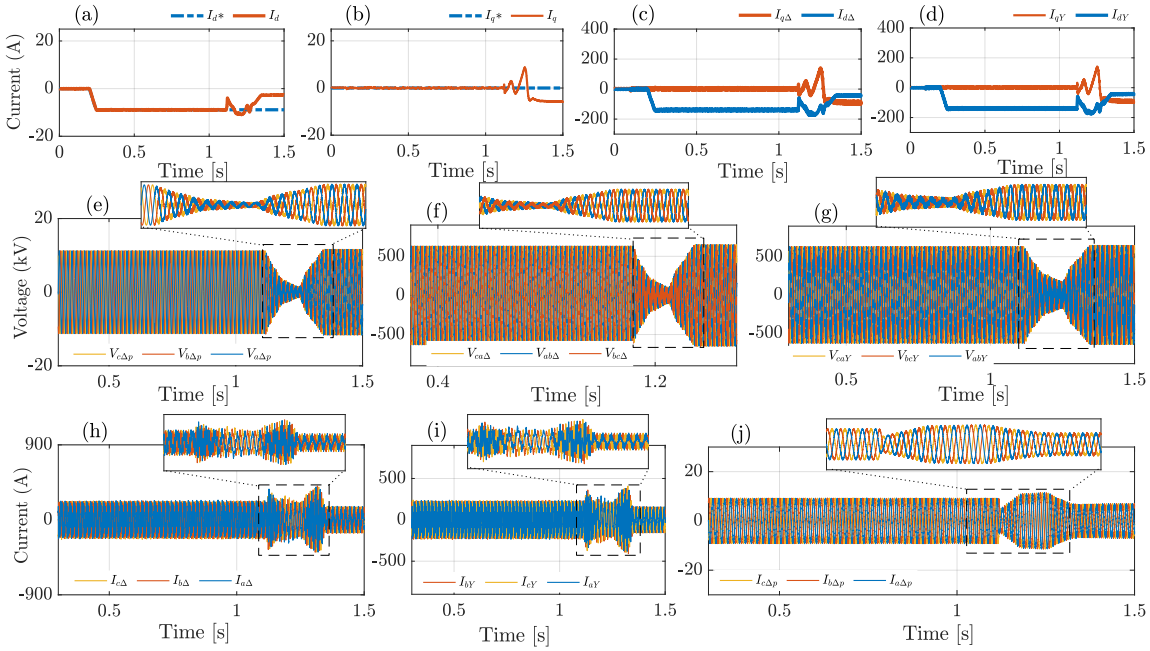

Figure 96 – Transition from grid-connected to islanded mode: (a)–(b) dq current components; (c) Δ-secondary and (d) Y-secondary dq currents under rated voltage charging conditions; three-phase voltages at (e) primary, (f) Δ-secondary, and (g) Y-secondary; and three-phase currents at (h) Δ-secondary, (i) Y-secondary, and (j) primary.

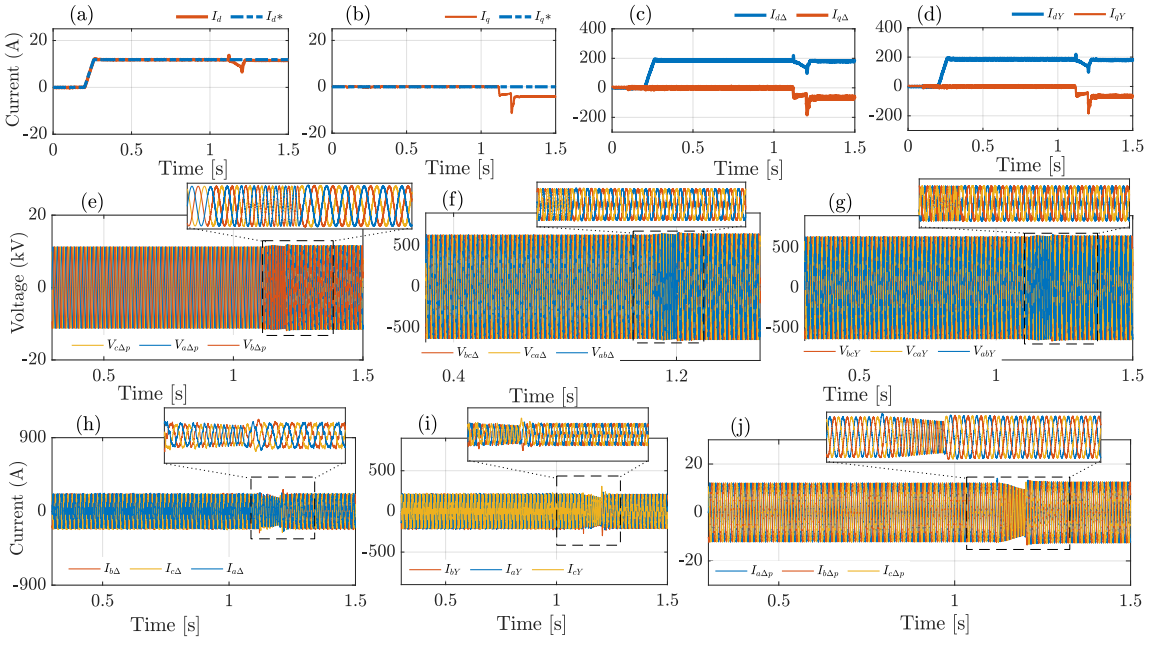

Figure 97 – Transition from grid-connected to islanded mode: (a)–(b) dq current components; (c) Δ-secondary and (d) Y-secondary dq currents under rated voltage discharging conditions; three-phase voltages at (e) primary, (f) Δ-secondary, and (g) Y-secondary; and three-phase currents at (h) Δ-secondary, (i) Y-secondary, and (j) primary.

5.4.4.2 Operation Under Faulted Grid Voltage Conditions

Considering the conditions of faulted grid voltage, the converter must remain connected, providing voltage support as required, and will assume the islanded mode only when the MGMC supervisory control permits.

Figs. 98 show the transition from grid-connected to islanded mode considering a three-phase voltage sag, Figs. 99, and transition from grid-connected to islanded mode considering a single-phase voltage sag and Fig. 103 double-phase voltage sag.

In all the three cases, the converter assumes the voltage support mode injecting reactive power to the grid and after that assumes the island mode where the voltage feedfoward is freezed and in ramp the voltage is established to the MG in islanded mode.

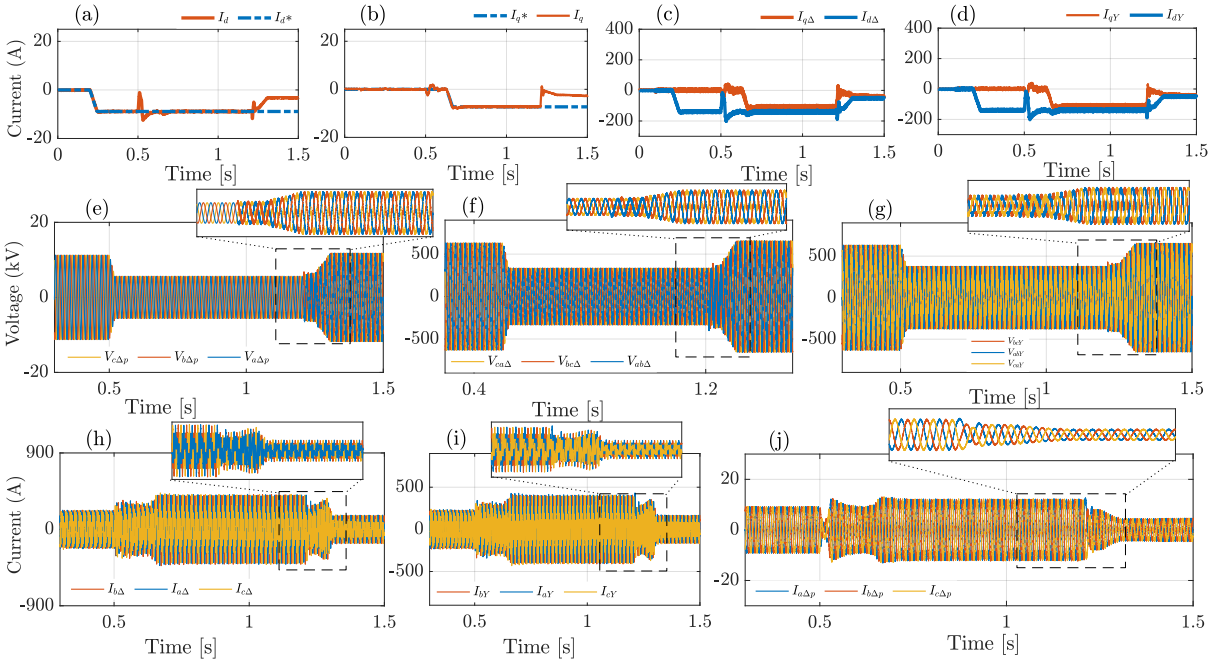

Figure 98 – Transition from grid-connected to islanded mode under a three-phase voltage sag during the charging scenario. The plots show: (a) the I_d component and (b) the I_q component of the converter current; dq-axis current components of the (c) Δ secondary and (d) Y secondary windings; three-phase voltages at the (e) primary, (f) Δ secondary, and (g) Y secondary sides; and three-phase currents at the (h) Δ secondary, (i) Y secondary, and (j) primary sides under the same condition.

The same results considering the discharging process are shown in Fig. 101 for the transition from grid-connected to islanded mode considering a three-phase voltage sag, Fig. 102 transition from grid-connected to islanded mode considering a single-phase voltage sag and Fig. 103, double-phase voltage sag. These results shows the seamless capacity of the ZHD converter transits from grid-connected to island mode even in both charging and discharging process after a fault event.

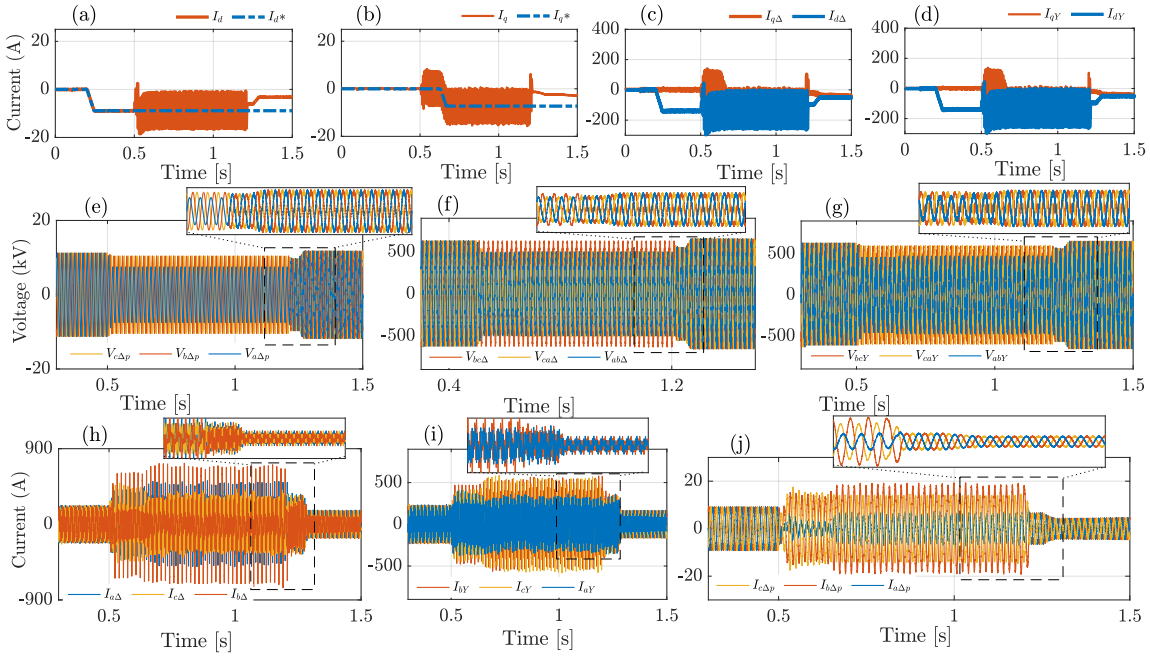

Figure 99 – Transition from grid-connected to islanded mode under a single-phase voltage sag during the charging scenario: (a)–(b) dq current components; (c) Δ-secondary and (d) Y-secondary dq currents; three-phase voltages at (e) primary, (f) Δ-secondary, and (g) Y-secondary; and three-phase currents at (h) Δ-secondary, (i) Y-secondary, and (j) primary.

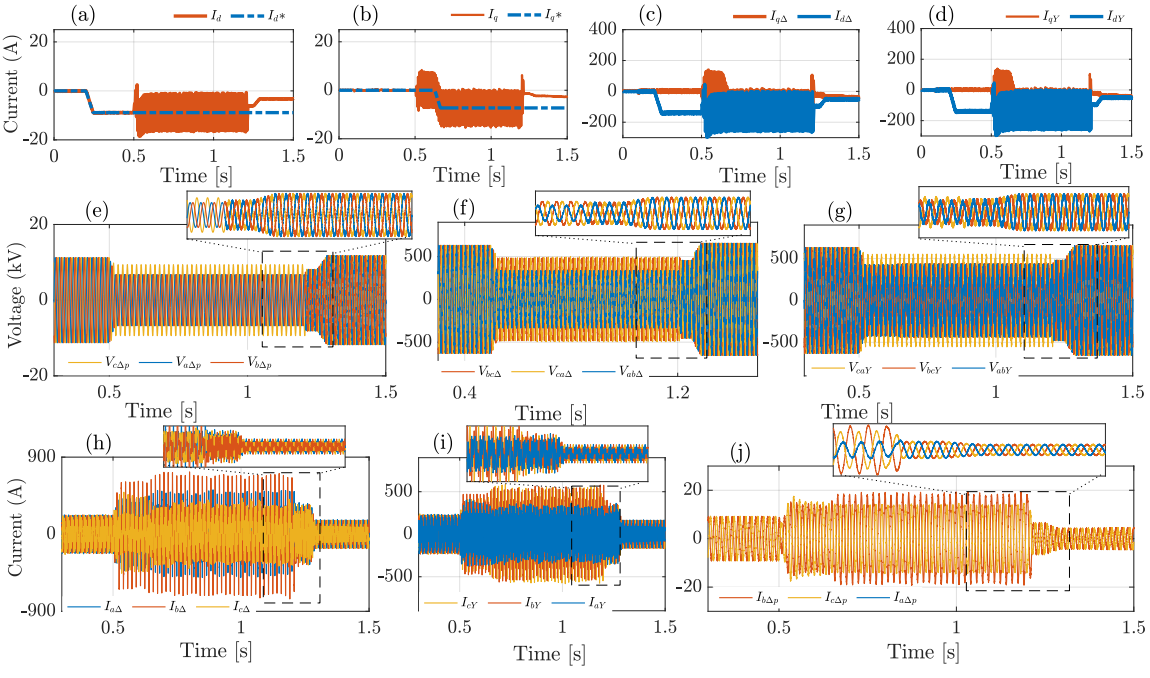

Figure 100 – Transition from grid-connected to islanded mode under a double-phase voltage sag during the charging scenario: (a)–(b) dq current components; (c) Δ-secondary and (d) Y-secondary dq currents; three-phase voltages at (e) primary, (f) Δ-secondary, and (g) Y-secondary; and three-phase currents at (h) Δ-secondary, (i) Y-secondary, and (j) primary.

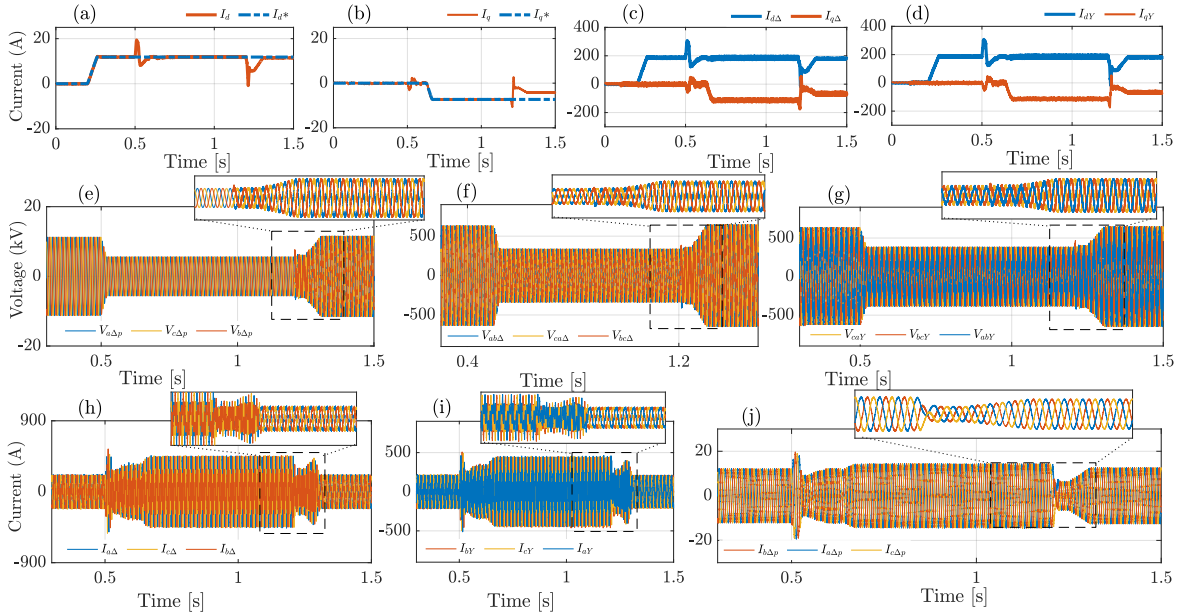

Figure 101 – Transition from grid-connected to islanded mode under a three-phase voltage sag during the discharging scenario: (a)–(b) dq current components; (c) Δ-secondary and (d) Y-secondary dq currents; three-phase voltages at (e) primary, (f) Δ-secondary, and (g) Y-secondary; and three-phase currents at (h) Δ-secondary, (i) Y-secondary, and (j) primary.

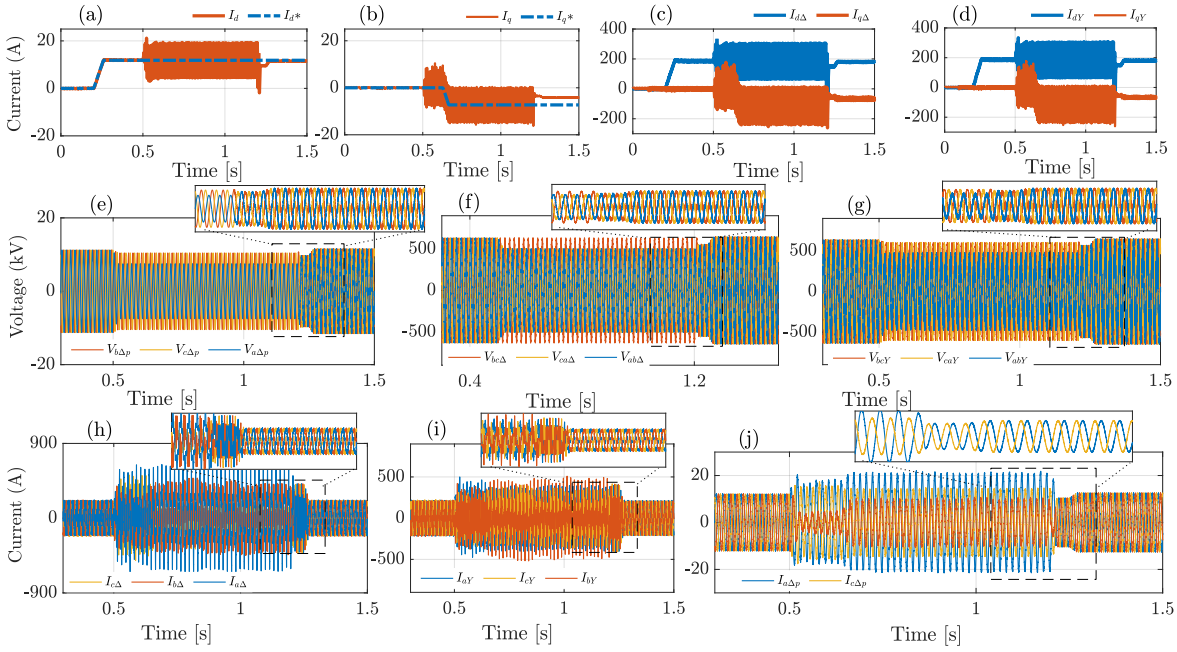

Figure 102 – Transition from grid-connected to islanded mode under a single-phase voltage sag during the discharging scenario: (a)–(b) dq current components; (c) Δ-secondary and (d) Y-secondary dq currents; three-phase voltages at (e) primary, (f) Δ-secondary, and (g) Y-secondary; and three-phase currents at (h) Δ-secondary, (i) Y-secondary, and (j) primary.

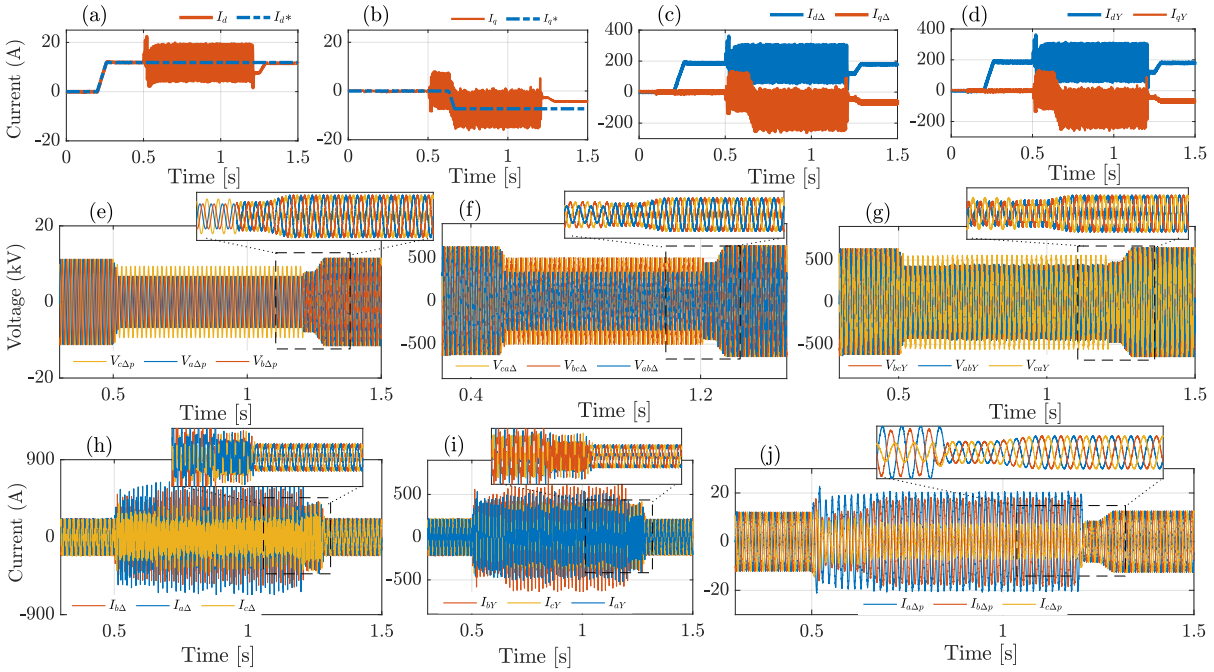

Figure 103 – Transition from grid-connected to islanded mode under a double-phase voltage sag in the discharging scenario: (a)–(b) dq current components; (c) Δ-secondary and (d) Y-secondary dq currents; three-phase voltages at (e) primary, (f) Δ-secondary, and (g) Y-secondary; and three-phase currents at (h) Δ-secondary, (i) Y-secondary, and (j) primary.

5.5 Hardware-in-the-loop Results

The ZHD MC converter with the parameters described in Table 17 was implemented on a real-time simulation platform to test and validate the proposed ZHD control hardware operating in both grid-connected and islanded operation modes.

Fig. 104 shows the real controller connected to the Hardware-in-the-Loop (HIL) test bench. The controller consists of a Texas Instruments TMS320F28335 Digital Signal Processor (DSP) responsible for the converter control and an Field-Programmable Gate Array (FPGA) model MAX 10 from Intel operating with sufficiently high sampling frequency (250 kHz) storing the switching angles and handling with the SHE PWM based on the modulation rates sent by the DSP. Parallel communication is performed between the DSP and the FPGA, ensuring a high data exchange rate between the devices.

5.5.1 Black-Start, Grid-connection and Intentional Island

Taking into account a capacitive load of 50 kVA (PF = 0.9) and a resistive load of 130 kW connected at the output of the ZHD converter, Fig. 105 shows the black start capability of the converter.

Fig. 106 (a) shows the ZHD MC converter transiting from grid-connected to islanded

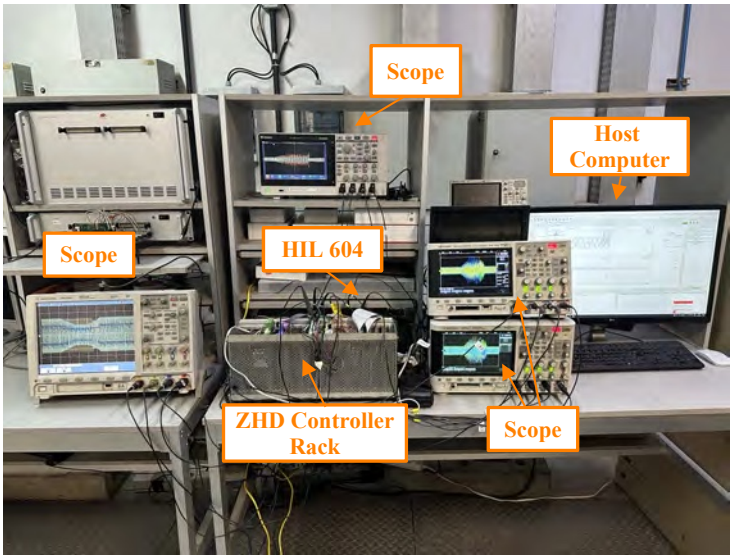

Figure 104 – Structure of tests and validation in Hardware-in-the-Loop.

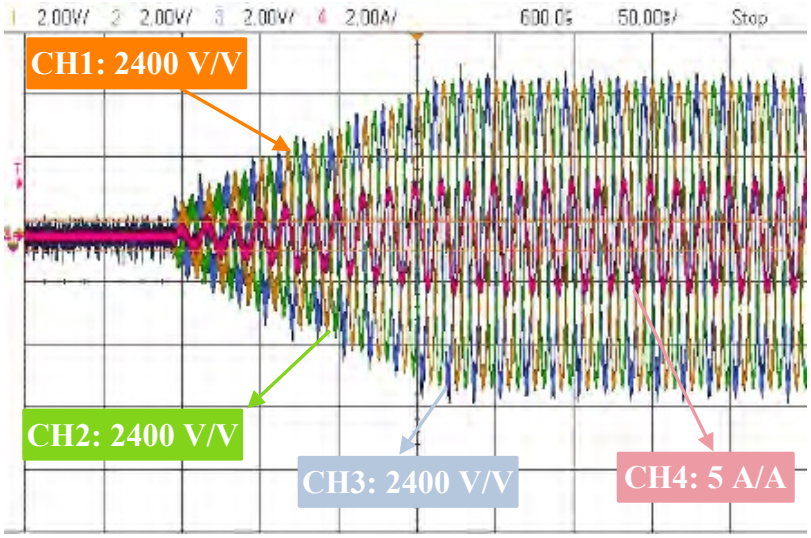

Figure 105 – ZHD converter black-start capability: phase A (CH1), B (CH2), and C (CH3) output voltages and phase A output current (CH4).

mode by only disabling the current regulator gains, the zoomed view of the ZHD current waveform in Fig. 106 (b) shows a current harmonic FFT practically a sinusoidal current waveform. Finally, Fig. 106 (c) shows the islanded to grid-connected mode transition, only by enabling the current regulator gains and in (d) the islanded mode zoomed view showing the converter delivering a practically sinusoidal voltage waveform.

5.5.2 Performance Under Symmetrical and Asymmetrical Voltages Sags

The behavior of the ZHD converter under symmetrical and asymmetrical voltage sags was assessed for both charging and discharging operating modes, considering a grid voltage drop of 20%. Figs. 107 and 108 illustrate the three-phase voltage sag results,

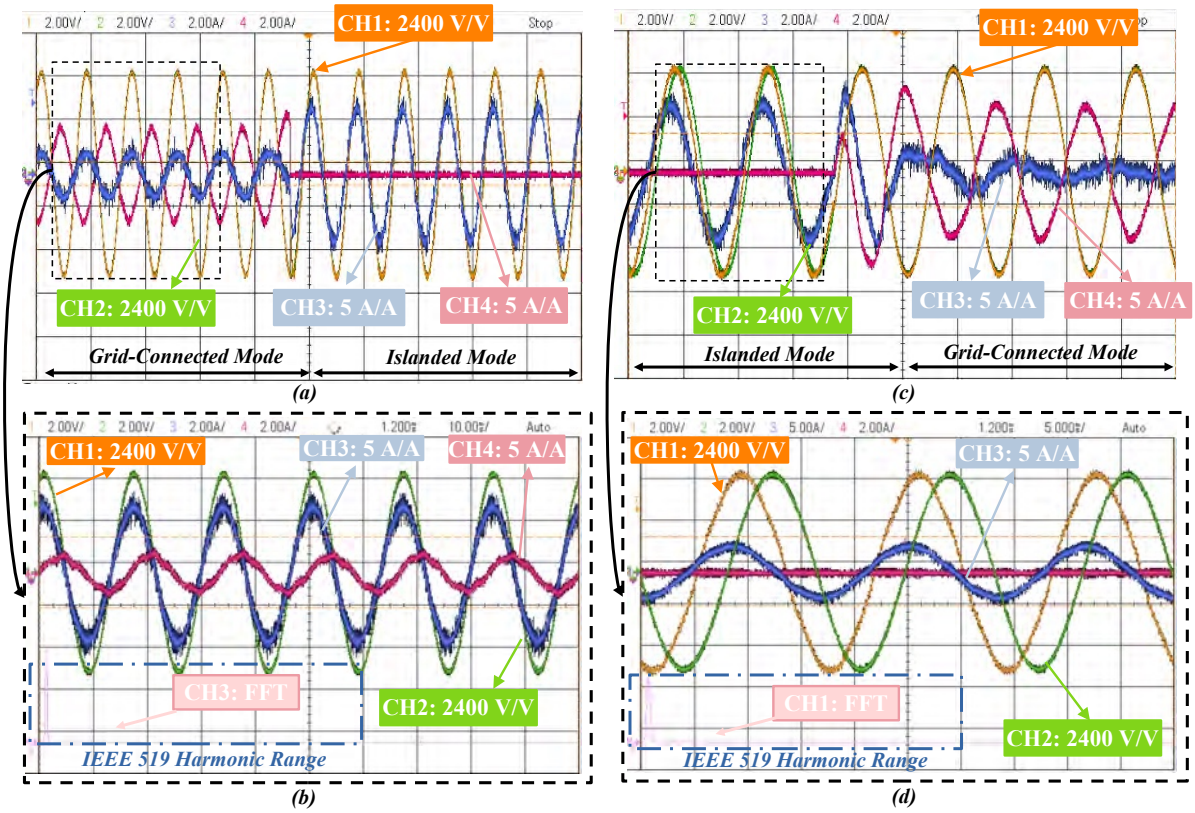

Figure 106 – (a) Intentional Islanded, (b) zoomed view of the islanded case, (c) grid-Connection, and (d) zoomed view of the grid-connection mode: ZHD converter phase A voltage (CH1), phase A grid voltage (CH2), ZHD phase A current (CH3) and phase A load current (CH4).

while Figs. 109 and 110 correspond to the single-phase case, and Figs. 111 and 112 to the double-phase case considering of 44% of reactive power injection (recommended by the IEEE 1547 standard).

In all cases, the converter successfully withstood the voltage sags while supporting the grid through reactive power injection. However, during these events, the harmonic cancellation deteriorated, as perfect cancellation cannot be achieved in practice.The reduction of the modulation index required to maintain current control leads to an increase in harmonic distortion, predominantly the non-eliminated harmonics of 5th and 7th orders associated with the applied SHE-PWM angle set, as shown in Figs. 32. Nevertheless, this effect does not compromise power quality, as it occurs only for a short duration.

5.5.3 Non-intentional Island: Island Occurrence After Voltages Sags

Under the same voltage sag scenarios, the islanding capability of the converter following a grid fault was also evaluated, considering a grid voltage drop of 50%. Figures 113 and 114 present the results for the three-phase voltage sag, while Figs. 115 and 116 correspond to the single-phase case, and Figs. 117 and 118 to the double-phase case, each followed by the islanding event. These results demonstrate the seamless islanding capability

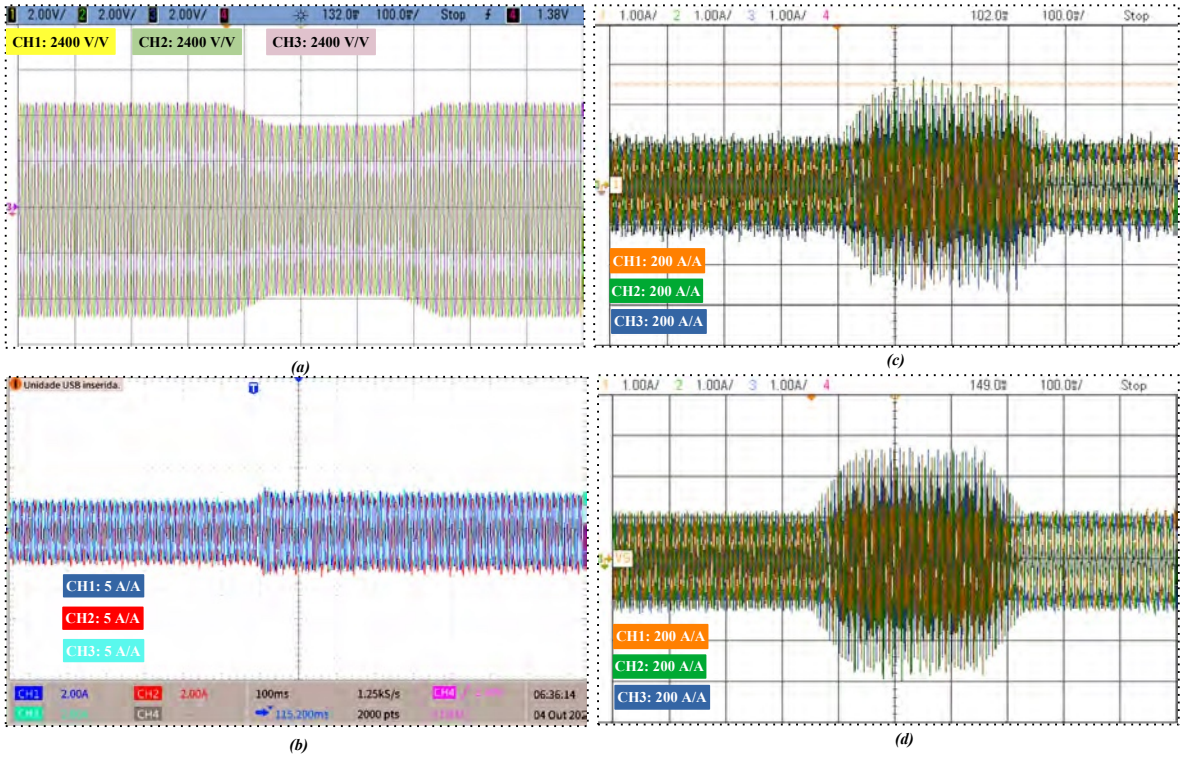

Figure 107 – Three-phase voltage sag under discharging operation: (a) Primary voltages; (b) Primary currents; (c) Delta secondary currents and (d) Star secondary currents.

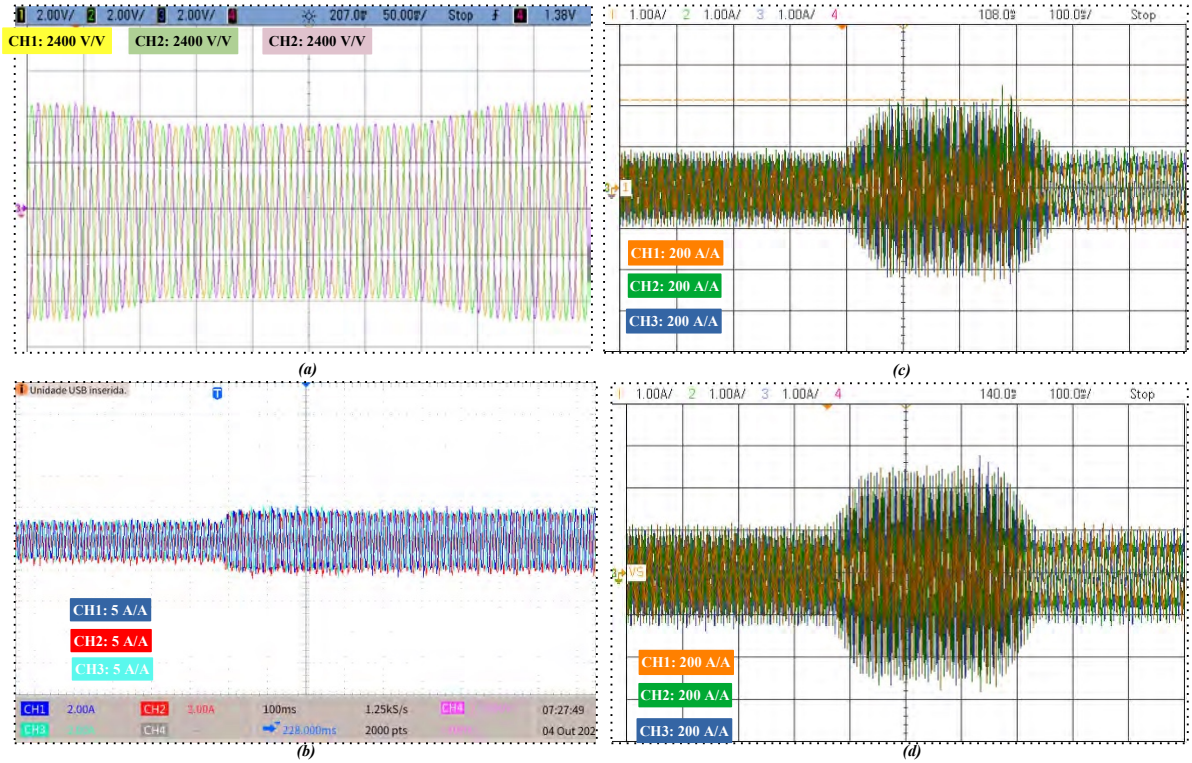

Figure 108 – Three-phase voltage sag under charging operation: (a) Primary voltages; (b) Primary currents; (c) Delta secondary currents and (d) Star secondary currents.

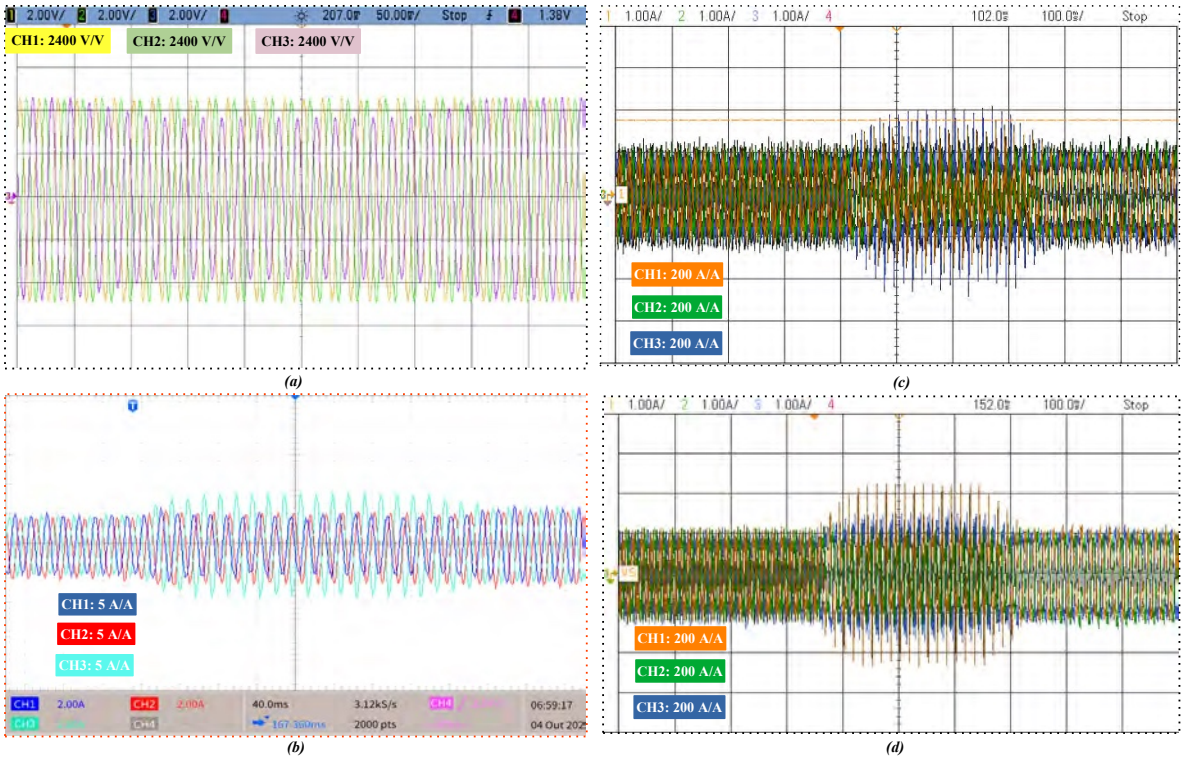

Figure 109 – Single-phase voltage sag under discharging operation: (a) Primary voltages; (b) Primary currents; (c) Delta secondary currents and (d) Star secondary currents.

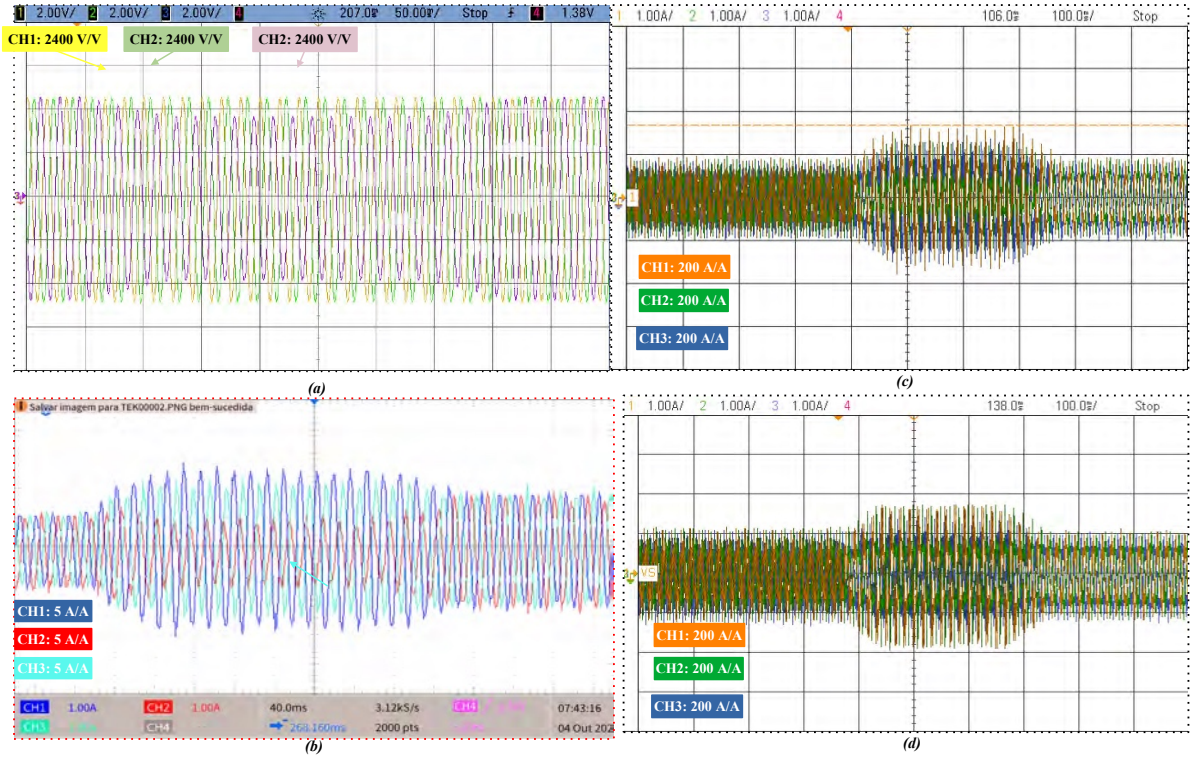

Figure 110 – Single-phase voltage sag under charging operation: (a) Primary voltages; (b) Primary currents; (c) Delta secondary currents and (d) Star secondary currents.

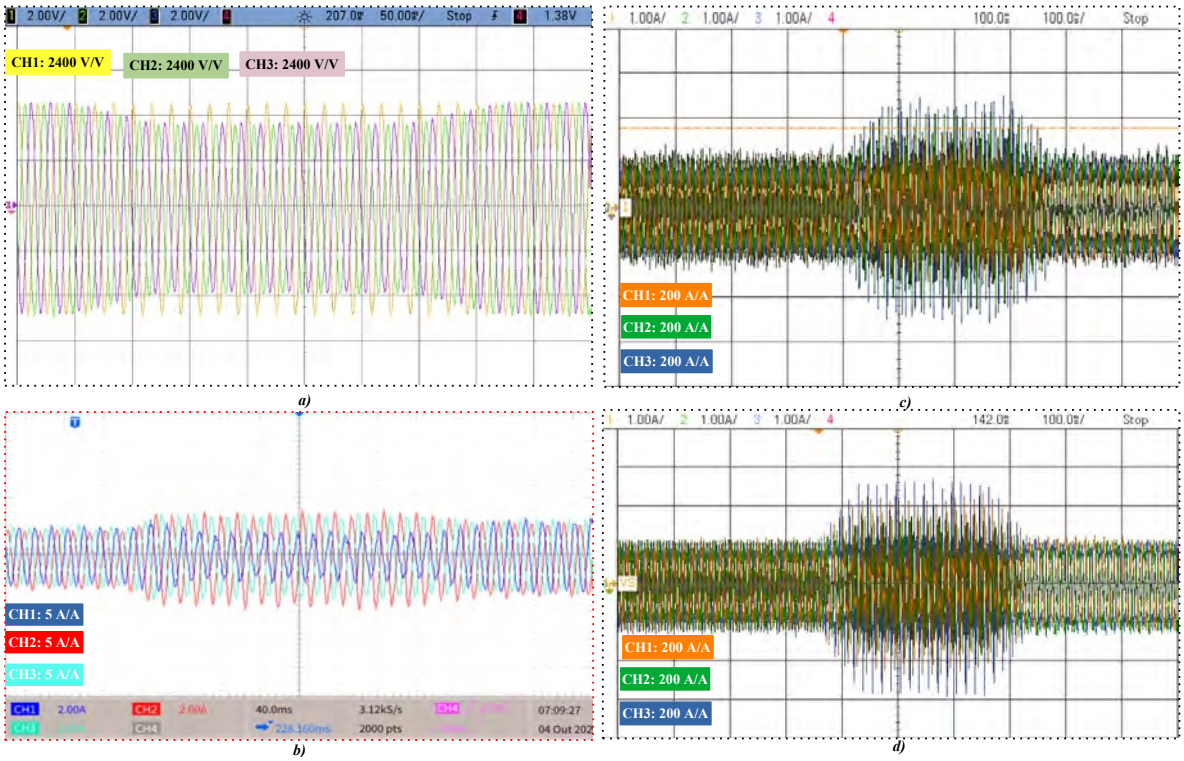

Figure 111 – Double-phase voltage sag under discharging operation: (a) Primary voltages; (b) Primary currents; (c) Delta secondary currents and (d) Star secondary currents.

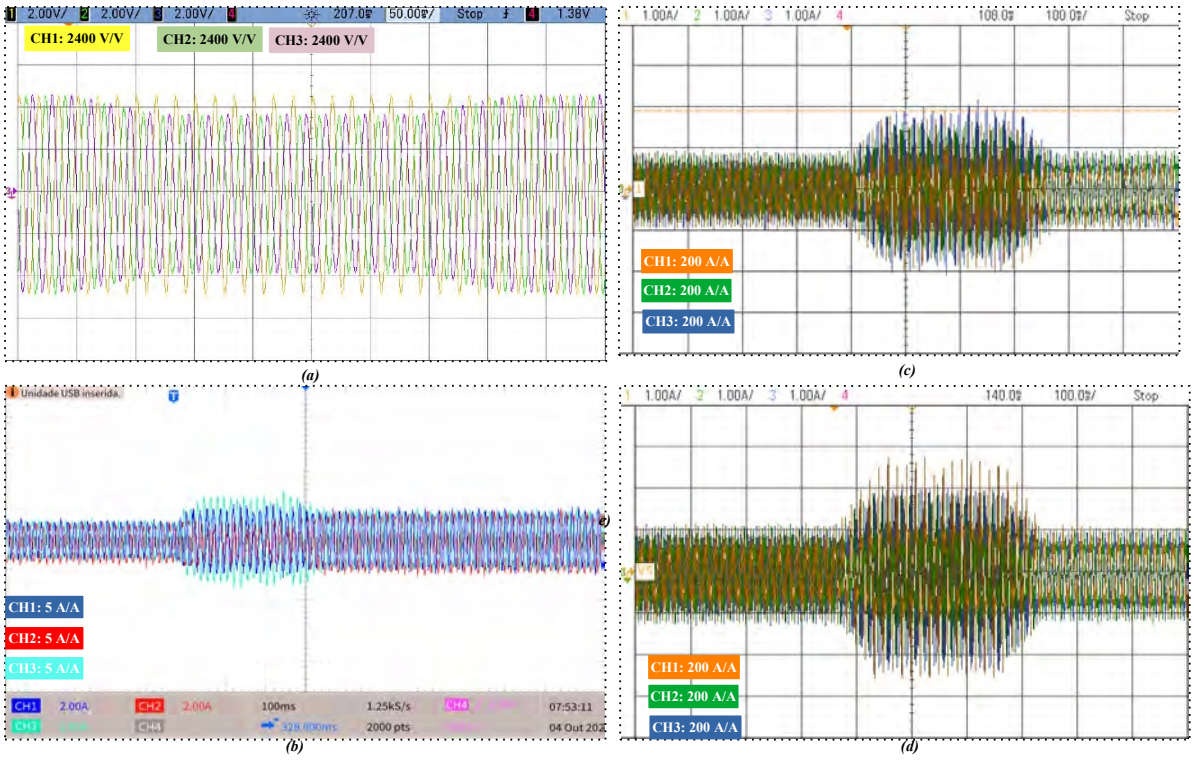

Figure 112 – Double-phase voltage sag under charging operation: (a) Primary voltages; (b) Primary currents; (c) Delta secondary and (d) Star secondary currents.

of the ZHD converter after a voltage fault occurrence. In all cases, the converter remained connected and continued supporting the grid during the fault. However, once the MGMC commands the transition to islanded operation, the current control voltage feedforward is frozen and the current controller gains are disabled. After a few cycles, the voltage is restored to its nominal value under islanded conditions.

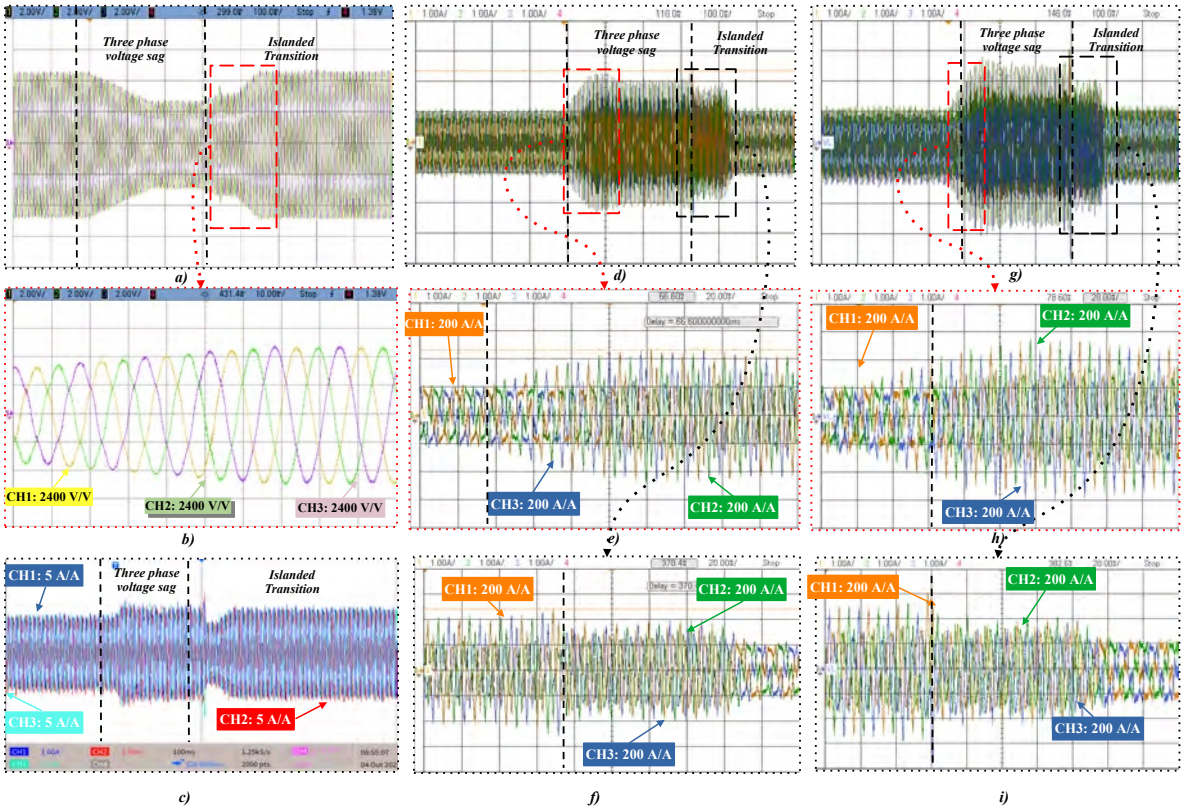

Figure 113 – Three-phase voltage sag under discharging operation followed by island event: (a) Primary voltages; (b) Primary currents; (c) Zoomed view of primary currents; (d) Delta secondary currents with zoomed views in (e) and (f); (g) Star secondary currents with zoomed views in (h) and (i).

5.5.4 Unintentional Islanding: Island occurrence under Unexpected Disconnection

The islanding case caused by an unexpected circuit breaker opening was also evaluated. Figures 119, 120, and 121 present the results for discharging, zero power exchange, and charging conditions, respectively, considering a detection and transition time of five fundamental cycles (representative of a typical protection relay response). The results demonstrate that, even under these conditions, the transition occurs in a seamless manner.

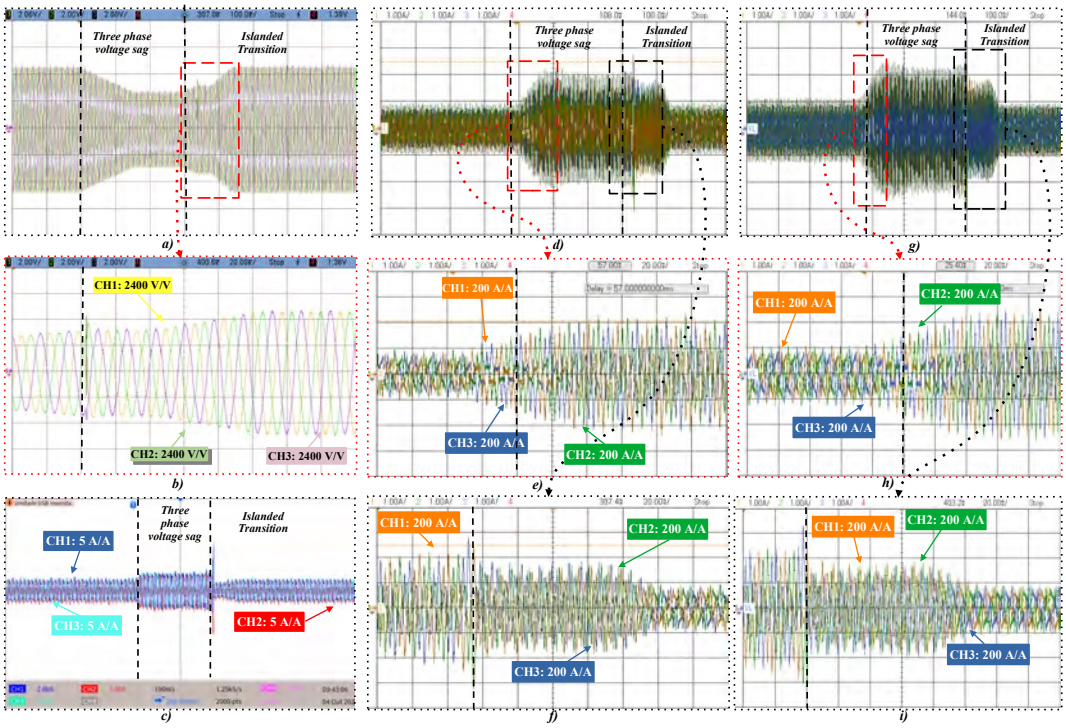

Figure 114 – Three-phase voltage sag under charging operation followed by island event: (a) Primary voltages; (b) Primary currents; (c) Zoomed view of primary currents; (d) Delta secondary currents with zoomed views in (e) and (f); (g) Star secondary currents with zoomed views in (h) and (i).

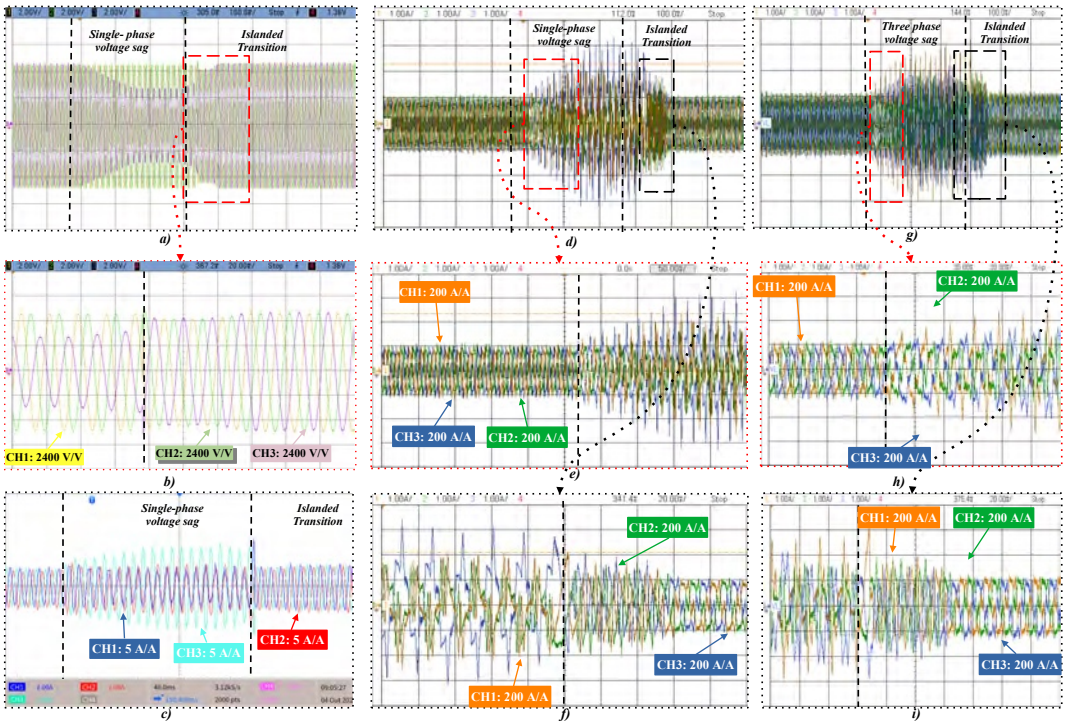

Figure 115 – Single-phase voltage sag under discharging operation followed by island event: (a) Primary voltages; (b) Primary currents; (c) Zoomed view of primary currents; (d) Delta secondary currents with zoomed views in (e) and (f); (g) Star secondary currents with zoomed views in (h) and (i).

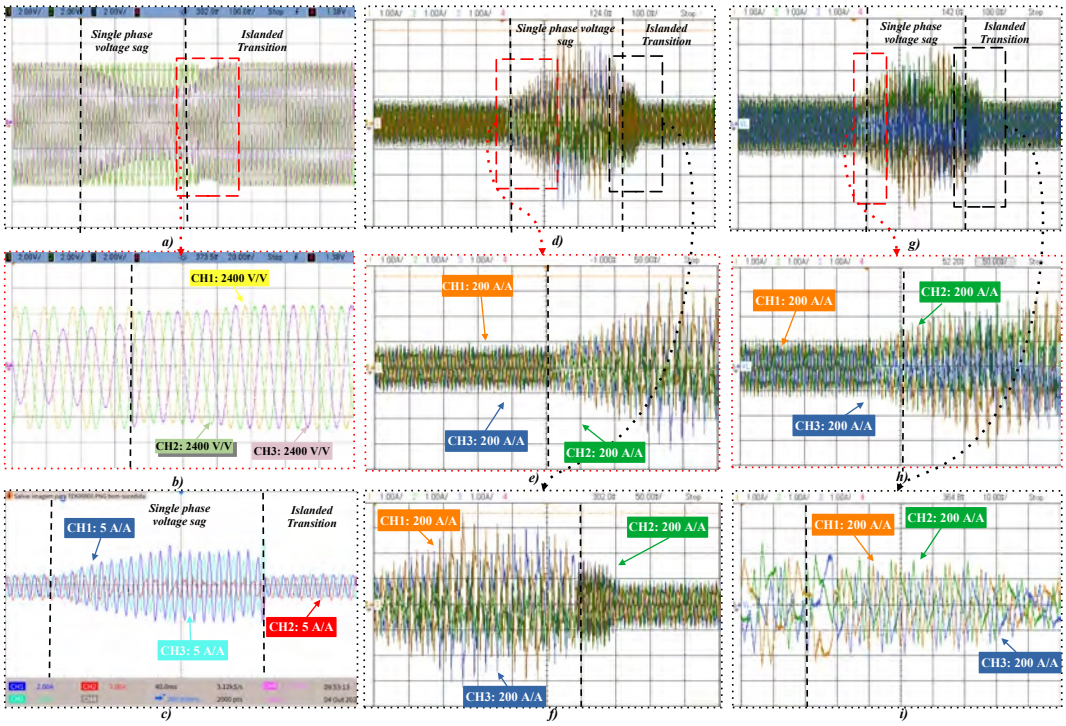

Figure 116 – Single-phase voltage sag under charging operation followed by island event: (a) Primary voltages; (b) Primary currents; (c) Zoomed view of primary currents; (d) Delta secondary currents with zoomed views in (e) and (f); (g) Star secondary currents with zoomed in (h) and (i).

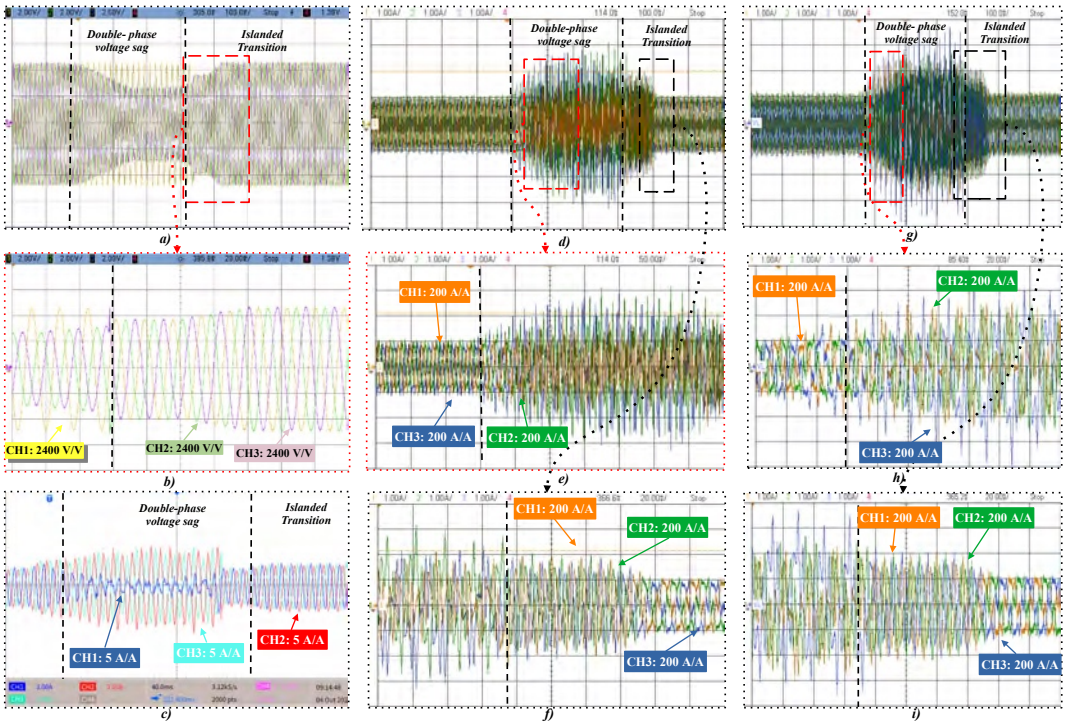

Figure 117 – Double-phase voltage sag under discharging operation followed by island event: (a) Primary voltages; (b) Primary currents; (c) Zoomed view of primary currents; (d) Delta secondary currents with zoomed views in (e) and (f); (g) Star secondary currents with zoomed views in (h) and (i).

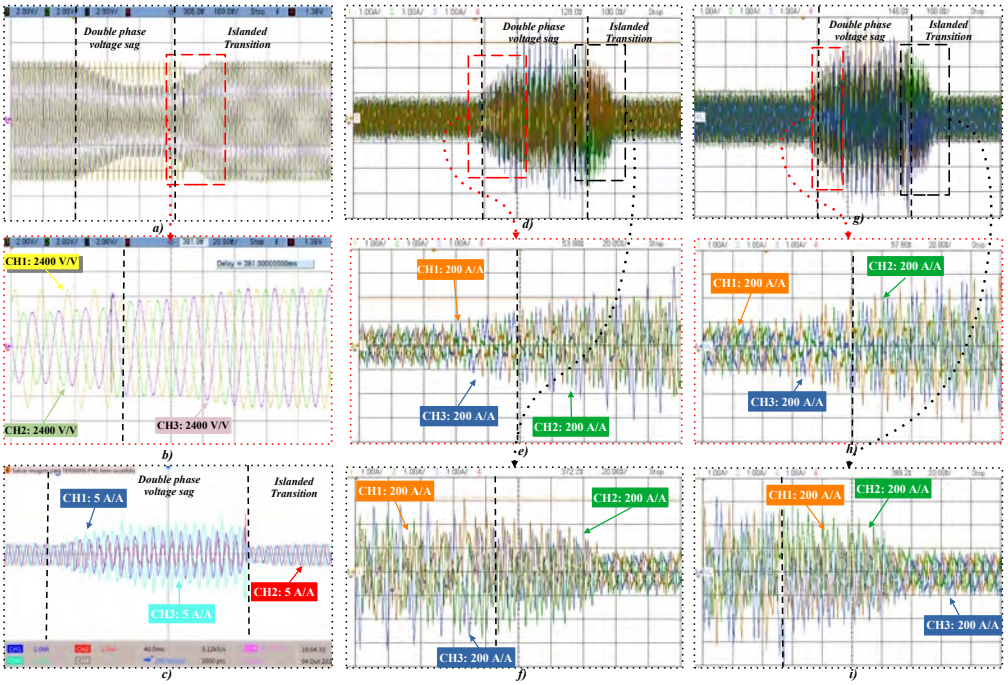

Figure 118 – Double-phase voltage sag under charging operation followed by island event: (a) Primary voltages; (b) Primary currents; (c) Zoomed view of primary currents; (d) Delta secondary currents with zoomed views in (e) and (f); (g) Star secondary currents with zoomed views in (h) and (i).

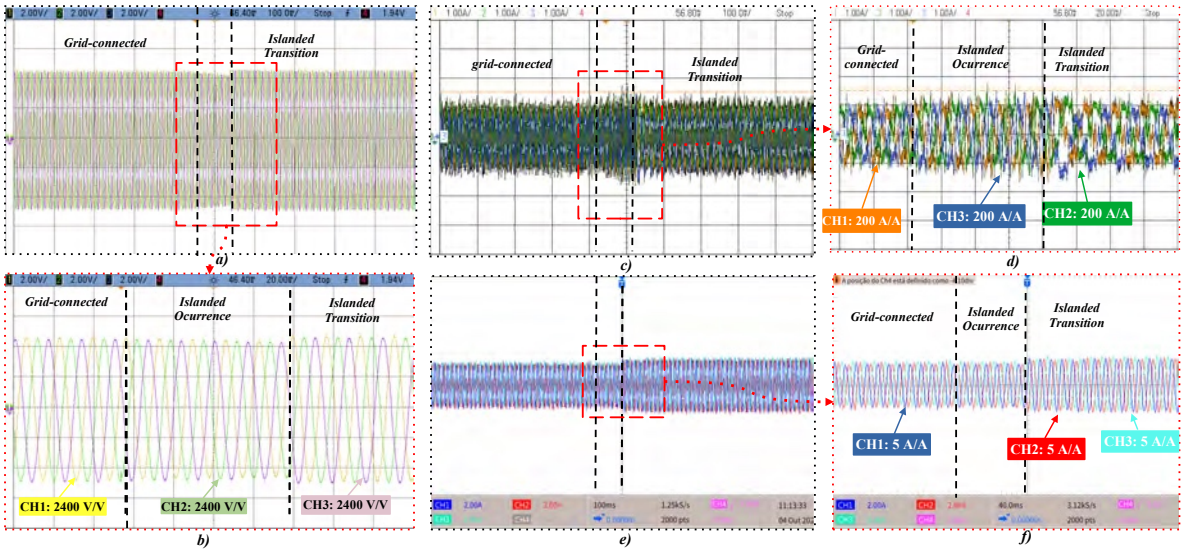

Figure 119 – Islanded event characterization during an unexpected islanding condition while discharging: (a) Primary voltages and (b) their zoomed view; (c) Secondary currents and (d) their zoomed view; (e) Primary current and its zoomed view in (f).

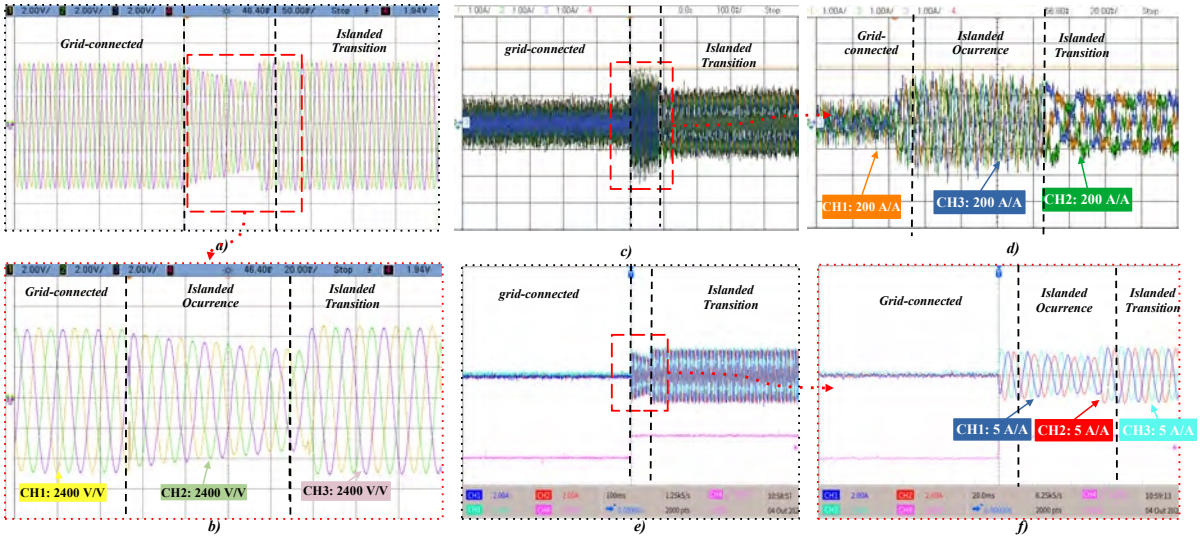

Figure 120 – Islanded event characterization during an unexpected islanding condition with zero exchange condition: (a) Primary voltages and (b) their zoomed view; (c) Secondary currents and (d) their zoomed view; (e) Primary current and its zoomed view in (f).

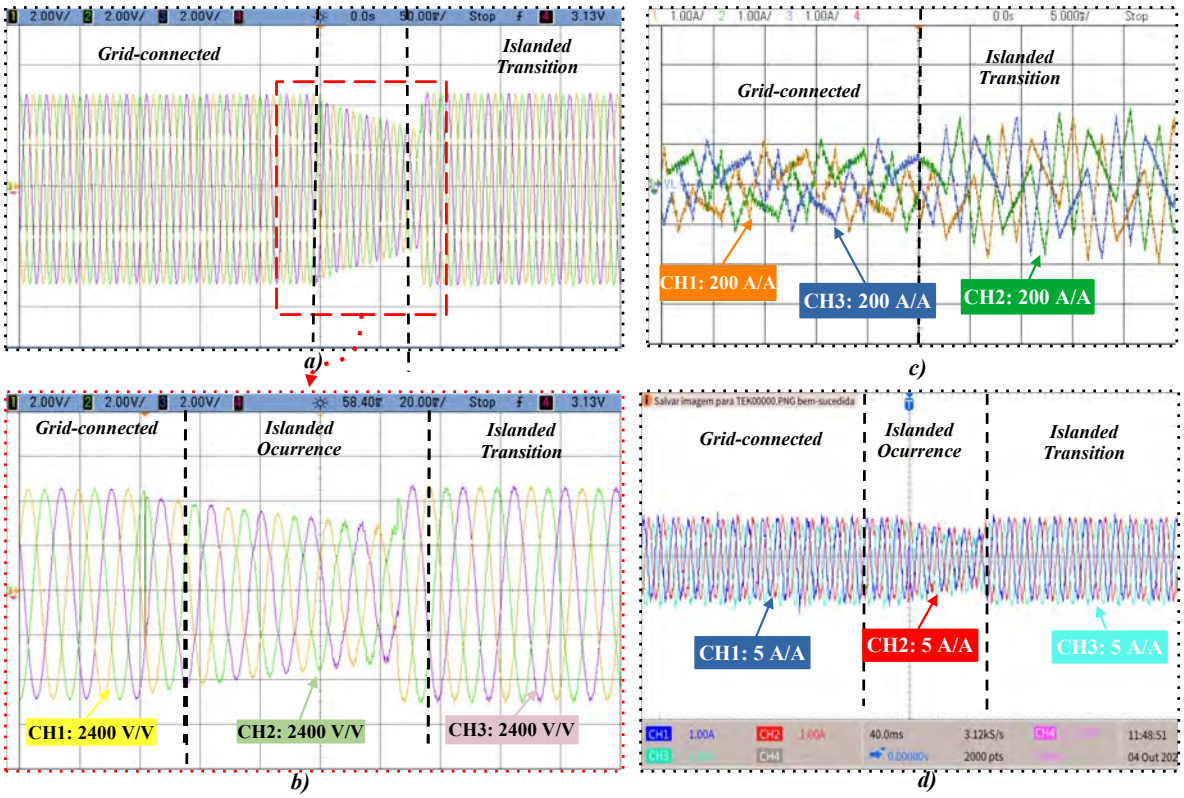

Figure 121 – Islanded event characterization during an unexpected islanding condition while charging: (a) Primary voltages and (b) their zoomed view; (c) Secondary currents and (d) Primary current.

5.6 Conclusions

The Zero Harmonic Distortion (ZHD) converter represents a notable advancement in master converter design for medium-voltage microgrids, delivering high-quality sinusoidal waveforms and reliable performance without the need for capacitive filtering. Its simplified control strategy—eliminating the voltage closed-loop and relying solely on current control during grid-connected operation—ensures seamless transitions between grid-connected and islanded modes. The converter's capability to maintain stability and power quality during these transitions highlights its suitability for resilient microgrid operation. The effectiveness of the ZHD converter has been validated through simulation and hardware-in-the-loop results, demonstrating its strong potential for robust and efficient integration into medium-voltage microgrid systems.

6 Zero Harmonic Distortion Grid-Connected Grid-Forming Converter: A Battery Energy Storage System in Medium Voltage Power Systems Applications

This chapter proposes the Zero Harmonic Distortion (ZHD) converter as a grid-connected grid-forming (GFM) converter, owing to its inherent sinusoidal voltage characteristic achieved without the use of capacitive filters, its low component count, and its implementation based on off-the-shelf power circuitry. The converter employs a simple open-loop control structure, which avoids potential control interactions and resonances in grid-connected operation. Simulation and hardware-in-the-loop (HIL) results demonstrate the ZHD converter capability to operate as a grid-connected voltage source without relying on internal closed control loops, functioning effectively in both voltage and reactive power modes. These results highlight the ZHD converter as a promising alternative for future grid-forming battery energy storage systems (BESS) in medium-voltage applications.

6.1 Introduction

The increase of renewable energy resources interfaced by voltage source converters (VSCs) has stimulated considered interest in grid-forming (GFM) control (Matevosyan et al., 2019; Lasseter; Chen; Pattabiraman, 2020b; Ndreko; Rüberg; Winter, 2020). Differently from grid-following (GFL) control that handles VSCs as a current source depended of the grid voltage, the GFM-VSC is controlled as a voltage source behind an impedance, and its stable operation does not depend on the strength of the ac grid, exhibiting improved performance compared to GFL-VSC in weak grids (Li; Gu; Green, 2022b). This voltage source characteristic arises from the PCC voltage magnitude regulation, while synchronization is achieved through active power control, commonly referred to as the power synchronization loop (Li; Gu; Green, 2022b).

Among the numerous advantages of GFM converters, such as black start capability, inertia, and damping, numerous studies demonstrate that they can enhance voltage stiffness, thereby improving the stability of renewable energy resources interfaced by GFL converters under weak-grid conditions, such as those found in offshore wind power plants (WPPs) and solar farms. This improvement is particularly notable in converter structures based on battery energy storage systems (BESS) (Quan et al., 2020; Cherevatskiy et al., Oct.

2019; Li et al., 2020; Fang et al., 2018; Rahmoun et al., 2017).

As highlighted before, the most widely applied BESS solutions are based on 2- and 3-level (VSC) connected to line frequency transformers due to the cost-effectiveness coupled with the need to ensure the galvanic isolation required in the integration of renewable energy and in the grid-connected battery energy systems standards (Blaabjerg et al., 2023; Wang et al., 2016b; Engelbrecht et al., 2023). To achieve output sinusoidal voltage waveforms, conventional VSCs require the use of capacitive LC or LCL filters on the grid side, which contributes to resonances and instability issues (Juntunen et al., 2015; Enslin; Heskes, 2004; He et al., 2013; Dang; Ellinger; Petzoldt, 2014; Agorreta et al., 2011), what is a concern in solar farms (Hu et al., 2015) and also in offshore weak grid WPPs due to long alternating current cables, transformers, shunt reactors, and converter filters (Kocewiak et al., 2019; Zhou et al., 2014).

In addition, the GFM BESS converter control structure is generally based on closed control loops, and the necessity of a vector voltage control (VVC) may cause control interactions and oscillations in grid-connected mode, complicating the controllers parameters tuning (Zhao et al., 2024; Zhao et al., 2022; Qoria et al., 2018; Dokus; Mertens, 2021).

In this chapter, the ZHD converter is proposed as a grid-forming (GFM) converter for grid-connected operation. The converter inherent sinusoidal voltage eliminates the need for output capacitive filters, allowing a simplified voltage open-loop control implementation. This approach removes the necessity for the commonly applied virtual voltage control (VVC) schemes used in commercial solutions, which can lead to control interactions and resonances in grid-connected applications. The converter's capability to regulate voltage and reactive power, as well as to operate under current limitation conditions, is demonstrated through simulation and hardware-in-the-loop (HIL) results.

6.2 ZHD GFM Grid-Connected Control Scruture

The intrinsic voltage source nature of the ZHD converter implies that one does not need vector voltage control (VVC), vector current control (VCC) and filter capacitors for voltage source operation, as shown in Chapter 4 as GFM converter in islanded microgrid applications only a open-loop control structure. In this way, in addition to the absence of capacitors avoiding resonance and feroresonance problems, the ZHD avoids problems with respect to control resonance and control interaction problems, that is an important concern in grid-connected mode (Zhao et al., 2024; Zhao et al., 2022; Qoria et al., 2018; Dokus; Mertens, 2021).

The same ZHD open-loop voltage control of Chapter 4 and shown in Fig. 122 in dq frame and only a disturbance feedforward control is responsible for rejecting load

variations, thus compensating the voltage reference commands. E_d and E_q are the voltages generated by the converter and V_d, V_q, I_d, and I_q are the measured voltages and currents, respectively. R_{zhd} and L_{zhd} represent the ZHD resistance and inductance of the impedance given by (3.18), and ω_{ref} is the reference frequency.

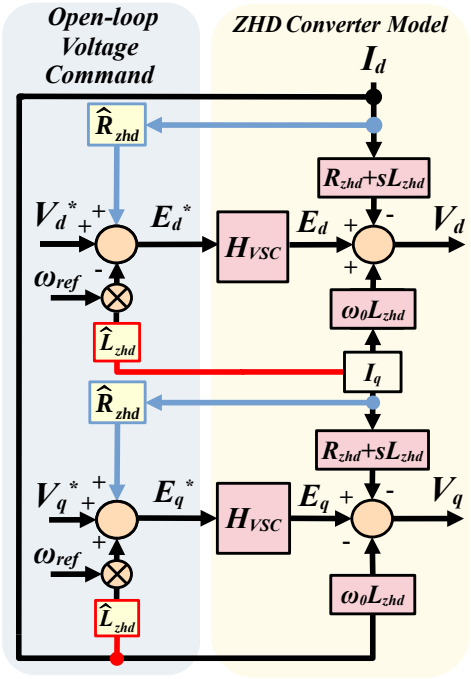

Figure 122 – Open-loop voltage control of ZHD GFM converter.

Unlike Chapter 5 that deals with the ZHD converter as a GFL converter and Chapter 4 that deals with the ZHD as a GFM converter in islanded applications, this Chapter proposes addresses the use of ZHD as a GFM grid-connected converter, where the synchronism with the grid is implemented through the power synchronization control. Fig. 124 shows the complete ZHD grid-connected GFM control. The measured currents in the dq reference frame, I_d and I_q, creates a corrective signal that is incorporated to the references voltages V_d^* and V_q^*. Based on a virtual impedance principle, voltage and phase compensation at the primary side is possible. $\hat{R}_{zhd}$ and $\hat{L}_{zhd}$ are the estimated resistance and inductance of ZHD converter, respectively. E_d^* and E_q^* symbolize voltage commands, and considering the transformer winding ratio a, such signals serve to determine the reference of modulation indexes $m_{\Delta,Y}$ and phase compensation $\delta_{\Delta,Y}$.

The modulation signals and the sum of phase compensation and the angle references θ_Y and θ_Δ, are compared in the LUTs generating the power switches command signals $\alpha_{1Y}, .., \alpha_{MY}$ and $\alpha_{1\Delta}, .., \alpha_{M\Delta}$ to the VSCs. The frequency ω_{ref} and angle reference θ_{ref} is generated by the active power control, responsible for by the grid synchronism, where P_{ref} is the power reference, P_o the measured output power filtered by the low-pass filter G_{LPF}, k_p is the gain of the power controller, ω_f the nominal frequency of the grid and θ_{synch} the angle of the presynchronization procedure to the grid connection.

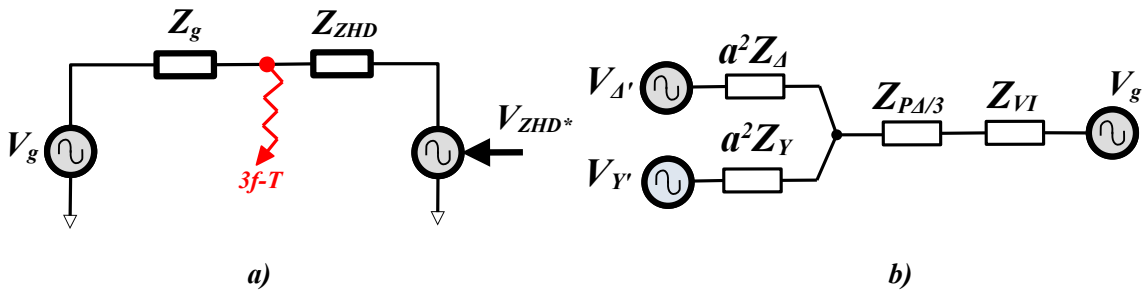

Figure 123 – (a) Three-phase short-circuit at PCC, (b) ZHD Per-phase equivalent circuit with virtual impedance.

6.2.1 ZHD Virtual Impedance Current limitation

Since the Grid-connected GFM converters requires a current limitation technique in order to protect the converter from overcurrent under faults. A virtual impedance (VI) was developed specifically to to the ZHD converter, since is a well known technique, commercially accepted and preserve converter voltage source behavavior under faults what is very value by the recent grid codes (Zhao et al., 2024).

Considering the equivalent circuit in Fig.123 (a) the voltage considering a three-phase short-circuit can be given by (6.1)

$$V^* = \sqrt{X_{ZHD}^2 + R_{ZHD}^2} \cdot I_g \tag{6.1}$$

Where (6.1) rearranged as:

$$(\tfrac{V^*}{I_g})^2 = X_{ZHD}^2 + R_{ZHD}^2 \tag{6.2}$$

Considering again the per-phase ZHD equivalent impedance now considering the presence of the virtual impedance in Fig.123 (b), (6.3) shows the ZHD equivalent impedance

$$Z_{ZHD} = \tfrac{a^2 Z_\Delta \cdot a^2 Z_Y}{a^2 Z_\Delta + a^2 Z_Y} + \tfrac{Z_P}{3} + Z_{VI} \tag{6.3}$$

Simplifying (6.3):

$$Z_{ZHD} = \tfrac{a^2 Z_\Delta Z_Y}{Z_\Delta + Z_Y} + \tfrac{Z_P}{3} + Z_{VI} \tag{6.4}$$

Considering that the both secondaries impedances are equal: $Z_\Delta \approx Z_Y \rightarrow Z_s$, (6.4) is rewritten as (6.5) and rearraged in real and imaginary parts in (6.6)

$$Z_{ZHD} = \tfrac{a^2 Z_s}{2} + \tfrac{Z_P}{3} + Z_{VI} \tag{6.5}$$

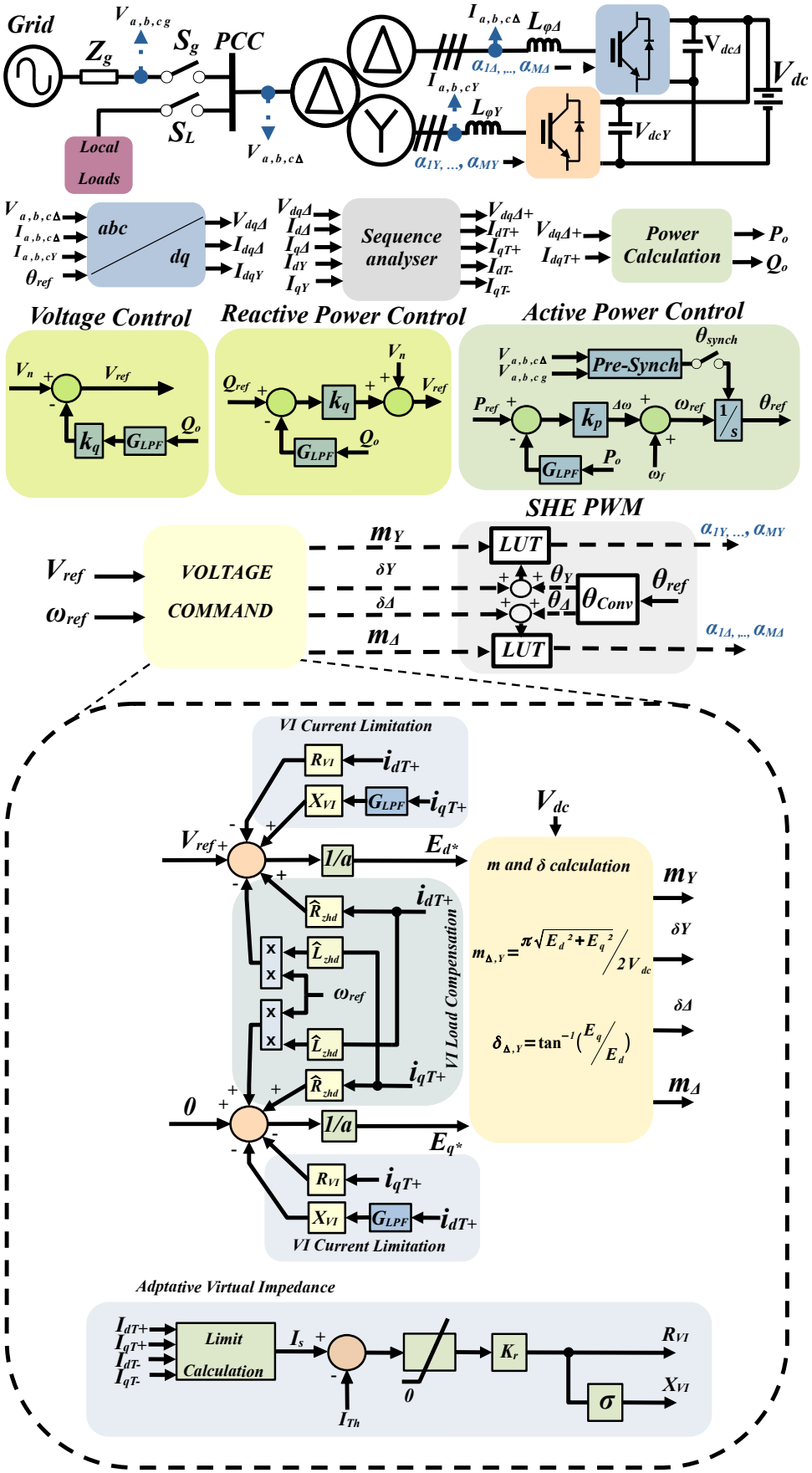

Figure 124 – Grid-connected GFM control of the ZHD converter.

$$Z_{ZHD} = \frac{a^2}{2}R_s + \frac{R_P}{3} + R_{VI} + j(\frac{a^2 X_s}{2} + \frac{X_P}{3} + X_{VI}) \tag{6.6}$$

Calling the imaginary and real part of the impedance of $X_B = \frac{a^2 X_s}{2} + \frac{X_P}{3}$ and $R_B = \frac{a^2 R_s}{2} + \frac{R_P}{3}$ and substitute in (6.2):

$$(\frac{V^*}{I_{max}})^2 = (X_B + X_{VI})^2 + (R_B + R_{VI})^2 \tag{6.7}$$

A second order equation can be obtained:

$$(\frac{V^*}{I_{max}})^2 = X_B^2 + 2X_{VI}X_B + X_{VI}^2 + R_B^2 + 2R_B R_{VI} + R_{VI}^2 \tag{6.8}$$

Since the relationship between the virtual resistance and reactance (X/R) is given by the :$R_{VI} = \frac{X_{VI}}{\sigma} \rightarrow X_{VI}\sigma^{-1}$, R_{VI} term being substituted in (6.9), and the second order equation can be reorganized as in (6.10).

$$(\frac{V^*}{I_{max}})^2 = X_B^2 + 2X_{VI}X_B + X_{VI}^2 + R_B^2 + 2R_B X_{VI}\sigma^{-1} + X_{VI}^2(\sigma^{-1})^2 \tag{6.9}$$

$$X_{VI}^2(1 + (\sigma^{-1})^2) + X_{VI}(2X_B + 2R_B\sigma^{-1}) + R_B^2 + X_B^2 - (\frac{V^*}{I_{max}})^2 = 0 \tag{6.10}$$

To solve the second order equation, the coefficients are divide in:

$$\begin{aligned} A_{VI} &= 1 + (\sigma^{-1})^2 \\ B_{VI} &= 2X_B + 2R_B\sigma^{-1} \\ C_{VI} &= R_B^2 + X_B^2 - (\frac{V^*}{I_{max}})^2 \end{aligned} \tag{6.11}$$

Substituting the R_B and X_B values in (6.11):

$$\begin{aligned} A_{VI} &= 1 + (\sigma^{-1})^2 \\ B_{VI} &= 2(\frac{a^2 X_s}{2} + \frac{X_P}{3}) + 2(\frac{a^2 R_s}{2} + \frac{R_P}{3})\sigma^{-1} \\ C_{VI} &= (\frac{a^2 R_s}{2} + \frac{R_P}{3})^2 + (\frac{a^2 X_s}{2} + \frac{X_P}{3})^2 - (\frac{V^*}{I_{max}})^2 \end{aligned} \tag{6.12}$$

X_{VI} can be solved by:

$$X_{VI} = -\frac{B_{VI} \pm \sqrt{B_{VI}^2 - 4A_{VI}C_{VI}}}{2A_{VI}} \tag{6.13}$$

Solving X_{VI} and R_{VI} by (6.13) the VI gain can be calculated as:

$$K_r = \frac{R_{VI}}{I_{max} - I_{th}} \tag{6.14}$$

In the adaptative Virtual impedance implementation the positive and negative sequence was decomposed in order to calculate and extract the second order component in the cases of asymmetrical voltage sags to avoid the that frequency perturbation on the SHE PWM modulator.

6.3 Simulation Results

The ZHD GFM converter in grid-connected operation was analyzed using the MATLAB/Simulink platform. The system and control parameters are described in Table 18.

Table 18 – Simulation Parameters

ZHD CONVERTER PARAMETERS			
Parameters	**Values**	**Parameters**	**Values**
Rated Power	280 kVA	Frequency	60 Hz
Primary Voltage	13.8 kV	Δ Secondary Voltage	440 V
Winding Connections	Dd0y1	Y Secondary Voltage	440 V
$L_{\phi\Delta}$ and $L_{\phi Y}$ reactors	0.59/0.506 mH	DC link voltage	650 V
THREE-WINDING THREE-PHASE TRANSFORMER - Dd0y1			
Parameters	**Values**	**Parameters**	**Values**
R_m	526.7 $k\Omega$	$R_{s\Delta}$	19.4 $m\Omega$
L_m	534.5 H	$L_{s\Delta}$	3.33 μH
$R_{P\Delta}$	10.5 Ω	R_{sY}	16 $m\Omega$
$L_{P\Delta}$	108.7 mH	L_{sY}	84.26 μH
LINEAR LOADS - R and RL			
Parameters	**Values**	**Parameters**	**Values**
Active Power	200 kW	Reactive Power	0 var
Active Power	48 kW	Reactive Power	36 kvar
NONLINEAR LOAD - THREE PHASE SIX PULSE RECTIFIER			
Parameters	**Values**	**Parameters**	**Values**
R_{AC}	152.35 Ω	L_{AC}	2.16 mH
C_{dc}	2.59 μH	R_L	34.56 $k\Omega$
CONTROL PARAMETERS			
Parameters: SCR=1	**Values**	**Parameters: SCR=5**	**Values**
k_p	0.03 p.u.	k_p	0.01 p.u.
ω_c	10 Hz	ω_c	10 Hz

6.3.1 Black-Start, Synchronization and Grid-Connection

The simulation scenario considering black start, islanding operation, grid connection, and unintentional island operations are listed:

- t = 0 s $\rightarrow$ (I) $\rightarrow$ Black start of the R load;

- t = 0.5 s $\rightarrow$ (II) $\rightarrow$ Islanded Operation;
- t = 1.25 s $\rightarrow$ (III) $\rightarrow$ Grid-connection;
- t = 2 s $\rightarrow$ (IV) $\rightarrow$ Step reference of 200 kW;
- t = 2.5 s $\rightarrow$ (V) $\rightarrow$ Connection of RL and nonlinear loads;
- t = 3 s $\rightarrow$ (VI) $\rightarrow$ Unintentional island;

Fig. 125 and 126, considering weak grid scenarios (SCR = 1) and stiff grid scenarios (SCR = 5), respectively, show the results of active and reactive power in (a) and (b), voltage and current in the ZHD converter in (c) and the zoomed view of each time event in (d) - (i).

In each case, the switch S_L is closed and Fig. 125 and 126 show the black-start capability of ZHD converter in (d) and operation in the island mode in (e) for time events I and II, where it is possible to perceive the converter providing a sinusoidal voltage waveform shape.

The connection to the grid occurs in time event III, where the switch to the grid S_g is closed through the presynchronization procedure that tracks the angle of the grid θ_{synch}. In both SCR conditions, after the connection to the grid, Fig. 125 and 126 (a) show the converter following the zero active power reference and in IV tracking the step power reference of 200 kW, even under load disturbance in V.

The waveforms zoomed view (f) and (g) also shows the converter capability to deliver sinusoidal waveforms in grid-connected mode, however, the delivered voltage waveforms are degraded during the operation with the nonlinear load in (h). Finally, in time event VI the grid switch S_g is open and the converter inherently assumes island operation as shown in (i).

The voltage regulation and the output phase for both grid scenarios are shown in Fig. 127 (a) and (b). The Fig. shows that in both grid strength cases the converter can regulate the voltage even in the presence of harmonics on the grid side. The voltage regulation stays well below the 5% range recommended by the standards, showing the converter capacity to regulate voltage in island mode, also as shown in Chapter 4, and in this Chapter in grid-connected operation in both weak and stiff grid cases, only with an open-loop voltage command structure.

The voltage FFTs in Fig. 127 show the converter delivering voltage waveforms free of harmonics up to 50^{th} order in Fig. 127 ((c)-(e)) for SCR=1, and in Fig. 127 ((g)-(i)) for SCR=5, only disturbed in the presence of harmonics at the output of the ZHD converter as shown in Fig. 127 (f) and (j).

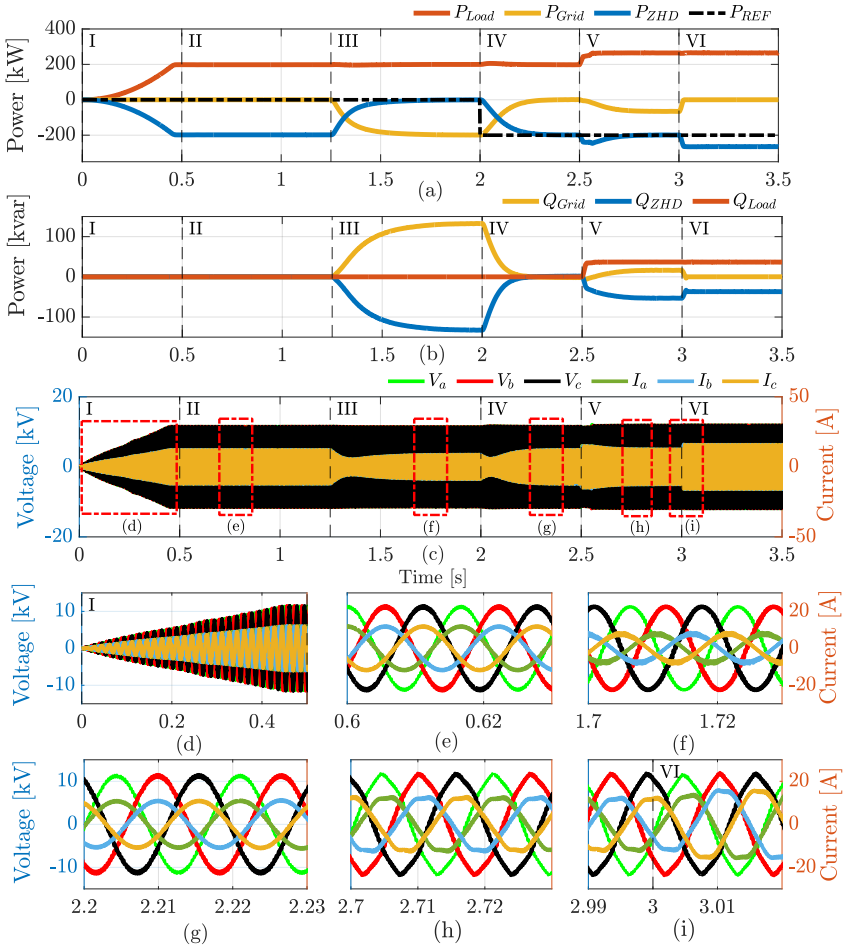

Figure 125 – SCR=1: (a) Active, and (b) Reactive power, (c) Voltage and current at the ZHD converter during different time intervals: (d) Event I, (e) Event II, (f) Event III, (g) Event IV, (h) Event V, and (i) Event VI.

6.3.2 Control Sensitivity Analysis

The control system sensitivity analysis was realized due to possible errors in the converter's estimated output impedance. For the same scenario considered in the last section, but considering the cases of ±20% of estimating error in the virtual impedance parameters $\hat{R}_{zhd}$ and $\hat{L}_{zhd}$ of the open-loop voltage command, Fig. 128 shows that the converter maintains effective voltage and phase regulation, as shown in (a), within the limit ±5% recommended by standards (IEEE. . . , 2018), with a maximum phase deviation of 2°. These results show that even in the context of errors in the ZHD estimated output impedance, the effect in voltage regulation also in the grid-connected mode is acceptable.

6.3.3 Converter Secondaries Impedance Mismatches

Again, considering the same simulation scenario of Section 6.3.1, another sensitivity analysis was realized considering now possible mismatches between the secondaries reactor impedances. Taking into account the mismatch scenarios of + 20% of Z_Δ and + 20% of Z_Y, Fig. 129 (a) and (b) show the voltage regulation and the output phase voltage. It is

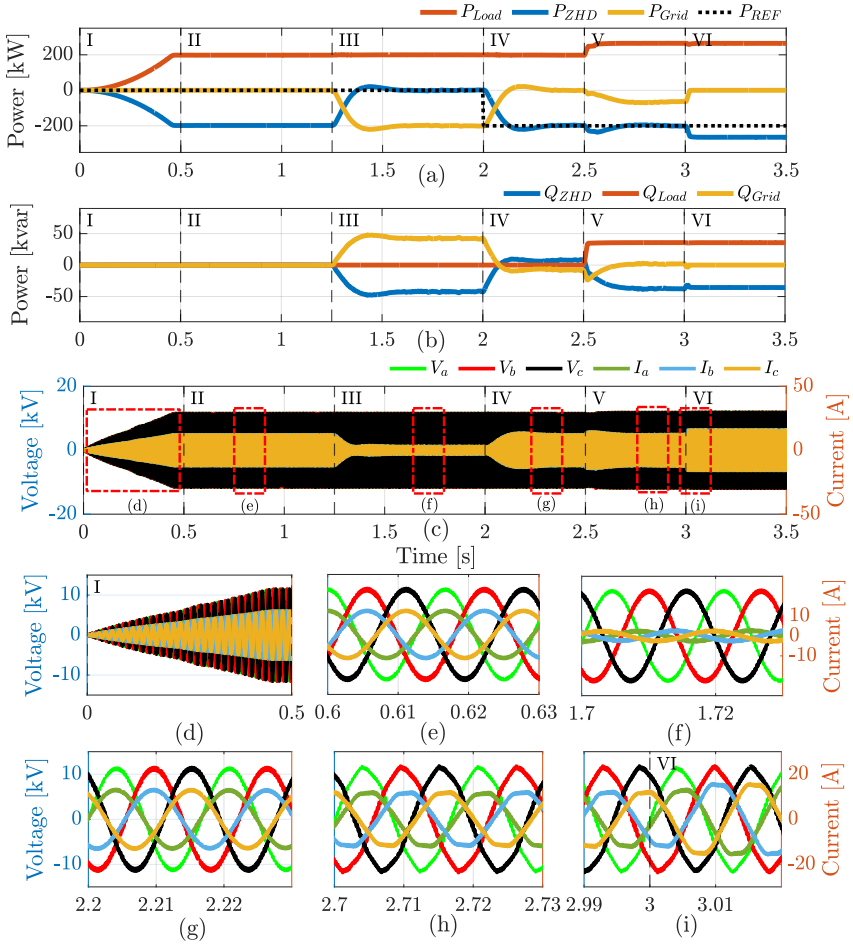

Figure 126 – SCR=5: (a) Active, and (b) Reactive power, (c) Voltage and current at the ZHD converter during distinct time events: (d) Event I, (e) Event II, (f) Event III, (g) Event IV, (h) Event V, and (i) Event VI.

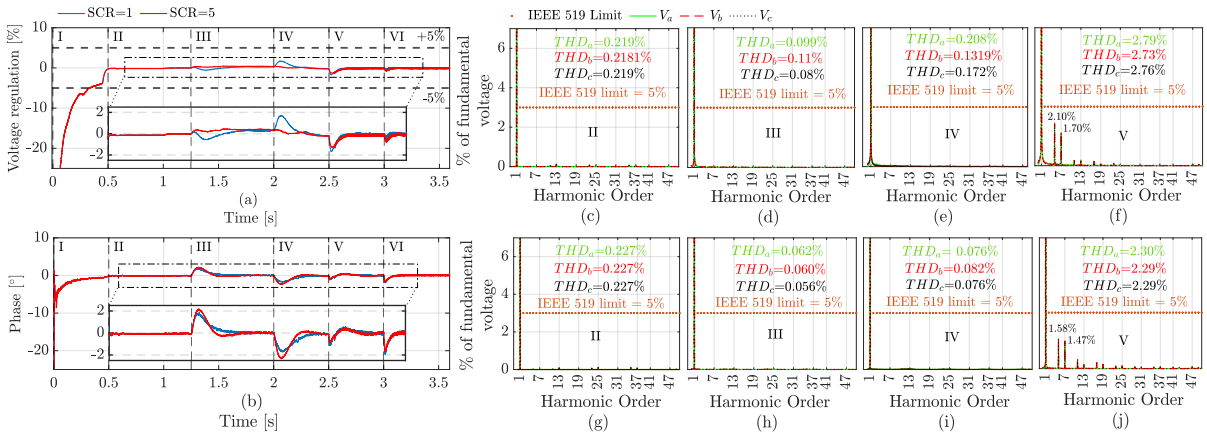

Figure 127 – (a) Voltage regulation and (b) Measured output voltage phase for SCR=1 and SCR=5 scenarios. Output voltage FFT of the ZHD converter for SCR=1 during time events: (c) II, (d) III, (e) IV, and (f) V; and for SCR=5 during time events: (g) II, (h) III, (i) IV, and (j) V.

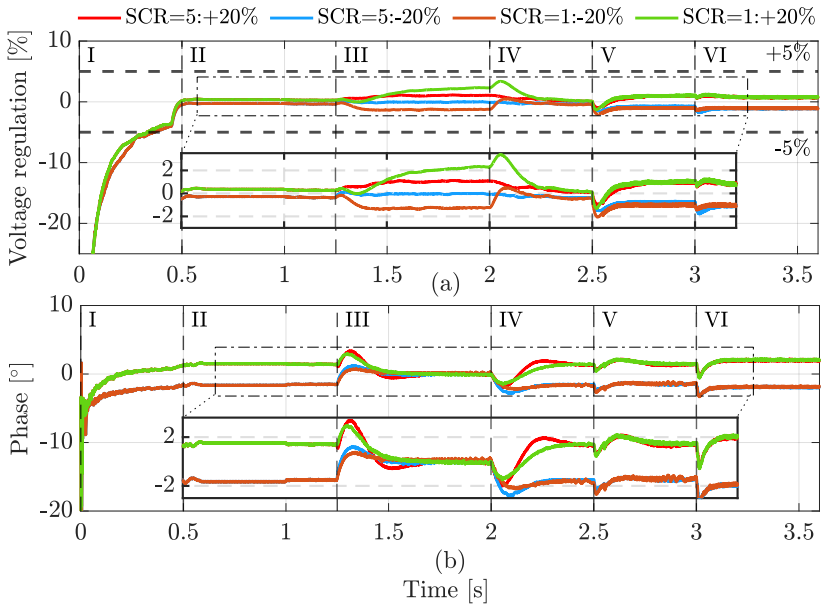

Figure 128 – (a) Voltage regulation and (b) output voltage phase under impedance estimation errors of ±20.

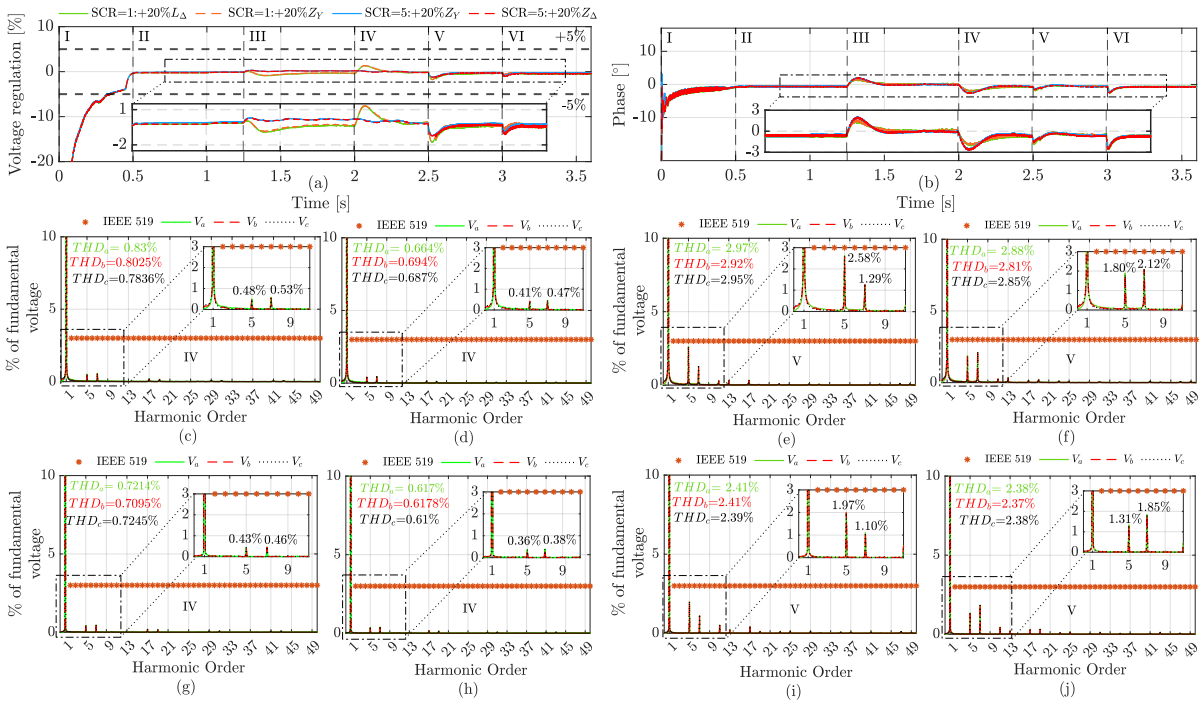

Figure 129 – (a) Voltage regulation, (b) output voltage phase, output voltage harmonic FFT considering: (c) +20% of Z_Δ, and (d) +20% of Z_Y for SCR=1 in time event IV, (e) +20% of Z_Δ, and (f) +20% of Z_Y for SCR=1 in time event V, (g) +20% of Z_Δ, and (h) +20% of Z_Y for SCR=5 in time event IV, (i) +20% of Z_Δ, and (j) +20% of Z_Y for SCR=5 in time event V.

possible to verify that even under these conditions the voltage regulation and the phase deviations remain at acceptable levels in both islanded and grid-connected modes. Fig. 129 (c) and (d) for time event IV and Fig. 129 (e) and (f) for time event V, shows the

FFT output voltage for +20% of Z_Δ and +20% of Z_Y considering an SCR = 1. Fig. 129 (g)-(j) shows the same scenarios considering an SCR=5. In these unbalance conditions the voltage FFTs (c), (d), (g), and (h) for time event IV show the presence of harmonics normally canceled in the transformer, due to the non-equal harmonic cancelation. However, the magnitude of these harmonics are practically negligible. The unbalance effect was also practically negligible in time event V. Comparing Fig. 129 (e) and (g) with Fig. 127 (f) and 129 (i) and (j) with Fig. 127 (j), it is possible to verify that even with the unbalance between the reactors, the voltage harmonic deterioration is also negligible and in practice can be easily compensated with a virtual impedance.

6.3.4 Voltage Control Mode

In practice, droop control must be implemented in voltage-control mode to ensure that the converter contributes reactive power to voltage regulation strictly according to its capability. Fig. 130 and 131 show the converter capability to regulate the PCC voltage for SCR = 1 and SCR = 5, respectively. By comparing these figures with Fig. 125 and 126, it becomes clear that the reactive power contribution of the ZHD converter in voltage-control mode with droop is inherently limited.

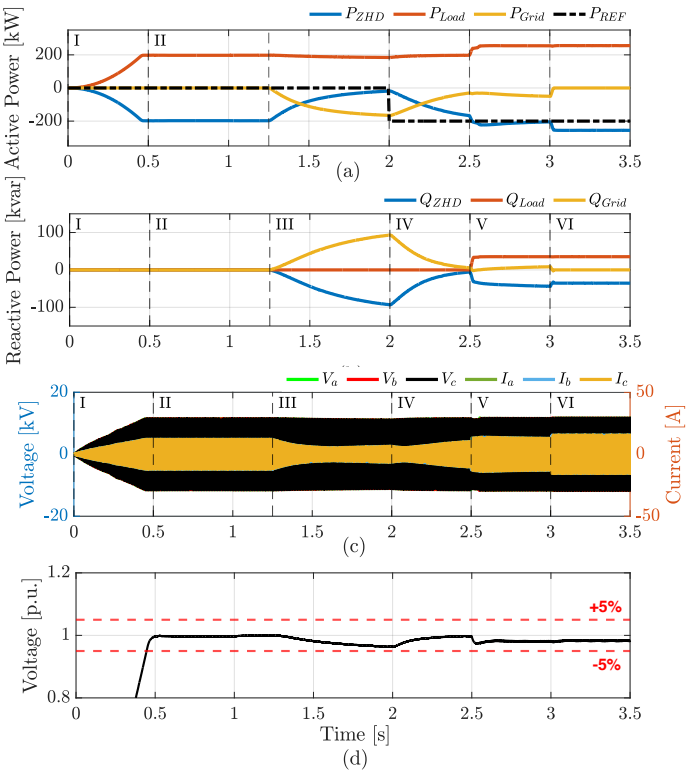

Figure 130 – SCR=1: (a) Active, and (b) Reactive power, (c) Voltage and current at the ZHD converter and (d) voltage regulation at PCC.

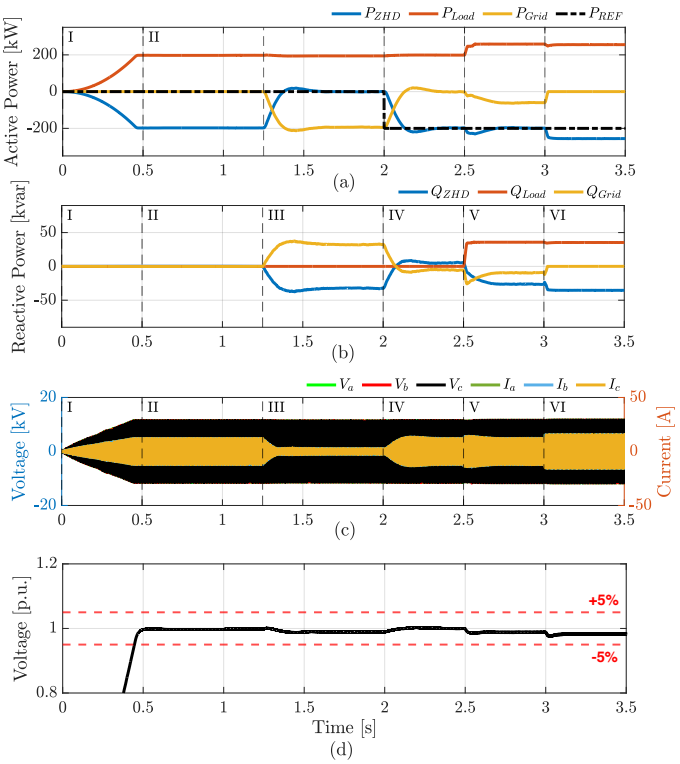

Figure 131 – SCR=5: (a) Active, and (b) Reactive power, (c) Voltage and current at the ZHD converter and (d) voltage regulation at PCC.

6.3.5 Reactive Control Mode

Reactive power regulation was also tested, where the reactive power loop was enabled by summing a voltage signal that modified the voltage command control, making it possible to exchange reactive power, as shown in Fig. 124. Also, for both cases of SCR, Fig. 132 and 133 show the simulation scenarios considering:

- t = 0 s → (I) → Black start of the R load;
- t = 0.5 s → (II) → Islanded Operation;
- t = 1.25 s → (III) → Grid-connection;
- t = 2 s → (IV) → Step reference of 200 kW;
- t = 2.6 s → (V) → Step reactive reference of +40 kVar;
- t = 3.6 s → (VI) → Step reactive reference of -40 kVar;

In both scenarios of weak and strong grids, it is possible to verify ZHD converter reactive power exchange capability.

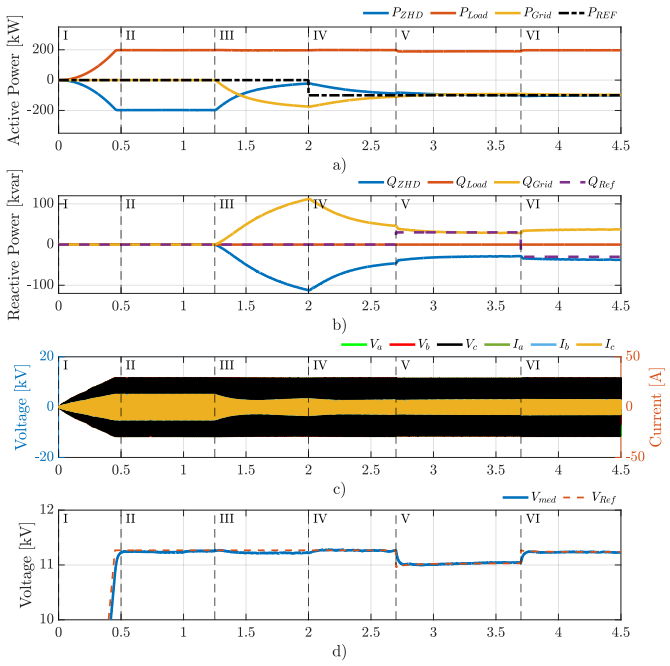

Figure 132 – SCR=1: (a) Active, and (b) Reactive power, (c) Voltage and current at the ZHD converter and (d) Reference voltage and measured voltage at PCC.

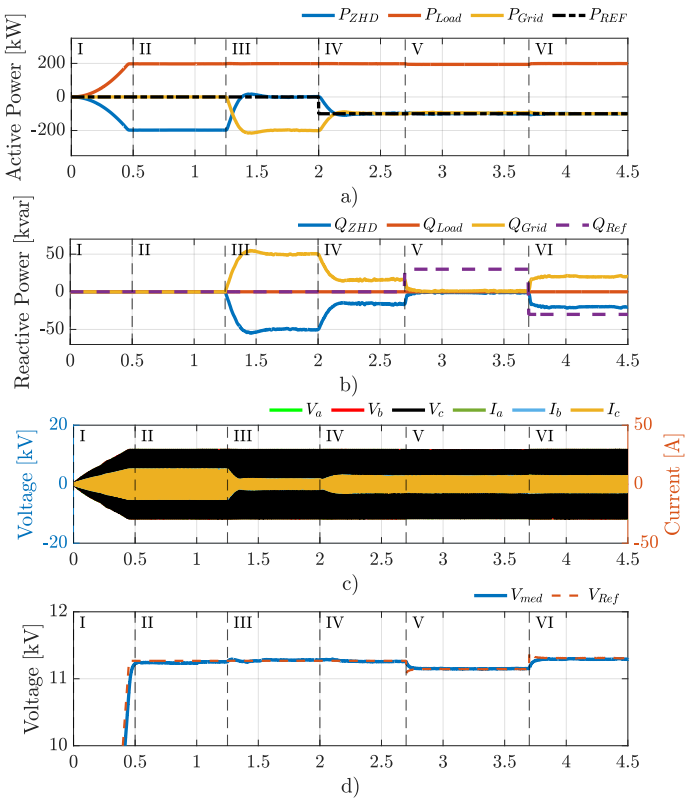

Figure 133 – SCR=5:(a) Active, and (b) Reactive power, (c) Voltage and current at the ZHD converter and (d) Reference voltage and measured voltage at PCC.

6.3.6 Operation Under Faults

Due to the GFM voltage source nature, an important case of study regarding the GFM operation is the necessity of current limitation, especially under grid faults. As seen in Fig. 124 the virtual impedance current limitation scheme was adopted due to the capacity to mantain the voltage source behavior, desired under grid faults, and easily adapted to the voltage command control without the necessity of additional closed control loops. In this operation the reactive power loop was desconsidered since it is naturraly bypassed under grid faults, since maintain a constant voltage under fault occurrence is required by recent standards.

Considering the Fig. 134, 135 and 136 it is possible to observe the ZHD converter under three-phase voltage sag. Fig. 134 shows the power flow, Fig. 135 shows the voltage at the primary and both secondaries of the transformer, and Fig. 134 the currents at the primary and in the secondaries of the transformer. The results show that the virtual impedance current limitation can work by limiting the converter current at the primary, and both the secondaries.

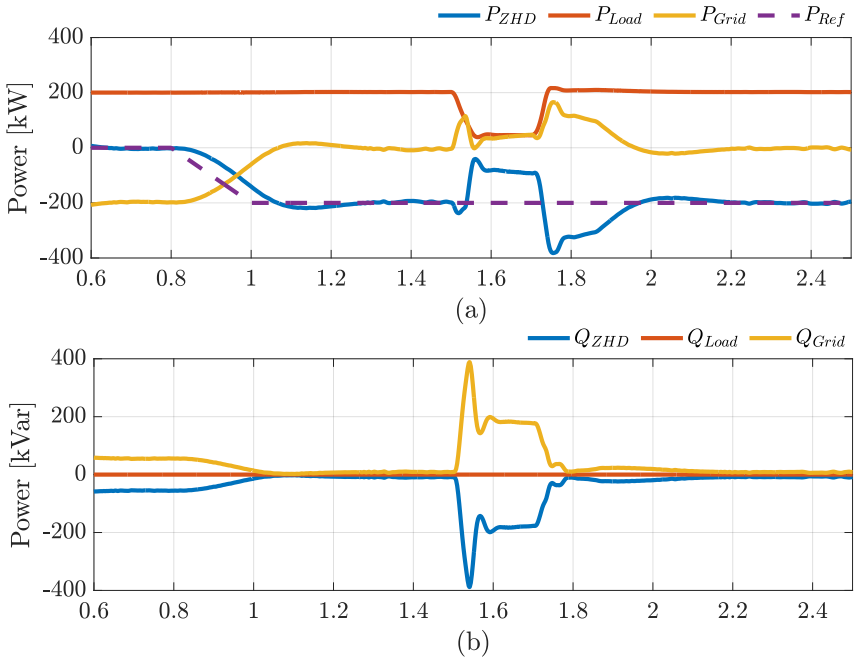

Figure 134 – (a) Active power of the ZHD converter, load, grid, and reference signal, and (b) reactive power of the ZHD converter, load, and grid under a three-phase voltage sag condition.

The same voltage sag scenarios were again evaluated considering single and double-phase voltage sags. Fig. 137, 138 and 139 show the results for single-phase A voltage sag and Fig. 140, 141 and 142 for double-phase A and B voltage sag.

In both cases, even in the presence of asymmetric voltage sags, the converter can still deliver sinusoidal waveforms once that was expected; Theoretically the harmonic

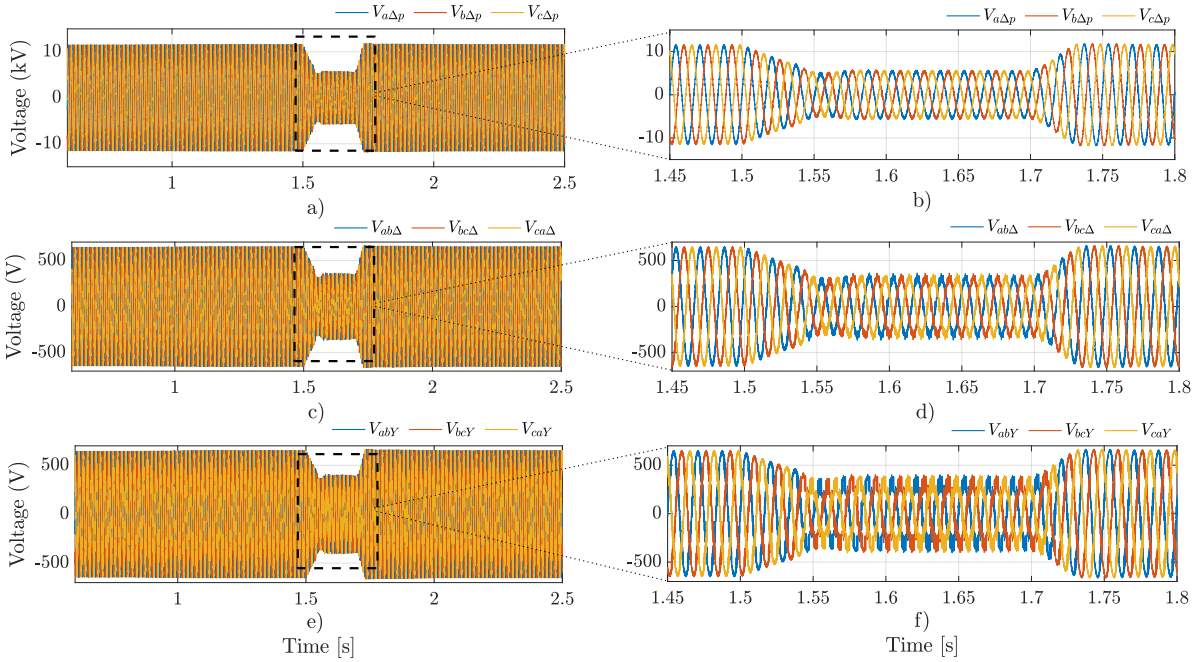

Figure 135 – Voltages at the primary and secondary sides of the transformer during a three-phase voltage sag: (a) primary-side voltage and (b) its zoomed view at the fault instants; (c) voltage at the Δ secondary and (d) its zoomed view at the fault instants; and (e) voltage at the Y secondary and (f) its zoomed view at the fault instants.

cancellation still occurs due to the fact that both converters receive the same modulation indexes and the flux-linked perturbation under these cases occurs only in the fundamental frequency (considering grid voltages free of harmonics). In this way, the harmonic current flow is a function just of the adjusted modulation index by the VI current limitation required to limit the current under fault scenarios. The current flow only in the secondaries and are limited by the secondary reactors.

The projected adaptive virtual impedance, designed to limit the primary current of the ZHD converter, demonstrated successful operation by effectively constraining the secondary currents. This limitation was achieved by imposing a maximum primary current of 1.5 p.u. during a three-phase short-circuit condition, as shown in Fig. 137.

For all simulated scenarios presented in Fig. 136, 139, and 142, the results indicate that an IGBT rated at 500 A is capable of handling the overcurrent conditions experienced by the ZHD GFM. This conclusion holds considering the converter admissible overcurrent capability of 1.5 p.u., confirming the suitability of such semiconductor devices for the studied operating conditions.

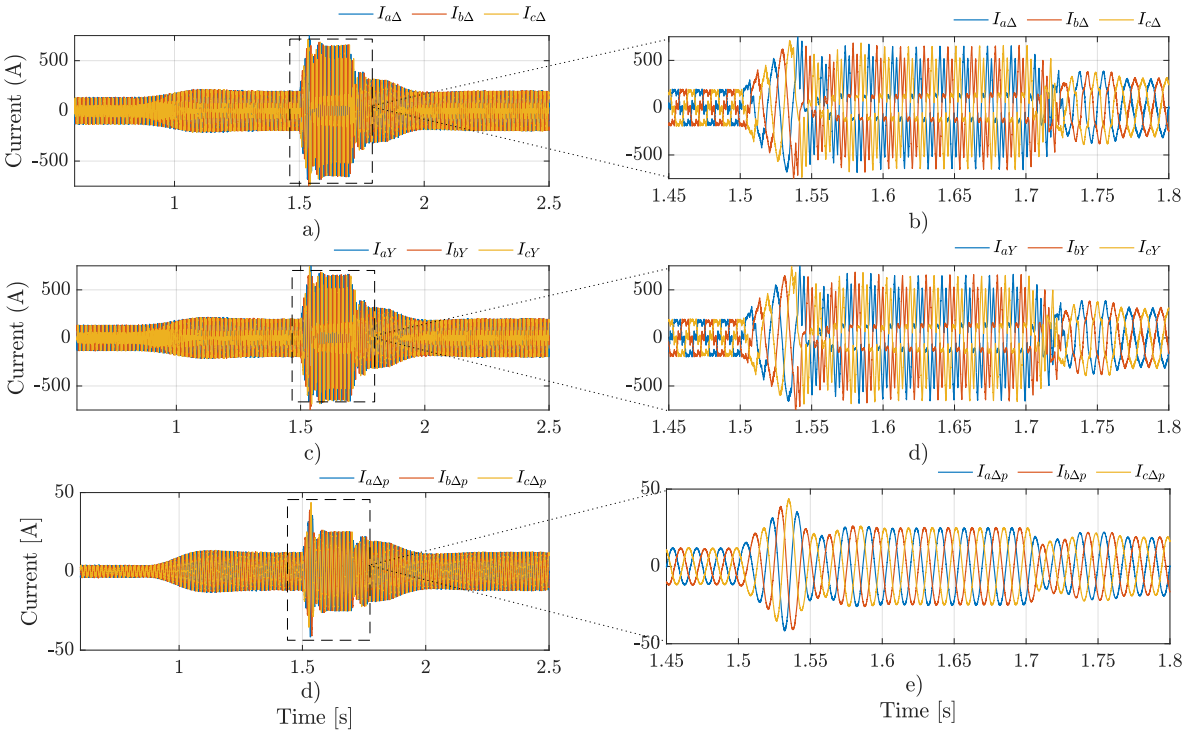

Figure 136 – Currents at the primary and secondary sides of the transformer during a three-phase voltage sag: (a) primary-side current and (b) its zoomed view at the fault instants; (c) current at the Δ secondary and (d) its zoomed view at the fault instants; and (e) current at the Y secondary and (f) its zoomed view at the fault instants.

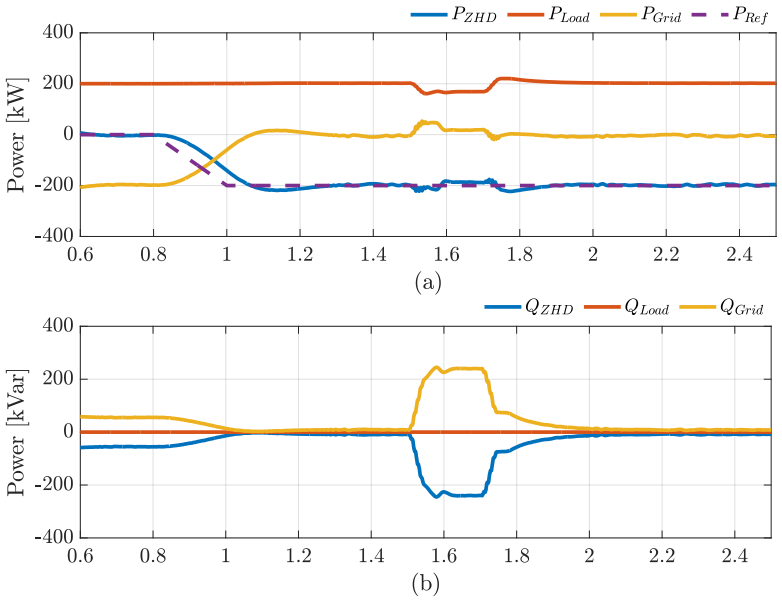

Figure 137 – Active and reactive power flow of the ZHD converter, load, and grid under a single-phase voltage sag condition: (a) active power of the ZHD converter, load, grid, and reference signal; and (b) reactive power of the ZHD converter, load, and grid, illustrating the converter's during unbalanced fault conditions.

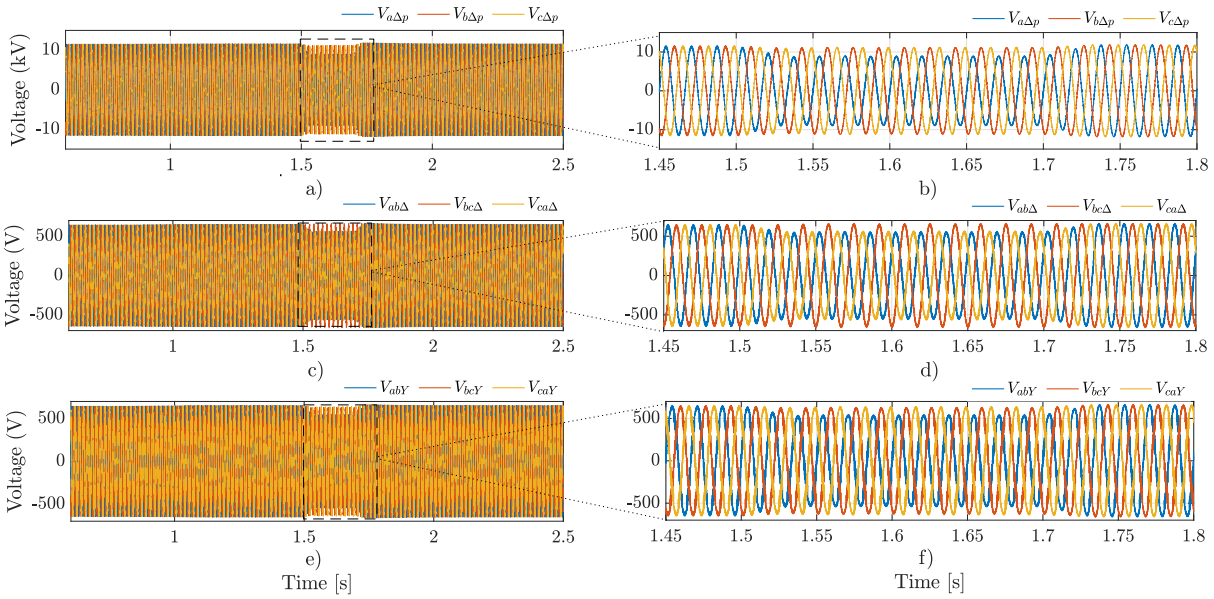

Figure 138 – Voltages at the primary and secondary sides of the transformer during a single-phase voltage sag: (a) primary-side voltage and (b) its zoomed view at the fault instants; (c) voltage at the Δ secondary and (d) its zoomed view at the fault instants; and (e) voltage at the Y secondary and (f) its zoomed view at the fault instants.

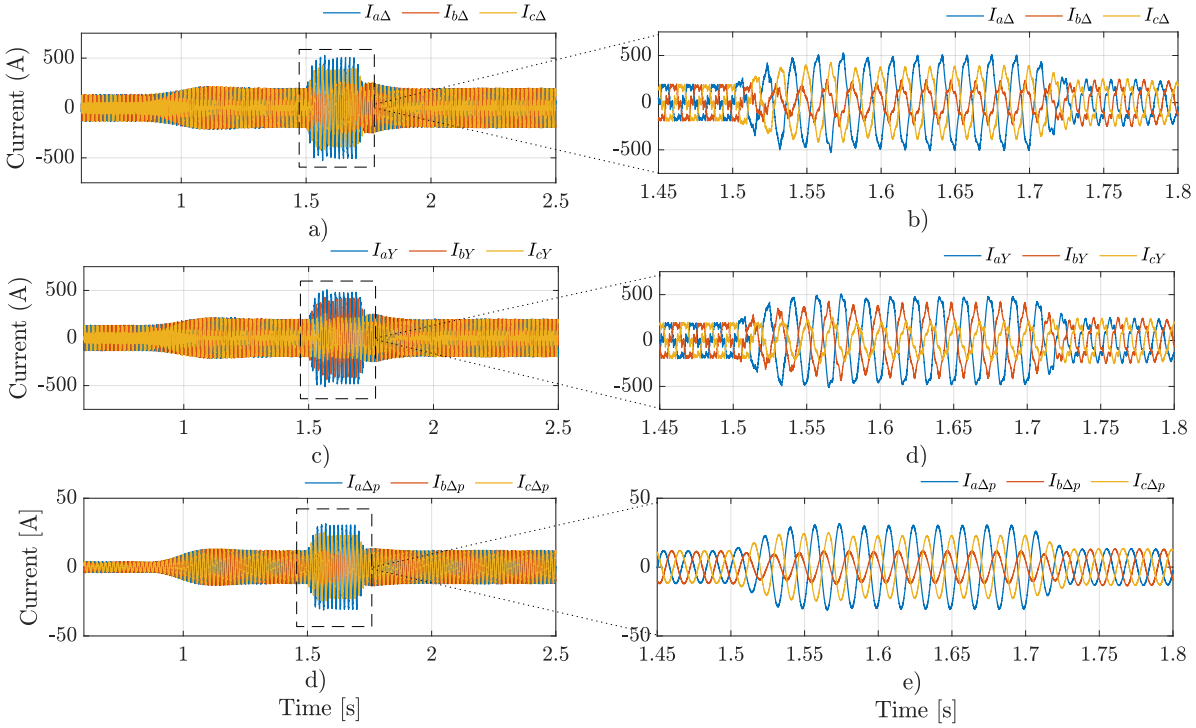

Figure 139 – Currents at the primary and secondary sides of the transformer during a single-phase voltage sag: (a) primary-side current and (b) its zoomed view at the fault instants; (c) current at the Δ secondary and (d) its zoomed view at the fault instants; and (e) current at the Y secondary and (f) its zoomed view at the fault instants.

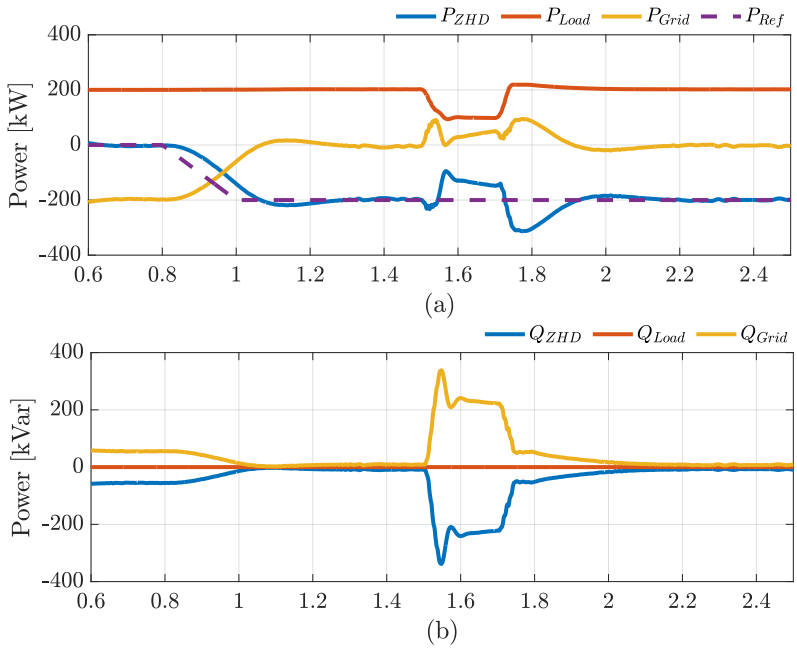

Figure 140 – a) active and (b) reactive power flow considering double-phase voltage sag.

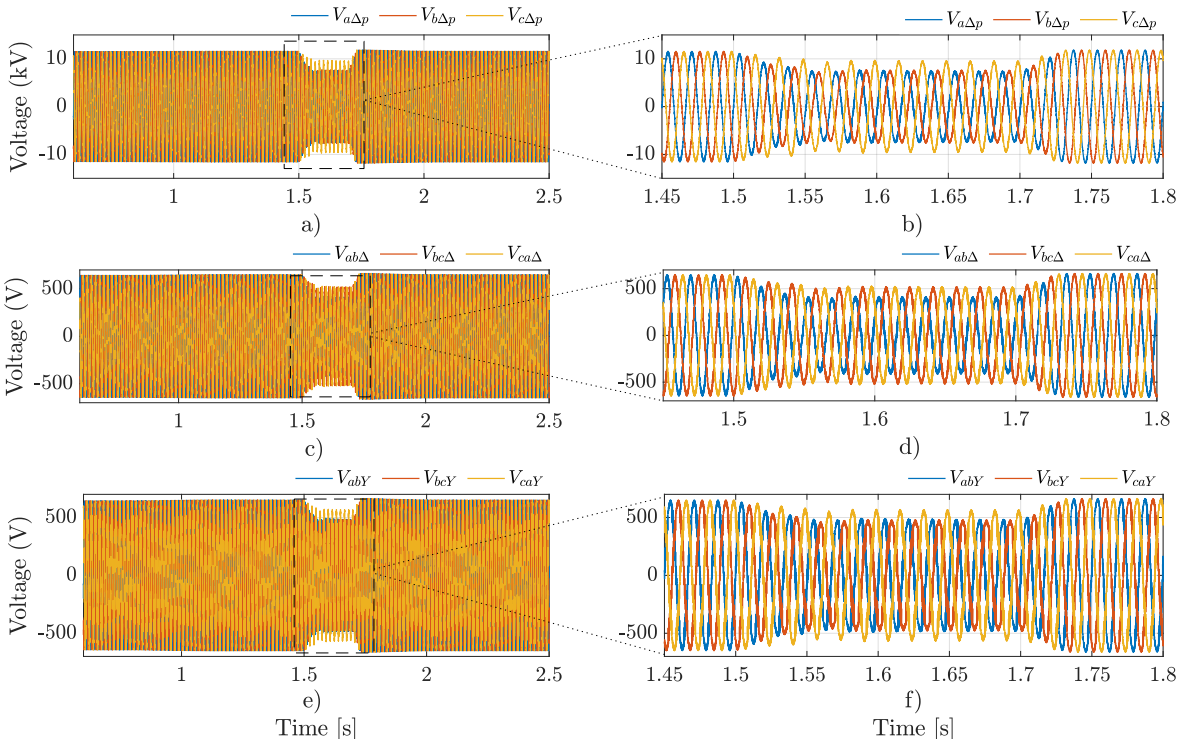

Figure 141 – Voltages at the primary and secondary sides of the transformer during a double-phase voltage sag. Figures (a) and (b) show the primary-side voltage and its zoomed view at the fault instants, respectively. Figures (c) and (d) present the voltage at the Δ secondary and its corresponding zoomed view, while Figures (e) and (f) illustrate the voltage at the Y secondary and its zoomed view at the fault instants, highlighting the voltage behavior and imbalance during the fault condition.

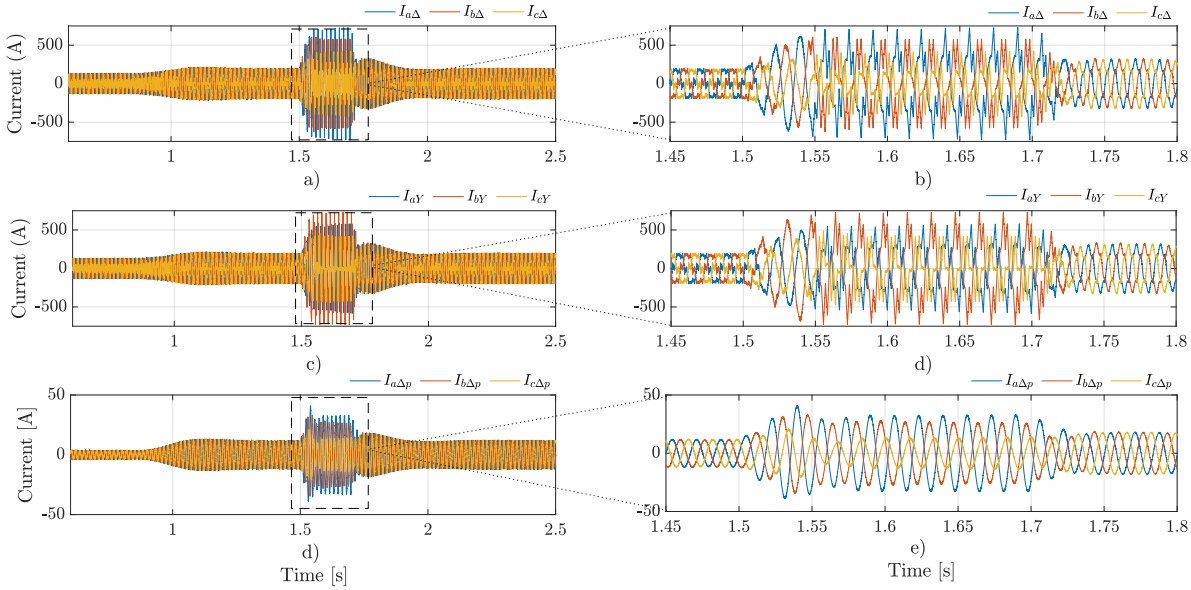

Figure 142 – Currents at the primary and secondary sides of the transformer during a double-phase voltage sag: (a) primary-side current and (b) its zoomed view at the fault instants; (c) current at the Δ secondary and (d) its zoomed view at the fault instants; and (e) current at the Y secondary and (f) its zoomed view at the fault instants.

6.4 Hardware-in-the-Loop-Results

The ZHD GFM converter with the same simulation parameters was implemented on a real-time simulation platform to test and validate the proposed ZHD control hardware operating as GFM grid-connected mode.

Fig. 143 shows the real controller connected to the Hardware-In-the-Loop (HIL) test bench. The controller consists of a Texas Instruments TMS320F28335 Digital Signal Processor (DSP) responsible for the converter control and an Field-Programmable Gate Array (FPGA) model MAX 10 from Intel operating with sufficiently high sampling frequency (250 kHz) storing the switching angles and handling with the SHE PWM based on the modulation rates sent by the DSP. Parallel communication is performed between the DSP and the FPGA, ensuring a high data exchange rate between the devices.

Fig. 144 illustrates the complete sequence of the black-start process. The ZHD converter is able to energize the 200 kW load through a ramp-based voltage build-up, allowing a smooth and stable transition until the load reaches its nominal operating point. The observed dynamic response confirms the converter robustness and its ability to initiate islanded operation without excessive transients or stability issues.

Starting from islanded mode, the grid synchronization is shown in Fig. 145, 146, and 147 for SCR = 1, 3, and 10. In all the cases, it is possible to observe the connecting process, with the converter leaving the island load supply and, at the connection instant,

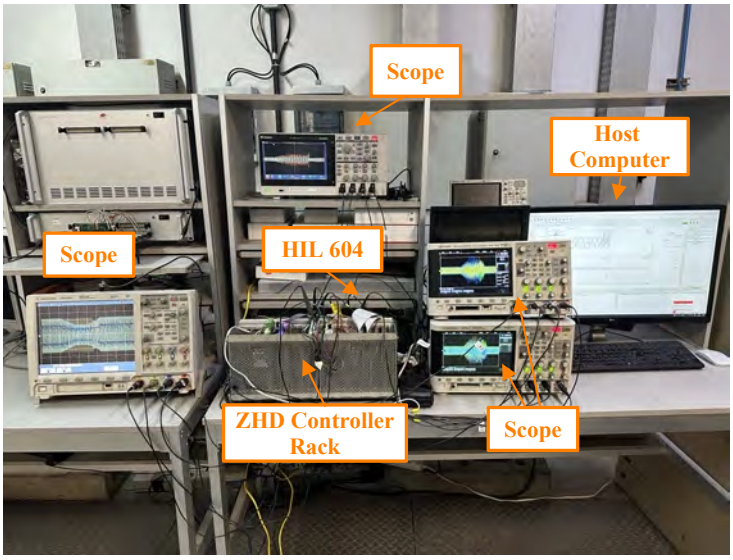

Figure 143 – Structure of tests and validation in Hardware-in-the-Loop.

setting the active-power reference to zero, remaining only in the voltage regulation at the PCC. It is also possible to observe, as expected, the higher reactive-power necessity to regulate the voltage in the weak grid cases.

In grid-connected mode under voltage control, with the converter injecting 150 kW, the voltage regulation capability was assessed. Fig. 148, 149, and 150 show the voltage regulation for an 80 kW load step at the PCC for SCR = 1, 3, and 10. In all the scenarios, after the load connection, the converter maintained the same active-power injection and regulated the voltage by injecting more reactive power, as seen in (a) and (b) of each figure. The ZHD output voltage and current FFT shown in (g)–(j) illustrate the free harmonic range.

Considering the same active power injection of 150 kW, the reactive control mode was assessed. Fig 151, 152, and 153 show the reactive power regulation for reference steps of 80 kvar and $-80kvar$ for SCR = 1, 3, and 10. In all the cases, the converter could inject or absorb reactive power from the grid.

Another operating condition evaluated is the grid-connected mode with the converter in voltage control mode. Fig. 154 illustrates the active power regulation performance when the active power reference is stepped from 0 to 150 kW. The results for SCR = 1, 3, and 10 are shown in subfigures (a), (c), and (e), respectively, highlighting the converter's capability to track the active power reference across different grid strengths.

Fig. 155, 156 and 157 shows the converter under current limitation mode, considering the cases of three, single and double phase voltage sag, with the proposed VI impedance projected to a maximum current of 1.3 p.u.

Finally, Fig. 158 and 159 illustrate the converter's islanding capability, presenting the transition from grid-connected mode to island mode for SCR = 1 and 10. Since, the

converter is under voltage control mode the operation in island mode is natural.

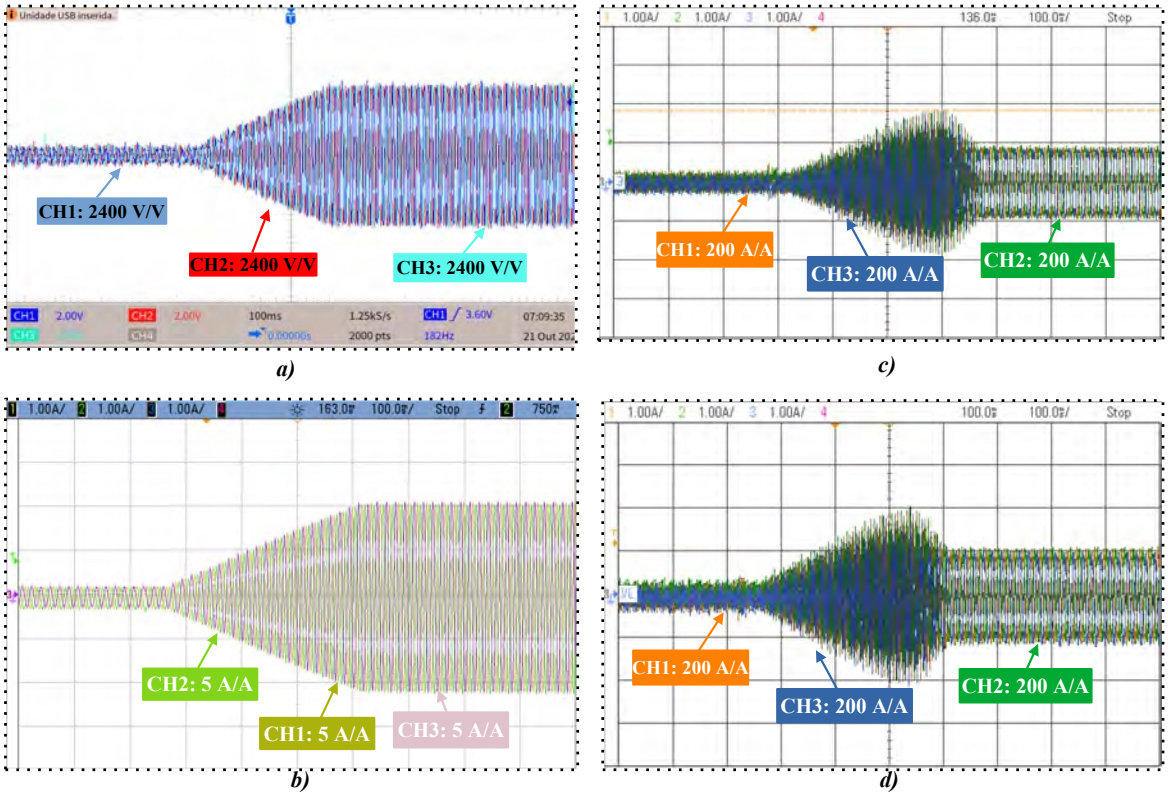

Figure 144 – Black-Start Capability: (a) Primary-side output voltages, (b) primary-side output currents, (c) currents at the Δ secondary winding, and (d) currents at the Y secondary winding.

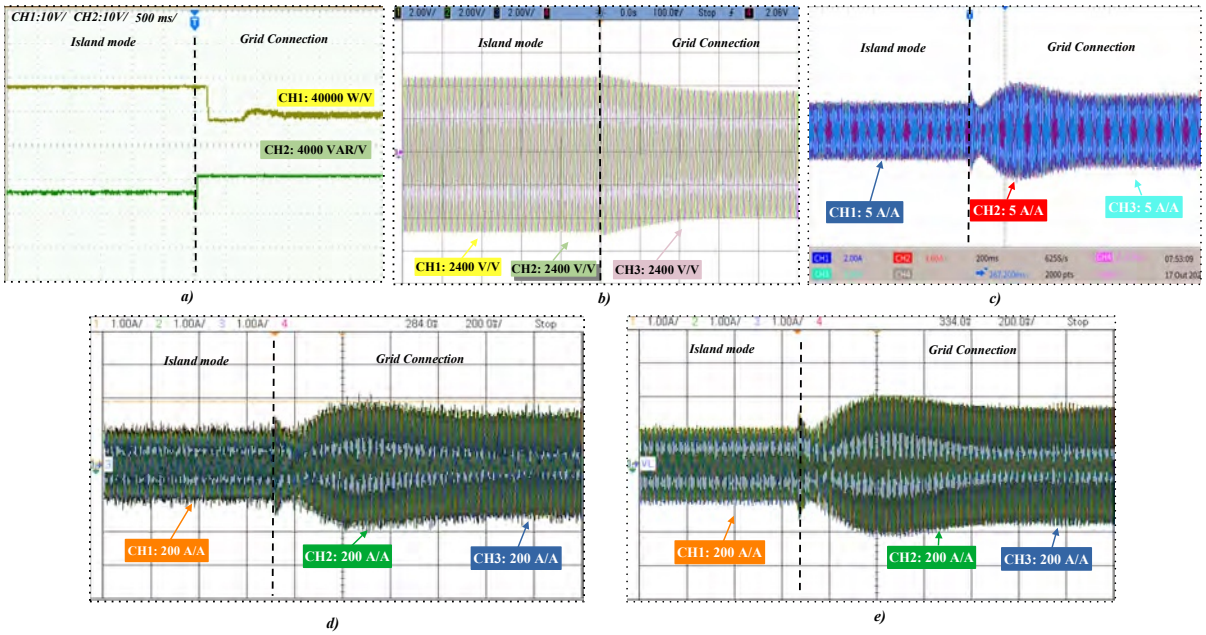

Figure 145 – Grid Connection in a Weak Grid (SCR = 1): (a) Active and reactive power, (b) output voltages, (c) primary-side output currents, (d) currents at the Δ secondary winding, and (e) currents at the Y secondary winding.

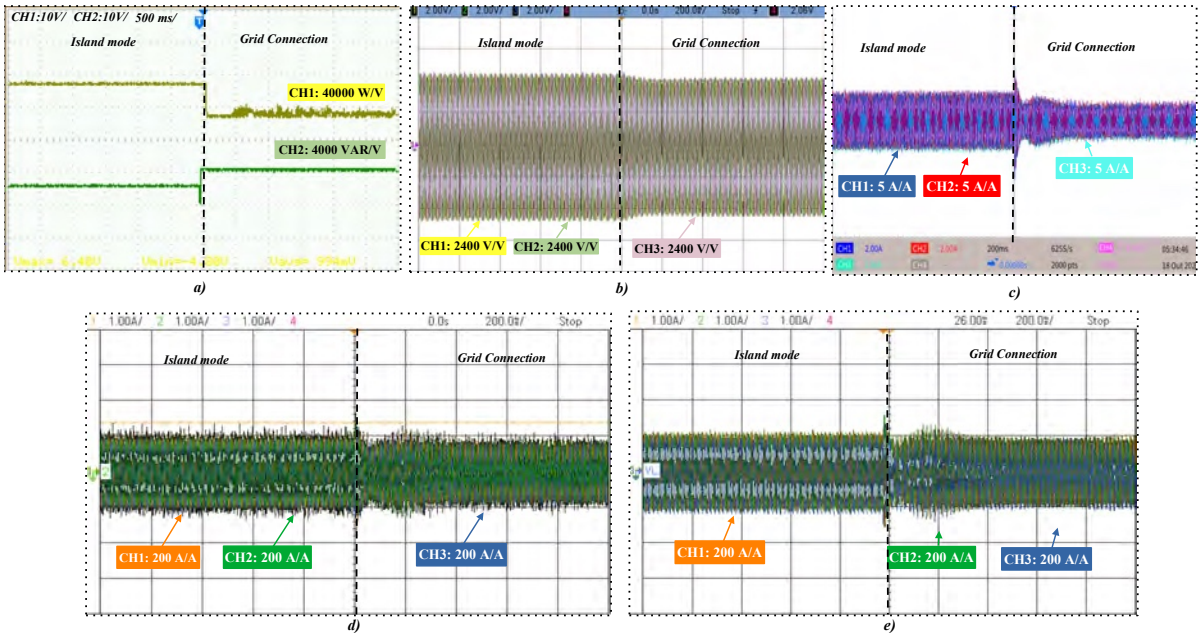

Figure 146 – Grid Connection in a medium Weak Grid (SCR = 3): (a) Active and reactive power, (b) output voltages, (c) primary-side output currents, (d) currents at the Δ secondary winding, and (e) currents at the Y secondary winding.

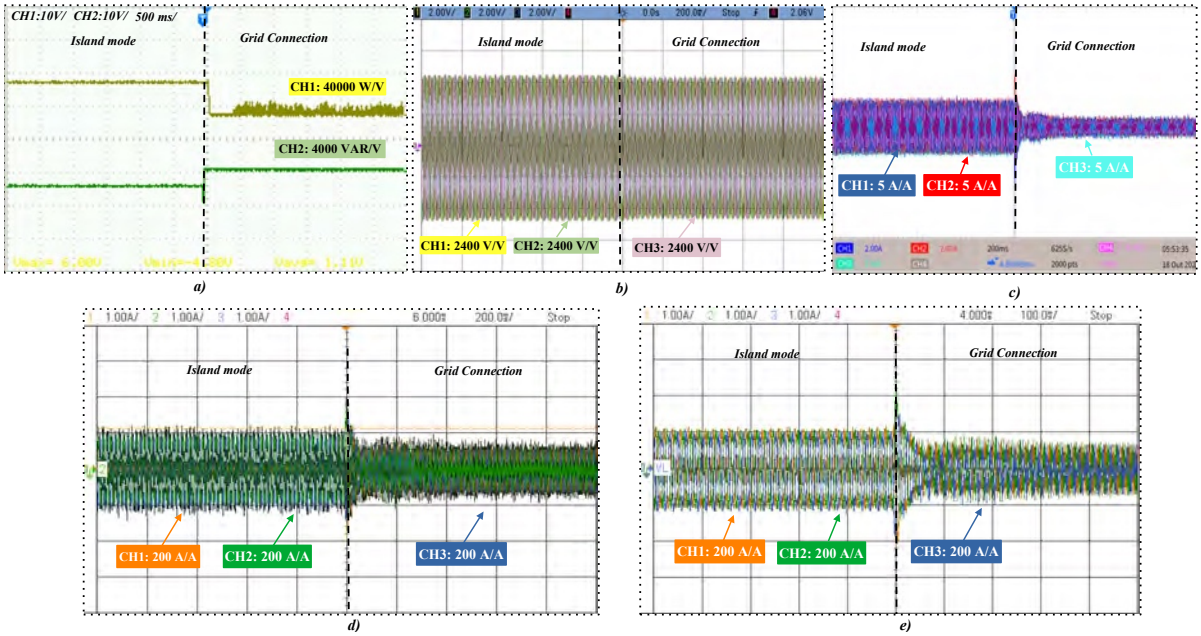

Figure 147 – Grid Connection in a Strong Grid (SCR = 10): (a) Active and reactive power during the grid-connection process, showing the transition from islanded operation to synchronized grid-connected operation; (b) output voltages of the ZHD converter, illustrating the voltage alignment with the strong grid; (c) primary-side output currents, highlighting the converter's current behavior as synchronization is achieved; (d) currents at the Δ secondary winding, showing the transformer's response under strong grid conditions; and (e) currents at the Y secondary winding, completing the representation of the current distribution across the transformer windings during grid connection.

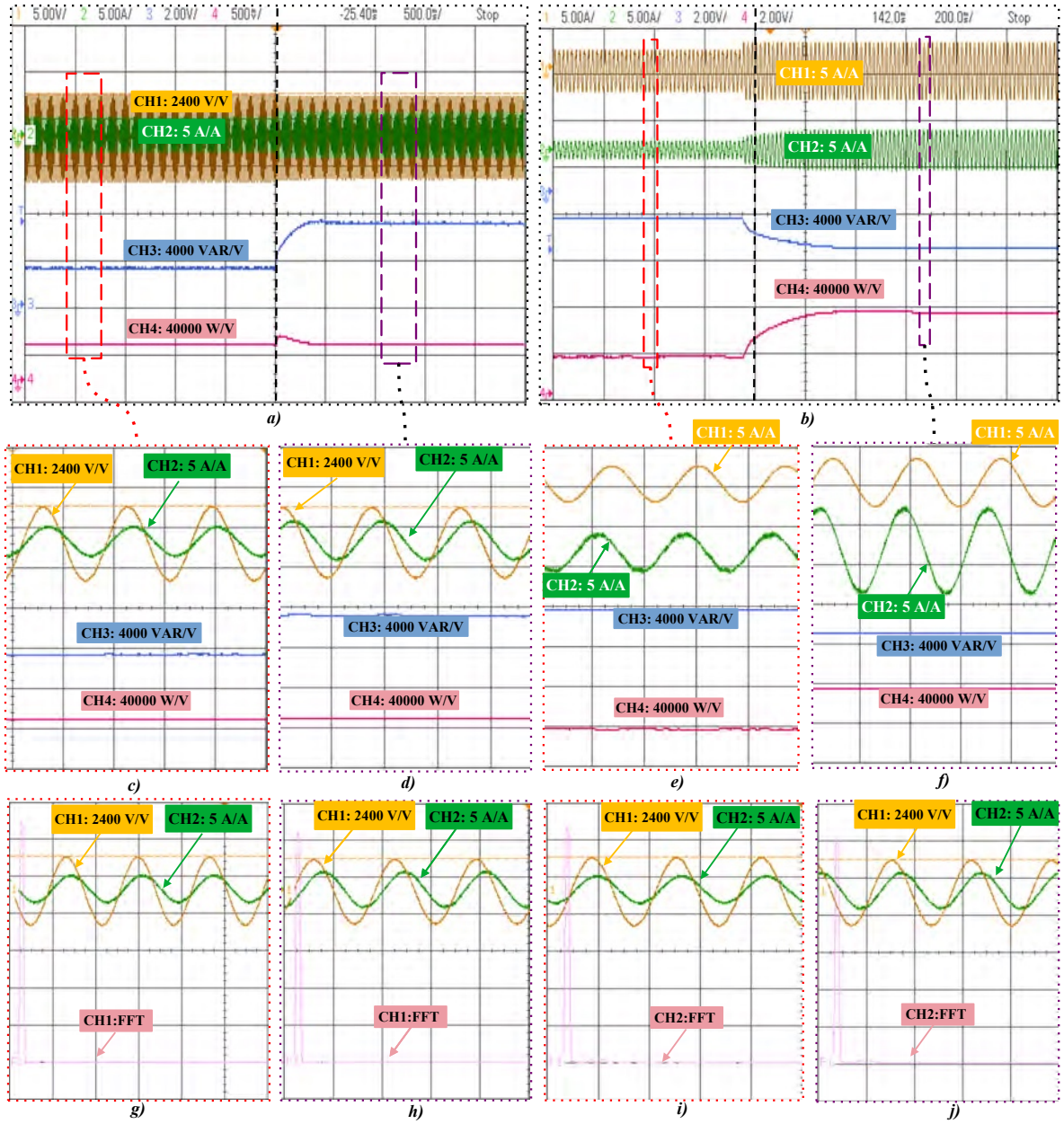

Figure 148 – Voltage Regulation under a Load Step (SCR = 1): (a) Grid voltage, current, and active and reactive power, illustrating the converter's dynamic response during the applied load variation; (b) load current, grid current, and active and reactive power at the grid side, showing the redistribution of power flows as the load changes; (c) zoomed view of the signals in (a) before the load step, highlighting the pre-disturbance steady-state conditions; (d) zoomed view of the signals in (a) after the load step, evidencing the converter's voltage regulation capability; (e) zoomed view of the signals in (b) before the load step, detailing the initial operating point of load and grid currents; (f) zoomed view of the signals in (b) after the load step, showing the updated current and power behavior following the disturbance; (g) output ZHD voltage FFT before the load step and (h) after the load step, indicating the harmonic profile of the output voltage; (i) output ZHD current FFT before the load step and (j) after the load step, showing the corresponding harmonic content of the output current.

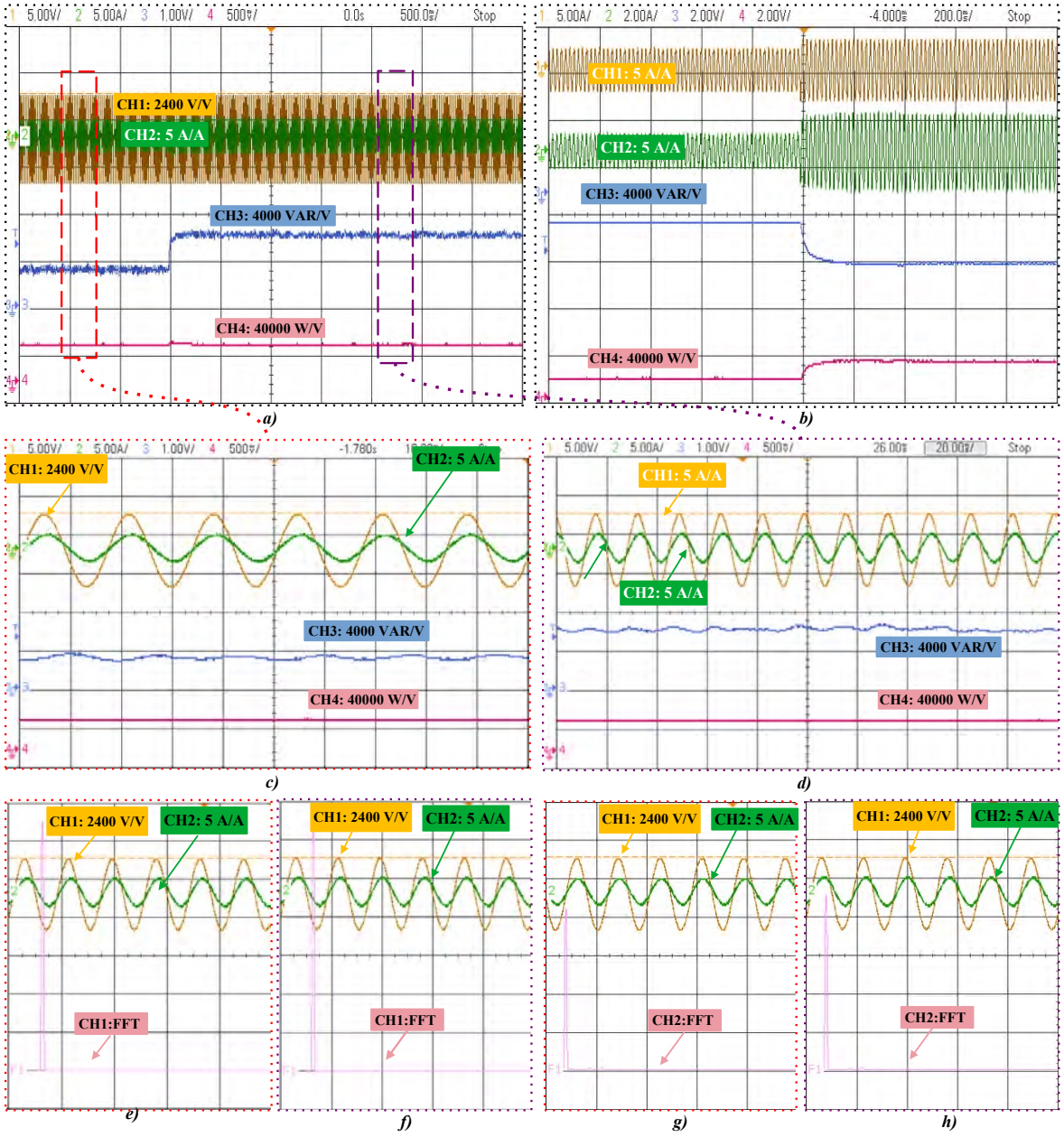

Figure 149 – Voltage Regulation under a Load Step (SCR = 3): (a) Grid voltage, current, and active and reactive power, illustrating the converter's response during the load transition; (b) load current, grid current, and active and reactive power measured at the grid side, highlighting the redistribution of power flows; (c) zoomed view of the signals from (a) before the load step, detailing the steady-state operation; (d) zoomed view of the signals from (a) after the load step, showing the voltage regulation performance; (e) zoomed view of the signals from (b) before the load step, emphasizing the pre-disturbance grid and load conditions; (f) zoomed view of the signals from (b) after the load step, illustrating the dynamic adjustment of currents and power; (g) output ZHD voltage FFT before the load step and (h) after the load step, evidencing the harmonic content and its variation due to the disturbance; (i) output ZHD current FFT before the load step and (j) after the load step, showing the harmonic behavior of the output current.

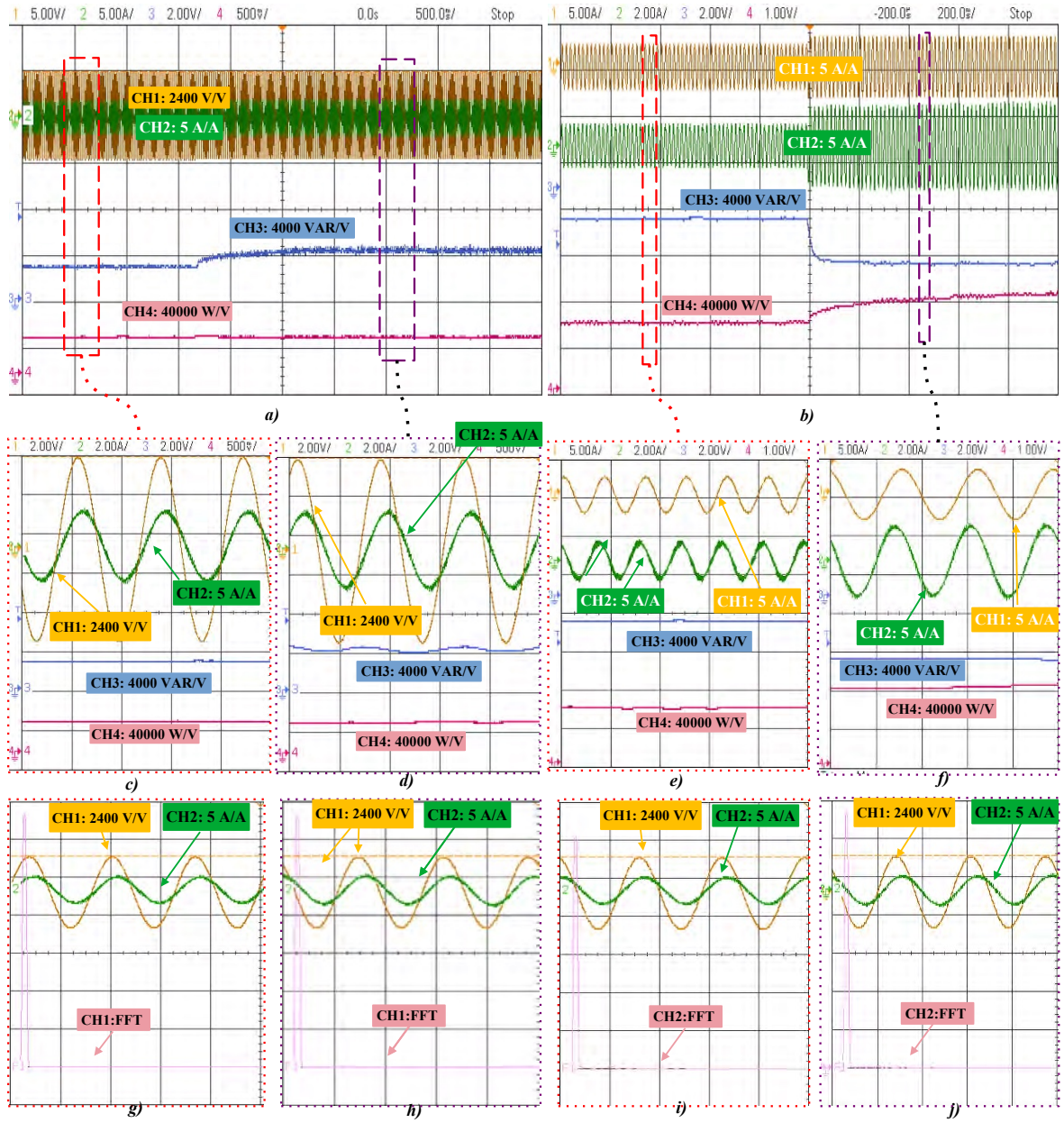

Figure 150 – Voltage Regulation under a Load Step (SCR = 10): (a) Grid voltage, current, and active and reactive power; (b) load current, grid current, and active and reactive power at the grid side; (c) zoomed view before and (d) after the load step from (a), highlighting the dynamic response of the grid voltage and power flow; (e) zoomed view before and (f) after the load step from (b), emphasizing the changes in load and grid currents; (g) output ZHD voltage FFT before and (h) after the load step, showing the harmonic spectrum variation; and (i) output ZHD current FFT before and (j) after the load step, illustrating the harmonic content of the output current under the transient condition.

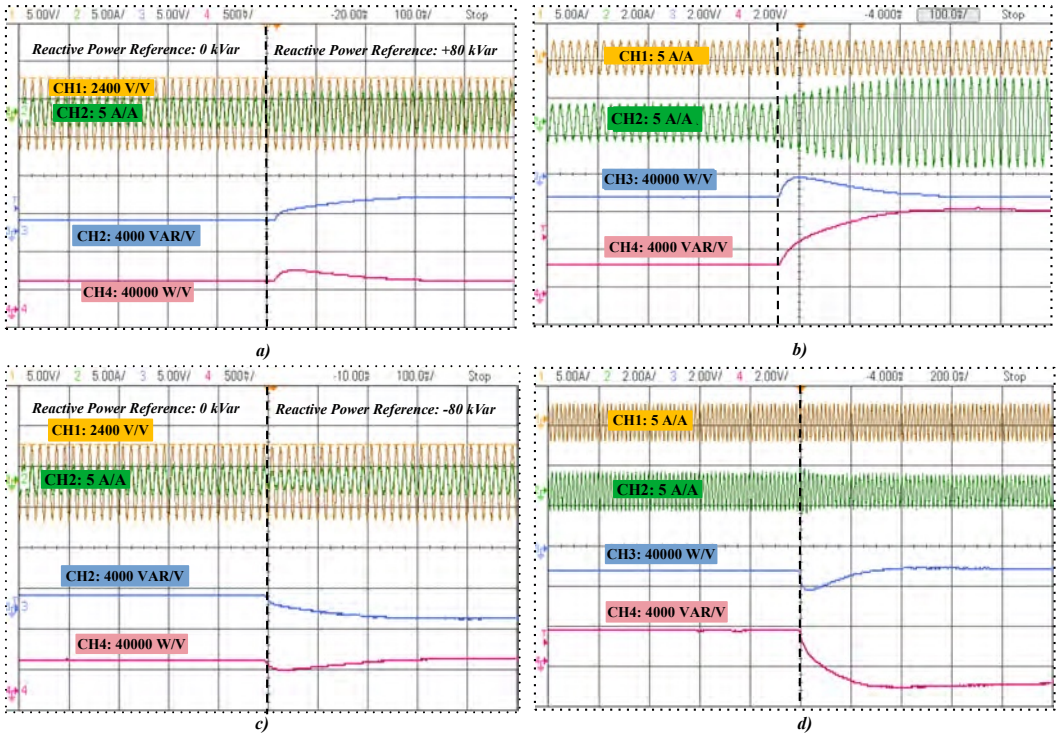

Figure 151 – Reactive power regulation (SCR = 1): (a),(c) phase-A ZHD voltage, current, and active/reactive power; (b),(d) phase-A load and grid currents and active/reactive power for ±80 kVar step references.

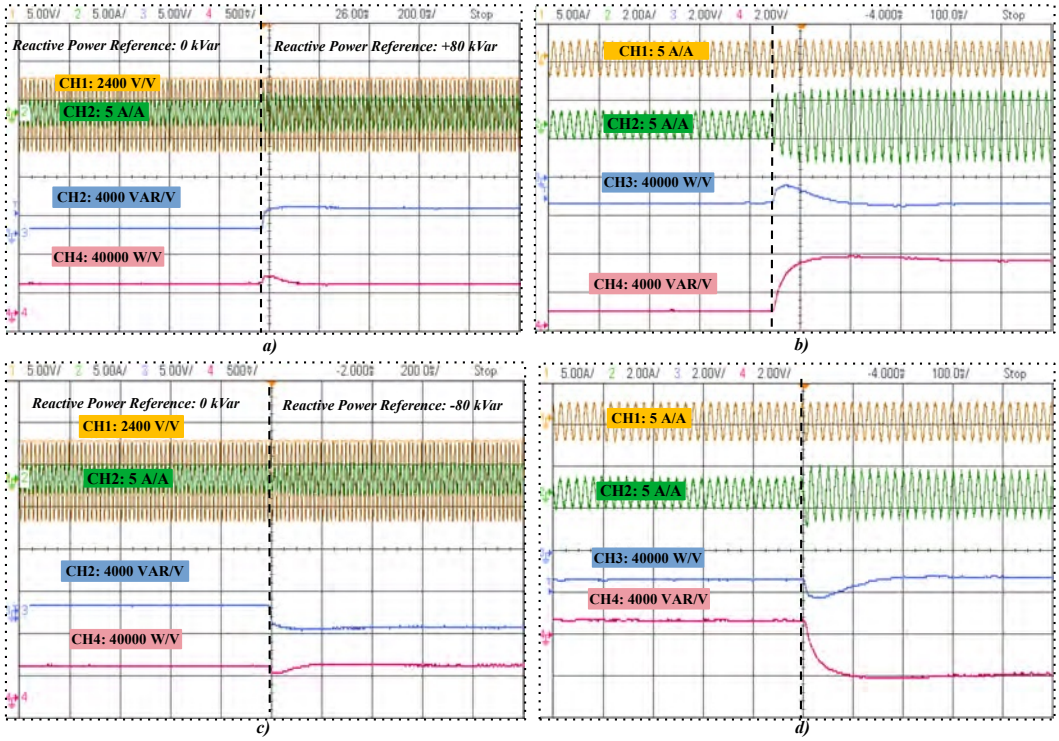

Figure 152 – Reactive power regulation (SCR = 3): (a),(c) phase-A ZHD voltage, current, and active/reactive power; (b),(d) phase-A load and grid currents and active/reactive power for ±80 kVar step references.

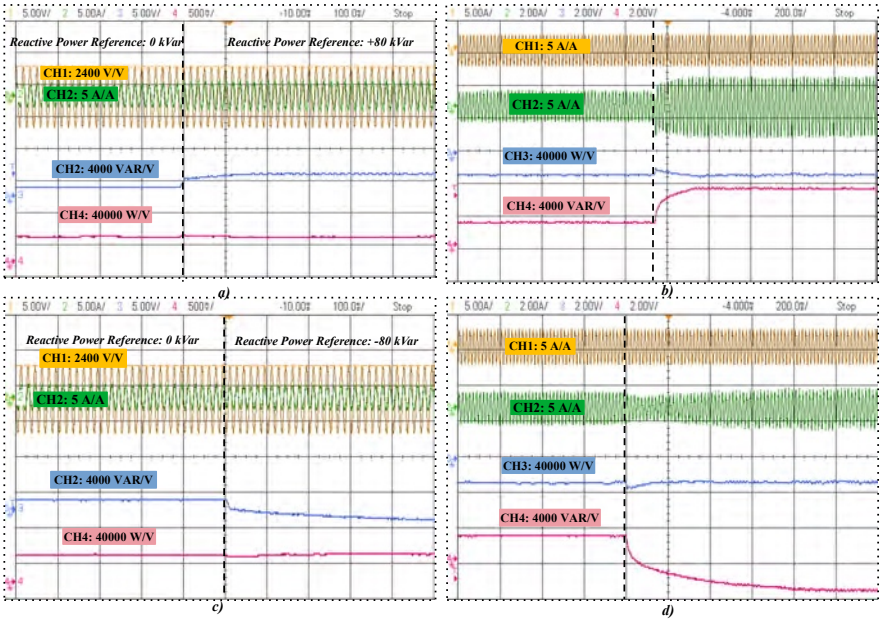

Figure 153 – Reactive power regulation (SCR = 10): (a),(c) phase-A ZHD voltage, current, and active/reactive power; (b),(d) phase-A load and grid currents and active/reactive power for ±80 kVar step references.

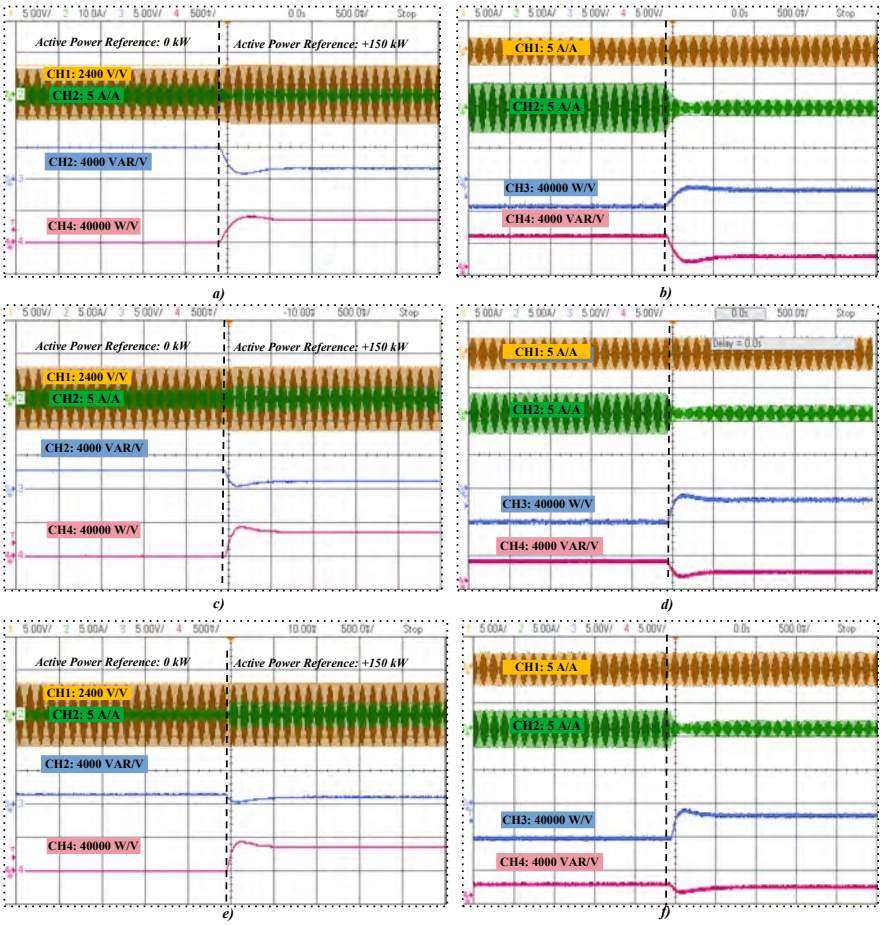

Figure 154 – Active power regulation: phase-A ZHD voltage, current, and active/reactive power, and phase-A load and grid currents for a +150 kW step reference under (a),(b) SCR = 1; (c),(d) SCR = 3; and (e),(f) SCR = 10.

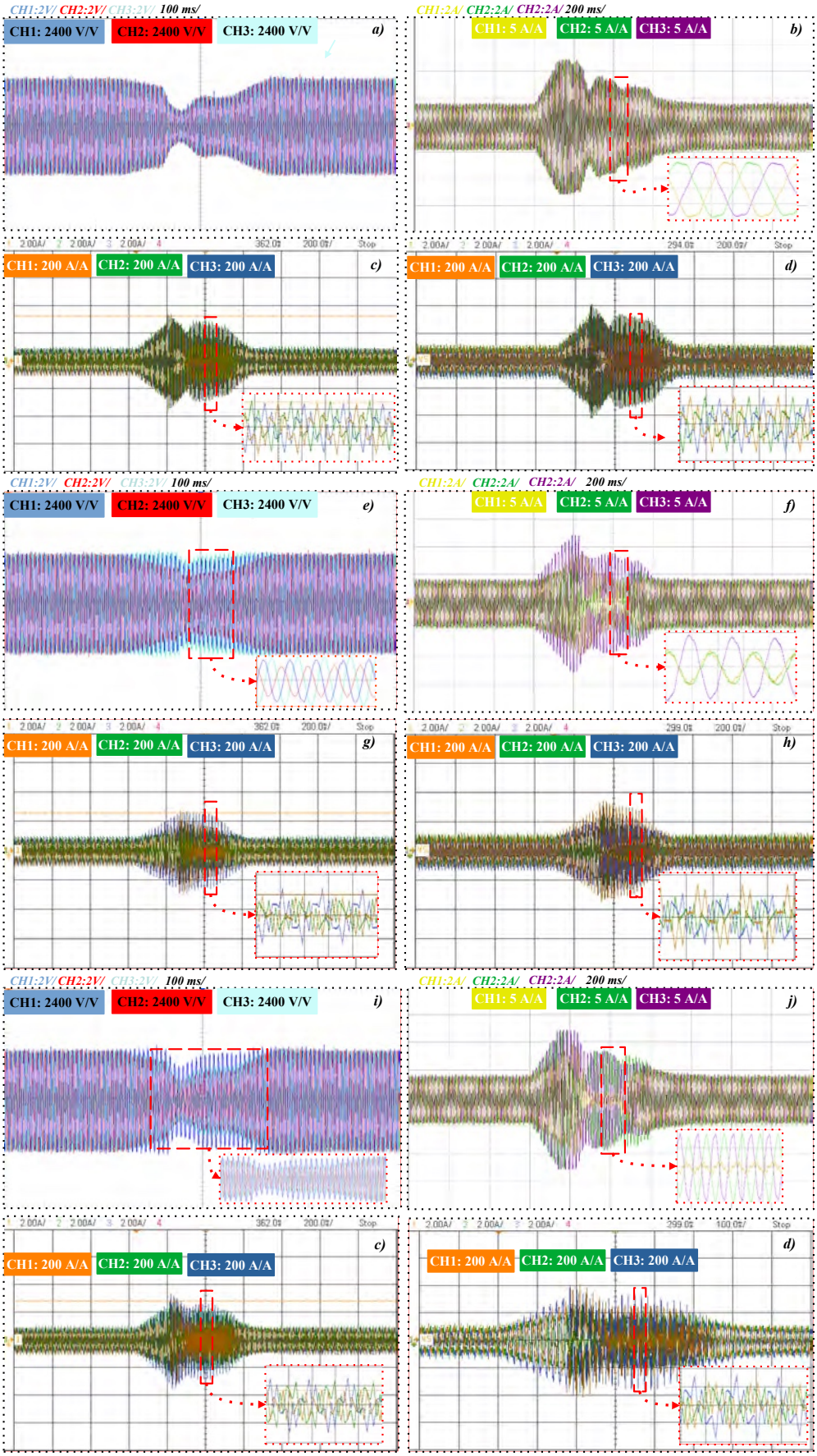

Figure 155 – Current Limitation (SCR = 1): (a) Three-phase, (e) single-phase, and (i) double-phase voltage sags; corresponding (b), (f), and (j) primary-side output currents; (c), (g), and (k) Δ-secondary currents; and (d), (h), and (l) Y-secondary currents.

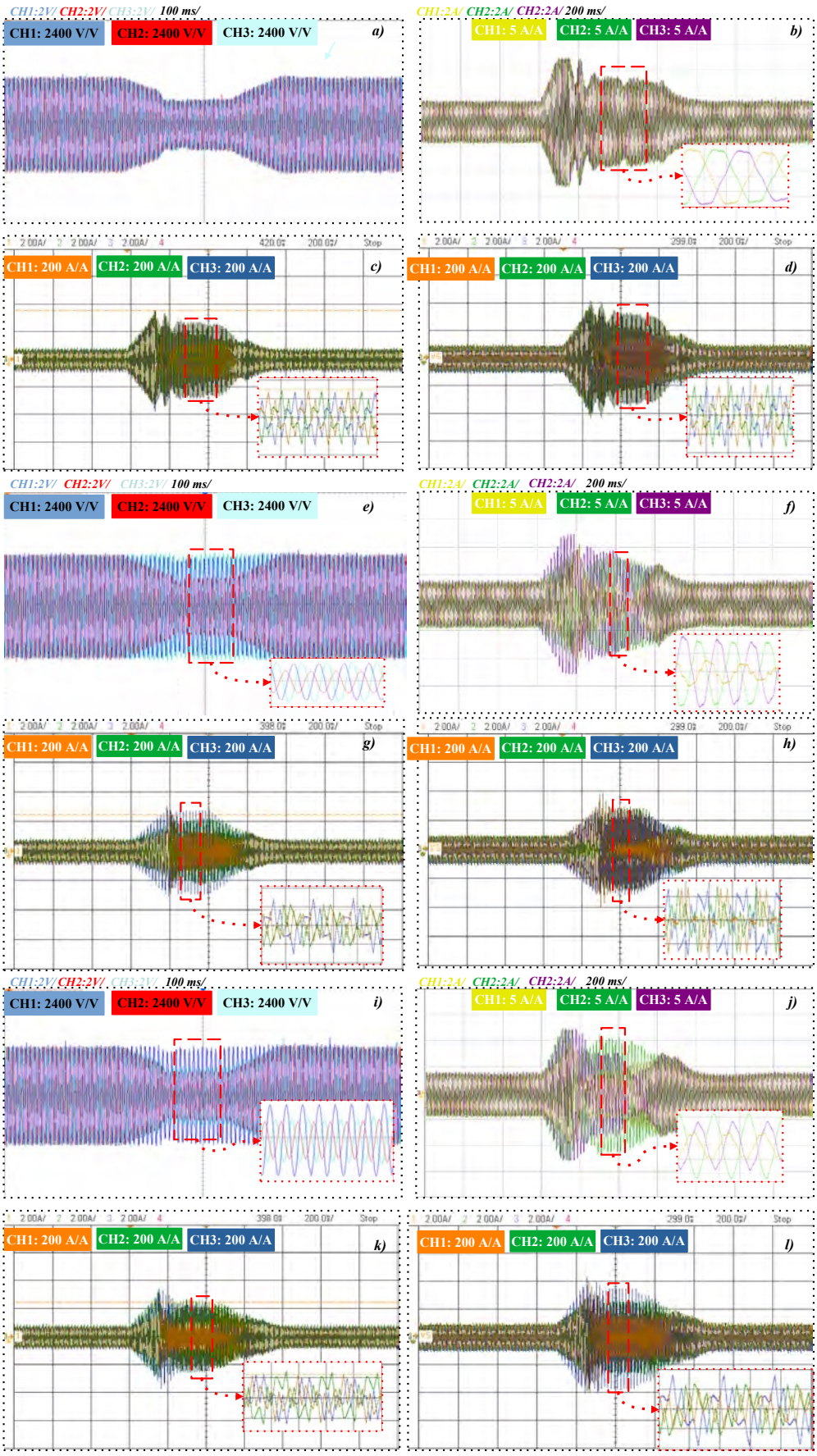

Figure 156 – Current Limitation (SCR = 3): (a) Three-phase, (e) single-phase, and (i) double-phase voltage sags; corresponding (b), (f), and (j) primary-side output currents; (c), (g), and (k) Δ-secondary currents; and (d), (h), and (l) Y-secondary currents.

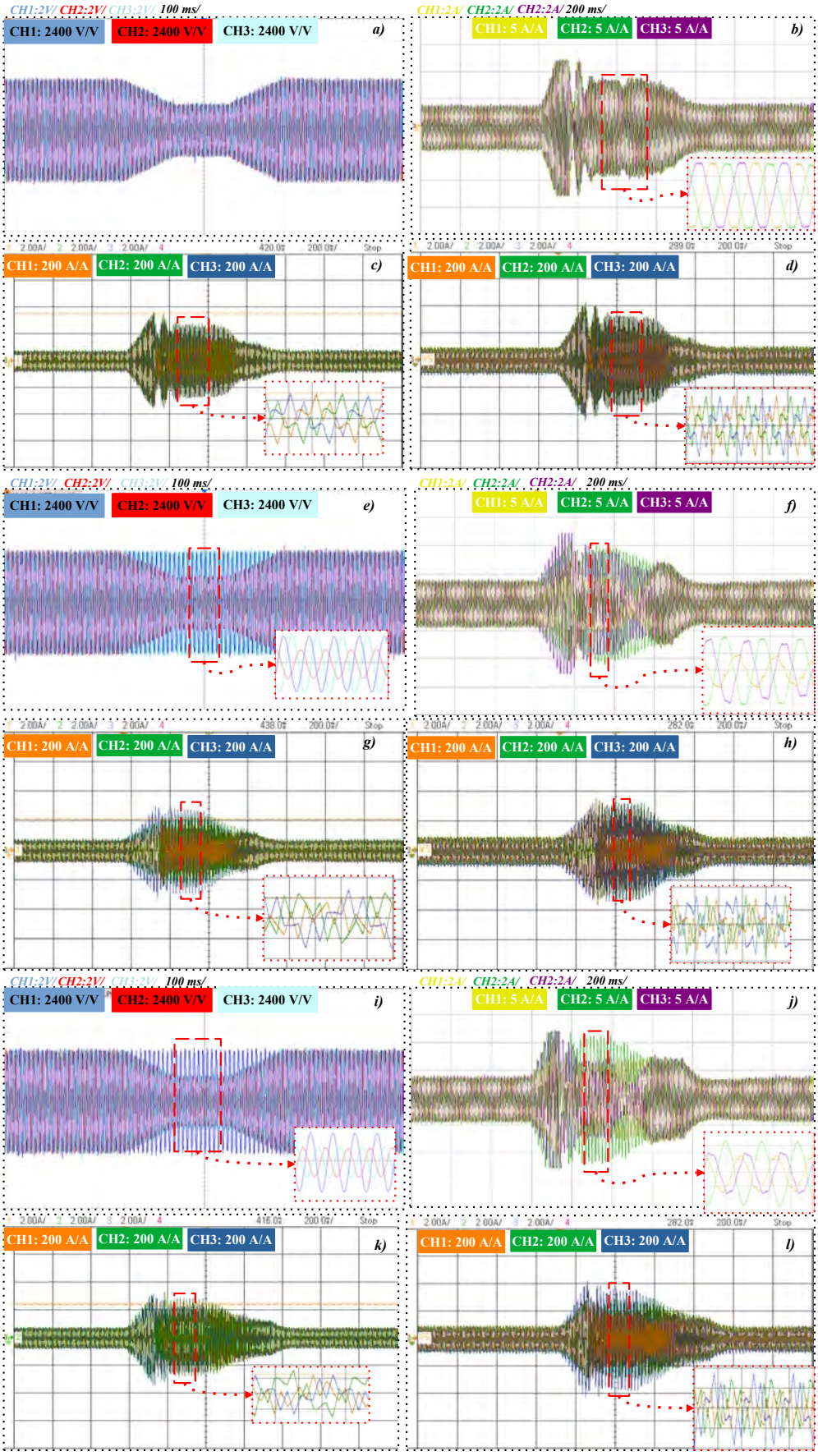

Figure 157 – Current Limitation (SCR = 10): (a) Three-phase, (e) single-phase, and (i) double-phase voltage sags; corresponding (b), (f), and (j) primary-side output currents; (c), (g), and (k) Δ-secondary currents; and (d), (h), and (l) Y-secondary currents.

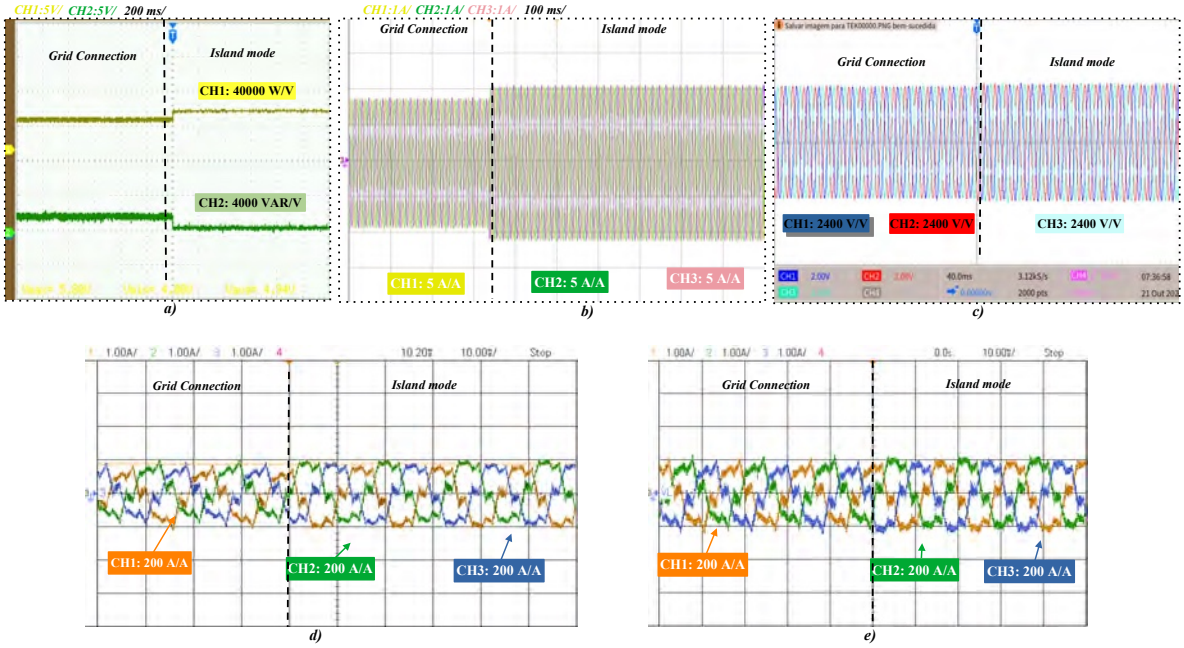

Figure 158 – Transition from Grid-Connected to Islanded Mode (SCR = 1): (a) Active and reactive power, (b) output current, (c) currents at the Δ secondary, and (d) currents at the Y secondary.

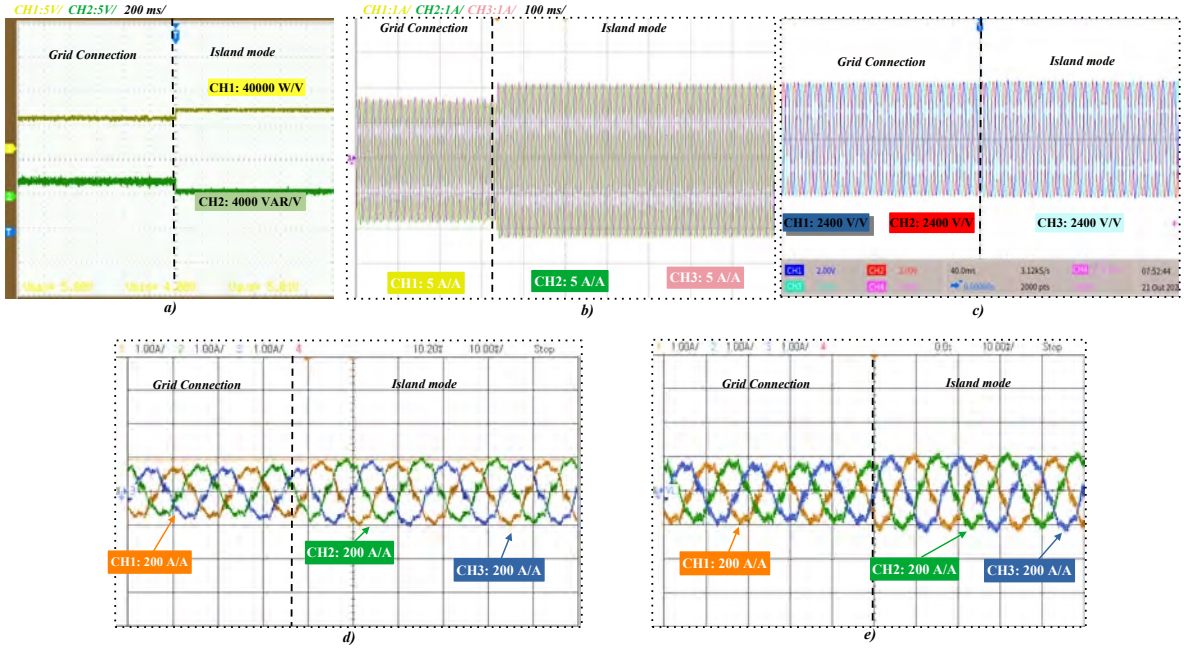

Figure 159 – Transition from Grid-Connected to Islanded Mode (SCR = 10): (a) Active and reactive power, (b) output current, (c) currents at the Δ secondary, and (d) currents at the Y secondary.

6.5 Conclusions

This chapter presented the Zero Harmonic Distortion (ZHD) converter as a promising solution for grid-forming applications in grid-connected systems. Unlike conventional converters, the ZHD does not require capacitive sinusoidal filters, as it inherently produces a sinusoidal output voltage. This characteristic leads to reduced cost, improved efficiency, and a more compact design. Built upon a widely adopted industrial power stage, the ZHD employs a straightforward open-loop voltage control structure, which avoids typical issues related to control interaction and resonances in grid-connected grid-forming applications. The simulation results demonstrated the converter's black-start capability, its stable islanded operation, and its effectiveness when operating as a grid-connected grid-forming converter. These results were achieved even under challenging conditions, including grid-side harmonic distortion, impedance estimation errors, and unbalance between the secondary windings. Overall, the ZHD converter emerges as a viable, robust, and technically attractive alternative for medium-voltage battery energy storage system (BESS) applications, reinforcing its potential as an effective grid-forming solution for grid-connected operation.

7 Conclusions and Future Work

The Zero Harmonic Distortion (ZHD) converter is proposed in this dissertation as a grid-forming solution for microgrid and power system applications. This chapter summarizes the main conclusions and highlights future research perspectives for extending the ZHD concept to broader microgrid and power system applications.

7.1 Conclusions

In this dissertation, the main focus was on the proposition of the ZHD as a grid-forming converter in island, microgrids and power systems applications due to your inherently sinusoidal voltage source behavior, eliminating characteristic harmonics up to the 50th order without capacitive filtering elements that typically impacts efficiency, compactness, reliability, contributes for resonance, feroresonance and control interaction issues. Owing to its voltage-source nature and reduction of control loops, the ZHD converter enables simplified transitions between grid-following (GFL) and islanded modes, and in grid-forming (GFM) grid-connected operation, it inherently avoids control-induced oscillations and resonances.

In Chapter 2, a detailed overview and comparison of power electronics were presented with respect to control strategies, operation modes, grid synchronization, and converter topologies. In medium-voltage systems, transformer-based and transformerless converter topologies were discussed. Although transformerless configurations have gained visibility, most commercial applications are still based on two- and three-level converters connected to the medium-voltage grid through low-frequency transformers, highlighting the relevance of the ZHD converter, which is based on a common and well-established industrial structure.

At Chapter 3, the ZHD concept was discussed in detail, including its operating principles, equivalent per-phase fundamental and harmonic modeling, the impact of harmonics on the transformer primary side, the analysis of symmetrical and asymmetrical faults, and the technical feasibility concerning converter topologies, output impedance, and power range considering the implementation using two and three-level converters.

In Chapter 4, the ZHD converter was evaluated under islanded-mode operation, where an open-loop control structure based solely on virtual impedance compensation was proposed, taking advantage of the converter's inherently sinusoidal output waveform. Using a two-level converter, the voltage and frequency regulation capability as well as the harmonic performance were verified. The impact of the secondary reactors on harmonic

behavior under nonlinear load conditions was analyzed, demonstrating the need for a design compromise between harmonic performance and reactor sizing. Hardware-in-the-Loop (HIL) and experimental results validated the islanded operation of the ZHD converter. A sensitivity analysis considering impedance estimation errors confirmed robust voltage regulation in both stand-alone and parallel operation, which was also verified through HIL testing. Finally, the ZHD converter employing three-level topologies was assessed, where simulation results demonstrated proper voltage and frequency regulation along with improved harmonic performance due to the reduced size of the secondary reactors.

In Chapter 5, a hybrid grid-following (GFL) and grid-forming (GFM) operation applicable to microgrid systems was proposed. After revisiting the GFL control approach developed in previous works, this study introduced a hybrid control strategy that enables current control only during grid-connected operation and disables it in islanded mode, taking advantage of the ZHD converter's inherent voltage-source characteristic, which eliminates the need for closed-loop voltage control. Another contribution of this chapter was the evaluation of the grid-connected operation under symmetrical and asymmetrical fault conditions. The results demonstrated that the converter naturally supports seamless transitions between grid-connected and islanded modes, even under normal or faulted grid conditions.

Finally, Chapter 6 presented the control structure of the ZHD converter for grid-forming operation under grid-connected conditions. The converter inherent voltage-source characteristic, with its capability to regulate voltage without internal closed-loop control, demonstrated the remarkable advantages of the ZHD converter compared to conventional topologies. The well-established virtual impedance–based current limitation technique was adapted and implemented for the ZHD converter to ensure safe operation under fault conditions. Simulation and Hardware-in-the-Loop (HIL) results validated the proposed approach, demonstrating effective voltage and reactive power regulation, as well as current limitation performance under both symmetrical and asymmetrical grid faults.

In summary, this dissertation concludes that the ZHD converter is a grid-forming solution with remarkable advantages in terms of power quality, control simplicity, and operational robustness. Its inherently sinusoidal voltage-source characteristic eliminates the need for closed-loop voltage control, enabling simplified transitions between grid-following and islanded modes and ensuring stable operation under both normal and faulted grid conditions. Furthermore, the converter demonstrates effective voltage and frequency regulation, black-start capability, and fault current limitation through a virtual impedance–based approach, all within a common industrial structure compatible with two- and three-level topologies. These attributes position the ZHD converter as a promising technology for future microgrid and power system applications, where reliability, scalability, and harmonic performance are critical design requirements.

7.2 Future Work

The ZHD control structures developed in this work were validated through simulation and Hardware-in-the-Loop (HIL) results, providing a strong foundation for future research and development. Prospective topics include:

- Experimental validation of the proposed control structures on a full-power prototype.
- Calculation of new Selective Harmonic Elimination (SHE-PWM) angle sets targeting the elimination of the 5th and 7th harmonics.
- Expansion of the ZHD concept to a multi-cell converter architecture.
- Extension of the proposed control structures for Medium-Voltage DC (MVDC) systems.
- Development of control strategies for ZHD-based grid-forming E-STATCOM applications.
- Characterization of the ZHD converter from a power system stability perspective, focusing on low- and high-frequency resonances and potential control interactions.
- Design of a hybrid synchronization scheme combining PLL and Power Synchronization Control (PSC) techniques.
- Implementation of hybrid control strategy and grid-connected GFM operation using three-level ZHD converters.

7.3 Publication List

This Ph.D. project has resulted one patent submission in eight conference papers accepted for publication and two journal papers, with invitations to submit the latest two conference papers for journal review.

Submitted patent:

- "PROCESSO PARA CONTROLE DE CONVERSORES FORMADORES DE MICRORREDES SEM MUDANÇA DE MODOS DE CONTROLE EM OPERAÇÃO CONECTADA E ILHADA", 22/12/2025, BR1020250286572.

Accepted Conference Papers:

- G. V. Ramos, T. M. Parreiras, D. A. d. L. Brandão, S. M. Silva, and B. d. J. C. Filho, "A Zero Harmonic Distortion Grid-Forming Converter for Islanded Microgrids," IEEE Industry Applications Society Annual Meeting (IAS), Nashville, TN, USA, 2023, pp. 1–8, doi: 10.1109/IAS54024.2023.10406502.

• G. V. Ramos, T. M. Parreiras, and B. de Jesus Cardoso Filho, "Control Performance Assessment of a Zero Harmonic Distortion Grid-Forming Converter in Islanded Microgrids," IEEE 8th Southern Power Electronics Conference and 17th Brazilian Power Electronics Conference (SPEC/COBEP), Florianópolis, Brazil, 2023, pp. 1–8, doi: 10.1109/SPEC56436.2023.10407128.

• G. V. Ramos, T. M. Parreiras, and B. d. J. C. Filho, "The Three-Level Zero Harmonic Distortion Grid-Forming Converter: A Practical Filterless Solution for Sinusoidal Voltages," IEEE 21st International Power Electronics and Motion Control Conference (PEMC), Pilsen, Czech Republic, 2024, pp. 1–6, doi: 10.1109/PEMC61721.2024.10726351.

• G. V. Ramos, T. M. Parreiras, and B. D. J. C. Filho, "A Three-Level Zero Harmonic Distortion Grid-Forming Converter for Medium Voltage Islanded Microgrids," Energy Conversion Congress & Expo Europe (ECCE Europe), Darmstadt, Germany, 2024, pp. 1–7, doi: 10.1109/ECCEEurope62508.2024.10751867.

• G. V. Ramos, T. M. Parreiras, F. Zhao, X. Wang, and B. d. J. C. Filho, "A Zero Harmonic Distortion Grid-Connected Grid-Forming Converter for Battery Energy Storage System Applications," IEEE Applied Power Electronics Conference and Exposition (APEC), Atlanta, GA, USA, 2025, pp. 1615–1621, doi: 10.1109/APEC48143.2025.10977568.

• G. V. Ramos, D. A. de L. Brandão, T. M. Parreiras, D. I. Brandao, and B. d. J. C. Filho, "A Zero Harmonic Distortion Master Converter for Medium Voltage Microgrids," IEEE Applied Power Electronics Conference and Exposition (APEC), Atlanta, GA, USA, 2025, pp. 1355–1362, doi: 10.1109/APEC48143.2025.10977510.

Accepted Journal Papers:

• G. V. Ramos, D. A. d. L. Brandão, T. M. Parreiras, S. M. Silva, and B. J. C. Filho, "A Zero Harmonic Distortion Grid-Forming Converter for Medium Voltage Islanded Microgrids," IEEE Transactions on Industry Applications, vol. 61, no. 1, pp. 809–820, Jan.–Feb. 2025, doi: 10.1109/TIA.2024.3462913.

• G. V. Ramos, T. M. Parreiras, and B. J. Cardoso Filho, "Control Performance Assessment of a Zero Harmonic Distortion Grid-Forming Converter for Medium Voltage Islanded Microgrids," Eletrônica de Potência, vol. 29, p. e202441, Oct. 2024.

Papers Under Preparation:

• G. V. Ramos, T. M. Parreiras, F. Zhao, X. Wang, and B. d. J. C. Filho, "A Zero Harmonic Distortion Grid-Connected Grid-Forming Converter for Battery Energy Storage Systems in Power System Applications," to be submitted for journal review.

• G. V. Ramos, D. A. de L. Brandão, T. M. Parreiras, D. I. Brandao, and B. d. J. C. Filho, "A Zero Harmonic Distortion Utility-Interactive Converter for Medium Voltage Microgrids," to be submitted for journal review.

Additional Contributions:

• D. A. de L. Brandão, G. V. Ramos, D. I. Brandao, and I. A. Pires, “Simultaneous, Coordinated and Centralized Control of Fast Charging Stations and Advanced Microgrids,” IEEE 21st International Power Electronics and Motion Control Conference (PEMC), Pilsen, Czech Republic, 2024, pp. 1–6, doi: 10.1109/PEMC61721.2024.10726331.

• D. A. de L. Brandão, J. M. S. Callegari, G. V. Ramos, D. I. Brandao, and I. A. Pires, “Coordinated Control of a Cluster of Advanced Microgrids and Fast Charging Stations in Islanded Mode,” IEEE International Electric Machines & Drives Conference (IEMDC), Houston, TX, USA, 2025, pp. 506–511, doi: 10.1109/IEMDC60492.2025.11061082.

• D. A. d. L. Brandao, A. R. Fialho, G. V. Ramos, T. M. Parreiras, I. A. Pires and B. d. J. Cardoso Filho, "Zero Harmonic Distortion Technology for Next-Generation Lite MVDC Distribution Systems,"IECON 2025 – 51st Annual Conference of the IEEE Industrial Electronics Society, Madrid, Spain, 2025, pp. 1-6, doi: 10.1109/IECON58223.2025.11221443.

References

Aboushal, M.; Moustafa, M. A new unified control strategy for inverter-based micro-grid using hybrid droop scheme. *Alexandria Engineering Journal*, v. 58, 11 2019. 56.

Adjustable speed electrical power drive systems - Part 3: EMC requirements and specific test methods for PDS and machine tools. *IEC 61800-3:2021*, 2022. 77.

Aghdam, S. A.; Agamy, M. Virtual oscillator-based methods for grid-forming inverter control: A review. *IET Renew. Power Gener.*, v. 16, n. 5, p. 835–855, 2022. 63.

Agorreta, J. L.; Borrega, M.; López, J.; Marroyo, L. Modeling and control of n -paralleled grid-connected inverters with lcl filter coupled due to grid impedance in pv plants. *IEEE Transactions on Power Electronics*, v. 26, n. 3, p. 770–785, 2011. Doi:10.1109/TPEL.2010.2095429. 163.

Ali, Z. et al. Three-phase phase-locked loop synchronization algorithms for grid-connected renewable energy systems: A review. *Renewable and Sustainable Energy Reviews*, v. 90, p. 434–452, 2018. ISSN 1364-0321. Available on: <https://www.sciencedirect.com/science/article/pii/S1364032118301813>. 44.

Almeida, C.; Filho, B. C. Shifting resonances in wind farms to higher frequencies due to tupf converters. *Journal of Control, Automation and Electrical Systems*, v. 29, 08 2018. 75.

Almeida, C. E. *Identificação e manejo de ressonâncias em parques eólicos: aplicação dos conversores TUPF*. Tese (Doutorado) — Universidade Federal de Minas Gerais, 2019. 75.

Almeida, C. E.; Filho, B. de J. C. Impact of active front end topology on wind farm resonance. In: *2017 IEEE Power Energy Society General Meeting*. 2017. p. 1–5. 40, 73, 74, 75, 129, and 140.

Alves, M. H. da S.; Parreiras, T. M.; Filho, B. de J. C. The true unity power factor converter applied to photovoltaic applications. In: *2019 IEEE 15th Brazilian Power Electronics Conference and 5th IEEE Southern Power Electronics Conference (COBEP/SPEC)*. 2019. p. 1–6. 73, 75, 129, and 140.

Alves, M. H. S. *Conversor de fator de potência verdadeiramente unitário como inversor central em geração fotovoltaica*. 2020. 75.

Anderson, J.; Peng, F. Four quasi-z-source inverters. In: *2008 IEEE Power Electronics Specialists Conference*. 2008. p. 2743–2749. 95.

Andishgar, M.; Gholipour, E.; Hooshmand, R.-A. An overview of control approaches of inverter-based microgrids in islanding mode of operation. *Renewable and Sustainable Energy Reviews*, v. 80, p. 1043–1060, 12 2017. 58.

Anttila, S.; Döhler, J. S.; Oliveira, J. G.; Boström, C. Grid forming inverters: A review of the state of the art of key elements for microgrid operation. *Energies*, v. 15, n. 15, 2022. ISSN 1996-1073. Available on: <https://www.mdpi.com/1996-1073/15/15/5517>. 11, 25, 38, 39, 44, 49, 54, 65, and 67.

Antunes, H.; Silva, S.; Filho, B.; Ferreira, R.; Brandao, D. I. A new configuration for a grid forming converter in ac islanded microgrid. In: *PCIM Europe 2017; International Exhibition and Conference for Power Electronics, Intelligent Motion, Renewable Energy and Energy Management*. 2017. p. 1–8. 39, 66, 67, 69, and 75.

Antunes, H. M. A.; Silva, S. M.; Brandao, D. I.; Ferreira, R. V.; Filho, B. d. J. C. Analysis of a grid-forming converter based on repetitive control in centralized ac microgrid. In: *2017 IEEE 8th International Symposium on Power Electronics for Distributed Generation Systems (PEDG)*. 2017. p. 1–8. 39 and 75.

Arachchige, L. W.; Rajapakse, A. Microgrids research: A review of experimental microgrids and test systems. *Renewable and Sustainable Energy Reviews*, v. 15, p. 186–202, 01 2011. 57.

Aragon, D.; Unamuno, E.; Ceballos, S.; Barrena, J. Comparative small-signal evaluation of advanced grid-forming control techniques. *Electric Power Systems Research*, v. 211, p. 108154, 2022. ISSN 0378-7796. Available on: <https://www.sciencedirect.com/science/article/pii/S0378779622003728>. 64.

Araujo, L. S.; Brandao, D. I. Self-adaptive control for grid-forming converter with smooth transition between microgrid operating modes. *International Journal of Electrical Power & Energy Systems*, v. 135, p. 107479, 2022. ISSN 0142-0615. Doi:10.1016/j.ijepes.2021.107479. Available on: <https://www.sciencedirect.com/science/article/pii/S0142061521007183>. 128.

Arghir, C.; Jouini, T.; Dörfler, F. Grid-forming control for power converters based on matching of synchronous machines. *Automatica*, v. 95, p. 273–282, 2018. ISSN 0005-1098. Available on: <https://www.sciencedirect.com/science/article/pii/S0005109818302796>. 57, 64, and 65.

Arnedo, L.; Dwari, S.; Blasko, V.; Park, S. 80 kw hybrid solar inverter for standalone and grid connected applications. In: *2012 Twenty-Seventh Annual IEEE Applied Power Electronics Conference and Exposition (APEC)*. 2012. p. 270–276. Doi:10.1109/APEC.2012.6165830. 128.

Ashabani, M.; Freijedo, F. D.; Golestan, S.; Guerrero, J. M. Inducverters: Pll-less converters with auto-synchronization and emulated inertia capability. *IEEE Transactions on Smart Grid*, v. 7, n. 3, p. 1660–1674, 2016. 44.

Awal, M. A.; Yu, H.; Husain, I.; Yu, W.; Lukic, S. M. Selective harmonic current rejection for virtual oscillator controlled grid-forming voltage source converters. *IEEE Transactions on Power Electronics*, v. 35, n. 8, p. 8805–8818, 2020. 62.

Awal, M. A.; Yu, H.; Tu, H.; Lukic, S. M.; Husain, I. Hierarchical control for virtual oscillator based grid-connected and islanded microgrids. *IEEE Transactions on Power Electronics*, v. 35, n. 1, p. 988–1001, 2020. 62 and 65.

Azevedo, G. M. S.; Cavalcanti, M. C.; Neves, F. A. S.; Limongi, L. R.; Bradaschia, F. A control of microgrid power converter with smooth transient response during the change of connection mode. In: *2013 Brazilian Power Electronics Conference*. 2013. p. 1008–1015. 39, 52, 66, and 75.

Baghaee, H.; Mirsalim, M.; Gharehpetian, G. B.; Talebi, H. A new current limiting strategy and fault model to improve fault ride-through capability of inverter interfaced ders in autonomous microgrids. *Sustainable Energy Technologies and Assessments*, v. 24, p. 71–81, 12 2017. 56.

Bahrani, B.; Rufer, A. A cascade voltage controller for three-phase islanded microgrids. In: *2013 IEEE Power Energy Society General Meeting*. 2013. p. 1–6. 39, 66, and 75.

Baimel, D.; Belikov, J.; Guerrero, J. M.; Levron, Y. Dynamic modeling of networks, microgrids, and renewable sources in the dq0 reference frame: A survey. *IEEE Access*, v. 5, p. 21323–21335, 2017. 54.

Barklund, E.; Pogaku, N.; Prodanovic, M.; Hernandez-Aramburo, C.; Green, T. C. Energy management in autonomous microgrid using stability-constrained droop control of inverters. *IEEE Transactions on Power Electronics*, v. 23, n. 5, p. 2346–2352, 2008. 56.

Beck, H.-P.; Hesse, R. Virtual synchronous machine. In: *2007 9th International Conference on Electrical Power Quality and Utilisation*. 2007. p. 1–6. 44 and 48.

Belila, A.; Amirat, Y.; Benbouzid, M.; Berkouk, E. M.; Yao, G. Virtual synchronous generators for voltage synchronization of a hybrid pv-diesel power system. *International Journal of Electrical Power Energy Systems*, v. 117, p. 105677, 2020. ISSN 0142-0615. Available on: <https://www.sciencedirect.com/science/article/pii/S0142061519302984>. 11 and 59.

Bergna-Diaz, G.; Suul, J. A.; D'Arco, S. Energy-based state-space representation of modular multilevel converters with a constant equilibrium point in steady-state operation. *IEEE Transactions on Power Electronics*, v. 33, n. 6, p. 4832–4851, 2018. 40, 72, and 75.

Bevrani, H.; Ise, T.; Miura, Y. Virtual synchronous generators: A survey and new perspectives. *International Journal of Electrical Power Energy Systems*, v. 54, p. 244–254, 2014. ISSN 0142-0615. Available on: <https://www.sciencedirect.com/science/article/pii/S0142061513003062>. 58 and 62.

Blaabjerg, F.; Yang, Y.; Kim, K. A.; Rodriguez, J. Power electronics technology for large-scale renewable energy generation. *Proceedings of the IEEE*, v. 111, n. 4, p. 335–355, 2023. Doi:10.1109/JPROC.2023.3253165. 163.

Blas, R. L.; Mauricio, J. M.; Gomez-Exposito, A.; Savaghebi, M.; Guerrero, J. Grid-forming vsc control in four-wire systems with unbalanced nonlinear loads. *Electric Power Systems Research*, v. 152, p. 249–256, 11 2017. 66.

Blaschke, F. The principle of field orientation applied to the new transvector closed loop system for rotating field machines. *Siemens Rev*, vol.34, p. pp.217–220, 1972. 48.

Bloemink, J. M.; Iravani, M. R. Control of a multiple source microgrid with built-in islanding detection and current limiting. *IEEE Transactions on Power Delivery*, v. 27, n. 4, p. 2122–2132, 2012. 55.

Bottrell, N.; Green, T. C. Comparison of current-limiting strategies during fault ride-through of inverters to prevent latch-up and wind-up. *IEEE Transactions on Power Electronics*, v. 29, n. 7, p. 3786–3797, 2014. 53.

Bouzid, A. E. M. et al. A survey on control of electric power distributed generation systems for microgrid applications. *Renewable and Sustainable Energy Reviews*, v. 44, p. 751–766, 05 2015. 25, 55, and 57.

Brandão, D. A.; Parreiras, T. M.; Pires, I. A.; Filho, B. d. J. C. Robust implementation of zero harmonic distortion converter in distorted grids. In: *2022 IEEE Industry Applications Society Annual Meeting (IAS)*. 2022. p. 1–9. 75.

Brandão, D. A. d. L.; Parreiras, T. M.; Pires, I. A.; F., B. d. J. C. Electric arc furnace reactive compensation system using zero harmonic distortion converter. *IEEE Transactions on Industry Applications*, v. 58, n. 5, p. 6833–6841, 2022. 74, 75, 129, and 140.

Brandão, D. A. de L. *Carregador Veicular Ultra-rápido Com Conversor True Unit Power Factor: Implementação e Validação Em Hardware-in-the-loop*. 2021. 75.

Brandão, D. A. L.; Parreiras, T. M.; Pires, I. A.; Filho, B. d. J. C. Electric arc furnace reactive compensation system using true power factor - reactive compensator converter. In: *2021 IEEE Industry Applications Society Annual Meeting (IAS)*. 2021. p. 1–8. 75.

Brandão, D. A. d. L.; Parreiras, T. M.; Pires, I. A.; Filho, B. d. J. C. Extreme fast charging station for multiple vehicles with sinusoidal currents at the grid side. In: *2022 IEEE Transportation Electrification Conference and Expo, Asia-Pacific (ITEC Asia-Pacific)*. 2022. p. 1–6. 74, 75, 129, and 140.

Bratcu, A. I.; Aulagnier, V. Control of energy storage systems for three-phase applications. In: *2015 19th International Conference on System Theory, Control and Computing (ICSTCC)*. 2015. p. 666–672. 39, 67, and 75.

Braun, M. et al. The future of power system restoration: Using distributed energy resources as a force to get back online. *IEEE Power and Energy Magazine*, v. 16, n. 6, p. 30–41, 2018. 36.

Bruckner, T.; Bernet, S.; Guldner, H. The active npc converter and its loss-balancing control. *IEEE Transactions on Industrial Electronics*, v. 52, n. 3, p. 855–868, 2005. Doi: 10.1109/TIE.2005.847586. 96.

Cardenas, R.; Pena, R.; Clare, J.; Wheeler, P.; Zanchetta, P. A repetitive control system for four-leg matrix converters feeding non-linear loads. *Electric Power Systems Research*, v. 104, p. 18–27, 11 2013. 55.

Chandorkar, M.; Divan, D.; Adapa, R. Control of parallel connected inverters in standalone ac supply systems. *IEEE Transactions on Industry Applications*, v. 29, n. 1, p. 136–143, 1993. 48 and 65.

Cherevatskiy, S. et al. A 30mw grid forming bess boosting reliability in south australia and providing market services on the national electricity market. In: *18th Int'l Wind Integration Workshop*. Oct. 2019. p. 1–5. 162 and 163.

Cintron-Rivera, J. G.; Li, Y.; Jiang, S.; Peng, F. Z. Quasi-z-source inverter with energy storage for photovoltaic power generation systems. In: *2011 Twenty-Sixth Annual IEEE Applied Power Electronics Conference and Exposition (APEC)*. 2011. p. 401–406. 96.

Colombino, M.; Groß, D.; Brouillon, J.-S.; Dörfler, F. Global phase and magnitude synchronization of coupled oscillators with application to the control of grid-forming power inverters. *IEEE Transactions on Automatic Control*, v. 64, n. 11, p. 4496–4511, 2019. 57, 62, 63, and 65.

Cortes, P. et al. Model predictive control of an inverter with output *lc* filter for ups applications. *IEEE Transactions on Industrial Electronics*, v. 56, n. 6, p. 1875–1883, 2009. 55.

Cortés, P. R. *Aportaciones a los acondicionadores activos de corriente en derivación para redes trifásicas de cuatro hilos*. Tese (Doutorado) — Universitat Politècnica de Catalunya, 2005. 129 and 132.

Cossart, Q.; Colas, F.; Kestelyn, X. Simplified converters models for the analysis and simulation of large transmission systems using 100% power electronics. In: *2018 20th European Conference on Power Electronics and Applications (EPE'18 ECCE Europe)*. 2018. p. P.1–P.10. 44.

Dang, P.; Ellinger, T.; Petzoldt, J. Dynamic interaction analysis of apf systems. *IEEE Transactions on Industrial Electronics*, v. 61, n. 9, p. 4467–4473, 2014. Doi:10.1109/TIE.2013.2289896. 163.

D'Arco, S.; Suul, J. A. Virtual synchronous machines — classification of implementations and analysis of equivalence to droop controllers for microgrids. In: *2013 IEEE Grenoble Conference*. 2013. p. 1–7. 48, 56, 58, 59, and 65.

D'Arco, S.; Suul, J. A. Equivalence of virtual synchronous machines and frequency-droops for converter-based microgrids. *IEEE Transactions on Smart Grid*, v. 5, n. 1, p. 394–395, 2014. 62.

Dhople, S. V.; Johnson, B. B.; Hamadeh, A. O. Virtual oscillator control for voltage source inverters. In: *2013 51st Annual Allerton Conference on Communication, Control, and Computing (Allerton)*. 2013. p. 1359–1363. 63.

Dias, A. da S.; Alves, J. A.; Torri, P. J. Transformerless topologies for medium voltage converters. In: *2016 Petroleum and Chemical Industry Conference Europe (PCIC Europe)*. 2016. p. 1–9. 39, 68, and 69.

Dokus, M.; Mertens, A. On the coupling of power-related and inner inverter control loops of grid-forming converter systems. *IEEE Access*, v. 9, p. 16173–16192, 2021. Doi:10.1109/ACCESS.2021.3053060. 163.

Driesen, J.; Visscher, K. Virtual synchronous generators. In: *2008 IEEE Power and Energy Society General Meeting - Conversion and Delivery of Electrical Energy in the 21st Century*. 2008. p. 1–3. 44 and 48.

Du, W. et al. Modeling of grid-forming and grid-following inverters for dynamic simulation of large-scale distribution systems. *IEEE Transactions on Power Delivery*, v. 36, n. 4, p. 2035–2045, 2021. 37 and 39.

D'Arco, S.; Suul, J.; Fosso, O. A virtual synchronous machine implementation for distributed control of power converters in smartgrids. *Electric Power Systems Research*, v. 122, 05 2015. 58.

Electromagnetic compatibility (EMC) - Part 2-4: Environment - Compatibility levels in industrial plants for low-frequency conducted disturbances. *IEC 61000-2-4:2002*, 2002. 77.

Electromagnetic Compatibility (EMC) – Part 4-7: Testing and measurement techniques – General guide on harmonics and interharmonics measurements and instrumentation, for power supply systems and equipment connected thereto. *IEC International Standard 61000-4-7*, 2009. 77.

Engelbrecht, T. et al. Statcom technology evolution for tomorrow's grid: E-statcom, statcom with supercapacitor-based active power capability. *IEEE Power and Energy Magazine*, v. 21, n. 2, p. 30–39, 2023. Doi:10.1109/MPE.2022.3230969. 163.

Enslin, J.; Heskes, P. Harmonic interaction between a large number of distributed power inverters and the distribution network. *IEEE Transactions on Power Electronics*, v. 19, n. 6, p. 1586–1593, 2004. Doi:10.1109/TPEL.2004.836615. 163.

Fang, J.; Tang, Y.; Li, H.; Li, X. A battery/ultracapacitor hybrid energy storage system for implementing the power management of virtual synchronous generators. *IEEE Transactions on Power Electronics*, v. 33, n. 4, p. 2820–2824, 2018. Doi:10.1109/TPEL.2017.2759256. 162 and 163.

Farivar, G. G. et al. Grid-connected energy storage systems: State-of-the-art and emerging technologies. *Proceedings of the IEEE*, v. 111, n. 4, p. 397–420, 2023. 71 and 75.

Freytes, J.; Li, J.; Préville, G. de; Thouvenin, M. Grid-forming control with current limitation for mmc under unbalanced fault ride-through. *IEEE Transactions on Power Delivery*, v. 36, n. 3, p. 1914–1916, 2021. 39, 72, and 75.

Ganjian-Aboukheili, M.; Shahabi, M.; Shafiee, Q.; Guerrero, J. M. Seamless transition of microgrids operation from grid-connected to islanded mode. *IEEE Transactions on Smart Grid*, v. 11, n. 3, p. 2106–2114, 2020. 52.

Gao, F.; Iravani, M. R. A control strategy for a distributed generation unit in grid-connected and autonomous modes of operation. *IEEE Transactions on Power Delivery*, v. 23, n. 2, p. 850–859, 2008. 128.

Gervasio, F. A.; Bueno, E.; Mastromauro, R. A.; Liserre, M.; Stasi, S. Voltage control of microgrid systems based on 3lnpc inverters with lcl-filter in islanding operation. In: *2015 International Conference on Renewable Energy Research and Applications (ICRERA)*. 2015. p. 827–832. 39, 67, 69, and 75.

Gkountaras, A.; Dieckerhoff, S.; Sezi, T. Evaluation of current limiting methods for grid forming inverters in medium voltage microgrids. In: *2015 IEEE Energy Conversion Congress and Exposition (ECCE)*. 2015. p. 1223–1230. 53, 55, 56, 69, and 73.

Gonzalez-Espin, F.; Valdivia, V.; Hogan, D.; Diaz, D.; Foley, R. F. Operating modes of a commercial and industrial building microgrid with electrical generation and storage. In: *2014 IEEE 5th International Symposium on Power Electronics for Distributed Generation Systems (PEDG)*. 2014. p. 1–5. 39, 66, and 75.

Gonzatti, R. B. et al. Implementation of a grid-forming converter based on modified synchronous reference frame. In: *IECON 2014 - 40th Annual Conference of the IEEE Industrial Electronics Society*. 2014. p. 2116–2121. 66.

Gouveia, J.; Moreira, C. L.; Lopes, J. A. P. Grid-forming inverters sizing in islanded power systems – a stability perspective. In: *2019 International Conference on Smart Energy Systems and Technologies (SEST)*. 2019. p. 1–6. 56.

Grid-Forming Capabilities: Towards System Level Integration. *European Network of Transmission System Operators for Electricity-ENTSO-E*, 2021. 77.

Grid forming technology: bulk power system reliability con- siderations. *North American Electric Reliability Corporation-NERC*, 2021. 77.

Groß, D.; Colombino, M.; Brouillon, J.-S.; Dörfler, F. The effect of transmission-line dynamics on grid-forming dispatchable virtual oscillator control. *IEEE Transactions on Control of Network Systems*, v. 6, n. 3, p. 1148–1160, 2019. 57 and 62.

Guennegues, V.; Gollentz, B.; Meibody-Tabar, F.; Rael, S.; Leclere, L. A converter topology for high speed motor drive applications. In: *2009 13th European Conference on Power Electronics and Applications*. 2009. p. 1–8. 96.

Guerrero, J.; Vicuna, L. G. de; Matas, J.; Castilla, M.; Miret, J. Output impedance design of parallel-connected ups inverters with wireless load-sharing control. *IEEE Transactions on Industrial Electronics*, v. 52, n. 4, p. 1126–1135, 2005. 58.

Guerrero, J. M.; Vasquez, J. C.; Matas, J.; Castilla, M.; Vicuna, L. Garcia de. Control strategy for flexible microgrid based on parallel line-interactive ups systems. *IEEE Transactions on Industrial Electronics*, v. 56, n. 3, p. 726–736, 2009. 44.

Guerrero, J. M.; Vasquez, J. C.; Matas, J.; Vicuna, L. G. de; Castilla, M. Hierarchical control of droop-controlled ac and dc microgrids—a general approach toward standardization. *IEEE Transactions on Industrial Electronics*, v. 58, n. 1, p. 158–172, 2011. 58.

Han, H. et al. Review of power sharing control strategies for islanding operation of ac microgrids. *IEEE Transactions on Smart Grid*, v. 7, n. 1, p. 200–215, 2016. 45, 49, 52, 56, 67, 68, and 98.

Harnefors, L.; Kukkola, J.; Routimo, M.; Hinkkanen, M.; Wang, X. A universal controller for grid-connected voltage-source converters. *IEEE Journal of Emerging and Selected Topics in Power Electronics*, v. 9, n. 5, p. 5761–5770, 2021. 48.

Hatziargyriou, N.; Asano, H.; Iravani, R.; Marnay, C. Microgrids. *IEEE Power and Energy Magazine*, v. 5, n. 4, p. 78–94, 2007. 36.

He, J.; Li, Y. W.; Bosnjak, D.; Harris, B. Investigation and active damping of multiple resonances in a parallel-inverter-based microgrid. *IEEE Transactions on Power Electronics*, v. 28, n. 1, p. 234–246, 2013. Doi:10.1109/TPEL.2012.2195032. 163.

Henninger, S.; Schroeder, M.; Jaeger, J. Grid-forming droop control of a modular multilevel converter in laboratory. In: *2018 IEEE Power Energy Society General Meeting (PESGM)*. 2018. p. 1–5. 39 and 72.

Hesse, R.; Turschner, D.; Beck, H.-P. Micro grid stabilization using the virtual synchronous machine (visma). *Renewable energy & power quality journal*, v. 1, p. 676–681, 2009. 44.

High Penetration of Power Electronic Interfaced Power Sources and the potential contribution of grid forming converters. *European Network of Transmission System Operators for Electricity-ENTSO-E*, 2019. 77.

Hiller, M.; Sommer, R.; Beuermann, M. Converter topologies and power semiconductors for industrial medium voltage converters. In: *2008 IEEE Industry Applications Society Annual Meeting*. 2008. p. 1–8. 39, 68, and 69.

Hossain, M. A.; Pota, H. R.; Issa, W.; Hossain, M. J. Overview of ac microgrid controls with inverter-interfaced generations. *Energies*, v. 10, n. 9, 2017. ISSN 1996-1073. Available on: <https://www.mdpi.com/1996-1073/10/9/1300>. 49 and 52.

Hosseinpour, M.; Mohamadian, M.; Varjani, A. Design and analysis of the droop-controlled parallel four-leg inverters to share unbalanced and nonlinear loads. *Przeglad Elektrotechniczny*, v. 90, p. 105–110, 01 2014. 55.

Hu, H.; Shi, Q.; He, Z.; He, J.; Gao, S. Potential harmonic resonance impacts of pv inverter filters on distribution systems. *IEEE Transactions on Sustainable Energy*, v. 6, n. 1, p. 151–161, 2015. Doi:10.1109/TSTE.2014.2352931. 163.

Hu, J.; Zhu, J.; Dorrell, D. G.; Guerrero, J. M. Virtual flux droop method—a new control strategy of inverters in microgrids. *IEEE Transactions on Power Electronics*, v. 29, n. 9, p. 4704–4711, 2014. 58.

Hu, S.-H.; Kuo, C.-Y.; Lee, T.-L.; Guerrero, J. M. Droop-controlled inverters with seamless transition between islanding and grid-connected operations. In: *2011 IEEE Energy Conversion Congress and Exposition*. 2011. p. 2196–2201. Doi:10.1109/ECCE.2011.6064059. 128.

IEEE Standard for Harmonic Control in Electric Power Systems. *IEEE Std 519-2022 (Revision of IEEE Std 519-2014)*, p. 1–31, 2022. 40, 77, and 78.

IEEE Standard for Interconnection and Interoperability of Distributed Energy Resources with Associated Electric Power Systems Interfaces. *IEEE Std 1547-2018 (Revision of IEEE Std 1547-2003)*, p. 1–138, 2018. 40, 77, 78, and 170.

IEEE Standard for Interconnection and Interoperability of Inverter-Based Resources (IBRs) Interconnecting with Associated Transmission Electric Power Systems. *IEEE Std 2800-2022*, p. 1–180, 2022. 77.

IEEE Standard for Performance of Adjustable-Speed AC Drives Rated 375 kW and Larger. *IEEE Std 1566-2015 (Revision of IEEE Std 1566-2005)*, p. 1–74, 2015. 77.

Ishaq, S. et al. A review on recent developments in control and optimization of micro grids. *Energy Reports*, v. 8, p. 4085–4103, 2022. ISSN 2352-4847. Available on: <https://www.sciencedirect.com/science/article/pii/S2352484722000804>. 11, 54, and 66.

Jain, M.; Gupta, S.; Masand, D.; Agnihotri, G.; Jain, S. Real-time implementation of islanded microgrid for remote areas. *Journal of Control Science and Engineering*, v. 2016, p. 1–9, 01 2016. 55.

J.Machowski J.W.Bialek, a. In: _____. *Power System Dynamics: Stability And Control*. 2007. v. 2nd ed. Hoboken, NJ, USA: John Wiley Sons. 51.

Johnson, B.; Rodriguez, M.; Sinha, M.; Dhople, S. Comparison of virtual oscillator and droop control. In: *2017 IEEE 18th Workshop on Control and Modeling for Power Electronics (COMPEL)*. 2017. p. 1–6. 62.

Johnson, B. B.; Dhople, S. V.; Hamadeh, A. O.; Krein, P. T. Synchronization of parallel single-phase inverters with virtual oscillator control. *IEEE Transactions on Power Electronics*, v. 29, n. 11, p. 6124–6138, 2014. 44, 57, 62, and 63.

Johnson, B. B.; Sinha, M.; Ainsworth, N. G.; Dörfler, F.; Dhople, S. V. Synthesizing virtual oscillators to control islanded inverters. *IEEE Transactions on Power Electronics*, v. 31, n. 8, p. 6002–6015, 2016. 48 and 63.

Jouini, T.; Arghir, C.; Dörfler, F. Grid-forming control for power converters based on matching of synchronous machines. *Automatica*, v. 95, 06 2017. 44.

Juntunen, R. et al. Identification of resonances in parallel connected grid inverters with lc- and lcl-filters. In: *2015 IEEE Applied Power Electronics Conference and Exposition (APEC)*. 2015. p. 2122–2127. Doi:10.1109/APEC.2015.7104642. 163.

Justino, J. C. G.; Parreiras, T. M.; Filho, B. de J. C. Hundreds kw charging stations for e-buses operating under regular ultra-fast charging. In: *2014 IEEE Energy Conversion Congress and Exposition (ECCE)*. 2014. p. 892–899. 74, 75, 129, and 140.

Justino, J. C. G.; Parreiras, T. M.; Filho, B. J. C. Hundreds kw charging stations for e-buses operating under regular ultra-fast charging. *IEEE Transactions on Industry Applications*, v. 52, n. 2, p. 1766–1774, 2016. 75.

Katiraei, F.; Iravani, R.; Hatziargyriou, N.; Dimeas, A. Microgrids management. *IEEE Power and Energy Magazine*, v. 6, n. 3, p. 54–65, 2008. 44 and 45.

Khadem, S.; Basu, M.; Conlon, M. Parallel operation of inverters and active power filters in distributed generation system — a review. *Renewable and Sustainable Energy Reviews*, v. 15, n. 9, p. 5155–5168, 2011. ISSN 1364-0321. Available on: <https://www.sciencedirect.com/science/article/pii/S1364032111002814>. 57.

Kim, J.-W.; Choi, H.-S.; Cho, B. H. A novel droop method for converter parallel operation. *IEEE Transactions on Power Electronics*, v. 17, n. 1, p. 25–32, 2002. 58.

Kocewiak, H.; Aristi, I. A.; Gustavsen, B.; Hołdyk, A. Modelling of wind power plant transmission system for harmonic propagation and small-signal stability studies. *IET Renewable Power Generation*, v. 13, n. 5, p. 717–724, 2019. Doi:10.1049/iet-rpg.2018.5077. 163.

Kojima, M.; Hirabayashi, K.; Kawabata, Y.; Ejiogu, E.; Kawabata, T. Novel vector control system using deadbeat-controlled pwm inverter with output lc filter. *IEEE Transactions on Industry Applications*, v. 40, n. 1, p. 162–169, 2004. 55.

Krishnamoorthy, H. S.; Rana, D.; Garg, P.; Enjeti, P. N.; Pitel, I. J. Wind turbine generator–battery energy storage utility interface converter topology with medium-frequency transformer link. *IEEE Transactions on Power Electronics*, v. 29, n. 8, p. 4146–4155, 2014. 95.

Kroposki, B. et al. Achieving a 100 renewable grid: Operating electric power systems with extremely high levels of variable renewable energy. *IEEE Power and Energy Magazine*, v. 15, n. 2, p. 61–73, 2017. 36, 43, 44, and 51.

Kulkarni, O. V.; Doolla, S.; Fernandes, B. G. Mode transition control strategy for multiple inverter-based distributed generators operating in grid-connected and standalone mode. *IEEE Transactions on Industry Applications*, v. 53, n. 6, p. 5927–5939, 2017. 52.

Kulkarni, O. V.; Doolla, S.; Fernandes, B. G. Mode transition control strategy for multiple inverter-based distributed generators operating in grid-connected and standalone mode. *IEEE Transactions on Industry Applications*, v. 53, n. 6, p. 5927–5939, 2017. Doi:10.1109/TIA.2017.2743682. 128 and 129.

Kunisch, H.-J.; Kramer, K. G.; Dominik, H. Battery energy storage another option for load-frequency-control and instantaneous reserve. *IEEE Transactions on Energy Conversion*, EC-1, n. 3, p. 41–46, 1986. 48.

Kwon, J.; Yoon, S.; Choi, S. Indirect current control for seamless transfer of three-phase utility interactive inverters. *IEEE Transactions on Power Electronics*, v. 27, n. 2, p. 773–781, 2012. Doi:10.1109/TPEL.2011.2161335. 128 and 129.

E. V. Larsen & R. W. Delmerico. *Battery energy storage power conditioning system*. 1998. US5798633. U.S. Patent. 48.

Lasseter, R.; Paigi, P. Microgrid: a conceptual solution. In: *2004 IEEE 35th Annual Power Electronics Specialists Conference (IEEE Cat. No.04CH37551)*. 2004. v. 6, p. 4285–4290 Vol.6. 36, 43, and 98.

Lasseter, R. H.; Chen, Z.; Pattabiraman, D. Grid-forming inverters: A critical asset for the power grid. *IEEE Journal of Emerging and Selected Topics in Power Electronics*, v. 8, n. 2, p. 925–935, 2020. 37, 51, and 52.

Lasseter, R. H.; Chen, Z.; Pattabiraman, D. Grid-forming inverters: A critical asset for the power grid. *IEEE Journal of Emerging and Selected Topics in Power Electronics*, v. 8, n. 2, p. 925–935, 2020. Doi:10.1109/JESTPE.2019.2959271. 162.

Leon, J. I.; Vazquez, S.; Franquelo, L. G. Multilevel converters: Control and modulation techniques for their operation and industrial applications. *Proceedings of the IEEE*, v. 105, n. 11, p. 2066–2081, 2017. 71 and 75.

Li, G.; Chen, Y.; Luo, A.; Wang, H. An enhancing grid stiffness control strategy of statcom/bess for damping sub-synchronous resonance in wind farm connected to weak grid. *IEEE Transactions on Industrial Informatics*, v. 16, n. 9, p. 5835–5845, 2020. Doi:10.1109/TII.2019.2960863. 162 and 163.

Li, Y.; Gu, Y.; Green, T. C. Revisiting grid-forming and grid-following inverters: A duality theory. *IEEE Transactions on Power Systems*, v. 37, n. 6, p. 4541–4554, 2022. 51.

Li, Y.; Gu, Y.; Green, T. C. Revisiting grid-forming and grid-following inverters: A duality theory. *IEEE Transactions on Power Systems*, v. 37, n. 6, p. 4541–4554, 2022. Doi: 10.1109/TPWRS.2022.3151851. 162.

Li, Y.; Vilathgamuwa, D.; Loh, P. C. Design, analysis, and real-time testing of a controller for multibus microgrid system. *IEEE Transactions on Power Electronics*, v. 19, n. 5, p. 1195–1204, 2004. 128.

Li, Y. W.; Kao, C.-N. An accurate power control strategy for power-electronics-interfaced distributed generation units operating in a low-voltage multibus microgrid. *IEEE Transactions on Power Electronics*, v. 24, n. 12, p. 2977–2988, 2009. 58.

Li, Z. et al. Control of a grid-forming inverter based on sliding-mode and mixed H_2/H_∞ control. *IEEE Transactions on Industrial Electronics*, v. 64, n. 5, p. 3862–3872, 2017. 64 and 65.

Lidula, N.; Rajapakse, A. Microgrids research: A review of experimental microgrids and test systems. *Renewable and Sustainable Energy Reviews*, v. 15, n. 1, p. 186–202, 2011. ISSN 1364-0321. Available on: <https://www.sciencedirect.com/science/article/pii/S136403211000328X>. 65.

Limited, A. Application of advanced grid-scale inverters in the nem. *Available online: https://ahlecsolar.com.au/2021/03/12/sa-grid- forming-project-setting-worldwide-example/*, 2022. 39.

Lin, Y. et al. Pathways to the next-generation power system with inverter-based resources: Challenges and recommendations. *IEEE Electrification Magazine*, v. 10, n. 1, p. 10–21, 2022. 11 and 38.

Lin Yashen, J. H. E. B. B. J. J. D. F. R. H. L. H. N. V. P. G.-S. S. B. J. P.; Ellis., A. Research roadmap on grid-forming inverters. *National Renewable Energy Laboratory*, 2020. 77.

Lissandron, S.; Mattavelli, P. A controller for the smooth transition from grid-connected to autonomous operation mode. In: *2014 IEEE Energy Conversion Congress and Exposition (ECCE)*. 2014. p. 4298–4305. Doi:10.1109/ECCE.2014.6953987. 128.

Liu, J.; Miura, Y.; Ise, T. Comparison of dynamic characteristics between virtual synchronous generator and droop control in inverter-based distributed generators. *IEEE Transactions on Power Electronics*, v. 31, n. 5, p. 3600–3611, 2016. 62.

Liu, Q.; Tao, Y.; Liu, X.; Deng, Y.; He, X. Voltage unbalance and harmonics compensation for islanded microgrid inverters. *Power Electronics, IET*, v. 7, p. 1055–1063, 05 2014. 58.

Liu, Y.; Ge, B.; Abu-Rub, H.; Peng, F. Z. Control system design of battery-assisted quasi-z-source inverter for grid-tie photovoltaic power generation. *IEEE Transactions on Sustainable Energy*, v. 4, n. 4, p. 994–1001, 2013. 96.

Liu, Z.; Liu, J.; Zhao, Y. A unified control strategy for three-phase inverter in distributed generation. *IEEE Transactions on Power Electronics*, v. 29, n. 3, p. 1176–1191, 2014. Doi:10.1109/TPEL.2013.2262078. 128 and 129.

Lo, K.-Y.; Chen, Y.-M. Design of a seamless grid-connected inverter for microgrid applications. *IEEE Transactions on Smart Grid*, v. 11, n. 1, p. 194–202, 2020. 52.

Lo, K.-Y.; Chen, Y.-M. Design of a seamless grid-connected inverter for microgrid applications. *IEEE Transactions on Smart Grid*, v. 11, n. 1, p. 194–202, 2020. Doi:10.1109/TSG.2019.2919905. 128 and 129.

Lorenz, R.; Lipo, T.; Novotny, D. Motion control with induction motors. *Proceedings of the IEEE*, v. 82, n. 8, p. 1215–1240, 1994. 133.

Lourenço, L. F. N. et al. Stability analysis of grid-forming mmc-hvdc transmission connected to legacy power systems. *Energies*, v. 14, n. 23, 2021. ISSN 1996-1073. Available on: <https://www.mdpi.com/1996-1073/14/23/8017>. 39, 40, 67, 68, and 72.

Lu, X.; Wang, J.; Guerrero, J. M.; Zhao, D. Virtual-impedance-based fault current limiters for inverter dominated ac microgrids. *IEEE Transactions on Smart Grid*, v. 9, n. 3, p. 1599–1612, 2018. 56.

Luna, A. et al. Grid voltage synchronization for distributed generation systems under grid fault conditions. *IEEE Transactions on Industry Applications*, v. 51, n. 4, p. 3414–3425, 2015. 49 and 56.

Machado, A. A. P.; Brandao, D. I.; Pires, I. A.; Filho, B. d. J. C. Fault-tolerant utility interface power converter for low-voltage microgrids. In: *2017 IEEE 8th International Symposium on Power Electronics for Distributed Generation Systems (PEDG)*. 2017. p. 1–5. 39 and 75.

Machowski, J.; Bialek, J.; Bumby, J. Power system dynamics. stability and control. 01 2012. 59 and 62.

Majumder, R. et al. Improvement of stability and load sharing in an autonomous microgrid using supplementary droop control loop. *IEEE Transactions on Power Systems*, v. 25, n. 2, p. 796–808, 2010. 58.

Markovic, U.; Stanojev, O.; Aristidou, P.; Hug, G. Partial grid forming concept for 100Power Energy Society General Meeting (PESGM). 2018. p. 1–5. 46.

Matevosyan, J. et al. Grid-forming inverters: Are they the key for high renewable penetration? *IEEE Power and Energy Magazine*, v. 17, n. 6, p. 89–98, 2019. Doi:10.1109/MPE.2019.2933072. 162.

Matevosyan, J. et al. Grid-forming inverters: Are they the key for high renewable penetration? *IEEE Power and Energy Magazine*, v. 21, n. 2, p. 77–86, 2023. 37.

Mattavelli, P. An improved deadbeat control for ups using disturbance observers. *IEEE Transactions on Industrial Electronics*, v. 52, n. 1, p. 206–212, 2005. 55.

Medina, P.; Bizuayehu, A.; Catalão, J.; Rodrigues, E.; Contreras, J. Electrical energy storage systems: Technologies' state-of-the-art, techno-economic benefits and applications analysis. In: *2014 47th Hawaii International Conference on System Sciences*. 2014. p. 2295–2304. 36.

Miao, Z.; Xu, L.; Disfani, V. R.; Fan, L. An soc-based battery management system for microgrids. *IEEE Transactions on Smart Grid*, v. 5, n. 2, p. 966–973, 2014. 39 and 67.

Milano, F.; Dörfler, F.; Hug, G.; Hill, D. J.; Verbič, G. Foundations and challenges of low-inertia systems (invited paper). In: *2018 Power Systems Computation Conference (PSCC)*. 2018. p. 1–25. 36.

Miveh, M.; Rahmat, M. F.; Ghadimi, A.; Mustafa, M. Control techniques for three-phase four-leg voltage source inverters in autonomous microgrids: A review. *Renewable and Sustainable Energy Reviews*, v. 54, p. 1592–1610, 02 2016. 25 and 55.

Mobile and fixed offshore units — Electrical installations — Part 1: General requirements and conditions. *IEC 61892-1:2019*, 2019. 77.

Mohamed, Y. A.-R. I.; El-Saadany, E. F. Adaptive decentralized droop controller to preserve power sharing stability of paralleled inverters in distributed generation microgrids. *IEEE Transactions on Power Electronics*, v. 23, n. 6, p. 2806–2816, 2008. 58.

Mohamed, Y. A.-R. I.; Zeineldin, H. H.; Salama, M. M. A.; Seethapathy, R. Seamless formation and robust control of distributed generation microgrids via direct voltage control and optimized dynamic power sharing. *IEEE Transactions on Power Electronics*, v. 27, n. 3, p. 1283–1294, 2012. Doi:10.1109/TPEL.2011.2164939. 128.

Monadi, M. et al. Analysis of ferroresonance effects in distribution networks with distributed source units. In: *IECON 2013 - 39th Annual Conference of the IEEE Industrial Electronics Society*. 2013. p. 1974–1979. 40 and 74.

Mozina, C. J. Impact of smart grids and green power generation on distribution systems. *IEEE Transactions on Industry Applications*, v. 49, n. 3, p. 1079–1090, 2013. 40 and 74.

Nabae, A.; Takahashi, I.; Akagi, H. A new neutral-point-clamped pwm inverter. *IEEE Transactions on Industry Applications*, IA-17, n. 5, p. 518–523, 1981. Doi:10.1109/TIA.1981.4503992. 96.

Nazifi, H.; Radan, A. Current control assisted and non-ideal proportional-resonant voltage controller for four-leg three-phase inverters with time-variant loads. In: *4th Annual International Power Electronics, Drive Systems and Technologies Conference*. 2013. p. 355–360. 55.

Ndreko, M.; Rüberg, S.; Winter, W. Grid forming control scheme for power systems with up to 100% power electronic interfaced generation: a case study on great britain test system. *IET Renewable Power Generation*, v. 14, n. 8, p. 1268–1281, 2020. Doi:10.1049/iet-rpg.2019.0700. 162.

Nestor, S. Major grid-forming battery gains momentum. *Available online: https://www.energymagazine.com.au/major-grid- forming-battery-gains-momentum/.*, 2022. 39.

Ninad, N. A.; Lopes, L. A. C. Unbalanced operation of per-phase vector controlled four-leg grid forming inverter for stand-alone hybrid systems. In: *IECON 2012 - 38th Annual Conference on IEEE Industrial Electronics Society*. 2012. p. 3500–3505. 39, 66, and 75.

Ofir, R.; Markovic, U.; Aristidou, P.; Hug, G. Droop vs. virtual inertia: Comparison from the perspective of converter operation mode. In: *2018 IEEE International Energy Conference (ENERGYCON)*. 2018. p. 1–6. 62.

Ojo, Y.; Watson, J.; Lestas, I. An improved control scheme for grid-forming inverters. In: *2019 IEEE PES Innovative Smart Grid Technologies Europe (ISGT-Europe)*. 2019. p. 1–5. 52.

Oliveira, G. et al. Nonlinear control for modular multilevel converters with enhanced stability region and arbitrary closed loop dynamics. *International Journal of Electrical Power Energy Systems*, v. 126, p. 106590, 03 2021. 40, 72, and 75.

Ooi, B.; Wang, X. Voltage angle lock loop control of the boost type pwm converter for hvdc application. *IEEE Transactions on Power Electronics*, v. 5, n. 2, p. 229–235, 1990. 48.

Ortjohann, E. et al. Grid-forming three-phase inverters for unbalanced loads in hybrid power systems. In: *2006 IEEE 4th World Conference on Photovoltaic Energy Conference*. 2006. v. 2, p. 2396–2399. 39, 66, and 75.

O'Rourke, C. J.; Qasim, M. M.; Overlin, M. R.; Kirtley, J. L. A geometric interpretation of reference frames and transformations: dq0, clarke, and park. *IEEE Transactions on Energy Conversion*, v. 34, n. 4, p. 2070–2083, 2019. 54.

Paquette, A. D.; Divan, D. M. Virtual impedance current limiting for inverters in microgrids with synchronous generators. *IEEE Transactions on Industry Applications*, v. 51, n. 2, p. 1630–1638, 2015. 56.

Paquette, A. D.; Reno, M. J.; Harley, R. G.; Divan, D. M. Sharing transient loads : Causes of unequal transient load sharing in islanded microgrid operation. *IEEE Industry Applications Magazine*, v. 20, n. 2, p. 23–34, 2014. 46.

Parreiras, T.; Justino, J. C. G.; Rocha, A.; Filho, B. C. True unit power factor active front end for high capacity belt conveyor systems. *IEEE Transactions on Industry Applications*, v. 52, 10 2015. 75.

Parreiras, T. M. *Retificador Trifásico de Fator de Potência Verdadeiramente Unitário sem a Utilização de Filtros Senoidais*. 2015. 75.

Parreiras, T. M. *Sistema de Condicionamento de Potência Com Correntes Senoidais Na Rede de Alimentação*. Tese (Doutorado) — Universidade Federal de Minas Gerais, 2020. 15, 75, 90, 129, 130, 131, 132, 133, and 140.

Parreiras, T. M.; Alves, M. H. d. S.; Almeida, C. E.; Silva, S. M.; Filho, B. d. J. C. The true unit power factor converter with flexible arrangement for battery energy systems: Series and separate dc bus connection. In: *2020 IEEE Applied Power Electronics Conference and Exposition (APEC)*. 2020. p. 3405–3412. 74, 75, 129, and 140.

Parreiras, T. M.; Alves, M. H. d. S.; Bastos, R. R.; Pires, I. A.; Filho, B. d. J. C. The true unity power factor converter for basic oxygen furnace charging cranes. *IEEE Transactions on Industry Applications*, v. 57, n. 5, p. 5507–5516, 2021. 73, 75, 129, and 140.

Parreiras, T. M.; Alves, M. H. da S.; Bastos, R. R.; Pires, I. A.; Filho, B. d. J. C. The true unity power factor converter for bof charging cranes. In: *2020 IEEE Industry Applications Society Annual Meeting*. 2020. p. 1–9. 75.

Parreiras, T. M.; Filho, B. J. C. Current control of three level neutral point clamped voltage source rectifiers using selective harmonic elimination. In: *IECON 2014 - 40th Annual Conference of the IEEE Industrial Electronics Society*. 2014. p. 4608–4614. 75 and 80.

Parreiras, T. M.; Justino, J. C. G.; Filho, B. d. J. C. The true unity power factor converter — a practical filterless solution for sinusoidal currents. In: *2015 9th International Conference on Power Electronics and ECCE Asia (ICPE-ECCE Asia)*. 2015. p. 2557–2565. 73, 75, 129, and 140.

Parreiras, T. M.; Rocha, A. V.; Justino, J. C. G.; Filho, B. d. J. C. True unit power factor active front end for high capacity belt conveyor systems. In: *2015 IEEE Industry Applications Society Annual Meeting*. 2015. p. 1–9. 73, 75, 129, and 140.

Patel, H. S.; Hoft, R. G. Generalized techniques of harmonic elimination and voltage control in thyristor inverters: Part i–harmonic elimination. *IEEE Transactions on Industry Applications*, IA-9, n. 3, p. 310–317, 1973. 78, 79, 80, and 81.

Patel, H. S.; Hoft, R. G. Generalized techniques of harmonic elimination and voltage control in thyristor inverters: Part ii — voltage control techniques. *IEEE Transactions on Industry Applications*, IA-10, n. 5, p. 666–673, 1974. 78, 79, 80, and 81.

Pattabiraman, D.; Lasseter., R. H.; Jahns, T. M. Comparison of grid following and grid forming control for a high inverter penetration power system. In: *2018 IEEE Power Energy Society General Meeting (PESGM)*. 2018. p. 1–5. 51 and 52.

Peacok, B. World's largest 'grid-forming' battery to begin construction in australia. *Available online: https://www.pv- magazine.com/2021/08/10/worlds-largest-grid-forming-battery-to-begin-construction-in-australia/*, 2021. 39.

Peng, F. Z. Z-source inverter. *IEEE Transactions on Industry Applications*, v. 39, n. 2, p. 504–510, 2003. 95.

Peña, J. C. U.; Melo, G.; Canesin, C. A.; Sampaio, L. P. Robust control of a single-phase vsi with lcl filter for grid-tie and islanded operation modes applied to pv distributed generation in microgrids environment. In: *2014 IEEE Energy Conversion Congress and Exposition (ECCE)*. 2014. p. 785–792. 66.

Planas, E.; Muro, A. Gil de; Andreu, J.; Kortabarria, I.; Alegria, I. Martinez de. General aspects, hierarchical controls and droop methods in microgrids: A review. *Renewable and Sustainable Energy Reviews*, v. 17, p. 147–159, 01 2013. 58.

Plet, C. A.; Brucoli, M.; McDonald, J. D. F.; Green, T. C. Fault models of inverter-interfaced distributed generators: Experimental verification and application to fault analysis. In: *2011 IEEE Power and Energy Society General Meeting*. 2011. p. 1–8. 55.

Pogaku, N.; Prodanovic, M.; Green, T. C. Modeling, analysis and testing of autonomous operation of an inverter-based microgrid. *IEEE Transactions on Power Electronics*, v. 22, n. 2, p. 613–625, 2007. 57.

Qoria, T. et al. Tuning of cascaded controllers for robust grid-forming voltage source converter. In: *2018 Power Systems Computation Conference (PSCC)*. 2018. p. 1–7. Doi:10.23919/PSCC.2018.8443018. 163.

Qoria, T. et al. Inertia effect and load sharing capability of grid forming converters connected to a transmission grid. In: *15th IET International Conference on AC and DC Power Transmission (ACDC 2019)*. 2019. p. 1–6. 44.

Qoria, T. et al. Tuning of ac voltage-controlled vsc based linear quadratic regulation. In: *2019 IEEE Milan PowerTech*. 2019. p. 1–6. 55.

Qoria, T. et al. Power converters classification and characterization in power transmission systems. In: *2019 21st European Conference on Power Electronics and Applications (EPE '19 ECCE Europe)*. 2019. p. P.1–P.9. 11, 46, 47, 51, and 52.

Quan, X. et al. Photovoltaic synchronous generator: Architecture and control strategy for a grid-forming pv energy system. *IEEE Journal of Emerging and Selected Topics in Power Electronics*, v. 8, n. 2, p. 936–948, 2020. Doi:10.1109/JESTPE.2019.2953178. 162 and 163.

Rahmoun, A.; Armstorfer, A.; Biechl, H.; Rosin, A. Mathematical modeling of a battery energy storage system in grid forming mode. In: *2017 IEEE 58th International Scientific Conference on Power and Electrical Engineering of Riga Technical University (RTUCON)*. 2017. p. 1–6. Doi:10.1109/RTUCON.2017.8125625. 162 and 163.

Rese, L.; Costa, A. S.; Silva, A. S. e. Enhanced modeling and control of vsis in microgrids operating in grid-connected mode. In: *2012 IEEE PES Innovative Smart Grid Technologies (ISGT)*. 2012. p. 1–8. 39 and 66.

Rocabert, J.; Luna, A.; Blaabjerg, F.; Rodríguez, P. Control of power converters in ac microgrids. *IEEE Transactions on Power Electronics*, v. 27, n. 11, p. 4734–4749, 2012. 11, 37, 44, 45, 46, 49, 52, and 98.

Rodriguez, P. et al. Decoupled double synchronous reference frame pll for power converters control. *IEEE Transactions on Power Electronics*, v. 22, n. 2, p. 584–592, 2007. 129.

Rokrok, E.; Golshan, M. Comprehensive control scheme for an inverter-based distributed generation unit. *Iranian Journal of Science Technology, Transaction B: Engineering*, v. 33, p. 477–490, 12 2009. 55.

Rokrok, E.; Golshan, M. E. H. Adaptive voltage droop scheme for voltage source converters in an islanded multibus microgrid. *IET Generation Transmission Distribution*, v. 4, p. 562–578, 06 2010. 58.

Rokrok, E. et al. Impact of grid-forming control on the internal energy of a modular multilevel converter. In: *2020 22nd European Conference on Power Electronics and Applications (EPE'20 ECCE Europe)*. 2020. p. 1–10. 72.

Roscoe A.; Brogan, P. E. D. K. T. G. I. C. J. D. S. R. Practical experience of operating a grid forming wind park and its response to system events. *In Proceedings of the 18th Wind Integration Workshop, Dublin, Ireland, 14–18 October 2019*, 2019. 39.

Rosso, R.; Wang, X.; Liserre, M.; Lu, X.; Engelken, S. Grid-forming converters: Control approaches, grid-synchronization, and future trends—a review. *IEEE Open Journal of Industry Applications*, v. 2, p. 93–109, 2021. 37.

Saim, A. et al. Stability analysis and robust damping of multiresonances in distributed-generation-based islanded microgrids. *IEEE Transactions on Industrial Electronics*, v. 66, n. 11, p. 8958–8970, 2019. 39, 40, 67, 68, 74, and 98.

Sales, S. Grid-forming project setting worldwide example. *Available online: https://ahlecsolar.com.au/2021/03/12/sa-grid- forming-project-setting-worldwide-example/*, 2022. 39.

Sao, C.; Lehn, P. Autonomous load sharing of voltage source converters. *IEEE Transactions on Power Delivery*, v. 20, n. 2, p. 1009–1016, 2005. 58.

Savaghebi, M.; Jalilian, A.; Vasquez, J. C.; Guerrero, J. M. Autonomous voltage unbalance compensation in an islanded droop-controlled microgrid. *IEEE Transactions on Industrial Electronics*, v. 60, n. 4, p. 1390–1402, 2013. 58.

Seo, G.-S. et al. Dispatchable virtual oscillator control for decentralized inverter-dominated power systems: Analysis and experiments. In: *2019 IEEE Applied Power Electronics Conference and Exposition (APEC)*. 2019. p. 561–566. 65.

Serban, I.; Ion, C. Microgrid control based on a grid-forming inverter operating as virtual synchronous generator with enhanced dynamic response capability. *International Journal of Electrical Power Energy Systems*, v. 89, p. 94 – 105, 07 2017. 56 and 58.

Sharma, B. et al. Power sharing in three-level npc inverter based three-phase four-wire islanding microgrids with unbalanced loads. *IEEE Access*, v. 11, p. 20725–20740, 2023. 67.

Shi, Z.; Li, J.; Nurdin, H. I.; Fletcher, J. E. Comparison of virtual oscillator and droop controlled islanded three-phase microgrids. *IEEE Transactions on Energy Conversion*, v. 34, n. 4, p. 1769–1780, 2019. 62.

Silva, F. S. F. e; Ribeiro, L. A. de S.; Matos, J. G. de. Bidirectional dc-ac converter for isolated microgrids with voltage unbalance reduction capabilities. In: *2014 IEEE Energy Conversion Congress and Exposition (ECCE)*. 2014. p. 4985–4991. 39, 67, and 75.

Singh Luiz A.C. Lopes, N. A. N. M. Grid forming battery energy storage system (bess) for a highly unbalanced hybrid mini-grid. *Electric Power Systems Research*, v. 127, p. 126–133, 2015. 39, 66, and 75.

Steimer, P.; Manjrekar, M. Practical medium voltage converter topologies for high power applications. In: *Conference Record of the 2001 IEEE Industry Applications Conference. 36th IAS Annual Meeting (Cat. No.01CH37248)*. 2001. v. 3, p. 1723–1730 vol.3. 39, 68, and 69.

Sánchez-Sánchez, E.; Prieto-Araujo, E.; Gomis-Bellmunt, O. The role of the internal energy in mmcs operating in grid-forming mode. *IEEE Journal of Emerging and Selected Topics in Power Electronics*, v. 8, n. 2, p. 949–962, 2020. 40, 72, and 75.

Tang, Z.; Yang, Y.; Blaabjerg, F. Power electronics: The enabling technology for renewable energy integration. *CSEE Journal of Power and Energy Systems*, v. 8, n. 1, p. 39–52, 2022. 71, 73, and 75.

Taoufik, Q. et al. Direct ac voltage control for grid-forming inverters. *Journal of power electronics*, 12 2019. 57 and 75.

Taoufik, Q.; Wu, H.; Wang, X.; Colak, I. Variable virtual impedance-based overcurrent protection for grid-forming inverters: Small-signal, large-signal analysis and improvement. *IEEE Transactions on Smart Grid*, p. 1–1, 2022. 39 and 72.

Tayab, U. B.; Roslan, M. A.; Hwai, L.; Kashif, M. A review of droop control techniques for microgrid. *Renewable and Sustainable Energy Reviews*, v. 76, p. 717–727, 09 2017. 58.

Tayyebi, A.; Gross, D.; Anta, A.; Kupzog, F.; Dörfler, F. Interactions of grid-forming power converters and synchronous machines – a comparative study. 02 2019. 63.

Teodorescu, R.; Liserre, M.; Rodriguez, P. In: _____. *Grid Converters for Photovoltaic and Wind Power Systems*. 2007. 51.

Tuckey, A.; Round, S. Grid-forming inverters for grid-connected microgrids: Developing "good citizens" to ensure the continued flow of stable, reliable power. *IEEE Electrification Magazine*, v. 10, n. 1, p. 39–51, 2022. 11, 25, 38, 39, 44, 47, 52, 54, 56, 66, and 75.

Ullah, S.; Khan, L.; Sami, I.; Ullah, N. Consensus-based delay-tolerant distributed secondary control strategy for droop controlled ac microgrids. *IEEE Access*, v. 9, p. 6033–6049, 2021. 52.

Ullah, S.; Khan, L.; Sami, I.; Ro, J.-S. Voltage/frequency regulation with optimal load dispatch in microgrids using smc based distributed cooperative control. *IEEE Access*, v. 10, p. 64873–64889, 2022. 56.

Hitachi Power Semicondutor Devices. *Insulated Gate Bipolar Transistor (IGBT) and diode modules*, 2024. Accessed: Jun. 1, 2024. [Online] Avaliable: https://www.hitachienergy.com/products-and-solutions/semiconductors/insulated-gate-bipolar-transistor-igbt-and-diode-modules. 96.

Infineon Technologies: Semiconductor & System Solutions. *IGBTs – Insulated Gate Bipolar Transistors*, 2024. Accessed: Jun. 1, 2024. [Online] Avaliable: https://www.infineon.com/cms/en/product/power/igbt/igbt-modules/. 96.

(UPS)-Part 3: Method of specifying the performance and test requirements. *IEC 62040-3:1999*, 1999. 102 and 121.

Utility Type Battery Chargers NEMA Standard. *NEMA PE 5-1997(R2003)*, 1997. 73.

Vandoorn, T.; De Kooning, J.; Meersman, B.; Vandevelde, L. Review of primary control strategies for islanded microgrids with power-electronic interfaces. *Renewable and Sustainable Energy Reviews*, v. 19, p. 613–628, 2013. ISSN 1364-0321. Available on: <https://www.sciencedirect.com/science/article/pii/S1364032112006764>. 67 and 68.

Vartanian, C. et al. Ensuring system reliability: Distributed energy resources and bulk power system considerations. *IEEE Power and Energy Magazine*, v. 16, n. 6, p. 52–63, 2018. 36.

Vasquez, J. C.; Guerrero, J. M.; Luna, A.; Rodriguez, P.; Teodorescu, R. Adaptive droop control applied to voltage-source inverters operating in grid-connected and islanded modes. *IEEE Transactions on Industrial Electronics*, v. 56, n. 10, p. 4088–4096, 2009. 58.

Vasquez, J. C.; Guerrero, J. M.; Miret, J.; Castilla, M.; Vicuña, L. G. de. Hierarchical control of intelligent microgrids. *IEEE Industrial Electronics Magazine*, v. 4, n. 4, p. 23–29, 2010. 57.

Vazquez, S.; Lukic, S. M.; Galvan, E.; Franquelo, L. G.; Carrasco, J. M. Energy storage systems for transport and grid applications. *IEEE Transactions on Industrial Electronics*, v. 57, n. 12, p. 3881–3895, 2010. 95.

Vechiu, I.; Camblong, H.; Tapia, G.; Dakyo, B.; Curea, O. Control of a four-leg inverter for hybrid power system applications with unbalanced load. *Energy Conversion and Management*, v. 48, p. 2119–2128, 07 2007. 55.

Vukojevic, A.; Lukic, S. Microgrid protection and control schemes for seamless transition to island and grid synchronization. *IEEE Transactions on Smart Grid*, v. 11, n. 4, p. 2845–2855, 2020. Doi:10.1109/TSG.2020.2975850. 128 and 145.

Vyawahare, D. Dynamics of power flow in a stand-alone microgrid using four-leg inverters for nonlinear and unbalanced loads. In: Chauhan, R. K.; Chauhan, K. (Ed.). *Distributed Energy Resources in Microgrids*. Academic Press, 2019. p. 113–141. ISBN 978-0-12-817774-7. Available on: <https://www.sciencedirect.com/science/article/pii/B9780128177747000053>. 66.

Wang, G. et al. A review of power electronics for grid connection of utility-scale battery energy storage systems. *IEEE Transactions on Sustainable Energy*, v. 7, n. 4, p. 1778–1790, 2016. 39, 68, 69, 70, 71, 73, and 75.

Wang, G. et al. A review of power electronics for grid connection of utility-scale battery energy storage systems. *IEEE Transactions on Sustainable Energy*, v. 7, n. 4, p. 1778–1790, 2016. Doi:10.1109/TSTE.2016.2586941. 163.

Wang, X.; Blaabjerg, F. Harmonic stability in power electronic-based power systems: Concept, modeling, and analysis. *IEEE Transactions on Smart Grid*, v. 10, n. 3, p. 2858–2870, 2019. 39 and 40.

Wang, X.; Blaabjerg, F.; Chen, Z. Autonomous control of inverter-interfaced distributed generation units for harmonic current filtering and resonance damping in an islanded microgrid. In: *2012 IEEE Energy Conversion Congress and Exposition (ECCE)*. 2012. p. 211–218. 58.

Wang, X. et al. Grid-synchronization stability of converter-based resources—an overview. *IEEE Open Journal of Industry Applications*, v. 1, p. 115–134, 2020. 49, 52, and 56.

Wu, W. et al. A virtual inertia control strategy for dc microgrids analogized with virtual synchronous machines. *IEEE Transactions on Industrial Electronics*, v. 64, n. 7, p. 6005–6016, 2017. 56.

Wu, W. et al. Enhanced operation of grid-following vscs with alternating-voltage control in ultraweak grids. *IEEE Journal of Emerging and Selected Topics in Power Electronics*, v. 13, n. 2, p. 2270–2284, 2025. 56.

Xavier, L. et al. Power converters for battery energy storage systems connected to medium voltage systems: a comprehensive review. *BMC Energy*, v. 1, 07 2019. 39, 68, 69, 70, 71, and 75.

Yang, L.; Liu, J.; Wang, C.; Du, G. Sliding mode control of three-phase four-leg inverters via state feedback. *Journal of Power Electronics*, v. 14, p. 1028–1037, 2014. 55.

Yao, B. et al. Accelerated degradation testing and failure mechanism analysis of metallized film capacitors for ac filtering. *IEEE Transactions on Power Electronics*, v. 39, n. 5, p. 6256–6270, 2024. 40 and 74.

Yao, Z.; Xiao, L.; Yan, Y. Seamless transfer of single-phase grid-interactive inverters between grid-connected and stand-alone modes. *IEEE Transactions on Power Electronics*, v. 25, n. 6, p. 1597–1603, 2010. 55.

Yazdani, A.; Iravani, R. Grid-imposed frequency vsc system: Control in dq-frame. In: _____. 2010. p. 204–244. ISBN 9780470521564. 131.

Yazdani, A.; Iravani, R. *Voltage-Sourced Converters in Power Systems: Modeling, Control, and Applications*. Wiley, 2010. (IEEE Press). ISBN 9780470551561. Available on: <https://books.google.com.br/books?id=_x_4Cu-BKwkC>. 66.

Zhang, H.; Xiang, W.; Lin, W.; Wen, J. Grid forming converters in renewable energy sources dominated power grid: Control strategy, stability, application, and challenges. *Journal of Modern Power Systems and Clean Energy*, v. 9, n. 6, p. 1239–1256, 2021. 37.

Zhang, L.; Harnefors, L.; Nee, H.-P. Power-synchronization control of grid-connected voltage-source converters. *IEEE Transactions on Power Systems*, v. 25, n. 2, p. 809–820, 2010. 48.

Zhang, X.; Wang, J.; Li, C. Three-phase four-leg inverter based on voltage hysteresis control. In: *2010 International Conference on Electrical and Control Engineering*. 2010. p. 4482–4485. 55.

Zhao, F. et al. Control interaction modeling and analysis of grid-forming battery energy storage system for offshore wind power plant. *IEEE Transactions on Power Systems*, v. 37, n. 1, p. 497–507, 2022. Doi:10.1109/TPWRS.2021.3096850. 163.

Zhao, F.; Zhu, T.; Li, Z.; Wang, X. Low-frequency resonances in grid-forming converters: Causes and damping control. *IEEE Transactions on Power Electronics*, v. 39, n. 11, p. 14430–14447, 2024. Doi:10.1109/TPEL.2024.3424296. 163 and 165.

Zhong, Q.-C.; Nguyen, P.-L.; Ma, Z.; Sheng, W. Self-synchronized synchronverters: Inverters without a dedicated synchronization unit. *IEEE Transactions on Power Electronics*, v. 29, n. 2, p. 617–630, 2014. 11, 44, 52, 59, and 61.

Zhong, Q.-C.; Weiss, G. Synchronverters: Inverters that mimic synchronous generators. *IEEE Transactions on Industrial Electronics*, v. 58, n. 4, p. 1259–1267, 2011. 48, 59, and 65.

Zhou, J. Z.; Ding, H.; Fan, S.; Zhang, Y.; Gole, A. M. Impact of short-circuit ratio and phase-locked-loop parameters on the small-signal behavior of a vsc-hvdc converter. *IEEE Transactions on Power Delivery*, v. 29, n. 5, p. 2287–2296, 2014. Doi:10.1109/TPWRD.2014.2330518. 163.